The Gas-Phase Ligand Exchange of Select Alkaline Earth and Transition Metal β-diketonate Complexes

by

Kathleen Masena Fleming

Submitted in Partial Fulfillment of the Requirements

for the Degree of

Master of Science

in the

Chemistry

Program

YOUNGSTOWN STATE UNIVERSITY

May 2016

The Gas-Phase Ligand Exchange of Select Alkaline Earth and Transition Metal β-diketonate Complexes

Kathleen Masena Fleming

I hereby release this thesis to the public. I understand that this thesis will be made available from the OhioLINK ETD Center and the Maag Library Circulation Desk for public access. I also authorize the University or other individuals to make copies of this thesis as needed for scholarly research.

Signature:

Kathleen M. Fleming, Student Date

Approvals:

Dr. Brian D. Leskiw, Thesis Advisor Date

Dr. Howard D. Mettee, Committee Member Date

Dr. Ganesaratnam K. Balendiran, Committee Member Date

Dr. Salvatore A. Sanders, Dean of Graduate Studies Date

Abstract

Gas-phase ligand exchange reactions involving select alkaline earth and transition metal β-diketonate complexes were evaluated using a triple quadrupole mass spectrometer. Once co-sublimation reactions confirmed ligand exchange, selective reactions were initiated to elucidate the mechanism of exchange. A series of co-sublimation and selective reactions involving several β-diketonate complexes were investigated and are reported herein. The results from these gas-phase reactions have shed new light on the gas-phase ligand exchange of alkaline earth and transition metal β-diketonate complexes.

Acknowledgements

I would first like to thank the Youngstown State University Chemistry Department for the wealth of knowledge they have provided me the past several years. My acceptance to medical school is a direct result of my two years in the Master's program, and I have emerged from the program well-prepared and ready to tackle the challenges that lie ahead of me.

I would also like to thank Mr. Ray Hoff for his endless support with the mass spectrometer. Without his hard work and diligent efforts the data reported in this manuscript would not be possible.

My thesis would also not have been possible without the help of my committee members, Dr. Howard Mettee and Dr. Ganesaratnam Balendiran. I would like to thank them for their time and criticism, which was compulsory for the formation of the polished final product.

For their unconditional love and constant support, I want to thank my incredible parents, siblings, and friends. To my amazing boyfriend, I want to say thank you for your patience, forgiveness, and love. Ultimately, any success I have or will ever achieve is attributed to my outstanding support system, and for that I am eternally grateful.

And last, but certainly not least, Dr. Brian Leskiw, my advisor and the best mentor I have ever had. From the bottom of my heart, I want to thank him for his guidance, criticism, and the opportunity to work as his graduate student and teaching assistant. The time and effort he has put into the formation of my final thesis is inspiring, and I will continue to use the lessons he has taught me as I move onto future career endeavors.

Table of Contents

Chapters

List of Figures

List of Tables

List of Equations

Chapter 1: Literature Review

1.1 β-Diketonate Complexes

Metal β-diketonate complexes are a tremendously versatile class of coordination compounds. Within these compounds, a chelating metal center covalently interacts with ligands possessing two ketone functionalities located β- to each other along a carbon backbone. These complexes are both extremely stable in the liquid and solid phase, and readily sublime under reduced pressure[1]. Moreover, variability in the chelating metal center coupled to the functionalities of the attached ligands has made these complexes widely studied and applicable in a variety of physical and biological sciences[2–5].

1.2 β-Diketonate Complexes in OLEDs

Light emitting diodes, or LEDs, are widely used in electronic appliances, including television sets, remote controls, computer monitors, and cell phones. LEDs contain both a *p*-type and *n*-type semiconductor, and when a current is applied across the semiconductors, excess electrons from the *n*-type semiconductor are forced to fill in the "holes" generated by the *p*-type semiconductor. Filling in the holes causes the electrons to lose energy through the emission of photons. The color of the light is determined by the wavelength of the photon, which is ultimately generated by the band gap created within the semiconductor. When an organic substrate is used instead of an inorganic compound, it is then classified as an organic light-emitting diode, or OLED. OLEDs have many advantages to classic liquid crystal or plasma displays, including improved power efficiency, the potential for flexible screens, and eco-friendly disposal[6]. The biggest disadvantage is the decreased lifespan compared to conventional displays. However, OLED's utilizing trivalent rare-earth metal β-diketonate complexes are shown to limit

interactions with the surrounding environment due to the shielding of 4f electrons by the $5s^2 5p^6$ orbitals[7]. Furthermore, the quantum efficiency of OLED's using rare earth metals has been shown to be near 100%, which is four times higher than those of OLED's with other materials[8]. The first rare earth β-diketonate complexes utilized for OLEDs were trivalent terbium complexes, which were favored due to the solubility and volatility of the complex[9]. Since then, β-diketonate complexes using europium, ytterbium, samarium, and gadolinium have been evaluated for their efficiency as OLED's, and show much promise for future applications[5,10,11].

1.3 β-Diketonate Complexes as *in-vivo* Antitumor Agents

Metal β-diketonate complexes have also been used *in vivo* as cytotoxic antitumor agents. Alveolar echinococcosis (AE) is a rare disease resulting from the implantation of *Echinococcus multilocularis* (*E. multilocularis*) larva in the human liver[12]. Spores are ingested from contaminated food and become activated in the acidic environment of the stomach. When parasite larvae proliferate in the liver, they form tumor-like growths that can even metastasize to other organs. If not detected early, this disease is often fatal. Treatment options include surgery and intense chemotherapy, but since this disease is extremely rare (infecting only 1/100,000 of the population annually), limited research has been done on alternative parasitocidal compounds. However, in one study, ruthenium β-diketonate complexes were synthesized and their cytotoxicity against *E. multilocularis* was evaluated[12]. Two groups of compounds, pictured in Figure 1.1, were generated for comparison.

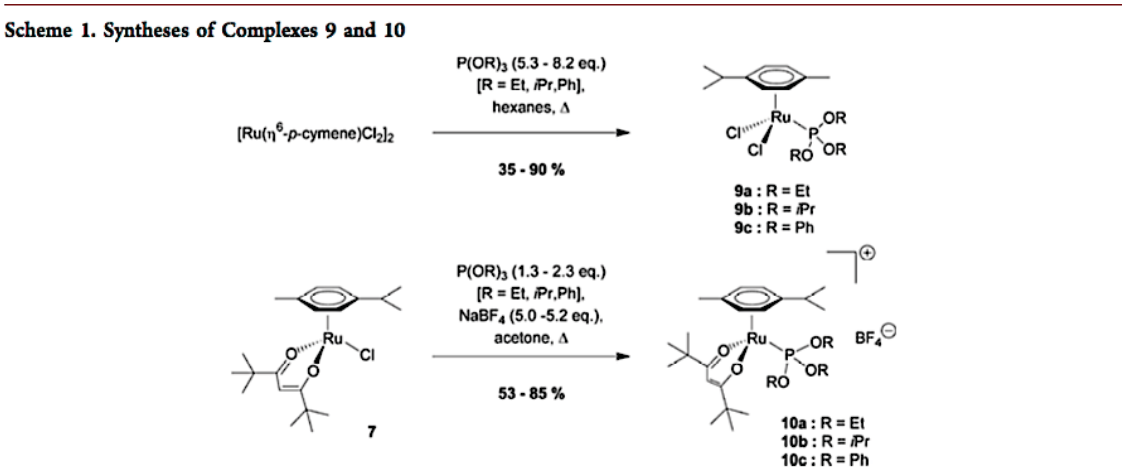

Figure 1.1: Novel η^6-areneruthenium(II) phosphite complexes[12].

Compounds in Group 9 in Figure 1.1 possessed two labile chloride ligands, whereas compounds in Group 10 replaced the chlorides with bis-chelated 2,2,6,6-tetramethylheptanedionate, a β-diketonate ligand. Toxicity was evaluated by monitoring phosphoglucoseisomerase (PGI) levels, which is released by the dying parasites; as more cells atrophy, more PGI is released. Parasites were exposed to ~20 mM concentrations of one of the novel compounds, and PGI levels were measured to assess the degree of parasite death. Compounds in Group 10 were by far better cytotoxic agents, with the percentage of PGI released nearing 100%, indicating that close to 100% of the parasites were killed within the five days of treatment. Other β-diketonate complexes utilizing platinum, hafnium, zirconium, ruthenium, and titanium have also been evaluated as antitumor agents, and show high efficacy towards ovarian cancer, testicular cancer, bladder cancer, as well as tumors of the head, neck, lung, and gastrointestinal tract [3,13–17].

1.4 β-Diketonate Complexes in thin-film deposition

The applications of β-diketonate complexes also extend into the realm of the gas phase, particularly in the synthesis of semiconductors and other heavy metal thin-films via metal-organic chemical vapor deposition (MOCVD)[18,19]. This process allows single

layers of a solid substrate to be deposited onto a semiconductor wafer in the gas phase. Wafers may be only a few nanometers thick, making conventional wet benchtop chemistry nearly impossible, but gas-phase deposition allows desired functionalities to be precisely layered. The thin film wafer is exposed to an atmosphere of the desired metal or substrate to be deposited, and the temperature within the chamber largely controls reactions on the surface.

Metal β-diketonate complexes are optimal substrates for MOCVD due to the variability in the ligands and chelating metals, as well as their inherent volatility in the gas phase[20]. Cerium ions chelated to 2,2,6,6-tetramethyl-3,5-heptanedionate (tmtm) ligands have shown to be a very effective liquid precursor in the formation of CeO_2 thin films due to its relative stability/volatility in the gas phase. Moreover, they also lack fluorinated ligands, which can help improve volatility but will also notoriously contaminate the thin films[21]. Yttrium, barium, and copper compounds also chelated to *tmtm* ligands have been used in the formation of $YBa_2Cu_3O_{7-x}$ high-temperature superconductors[22,23]. Other β-diketonate complexes used as precursor for rare earth thin films include lanthanum, samarium, neodymium, and gadolinium, all of which show much promise in future applications[24,25].

1.5 Keto-enol tautomerization in β-Diketonate Complexes

During the synthesis of β-diketonate complexes, the chelating metal cation forms a coordinate covalent bond with the diketonate functionalities. This bond readily forms because of the diketonate's innate ability to undergo keto-enol tautomerization, a state of chemical equilibrium in which the extraction of a β-proton produces an area of electron

delocalization. The delocalization is representative of a balance between the keto (or ketone) and enol (alcohol) tautomers.

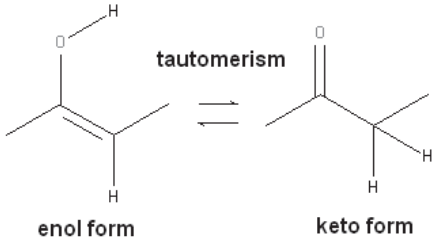

Figure 1.2: Keto-enol tautomerization.

In β-diketonates, this area of delocalization extends between the ketone moieties, demonstrated by the schematic below in Figure 1.3.

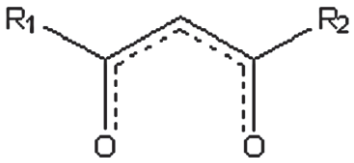

Figure 1.3: Schematic of delocalization in β-diketonate complexes.

Since there is no direct carbon-to-metal bonding, metal β-diketonates are thus classified as coordination complexes instead of organometallics. Moreover, the incidence of keto-enol tautomerization allows metal β-diketonates to exhibit bidentate chelation. During synthesis of the β-diketonate the ligand is exposed to a basic medium, wherein the central hydrogen is stripped, causing the area of electron delocalization across the entire molecule. It is this area of delocalization that allows the ligand to bond at two different areas of the metal, producing bidentate chelation.

Sloop *et. al*. examined whether the keto- or enol- form of fluorinated β-diketonates is preferred in bonding using Infrared Spectroscopy (IR), Nuclear Magnetic Resonance (NMR), and Ultraviolet-Visible Spectroscopy (UV-Vis)[26]. Overall, they found that equilibrium lies in favor of the enol-form because it maximizes conjugation across

the system. However, they also report that the preference of the keto- or enol- tautomer and the overall stability of the coordination complex is heavily influenced by whether the R-group is electron donating or electron withdrawing. This is also extremely important when examining the patterns of fragmentation of β-diketonate complexes in the gas phase, which will be the central focus of the mechanisms proposed herein.

1.6 Fragmentation Patterns of β-Diketonate Complexes

The first comprehensive review on the fragmentation patterns of metal β-diketonates, specifically metal acetylacetonates, was published by Macdonald and Shannon in 1966[27]. Although much work has been done with metal β-diketonates since then, they laid a strong foundation upon which all subsequent research has been built. These previously reported patterns of fragmentation, or loss channels, are important to better understanding the formation of ligand exchange products in the gas phase.

In this study, fragmentation patterns for metal bis-acetylacetonates ($M(acac)_2$ where M = Mg, Ni, Cu, and Ca), metal bis-diethylacetylaceonates ($M(eeac)_2$, where M = Mg, Ni, Cu, and Co), metal bis-trifluorotrimethylacetylacetonates ($M(tftm)_2$, where M = Mg, Ni, Cu, and Pd), metal bis-trifluoroacetylacetonates ($M(tfac)_2$ where M = Ni), and metal bis-dibenzoylmethanes ($M(dbm)_2$, where M = Ni, Cu, and Mn) were all determined experimentally. Discussions of these fragmentation patterns will be addressed in the following chapters, and will contribute to the formulations of proposed gas-phase ligand exchange mechanisms.

Chapter 2

Characterization of Metal β-Diketonate Complexes by Mass Spectrometry

2.1 Mass Spectrometry

Mass spectrometry is one of the most frequently used analytical techniques in chemistry and has been employed extensively to characterize metal β-diketonate complexes. The unknown sample is first ionized, separated by its mass-to-charge (*m/z*) ratio, and finally detected. A generic schematic of the components of a mass spectrometer is displayed in Figure 2.1.

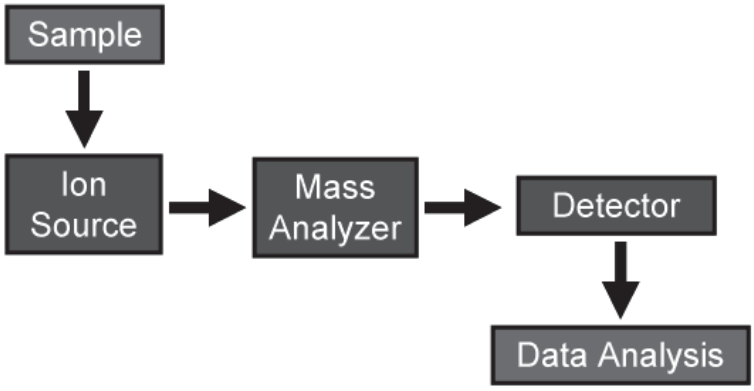

Figure 2.1: Generic schematic of a mass spectrometer.

Variations in ion sources and detectors give rise to different mass spectrometers, and each type of mass spectrometer provides unique insight into a given compound. Many different mass spectrometers have been used to analyze metal β-diketonate complexes, including chemical ionization (CI), matrix-assisted laser desorption/ionization time-of-flight (MALDI-TOF), fast atom bombardment (FAB), and finally electron impact (EI) mass spectrometry[28–32].

2.2 Chemical Ionization Mass Spectrometry

One mass spectrometric technique used previously to examine metal β-diketonates is chemical ionization (CI) mass spectrometry. Chemical ionization utilizes a reagent gas in

the ion source (typically ammonia or methane), which is ionized when bombarded by electrons. The primary ionized species subsequently reacts with other primary ion species, creating a secondary cation (such as CH_5^+ or NH_4^+), which then donates its proton to the analyte on a direct insertion probe. The generated cationic species can then be analyzed and detected[33]. A schematic of a basic CI source is presented in Figure 2.2.

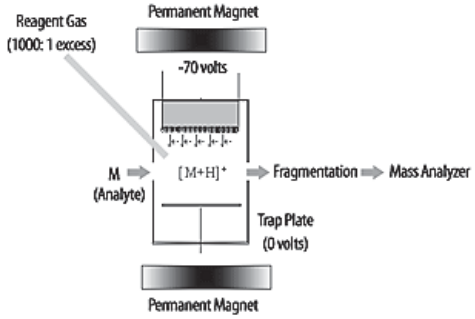

Figure 2.2: Schematic of Chemical Ionization mass spectrometer.

Work done by Dean *et. al.* provided the first analysis of metal β-diketonate characterization utilizing CI mass spectrometry as an ion source. Chemical ionization is a soft ionization technique, resulting in less fragmentation and a higher incidence of β-diketonate cluster ion formation. A cluster ion is a coordination complex in which more than two metal centers are present. Dean's group sought to evaluate the incidence of cluster ion formation when using CI mass spectrometry compared to a different ion souce, namely EI[28]. Schildcrout *et. al*. also studied cluster ion formation in metal β-diketonates, but focused mainly on EI mass spectrometry. He reported that ultimately β-diketonate cluster ions were formed from interactions between ionized metal-containing fragments and the neutral species of the same coordination compound[34]. In the Dean study, both methane and ammonia were used as the ionizing gas, and formation of high-mass cluster compounds were observed for the first time for copper(II), iron(III), and vanadium(III) acetylacetonates. Moreover, palladium(II) and zirconium(IV)

acetylacetonate cluster compounds were also reported for the first time[28]. The conditions of the reaction vessel were designed specifically to increase the abundance of cluster ions. Despite the formation of new high-mass clusters, the relative abundance of cluster ions was found to be approximately the same as under electron ionization mass spectroscopic conditions[28].

2.3 Matrix Assisted Laser Desorption/Ionization Time-of-Flight Mass Spectrometry

Another mass spectrometric technique used to examine transition metal β-diketonates is matrix assisted laser desorption/ionization time-of-flight mass spectrometry (MALDI-TOF MS). Like CI, MALDI-TOF is a softer method of ionization. The analyte is embedded into a matrix, which preserves the structural integrity of the molecule, and the matrix is loaded onto a metal plate. The sample (matrix and analyte) is then irradiated with a laser[33]. Although the exact mechanism of MALDI is unknown, it is thought that the matrix absorbs the radiation from the laser and then desorbs the analyte through the surface and into the gas phase[29]. Whether during desorption by the matrix or in the gas phase, the analyte is ionized and subsequently detected. A schematic of a MALDI-TOF mass spectrometer is presented in Figure 2.3.

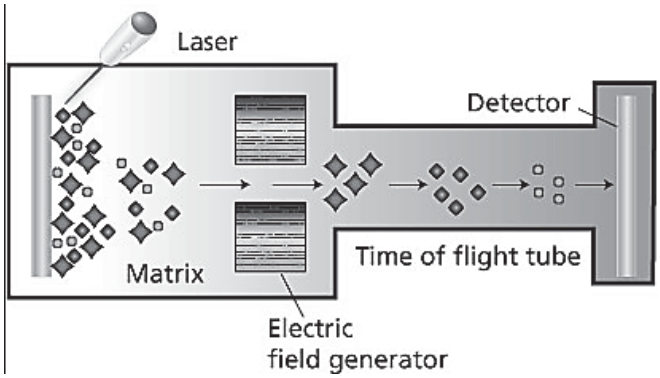

Figure 2.3: Schematic of MALDI-TOF mass spectrometer.

A time-of-flight tube is a particular type of mass analyzer that exploits the fact that the time it takes for the particle to travel from the source to the detector is directly

proportional to its molecular weight, meaning that a molecule with a larger molecular weight will take a longer time to travel through the time-of-flight tube than a smaller molecule. Thus, the time at which a molecule strikes a detector is representative of its molecular weight[33].

Wyatt *et. al.* sought to provide novel data and analysis on the electron-transfer processes of transition metal acetylacetonate complexes using MALDI-TOF MS[35]. Ten transition metal complexes were synthesized where five possessed (II) oxidation states and five possessed (III) oxidation states. The samples were embedded in 2-[(2E)-3-(4-*tert*-butylphenyl)-2-methylpropyl-2-enylidene]malonitrile (DCTB), an aprotic electron-transfer matrix. Ultimately, the study concluded that the observed spectra differed substantially based on the chelating metal center and its oxidation state.

However, the applications of MALDI-TOF MS to predict reactivity and mechanisms were severely limited by the uncertainty in the ionization energy (IE) of the matrix and the substrate. A review of the literature concluded that the amount of ion exchange an analyte will experience is largely dictated by the difference in the IE of the matrix and the substrate; the larger the difference, the more likely ion exchange is to occur. In order for a substrate to be ionized, a minimum difference of 0.2 to 0.3 eV is necessary[29]. The ionization energies of the novel $M(acac)_2$ and $M(acac)_3$ compounds, where M is the chelating transition metal center, were not known, creating uncertainty in any mechanistic predictions. Likewise, the IE of the DCTB matrix can be calculated no less than five different ways, each technique yielding a different value. There was no way to accurately predict the differences of IE or mechanistic likelihoods, so other periodic theories (such as Ligand Field Theory) were required to interpret the data. Ultimately,

MALDI-TOF MS proved too inconclusive and not sufficiently reliable to develop a predictive mechanism of the electron transfer process of metal β-diketonate complexes.

2.4 Fast-Atom Bombardment Mass Spectrometry

Fast-atom bombardment mass spectrometry (FAB-MS) is also a soft ionization technique. The sample is suspended in a liquid matrix, and ionization is accomplished by bombardment with high-energy atoms, typically of noble gases such as argon or xenon[33]. The schematic in Figure 2.4 outlines the basic components of FAB ionization.

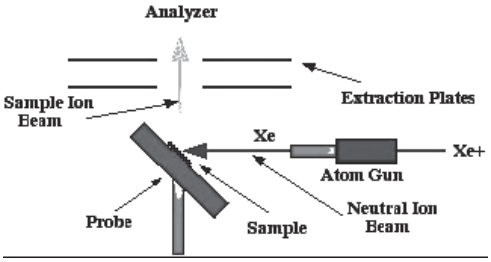

Figure 2.4: Schematic of Fast Atom Bombardment Ionization.

In a study utilizing FAB-MS to characterize metal β-diketonates, seven trivalent transition metals (V, Cr, Mn, Fe, Co, Ru and Os) were synthesized chelated to 2,4-pentanedionate (acac) ligands and 1,1,1-trifluoromethyl-2,4-pentanedionate (tfac) ligands. The samples were embedded in a 3-nitrobenzyl alcohol matrix, and then ionized via bombardment by argon atoms. Baseline mass spectra were obtained for both species. Cluster ion formation was demonstrated in five of the seven transition metals for *acac* complexes (V, Cr, Mn, Fe, and Co), and five of the *tfac* complexes (V, Cr, Mn, Fe, and Co)[34]. Adduct ions, or ions formed between the matrix and the analyte, were also observed, particularly in manganese *acac* complexes.

To further elucidate the structure of the adduct ions, collisionally activated dissociation (CAD) spectra were generated. CAD utilizes three separate chambers to examine the structural components of an analyte. The analyte is initially ionized in the

first quadrupole and then proceeds to a second quadrupole, where it is bombarded by a neutral species, typically either helium or argon. The additional kinetic energy and subsequent bombardment induces fragmentation, and these patterns of fragmentation and relative abundances can be an indicator of molecular structure. A schematic of a triple quadrupole mass spectrometer is presented in Figure 2.5.

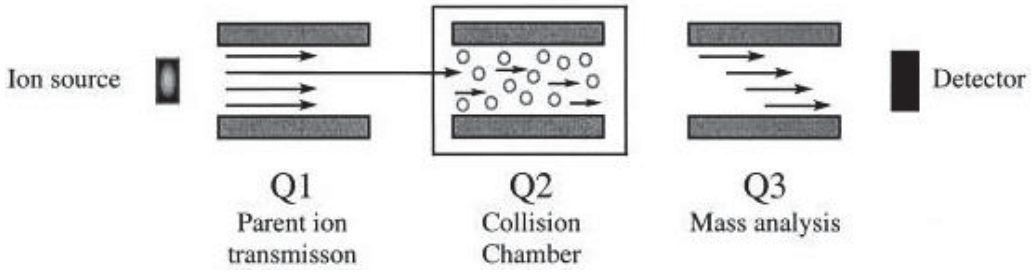

Figure 2.5: Schematic of CAD chamber.

CAD spectra were taken for masses 253, 324, 407, 460, and 711, corresponding to $[MnL_2]^+$, $[Mn_2L_2O]^+$, $[Mn_2L_3]^+$, $[Mn_2L_2+152u]^+$, and $[Mn_2L_3+152u]^+$, where 152u corresponds to the NBA matrix minus one hydrogen. Fragmentation patterns reported for the adduct ions did not show a strong abundance of a peak at *m/*z 152, which is likely demonstrative of a strong covalent bond between the metal and the matrix adduct[30].

It is also worth noting that partial ligand exchange reactions occurred when two tris-complexes with different ligands were placed in the same reaction vessel. It has been well documented in the literature that β-diketonates will fragment and decompose via stepwise, neutral losses of their ligand[30]. When the spectra suggested that ligand exchange occurred, the question arose whether ligand exchange was occurring in the liquid phase or the gas phase after desorption. Heteroleptic, or mixed ligand exchange, products were observed for all compounds except Ru and Os in moderate to high abundance. A split-tip FAB probe was used to isolate each species on each tip and sputter

the ions into the gas phase. The ligand was also introduced into the gas phase via a heated reservoir probe. However, neither experiment yielded any gas-phase ligand exchange products, indicating that ligand exchange occurred only in the liquid phase[30].

2.5 Electron Impact Mass Spectrometry

Much of the research reported in the previous section has focused on soft ionization techniques to analyze metal β-diketonates. However, harsher ionization techniques such as EI mass spectrometry will in fact promote fragmentation and ligand exchange in the gas phase[1]. The process begins when high-energy electrons are generated by heating a thin wire filament with a large current. The electrons generated are then focused into a beam, which is then accelerated towards a neutral species on a direct-insertion probe. The close proximity of the high-energy electrons creates a flux in the magnetic field around the analyte[33]. This stimulates ionization and fragmentation demonstrated in the schematic in Figure 2.6.

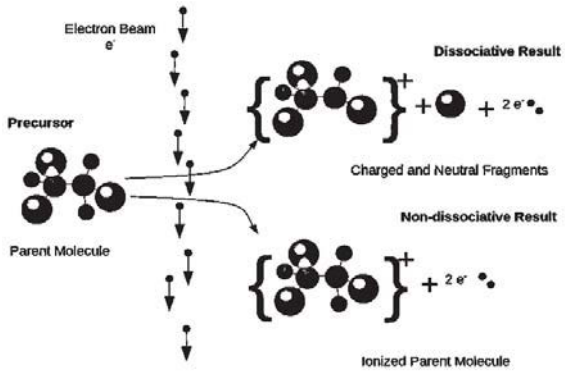

Figure 2.6: Schematic of harsh ionization in EI mass spectrometry.

Lerach *et. al.* sought to promote ligand exchange in the gas phase by employing this harsh ionization technique. As Schildcrout reported, cluster ion formation is caused by the interactions between ionized metal-containing fragments and neutral monomers of the same β-diketonate[34]. A similar process likely happens during ligand exchange

processes; an ionized metal-containing species or fragment interacts with a neutral ligand of a second β-diketonate to form the ligand exchange product. While fragmentation does not seem to be compulsory for ligand exchange, it appears to render the β-diketonates more active than ions generated by a softer ionization technique.

A previously reported method reported by Watson and Lin was adapted to synthesize the metal β-diketonate complexes and is briefly described herein[36]. A small amount of a metal chloride was dissolved in 100 mL of deionized water and mixed on a magnetic stir plate with a Teflon coated stir bar. Upon solvation of the metal ion, approximately 0.5 mL of the ligand was added to the mixture with stirring. Upon addition of a 1:1 (v/v) solution of H_2O:NH_4OH, the final product typically formed, but the solution was allowed to stir for an additional two hours to ensure completion. The solution was extracted using vacuum filtration and left to dry in a desiccator overnight.

To validate the occurrence of gas-phase ligand exchange, Lerach *et. al.* reported that two different β-diketonate compounds were placed on opposite sides of a sample-laden crucible. One ML_2 compound (where M=Cu(II) or Ni(II) and L=(acac) or (hfac)) was sublimed from the outside of the crucible while the other was sublimed from the inside of the crucible directly into the ionization chamber. They also reported that the relative locations of the ML_2 compounds did not alter the mass spectra or likelihood of ligand exchange[37].

A representative example of ligand exchange was the gas phase reaction between $Cu(acac)_2$ and $Ni(hfac)_2$. With special care taken to guarantee that the samples did not make contact in the liquid phase, the reaction was strictly limited to the gas phase. To better demonstrate the path of ligand exchange, samples were also run with $Cu(hfac)_2$ and

$Ni(acac)_2$. In both experiments, $[Cu(acac)(hfac)]^+$ and $[Ni(acac)(hfac)]^+$ were both observed with 100% relative ion abundance, indicating mixed ligand exchange occurred. Successful ligand exchange was also demonstrated with $Cu(hfac)_2$ and $Ni(tftm)_2$, as well as $Cu(acac)_2$ and $Ni(tftm)_2$[38].

2.6 Collision-Induced Reaction

The report by Lerach *et. al.* provided a stark contrast to the previously reported papers that hypothesized that ligand exchange with β-diketonates did not occur in the gas phase. However, more information is necessary to establish how these ligand exchange mechanisms proceed. Our hope is to use the principles of CAD to examine the mechanism of ligand exchange in β-diketonates, albeit at slightly different conditions. This technique has been termed collision-induced reaction (CIR), and is an unconventional use of a triple quadrupole mass spectrometer. First, a β-diketonate complex is sublimed and introduced into the ionization chamber. The harsh ionization of electron impact promotes fragmentation, which has been previously reported to encourage ligand exchange. A given fragment is then mass-selected using the first quadrupole and allowed to proceed to the next quadrupole, where only that particular ion is exposed to a second, neutral β-diketonate species that has been evaporated into the gas phase (instead of neutral argon, as is typically used to encourage more fragmentation). The second quadrupole acts as a collision cell where the mass-selected ion interacts with the second β-diketonate. The resultant products then proceed to the third and final quadrupole, which scans a set range of mass-to-charge ratios. The resulting mass spectra then exposes which fragments most contribute to ligand exchange, which subsequently allows reaction mechanisms to be proposed.

The experiments presented in Chapters 3, 4, 5, and 6 all utilize CIR analysis to evaluate the mechanism of gas phase ligand exchange between magnesium β-diketonate complexes and either nickel or copper β-diketonate complexes. Results reported in Chapter 7 utilize CIR analysis to evaluate the mechanism of ligand exchange between palladium and nickel β-diketonate complexes. Although this research is in its infancy stages, the studies reported herein contribute to the ever-expanding foundation of knowledge of this fascinating group of compounds.

Chapter 3

The Co-Sublimation and Gas-Phase Ligand Exchange Reactions of Magnesium Bis-Diethylacetylacetonate ($Mg(eeac)_2$) with Nickel Bis-Acetylacetonate ($Ni(acac)_2$), Nickel Bis-Trifluorotrimethylacetylacetonate ($Ni(tftm)_2$), and Nickel Bis-Dibenzoylmethane ($Ni(dbm)_2$)

3.1 Introduction

Presented herein is the first analysis of gas-phase ligand exchange reactions between metal β-diketonate complexes in which the chelating metal is an alkaline earth metal. The metal of choice, magnesium, occupies a (II) oxidation state, like many of the previous reported transition metals[1–3]. Fajans' Rules, developed by Kazimierz Fajans in 1923, are still used today to determine the covalency between two bonded atoms. The first rule states that covalency is increased by the high charge and smaller size of the anion. Magnesium is an interesting metal to investigate because it occupies the same valency as many of its transition metal counterparts, but has a much smaller atomic radius and lacks occupied d-orbitals. It is the purpose of the studies reported herein to explore and analyze these ligand exchange reactions with a comparison to previously reported studies with transition metal β-diketonates.

One key advantage to utilizing mass spectrometry to analyze these gas-phase reactions is its ability to reflect the isotopic distributions of metals present within the products. Many metals exhibit characteristic isotopic distributions that are easily discernable within a mass spectrum. For instance, magnesium has three stable isotopes; ^{24}Mg, which has a natural abundance of 78.99%, followed by ^{25}Mg and ^{26}Mg, present at 10.00% and 11.01%, respectively. Thus on a mass spectrum, a species possessing a

magnesium chelating metal will have one very prominent peak at the mass corresponding with that of ^{24}Mg, with two smaller peaks of virtually equal height to the immediate right, corresponding to the higher masses of ^{25}Mg and ^{26}Mg. Nickel, however, has five naturally occurring isotopes; ^{58}Ni has an abundance of 68.08%, while ^{60}Ni, ^{61}Ni, ^{62}Ni, and ^{64}Ni have abundances of 22.26%, 1.14%, 3.63%, and 0.93%, respectively. The mass spectrum of nickel is quite recognizable as it has one distinct peak corresponding with the mass of ^{58}Ni, and at a slightly higher mass, a shoulder that is roughly 1/3 of the height corresponding to the mass of ^{60}Ni. Thus, when a co-sublimation reaction is initiated and both magnesium and nickel are present, the isotopic distributions aid in distinguishing whether a compound contains magnesium or nickel, particularly in cases where species are isobaric, or possessing the same mass-to-charge (*m/z*) ratio.

3.2 Magnesium Bis-Diethylacetylacetonate ($Mg(eeac)_2$)

All of the studies presented within this Chapter utilize magnesium bis-diethylacetylacetonate ($Mg(eeac)_2$). The baseline positive EI mass spectrum for this species is presented in Figure 3.1 where the intact alkaline earth metal β-diketonate species $[Mg(eeac)_2]^+$ is present at *m/z* 278. Loss of an ethyl group to form [Mg(eeac-*Et*)(eeac)]$^+$ is displayed at *m/z* 249, while the loss of a second ethyl group from the parent compound to form [Mg(eeac-*Et*)(eeac-*Et*)]$^+$ is present at *m/z* 222. Although the predicted peak for [Mg(eeac-*Et*)(eeac-*Et*)]$^+$ would occur at *m/z* 220, the peak at *m/z* 222 indicates that the two *Et* constituents (for a total loss of *m/z* 58) are lost followed by migration of two hydrogens forming the observed product. Henceforth, this will be referred to as [Mg(eeac-*Et*)(eeac-*Et*)+2H]$^+$. [Mg(eeac)]$^+$, the single ligand species, is present at *m/z* 151 and the relative abundances of these species are displayed in Table 3.1.

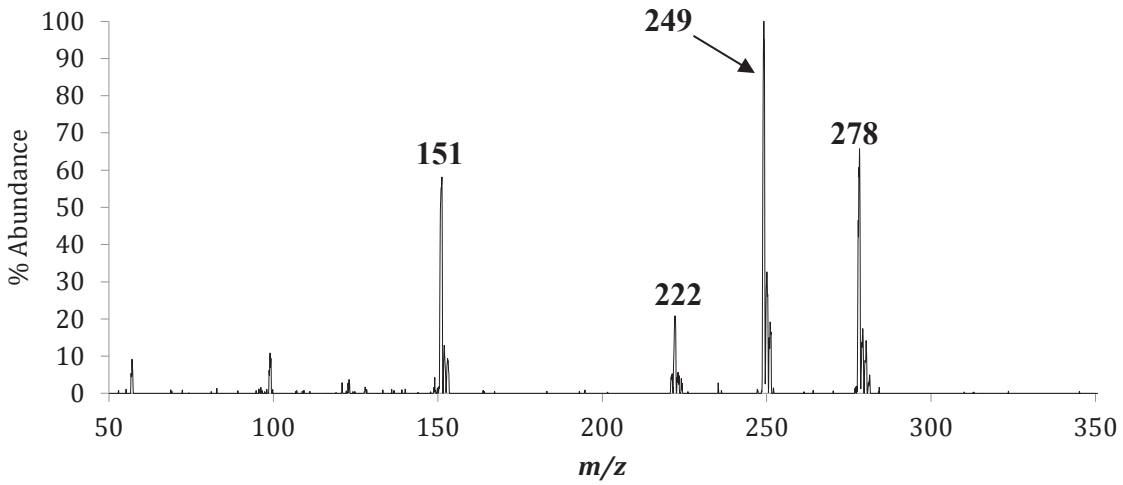

Figure 3.1: The 70 eV positive electron impact (EI) mass spectra of magnesium bis-diethylacetylacetonate, or $[Mg(eeac)_2]^+$, and its corresponding fragmentation pattern.

Species	*m/z*	Relative Abundance
$[Mg(eeac)_2]^+$	278	65
[Mg(eeac-*Et*)(eeac)]$^+$	249	100
[Mg(eeac-*Et*)(eeac-*Et*)+2H]$^+$	222	20
$[Mg(eeac)]^+$	151	58

Table 3.1: Fragmentation species and relative positive ion intensities of the mass spectral analysis of $Mg(eeac)_2$ presented in Figure 3.1.

3.3 The Co-Sublimation of $Mg(eeac)_2$ and Nickel Bis-Acetylacetonate ($Ni(acac)_2$)

The mass spectra presented in Figure 3.2(a)-(c) display the positive EI mass spectra of both $Mg(eeac)_2$, nickel bis-acetylacetonate, or $Ni(acac)_2$, and their respective co-sublimation reaction. The individual mass spectra are stacked vertically to aid in comparison and highlight the formation of new species, which is indicative that ligand exchange has occurred. Figure 3.2(a) is the positive EI mass spectrum of $Mg(eeac)_2$ and is reproduced from Figure 3.1 and will thus not be discussed further. The spectrum presented in Figure 3.2(b) displays the positive EI mass spectrum for $Ni(acac)_2$ in which

the intact species $[Ni(acac)_2]^+$ is present at *m/z* 256, as is the loss of a methyl group to form $[Ni(acac\text{-}CH_3)(acac)]^+$ at *m/z* 241. The single ligand species $[Ni(acac)]^+$ is observed at *m/z* 157, with subsequent loss of a methyl group forming $[Ni(acac\text{-}CH_3)]^+$ at *m/z* 142.

The co-sublimation mass spectrum displays many novel peaks, which as stated previously, is indicative that ligand exchange occurred. Interestingly, the intact complete nickel ligand exchange product $[Ni(eeac)_2]^+$ is also present at *m/z* 312, as is the loss of an ethyl group to form $[Ni(eeac\text{-}Et)(eeac)]^+$ at *m/z* 283. The complete magnesium ligand exchange product $[Mg(acac)_2]^+$ is also observed at *m/z* 222, including the loss of a methyl group to form $[Mg(acac\text{-}CH_3)(acac)]^+$ at *m/z* 207. The magnesium mixed ligand exchange product $[Mg(acac)(eeac)]^+$ is also evident at *m/z* 250. Finally, the single ligand exchange product $[Mg(acac)]^+$ is displayed at *m/z* 123. The relative abundance of each of the aforementioned species is reported in Table 3.2. The isobaric species $[Mg(eeac\text{-}Et)(eeac\text{-}Et)+2H]^+$ and $[Mg(acac)_2]^+$ both have calculated masses of *m/z* 222 and have been italicized within Table 3.2.

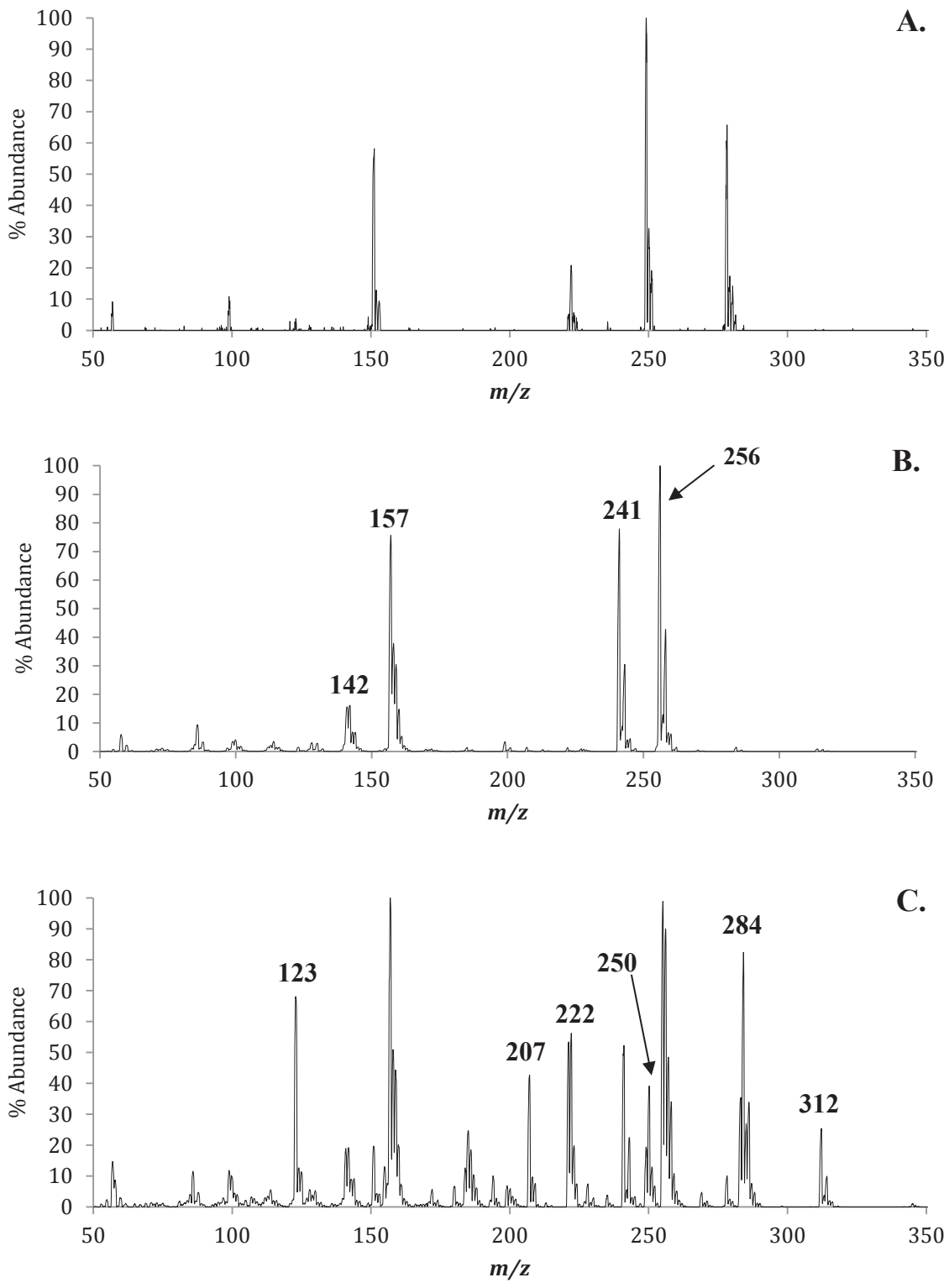

Figure 3.2: The positive EI mass spectra of (a) $Mg(eeac)_2$, (b) $Ni(acac)_2$, and (c) the gas-phase co-sublimation of $Mg(eeac)_2$ and $Ni(acac)_2$. The masses of parent compounds and fragments are labeled in (a) and (b). Masses of ligand exchange products and pertinent fragments are labeled in (c).

	Mass	Mass	MgL	NiL'	MgL & NiL'	MgL & NiL'
Species	Mg	Ni	Mg	Ni	Mg	Ni
$[ML_2]^+$	278	312	65		9	26
$[ML_2\text{-}C_2H_5]^+$	249	283	100		19	35
$[ML_2\text{-}2C_2H_5\text{+}2H]^+$	*222*	-	20		*55*	-
$[ML_2\text{-}2C_2H_5]^+$	-	254	0		-	25
$[ML]^+$	151	185	10		19	25
$[ML'_2]^+$	*222*	256		100	*55*	89
$[ML'_2\text{-}CH_3]^+$	207	241		77	43	52
$[ML']^+$	123	157		37	68	100
$[ML'\text{-}CH_3]^+$	108	142		7	2	18
$[MLL']^+$	250	284			40	82
$[M(L\text{-}C_2H_5)L']^+$	221	255			53	98

Table 3.2: The relative mass spectrometric abundances of the $Mg(eeac)_2$ and $Ni(acac)_2$ β-diketonate complexes as well as the co-sublimation experiment, as presented in Figure 3.2. L = (eeac), L' = (acac).

3.4 The Selective Reactions of $Mg(eeac)_2$ and $Ni(acac)_2$

After co-sublimation confirmed that ligand exchange did indeed occur, selective reactions using tandem mass spectrometry were employed to elucidate a possible mechanism of ligand exchange. The most abundant species from the $Mg(eeac)_2$ baseline mass spectrum, $[Mg(eeac)_2]^+$ at *m/z* 278, $[Mg(eeac\text{-}Et)(eeac)]^+$ at *m/z* 249, $[Mg(eeac\text{-}Et)(eeac\text{-}Et)+2H]^+$ at *m/z* 222, and $[Mg(eeac)]^+$ at *m/z* 151, were individually mass-selected in the first quadrupole and permitted to react with an atmosphere of neutral $Ni(acac)_2$ in the second quadrupole of the triple quadrupole mass spectrometer. All of the products from the individual reactions were then mass filtered using the third quadrupole as it scanned from *m/z* 50 to 650.

The first ligand exchange product of interest generated from a collision-induced reaction was the complete ligand exchange species $[Ni(eeac)_2]^+$ at *m/z* 312, which was produced from mass-selected $[Mg(eeac\text{-}Et)(eeac)]^+$ at *m/z* 249 reacting with neutral $Ni(acac)_2$, as presented in Figure 3.3. The third peak corresponds to the mass of the single ligand magnesium species $[Mg(eeac)]^+$ at *m/z* 151, which is a commonly displayed peak on other CIR spectra of mass-selected $Mg(eeac)_2$ fragments.

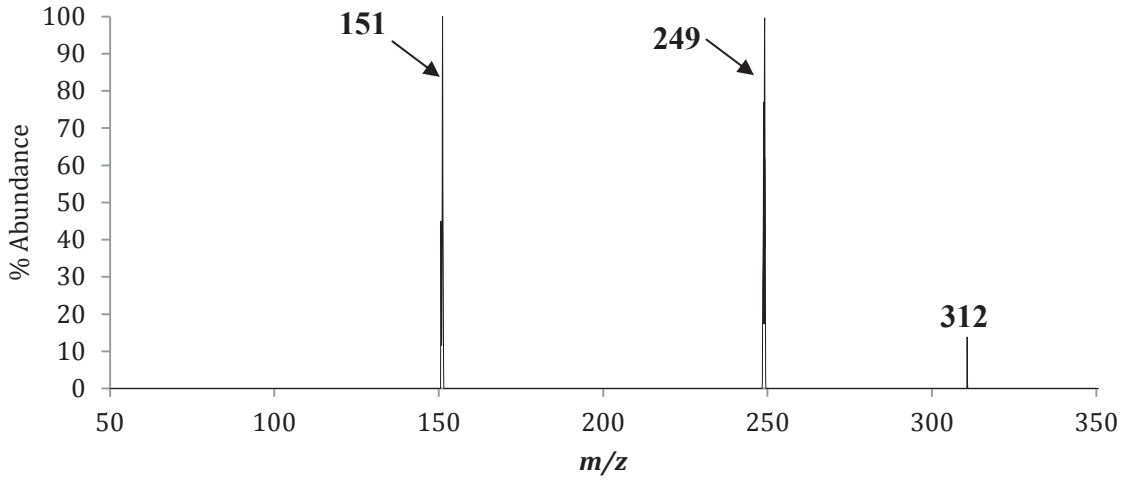

Figure 3.3: The positive mass spectrum obtained by scanning the third quadrupole following the selective reaction of *m/z* = 249 ($[Mg(eeac\text{-}Et)(eeac)]^+$) with neutral $Ni(acac)_2$ to produce the complete ligand exchange product $[Ni(eeac)_2]^+$ at *m/z* 312.

The proposed mechanism for the gas-phase formation of the nickel complete ligand exchange product $[Ni(eeac)_2]^+$ is presented in Equation 3.1.

$$[Mg(eeac\text{-}Et)(eeac)]^+ + Ni(acac)(acac) + Et \rightarrow [Ni(eeac)(eeac)]^+ + Mg(acac)(acac) \qquad \text{(Eqn 3.1)}$$

The next ligand exchange product generated from collision-induced reaction was the intact mixed ligand exchange species $[Ni(acac)(eeac)]^+$ at *m/z* 284 which was

generated by reacting neutral $Ni(acac)_2$ with $[Mg(eeac\text{-}Et)(eeac\text{-}Et)+2H]^+$ at *m/z* 222. The results from this reaction are depicted in Figure 3.4.

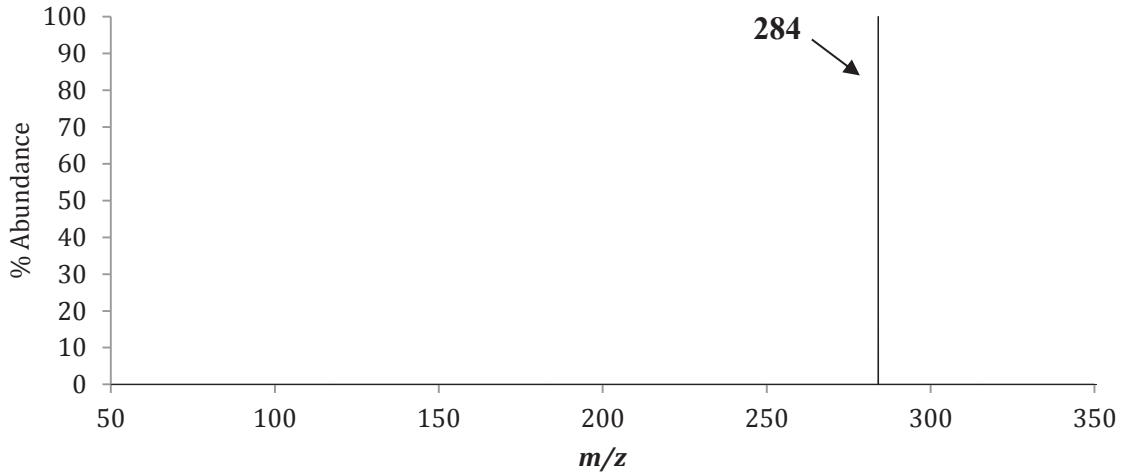

Figure 3.4: The positive mass spectrum obtained by scanning the third quadrupole following the selective reaction of *m/z* = 222 ($[Mg(eeac\text{-}\mathit{Et})(eeac\text{-}\mathit{Et})+2H]^+$) with neutral $Ni(acac)_2$ to produce the mixed ligand exchange product $[Ni(acac)(eeac)]^+$ at *m/z* 284.

The proposed mechanism for the gas-phase formation of the nickel mixed ligand exchange product $[Ni(acac)(eeac)]^+$ is presented in Equation 3.2.

$$[Mg(eeac\text{-}\mathit{Et})(eeac\text{-}\mathit{Et})]^+ + Ni(acac)(acac) + \mathit{Et} \rightarrow [Ni(acac)(eeac)]^+ + Mg(acac)(eeac\text{-}\mathit{Et}) \qquad \text{(Eqn 3.2)}$$

The final ligand exchange product of interest was generated from collision-induced reaction of $[Mg(eeac)]^+$ at *m/z* 151 to form $[Ni(acac)(eeac\text{-}Et)]^+$ at *m/z* 255, and can be readily observed in Figure 3.5.

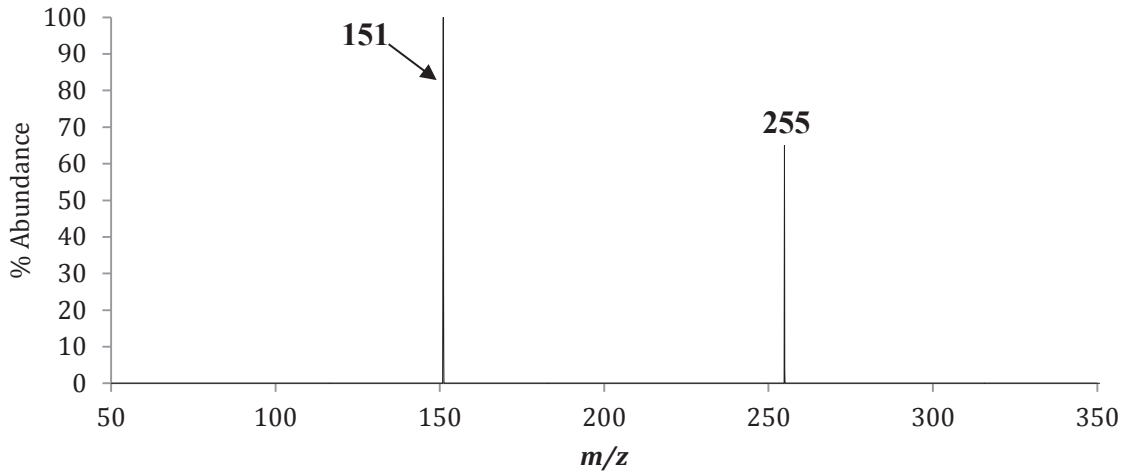

Figure 3.5: The positive mass spectrum obtained by scanning the third quadrupole following the selective reaction of *m/z* = 151 ($[Mg(eeac)]^+$) with neutral $Ni(acac)_2$ to produce the mixed ligand exchange fragment $[Ni(acac)(eeac\text{-}Et)]^+$ at *m/z* 255.

The proposed mechanism for the gas-phase formation of the nickel mixed ligand exchange fragment $[Ni(acac)(eeac\text{-}Et)]^+$ is displayed in Equation 3.3.

$$[Mg(eeac)]^+ + Ni(acac)(acac) \rightarrow$$

$$[Ni(acac)(eeac\text{-}Et)]^+ + Mg(acac) + Et \qquad \text{(Eqn 3.3)}$$

To provide a more holistic view of this mechanism, the reverse reactions were also investigated where mass-selected $[Ni(acac)_2]^+$ at *m/z* 256, $[Ni(acac\text{-}CH_3)(acac)]^+$ *m/z* 241, $[Ni(acac)]^+$ at *m/z* 157, and $[Ni(acac\text{-}CH_3)]^+$ at *m/z* 142 were reacted with neutral $Mg(eeac)_2$. The resultant products were scanned in the third quadrupole from *m/z* 50 to 650, and the proposed mechanisms provide some insight into how ligand exchange occurs between these two compounds.

The final product of interest generated from a collision-induced reaction of mass-selected $[Ni(acac\text{-}CH_3)(acac)]^+$ at *m/z* 241 with neutral $Mg(eeac)_2$ was $[Mg(acac)_2]^+$ at *m/z* 222 and is readily observed in Figure 3.5.

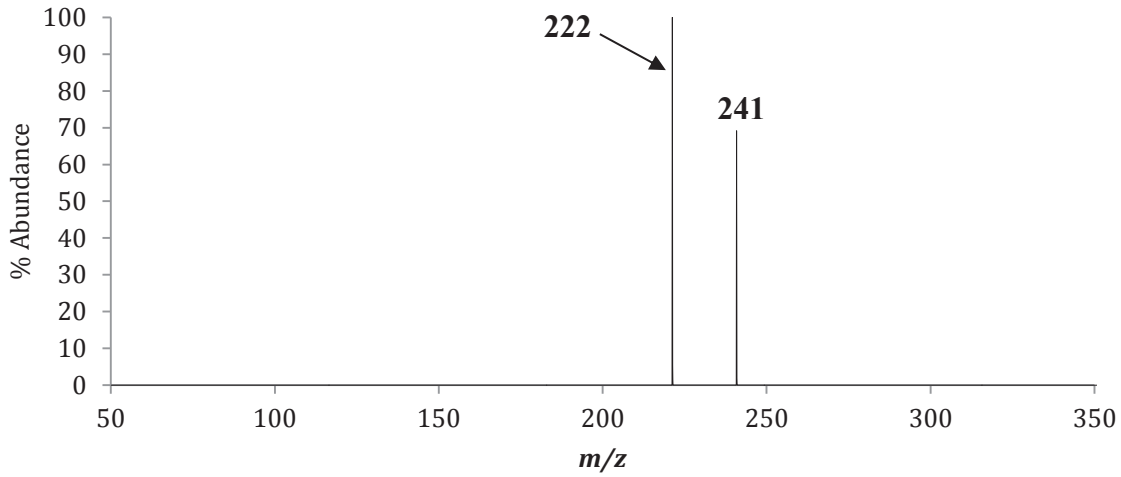

Figure 3.6: The positive mass spectrum obtained by scanning the third quadrupole following the selective reaction of *m/z* = 241 ($[Ni(acac\text{-}CH_3)(acac)]^+$) with neutral $Mg(eeac)_2$ to produce the complete ligand exchange product $[Mg(acac)_2]^+$ at *m/z* 222.

The proposed mechanism for the gas-phase formation of the magnesium complete ligand exchange product $[Mg(acac)_2]^+$ is presented in Equation 3.4.

$$[Ni(acac\text{-}CH_3)(acac)]^+ + Mg(eeac)(eeac) + CH_3 \rightarrow [Mg(acac)(acac)]^+ + Ni(eeac)(eeac) \qquad \text{(Eqn 3.4)}$$

The proposed mechanisms reported herein have provided much insight into the mechanism of gas-phase ligand exchange between $Mg(eeac)_2$ and $Ni(acac)_2$. Although additional work is necessary, the proposed equations have helped establish a foundation for others to expand upon.

Mass-selected $[Mg(eeac\text{-}Et)(eeac)]^+$ at *m/*z 249 when reacted with neutral $Ni(acac)_2$ was observed to promote the formation of the complete nickel ligand exchange product $[Ni(eeac)_2]^+$ at *m/z* 312, while mass-selected $[Mg(eeac\text{-}Et)(eeac\text{-}Et)+2H]^+$ promoted the formation of the nickel mixed ligand exchange product $[Ni(acac)(eeac)]^+$ at *m/z* 284. The single ligand species $[Mg(eeac)]^+$ at *m/z* 151 also generated a nickel ligand exchange fragment, $[Ni(acac)(eeac\text{-}Et)]^+$ at *m/z* 255. Interestingy, no ligand exchange

product of interest was generated from reactions involving mass-selected $[Mg(eeac)_2]^+$ at *m/z* 278.

The only ligand exchange product of interest generated from mass-selected nickel species was the collision-induced reaction of $[Ni(acac\text{-}CH_3)(acac)]^+$ at *m/*z 241 with neutral $Mg(eeac)_2$ to produce the complete ligand exchange product $[Mg(acac)_2]^+$ at m/z 222. No other ligand exchange products were observed from mass-selected $[Ni(acac)_2]^+$ at *m/z* 256, $[Ni(acac)]^+$ at *m/z* 157, or $[Ni(acac\text{-}CH_3)]^+$ at *m/z* 142.

3.5 The Co-Sublimation of $Mg(eeac)_2$ and Nickel Bis-Trifluorotrimethylacetylacetonate ($Ni(tftm)_2$)

The positive EI mass spectra of $Mg(eeac)_2$, $Ni(tftm)_2$, and the co-sublimation of both $Mg(eeac)_2$ and $Ni(tftm)_2$ are presented in Figure 3.7(a)-(c). Although the scans were conducted over masses *m/*z 50 to 650, the spectra are presented with a range of *m/*z 50 to 450 to highlight the isotopic distributions of the fragments and products. The spectra of $Mg(eeac)_2$ is presented again to aid in the comparison of the spectra, and the vertical stacking more clearly displays the presence of new species that correspond to particular ligand exchange processes.

Presented in Figure 3.7(b) is the intact $[Ni(tftm)_2]^+$ species at *m/z* 448, as is what appears to be the loss of a *tBu* group to form $[Ni(tftm\text{-}tBu)(tftm)]^+$ at *m/z* 391. Intact $[Ni(tftm)]^+$ is observed at *m/z* 253, as well as the loss of a CF_2 group to form $[Ni(tftm\text{-}CF_2)]^+$ at *m/z* 203, which represents a fluoride migration, a previously reported phenomenon in fluorinated β-diketonates[27, 36]. Finally, the peak at *m/z* 310 corresponds to the unique species $[Ni(tftm)+tBu]^+$, in which a lone *tBu* group reattaches to $[Ni(tftm)]^+$. The co-sublimation spectrum in Figure 3.7(c) displays many new peaks, demonstrating

complete, mixed, and partial ligand exchange. Complete ligand exchange is identified to occur at *m/z* 414, which represents intact $[Mg(tftm)_2]^+$, and at *m/z* 312, which corresponds to intact $[Ni(eeac)_2]^+$. Evidence for mixed ligand exchange is present at both *m/z* 346 and *m/z* 380, corresponding to $[Mg(eeac)(tftm)]^+$ and $[Ni(eeac)(tftm)]^+$, respectively. Loss of a *tBu* group from $[Mg(tftm)_2]^+$ to form $[Mg(tftm\text{-}tBu)(tftm)]^+$ is also observed at *m/z* 357, followed by the loss of a *tBu* group from the magnesium mixed ligand product $[Mg(eeac)(tftm)]^+$ to form $[Mg(eeac)(tftm\text{-}tBu)]^+$ at *m/z* 289. Loss of an ethyl group from $[Ni(eeac)_2]^+$ to form $[Ni(eeac\text{-}Et)(eeac)]^+$ is present at *m/z* 283, as is the loss of an *tBu* group from the nickel mixed ligand product $[Ni(eeac)(tftm)]^+$ to form $[Ni(eeac)(tftm\text{-}tBu)]^+$ at *m/z* 323. Finally, the single-ligand exchange product of nickel, $[Ni(eeac)]^+$, is displayed in high abundance at *m/z* 185. The relative abundances of species present in Figure 3.7 are reported in Table 3.3.

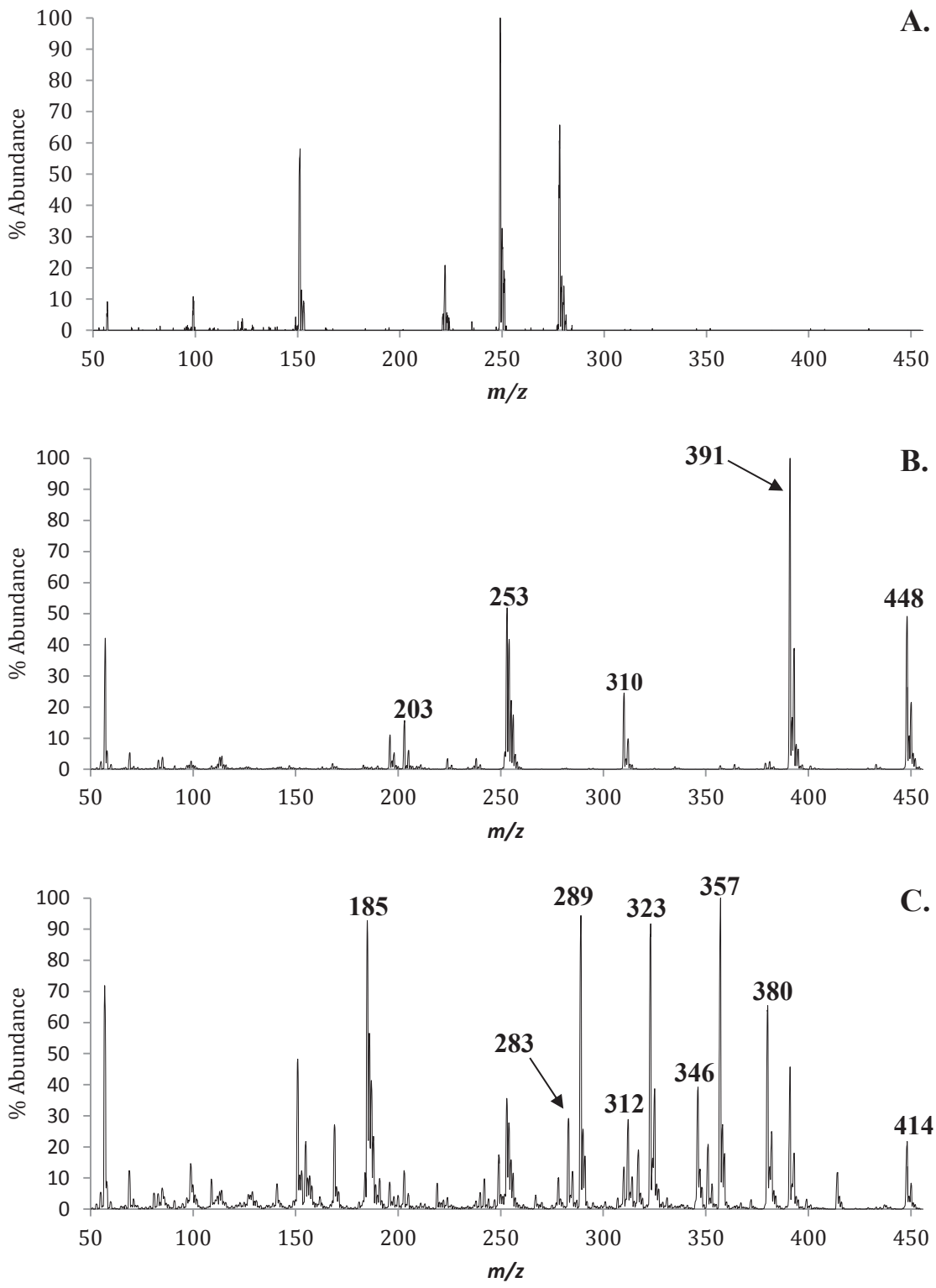

Figure 3.7: The positive EI mass spectra of (a) $Mg(eeac)_2$, (b) $Ni(tftm)_2$, and (c) the gas-phase co-sublimation of $Mg(eeac)_2$ and $Ni(tftm)_2$. The masses of parent compounds and fragments are labeled in (a) and (b). Masses of ligand exchange products and pertinent fragments are labeled in (c).

	Mass	Mass	MgL	NiL''	MgL & NiL''	MgL & NiL''
	Mg	Ni	Mg	Ni	Mg	Ni
$[ML_2]^+$	278	312	65		10	29
$[ML_2\text{-}C_2H_5]^+$	249	283	100		17	29
$[ML_2\text{-}2C_2H_5\text{+}2H]^+$	222	-	20		2	-
$[ML_2\text{-}2C_2H_5]^+$	-	254	0		-	28
$[ML]^+$	151	185	10		48	92
$[ML\text{-}C_2H_5]^+$	136	156	<1		1	10
$[ML''_2]^+$	414	448		49	12	22
$[ML''_2\text{-}tBu]^+$	357	391		100	100	46
$[ML''\text{+}tBu]^+$	276	310		24	<1	13
$[ML'']^+$	219	253		50	8	35
$[ML''\text{-}tBu]^+$	162	196		11	3	8
$[ML''\text{-}CF_2]^+$	169	203		15	27	12
$[MLL'']^+$	346	380			39	65
$[M(L\text{-}C_2H_5)L'']^+$	317	351			19	20
$[ML(L''\text{-}tBu)]^+$	289	323			94	91

Table 3.3: The relative mass spectrometric abundances of $Mg(eeac)_2$ and $Ni(tftm)_2$ β-diketonate complexes, as well as the co-sublimation experiment, as presented in Figure 3.7. L = (eeac); L'' = (tftm).

3.6 The Selective Reactions of $Mg(eeac)_2$ and $Ni(tftm)_2$

After ligand exchange was observed to occur quite readily through gas-phase reactions, collision-induced reaction analysis was employed in an attempt to establish reaction pathways. The four most prominent species detected from the positive EI mass spectrum were individually selected and permitted to react with an atmosphere of neutral $Ni(tftm)_2$ in the collision cell, including $[Mg(eeac)_2]^+$ at *m/z* 278, $[Mg(eeac\text{-}Et)(eeac)]^+$ at *m/z* 249, $[Mg(eeac\text{-}Et)(eeac\text{-}Et)\text{+}2H]^+$ at *m/z* 222, and $[Mg(eeac)]^+$ at *m/z* 151. All

resulting products were detected by scanning the third quadrupole over a range of *m/z* 50 to 650.

The first ligand exchange product of interest generated from collision-induced reaction was $[Mg(tftm\text{-}CF_2)(tftm)]^+$ at *m/z* 364, which was produced from mass-selected $[Mg(eeac)_2]^+$ at *m/z* 278 reacting with neutral $Ni(tftm)_2$, and is displayed in Figure 3.8.

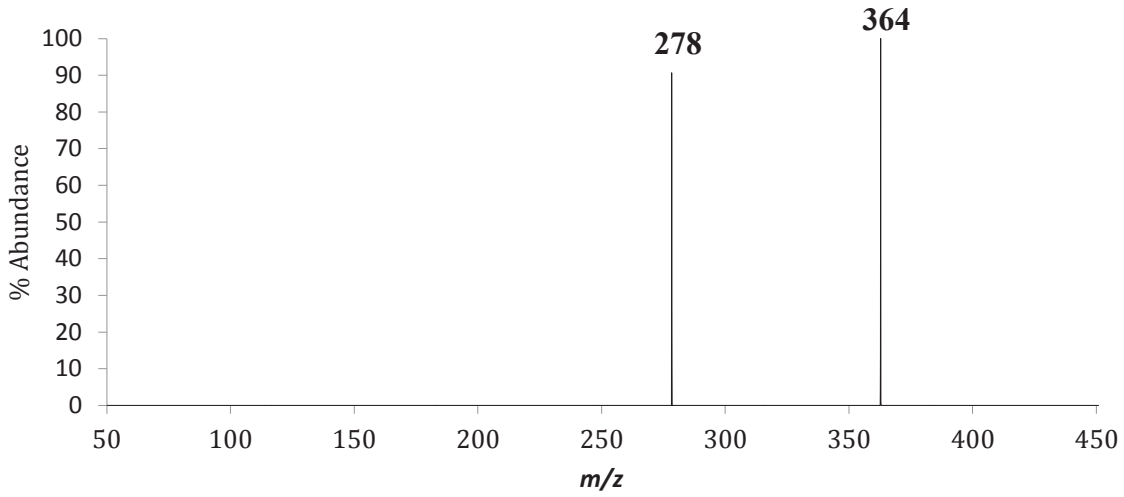

Figure 3.8: The positive mass spectrum obtained by scanning the third quadrupole following the selective reaction of *m/z* = 278 ($[Mg(eeac)_2]^+$) with neutral $Ni(tftm)_2$ to produce the complete ligand exchange fragment $[Mg(tftm\text{-}CF_2)(tftm)]^+$ at *m/z* 364.

The proposed mechanism for the gas-phase formation of the magnesium complete ligand exchange fragment $[Mg(tftm\text{-}CF_2)(tftm)]^+$ is presented in Equation 3.5.

$$[Mg(eeac)(eeac)]^+ + Ni(tftm)(tftm) \rightarrow$$
$$[Mg(tftm\text{-}CF_2)(tftm)]^+ + Ni(eeac)(eeac) + CF_2 \qquad \text{(Eqn 3.5)}$$

Another ligand product of interest generated from the collision-induced reaction of mass-selected $[Mg(eeac)_2]^+$ at *m/z* 278 and neutral $Ni(tftm)_2$ is presented in Figure 3.9 and corresponds to the magnesium mixed ligand exchange fragment $[Mg(eeac)(tftm\text{-}CF_2)]^+$ at *m/z* 296.

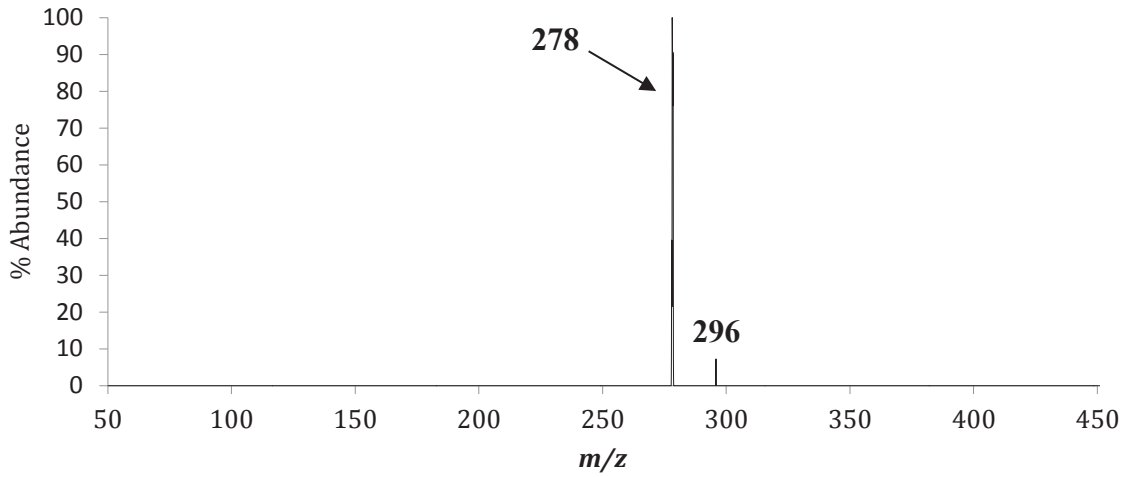

Figure 3.9: The positive mass spectrum obtained by scanning the third quadrupole following the selective reaction of *m/z* = 278 ($[Mg(eeac)_2]^+$) with neutral $Ni(tftm)_2$ to produce the mixed ligand exchange fragment $[Mg(eeac)(tftm\text{-}CF_2)]^+$ at *m/z* 296.

The proposed mechanism for the gas-phase formation of the magnesium mixed ligand exchange product $[Mg(eeac)(tftm\text{-}CF_2)]^+$ is presented in Equation 3.6.

$$[Mg(eeac)(eeac)]^+ + Ni(tftm)(tftm) \rightarrow$$
$$[Mg(eeac)(tftm\text{-}CF_2)]^+ + Ni(eeac)(tftm) + CF_2 \qquad \text{(Eqn 3.6)}$$

The final species generated from the collision-induced reaction of mass-selected $[Mg(eeac)_2]^+$ at *m/z* 278 with neutral $Ni(tftm)_2$ is presented in Figure 3.10 and corresponds to the formation of the fluorine migration product $[Mg(tftm\text{-}CF_2)]^+$ at *m/z* 169.

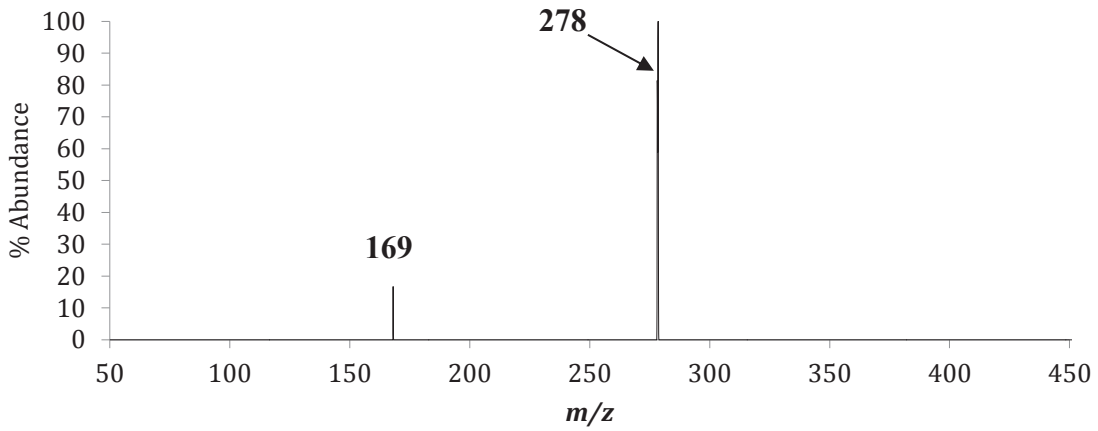

Figure 3.10: The positive mass spectrum obtained by scanning the third quadrupole following the selective reaction of *m/z* = 278 ($[Mg(eeac)_2]^+$) with neutral $Ni(tftm)_2$ to produce the ligand exchange fragment $[Mg(tftm\text{-}CF_2)]^+$ at *m/z* 169.

The proposed mechanism for the gas-phase formation of the magnesium single ligand exchange fragment $[Mg(tftm\text{-}CF_2)]^+$ is displayed in Equation 3.7.

$$[Mg(eeac)(eeac)]^+ + Ni(tftm)(tftm) \rightarrow$$
$$[Mg(tftm\text{-}CF_2)]^+ + Ni(tftm)(eeac) + CF_2 + (eeac) \qquad \text{(Eqn 3.7)}$$

In order to provide a complete picture of ligand exchange, the most abundant species from the $Ni(tftm)_2$ mass spectrum, namely $[Ni(tftm)_2]^+$ at *m/z* 448, $[Ni(tftm\text{-}tBu)(tftm)]^+$ at *m/z* 391, $[Ni(tftm)+tBu)]^+$ at *m/z* 310, $[Ni(tftm)]^+$ at *m/z* 253, and $[Ni(tftm\text{-}CF_2)]^+$ at *m/z* 203, were mass-selected and permitted to react with an atmosphere of neutral $Mg(eeac)_2$ in the second quadrupole.

Mass-selected nickel ions also produced several ligand exchange products of interest, the first of which was $[Mg(tftm\text{-}CF_2)(tftm)]^+$ at *m/z* 364 generated from mass-selected $[Ni(tftm)_2]^+$ at *m/z* 448. The spectrum displaying this exchange is presented in Figure 3.11.

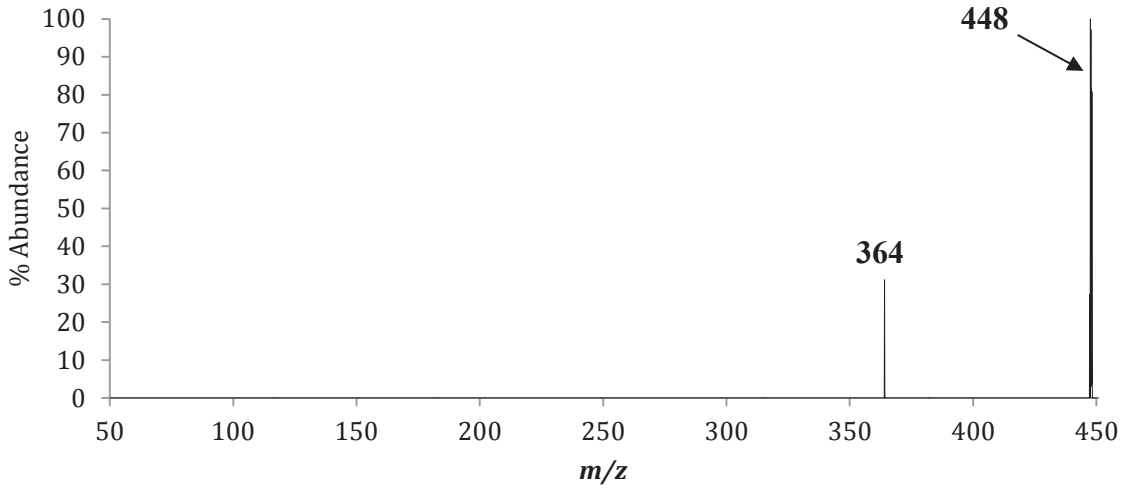

Figure 3.11: The positive mass spectrum obtained by scanning the third quadrupole following the selective reaction of *m/z* = 448 ($[Ni(tftm)_2]^+$) with neutral $Mg(eeac)_2$ to produce the complete ligand exchange fragment $[Mg(tftm\text{-}CF_2)(tftm)]^+$ at *m/z* 364.

The proposed mechanism for the gas-phase formation of the magnesium complete ligand exchange fragment $[Mg(tftm\text{-}CF_2)(tftm)]^+$ is presented in Equation 3.8.

$$[Ni(tftm)(tftm)]^+ + Mg(eeac)(eeac) \rightarrow$$

$$[Mg(tftm\text{-}CF_2)(tftm)]^+ + Ni(eeac)(eeac) + CF_2 \qquad \text{(Eqn 3.8)}$$

A second product, $[Ni(eeac\text{-}Et)(eeac)]^+$ at *m/z* 283, was also generated from $[Ni(tftm)_2]^+$ at *m/z* 448 reacting with neutral $Mg(eeac)_2$, and is displayed in Figure 3.12.

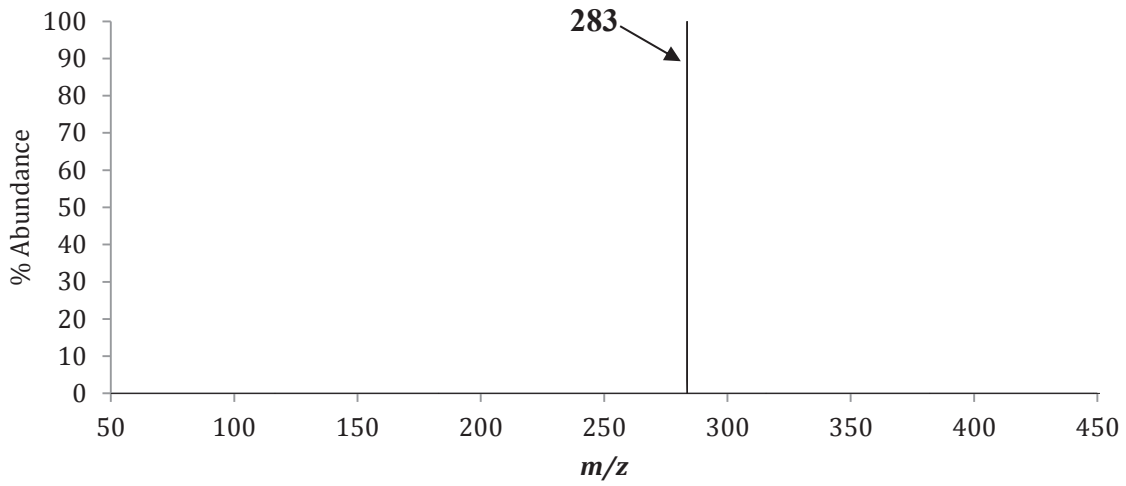

Figure 3.12: The positive mass spectrum obtained by scanning the third quadrupole following the selective reaction of *m/z* = 448 ($[Ni(tftm)_2]^+$) with neutral $Mg(eeac)_2$ to produce the complete ligand exchange fragment $[Ni(eeac\text{-}Et)(eeac)]^+$ at *m/z* 283.

The proposed mechanism for the gas-phase formation of the nickel complete ligand exchange fragment $[Ni(eeac\text{-}Et)(eeac)]^+$ is displayed in Equation 3.9.

$$[Ni(tftm)(tftm)]^+ + Mg(eeac)(eeac) \rightarrow$$

$$[Ni(eeac\text{-}Et)(eeac)]^+ + Mg(tftm)(tftm) + Et \quad \text{(Eqn 3.9)}$$

One ligand exchange product of interest, $[Mg(tftm\text{-}tBu)(tftm)]^+$ at *m/z* 357, was generated from the reaction of mass-selected $[Ni(tftm)+tBu]^+$ at *m/z* 310 and neutral $Mg(eeac)_2$, which is displayed in Figure 3.13.

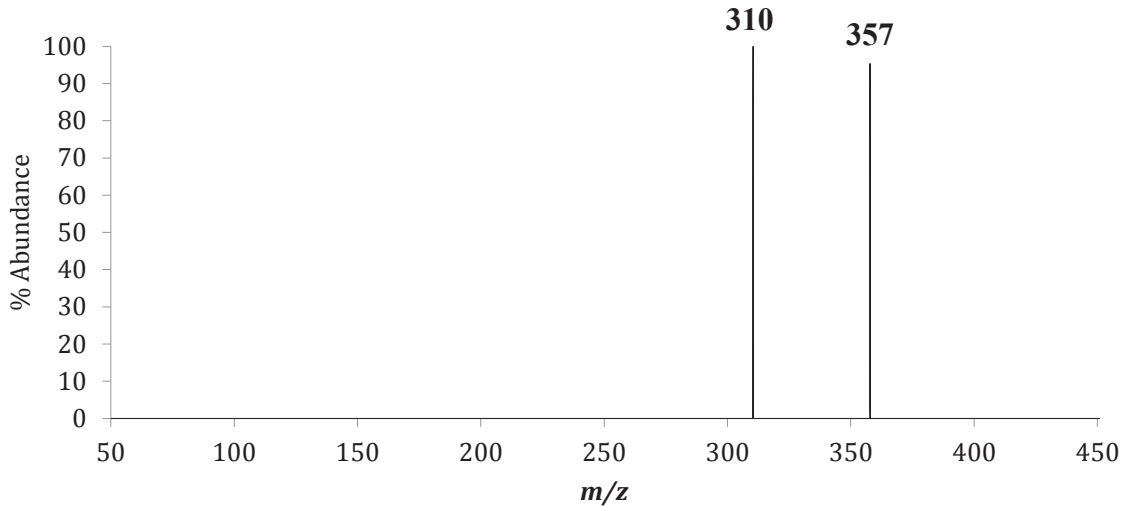

Figure 3.13: The positive mass spectrum obtained by scanning the third quadrupole following the selective reaction of *m/z* = 310 ([Ni(tftm)+*tBu*]$^+$) with neutral Mg(eeac)$_2$ to produce the complete ligand exchange fragment [Mg(tftm-*tBu*)(tftm)]$^+$ at *m/z* 357.

The proposed mechanism for the gas-phase formation of the magnesium complete ligand exchange fragment [Mg(tftm-*tBu*)(tftm)]$^+$ is presented in Equation 3.10.

$$[\text{Ni(tftm)}+tBu]^+ + \text{Mg(eeac)(eeac)} + \text{(tftm)} \rightarrow [\text{Mg(tftm-}tBu\text{)(tftm)}]^+ + \text{Ni(eeac)(eeac)} + 2tBu \qquad \text{(Eqn 3.10)}$$

Although additional work is necessary, the gas-phase reactions presented in Section 3.6 have shed much new light on the mechanism of ligand exchange between Mg(eeac)$_2$ and Ni(tftm)$_2$.

Mass-selected [Mg(eeac)$_2$]$^+$ at *m/z* 278 reacting with neutral Ni(tftm)$_2$ was observed to yield three ligand exchange products of interest; [Mg(tftm-CF$_2$)(tftm)]$^+$ at *m/z* 364, [Mg(eeac)(tftm-CF$_2$)]$^+$ at *m/z* 296, and [Mg(tftm-CF$_2$)]$^+$ at *m/z* 169. Based on these results, it appears as though a fluoride migration may play an important role in the formation of magnesium complete and mixed ligand exchange products from mass-selected magnesium precursors. Interestingly, no ligand exchange products of interested

were generated from $[Mg(eeac\text{-}Et)(eeac)]^+$ at *m/z* 249, $[Mg(eeac\text{-}Et)(eeac\text{-}Et)+2H]^+$ at *m/z* 222, or $[Mg(eeac)]^+$ at *m/z* 151.

Mass-selected $[Ni(tftm)_2]^+$ at *m/z* 448 reacting with neutral $Mg(eeac)_2$ generated two ligand exchange products, $[Mg(tftm\text{-}CF_2)(tftm)]^+$ at *m/z* 364 and $[Ni(eeac\text{-}Et)(eeac)]^+$ at *m/z* 283. Similarly, mass-selected $[Ni(tftm)+tBu]^+$ at *m/z* 310, reacting with neutral $Mg(eeac)_2$, was observed to yield only one ligand exchange product, $[Mg(tftm\text{-}tBu)(tftm)]^+$ at *m/z* 357. No ligand exchange products were observed to form from the following mass-selected ions: $[Ni(tftm\text{-}tBu)(tftm)]^+$ at *m/z* 391, $[Ni(tftm)]^+$ at *m/z* 253, or $[Ni(tftm\text{-}tBu)]^+$ at *m/z* 196.

3.7 The Co-Sublimation of $Mg(eeac)_2$ and Nickel Bis-Dibenzoylmethane ($Ni(dbm)_2$)

The positive EI mass spectra of $Mg(eeac)_2$ and $Ni(dbm)_2$ are presented in Figure 3.14(a) and 3.14(b), respectively. Although scans were completed from *m/z* 50 to 650, the spectra presented have a range of *m/z* 50 to 550 to better highlight the characteristic isotopic abundances in the products. The $Mg(eeac)_2$ is reproduced from Figure 3.1 and will not be discussed further. The spectrum of $Ni(dbm)_2$ displays multiple peaks; intact $[Ni(dbm)_2]^+$ is prominent at *m/z* 504, and the loss of one (dbm) ligand to form $[Ni(dbm)]^+$ is present at *m/z* 281, as is the intact *dbm* ligand at *m/z* 223. However, the intact ligand and fragments were not subjected to analysis with the collision cell as no metal chelator would be available to undergo ligand exchange.

The positive EI mass spectrum describing the co-sublimation of $Mg(eeac)_2$ and $Ni(dbm)_2$ is presented in Figure 3.14(c). No ligand exchange products with copper are identified, but ligand exchange with magnesium appears to occur quite readily. The complete ligand exchange product $[Mg(dbm)_2]^+$ is clearly present at *m/z* 470. The

heteroleptic, or mixed ligand, product $[Mg(dbm)(eeac)]^+$ is present at *m/z* 374, as is the mixed ligand fragment $[Mg(dbm)(eeac\text{-}Et)]^+$ at *m/z* 345. The single ligand exchange product $[Mg(dbm)]^+$ is also readily observed at *m/z* 247. The relative intensities of the ions and fragments formed in the baseline mass spectra and the co-sublimation reaction are displayed in Table 3.4.

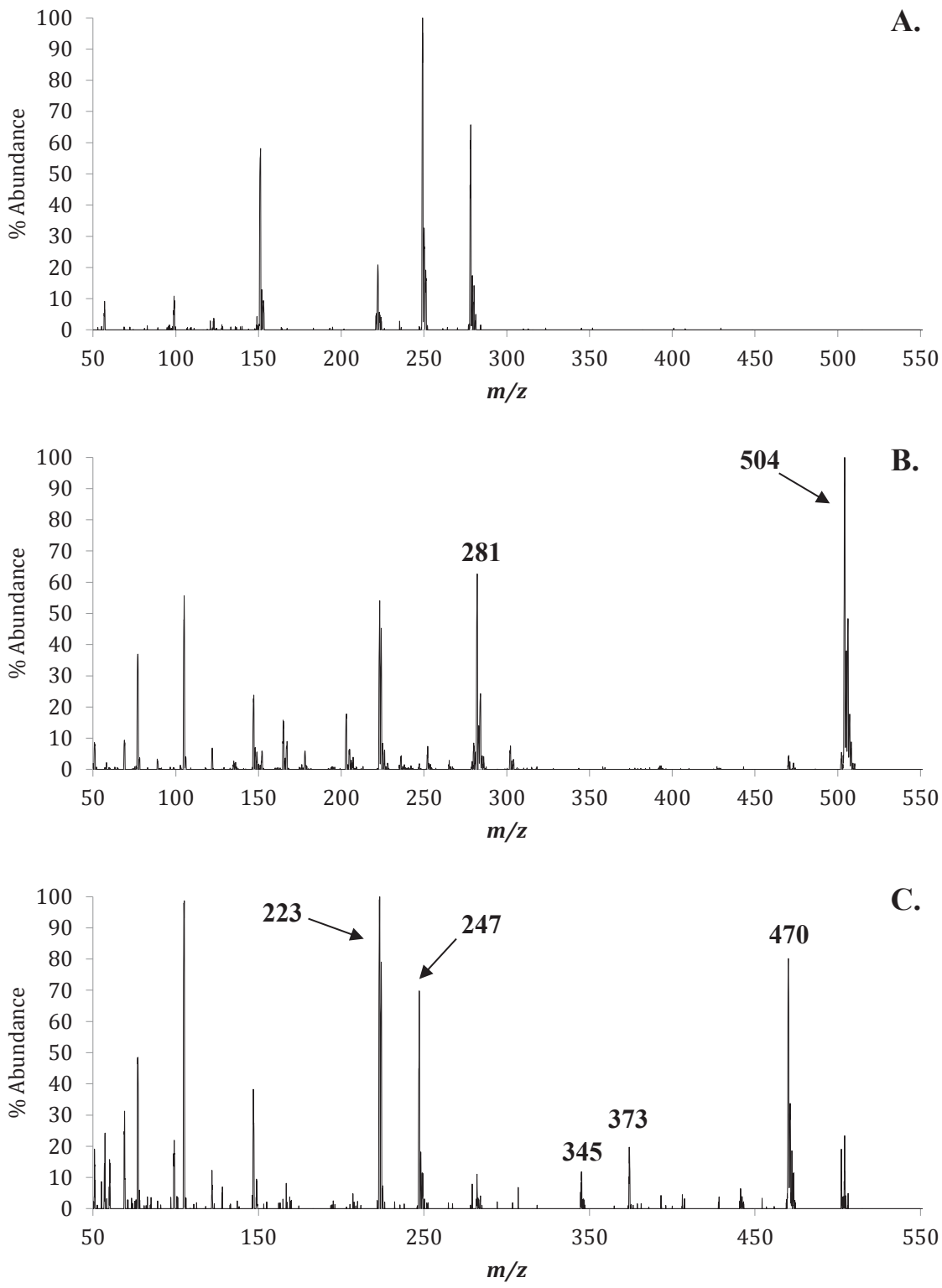

Figure 3.14: The positive EI mass spectra of (a) $Mg(eeac)_2$, (b) $Ni(dbm)_2$, and (c) the gas-phase co-sublimation of $Mg(eeac)_2$ and $Ni(dbm)_2$. The masses of parent compounds and fragments are labeled in (a) and (b). Masses of ligand exchange products and pertinent fragments are labeled in (c).

	Mass	Mass	MgL	NiL'''	MgL_2 & NiL'''_2	MgL & NiL'''_2
Species	Mg	Ni	Mg	Ni	Mg	Ni
$[ML_2]^+$	278	312	65		7	0
$[ML_2\text{-}C_2H_5]^+$	249	283	100		11	3
$[ML_2\text{-}2C_2H_5\text{+}2H]^+$	222	-	20		0	-
$[ML_2\text{-}2C_2H_5]^+$	-	254			-	0
$[ML]^+$	151	185	10		0	0
$[ML\text{-}C_2H_5]^+$	136	156	<1		0	0
$[ML'''_2]^+$	470	504		38	80	23
$[ML'''\text{-}Ph]^+$	393	427		<1	4	0
$[ML''']^+$	247	281		14	69	11
$[MLL''']^+$	374	408			18	0
$[M(L\text{-}C_2H_5)L''']^+$	345	379			11	<1

Table 3.4: The relative mass spectrometric abundances of the magnesium and nickel β-diketonate complexes as well as the co-sublimation experiment, as presented in Figure 3.14. L = (eeac); L''' = (dbm).

3.8 The Selective Reactions of $Mg(eeac)_2$ and $Ni(dbm)_2$

After co-sublimation experiments clearly identified the presence of new peaks and thus ligand exchange, additional reactions were examined to further investigate the contribution of each fragment. The most abundant magnesium species, $[Mg(eeac)_2]^+$ at *m/z* 278, [Mg(eeac-*Et*)(eeac)]$^+$ at *m/z* 249, [Mg(eeac-*Et*)(eeac-*Et*)+2H]$^+$ at *m/z* 222, and $[Mg(eeac)]^+$ at *m/z* 151, were each mass-selected and permitted to react with an atmosphere of neutral $Ni(dbm)_2$. All resulting products were scanned in the third quadrupole from *m/z* 50 to 650. Any ligand exchange products generated from collision-induced reaction are discussed herein.

The first product generated from collision-induced reaction was $[Ni(dbm)(eeac)]^+$ at *m/z* 407 and was produced by reacting mass-selected $[Mg(eeac)_2]^+$ at *m/z* 278 with neutral $Ni(dbm)_2$. The results from this reaction are presented in Figure 3.15.

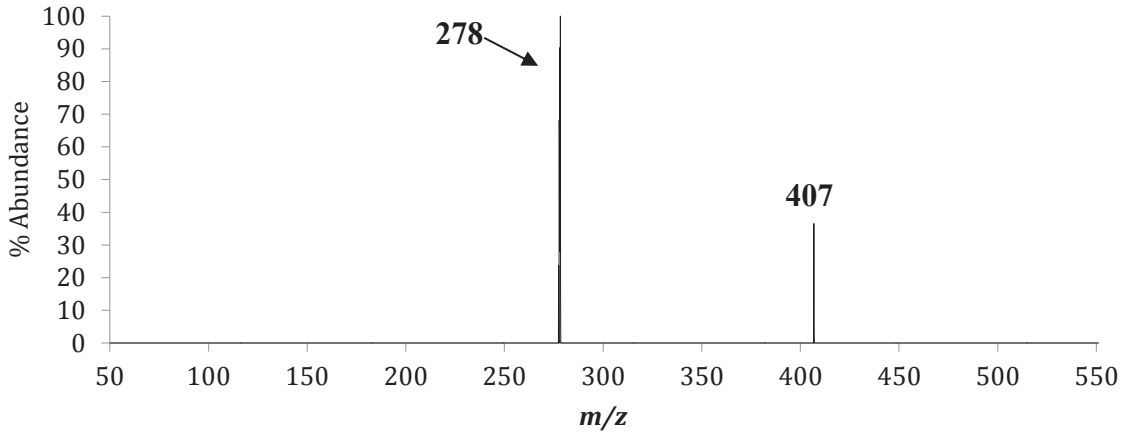

Figure 3.15: The positive mass spectrum obtained by scanning the third quadrupole following the selective reaction of *m/z* = 278 ($[Mg(eeac)_2]^+$) with neutral $Ni(dbm)_2$ to produce the ligand exchange fragment $[Ni(dbm)(eeac)]^+$ at *m/z* 407.

The proposed mechanism for the gas-phase formation of the nickel mixed ligand exchange product $[Ni(dbm)(eeac)]^+$ is displayed in Equation 3.11.

$$[Mg(eeac)(eeac)]^+ + Ni(dbm)(dbm) \rightarrow [Ni(dbm)(eeac)]^+ + Mg(dbm)(eeac) \qquad \text{(Eqn 3.11)}$$

The reaction between neutral $Ni(dbm)_2$ and mass-selected $[Mg(eeac\text{-}Et)(eeac)]^+$ at *m/z* 249 also generated one ligand exchange product, $[Ni(eeac\text{-}Et)(eeac)]^+$ at *m/z* 283, which is displayed in Figure 3.16.

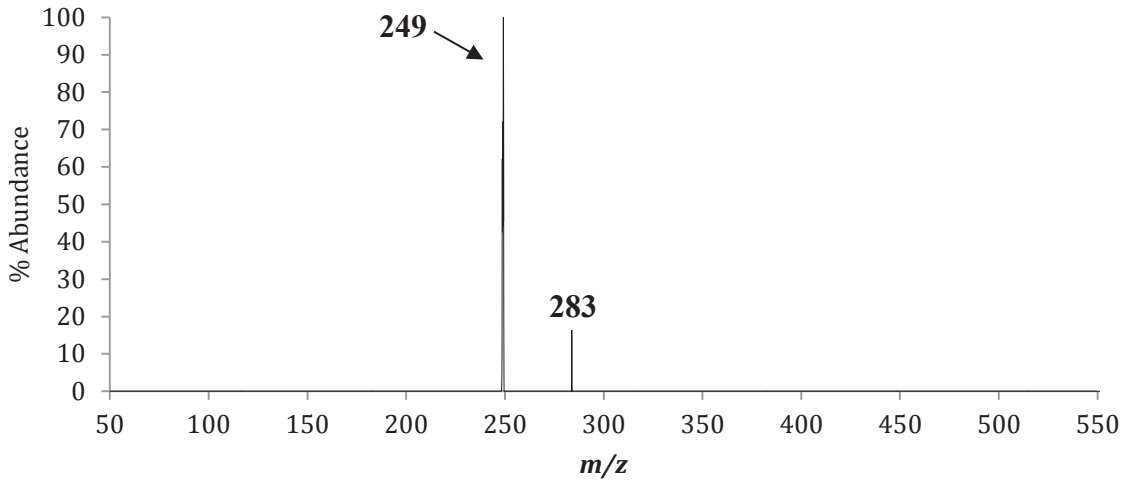

Figure 3.16: The positive mass spectrum obtained by scanning the third quadrupole following the selective reaction of *m/z* = 249 ($[Mg(eeac\text{-}Et)(eeac)]^+$) with neutral $Ni(dbm)_2$ to produce the ligand exchange fragment $[Ni(eeac\text{-}Et)(eeac)]^+$ at *m/z* 283.

The proposed mechanism for the gas-phase formation of the nickel complete ligand exchange fragment $[Ni(eeac\text{-}Et)(eeac)]^+$ is displayed in Equation 3.12.

$$[Mg(eeac\text{-}Et)(eeac)]^+ + Ni(dbm)(dbm) \rightarrow [Ni(eeac\text{-}Et)(eeac)]^+ + Mg(dbm)(dbm) \quad \text{(Eqn 3.12)}$$

To provide a more complete picture of ligand exchange, both $[Ni(dbm)_2]^+$ at *m/z* 504 and $[Ni(dbm)]^+$ at *m/z* 282 were isolated and permitted to react with an atmosphere of neutral $Mg(eeac)_2$. The magnesium mixed ligand exchange product $[Mg(dbm)(eeac)]^+$ at *m/z* 374 was observed to form following the reaction with neutral $Mg(eeac)_2$ and is displayed in Figure 3.17.

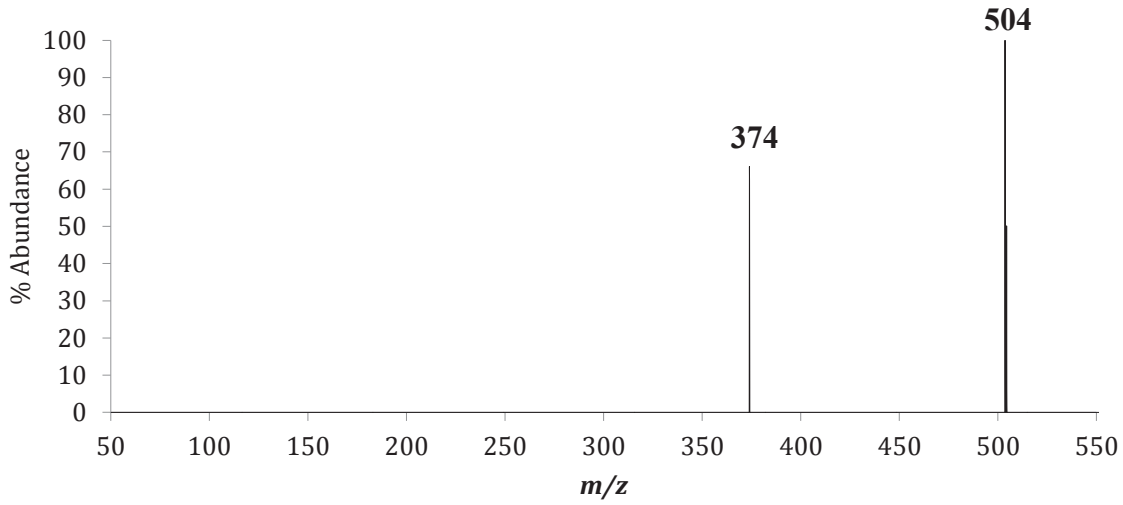

Figure 3.17: The positive mass spectrum obtained by scanning the third quadrupole following the selective reaction of *m/z* = 504 ($[Ni(dbm)_2]^+$) with neutral $Mg(eeac)_2$ to produce the mixed ligand exchange species $[Mg(dbm)(eeac)]^+$ at *m/z* 374.

The proposed mechanism of the gas-phase formation for the magnesium mixed ligand exchange product $[Mg(dbm)(eeac)]^+$ is presented in Equation 3.13.

$$[Ni(dbm)(dbm)]^+ + Mg(eeac)(eeac) \rightarrow [Mg(dbm)(eeac)]^+ + Ni(dbm)(eeac) \qquad \text{(Eqn 3.13)}$$

The second ligand exchange product generated from the reaction between neutral $Mg(eeac)_2$ and mass-selected $[Ni(dbm)_2]^+$ at *m/z* 504 was $[Mg(dbm)(dbm\text{-}Ph)]^+$ at *m/z* 393, which is displayed in Figure 3.18.

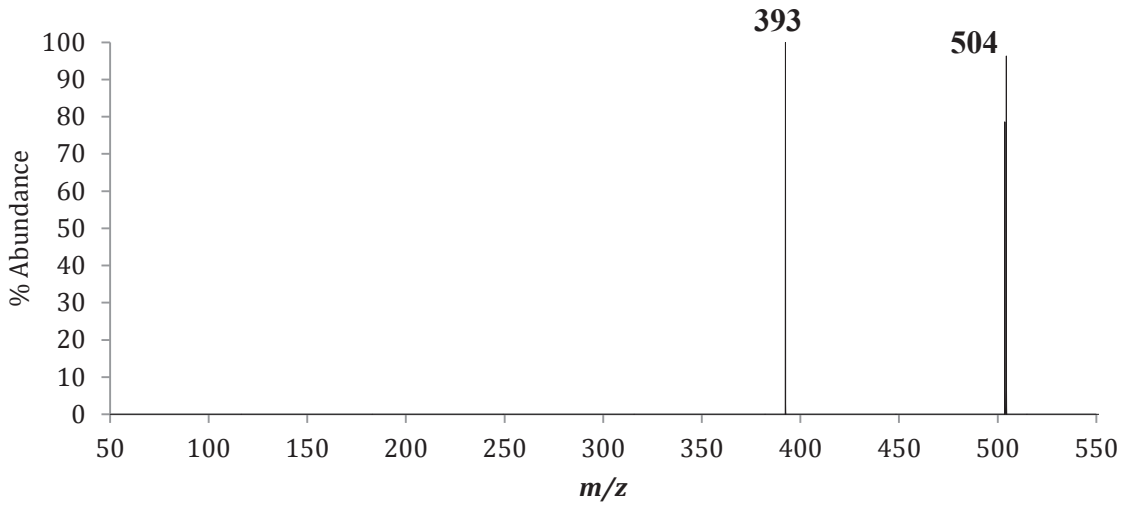

Figure 3.18: The positive mass spectrum obtained by scanning the third quadrupole following the selective reaction of *m/z* = 504 ($[Ni(dbm)_2]^+$) with neutral $Mg(eeac)_2$ to produce the mixed ligand exchange fragment $[Mg(dbm)(dbm\text{-}Ph)]^+$ at *m/z* 393.

The proposed mechanism for the gas-phase formation of the magnesium complete ligand exchange fragment $[Mg(dbm)(dbm\text{-}Ph)]^+$ is displayed in Equation 3.14.

$$[Ni(dbm)(dbm)]^+ + Mg(eeac)(eeac) \rightarrow$$
$$[Mg(dbm)(dbm\text{-}Ph)]^+ + Ni(eeac)_2 + \text{benzene} \qquad \text{(Eqn 3.14)}$$

One last ligand exchange product of interest was generated from the collision-induced reaction of mass-selected $[Ni(dbm)]^+$ at *m/z* 282 with neutral $Mg(eeac)_2$ to form the magnesium mixed ligand exchange product $[Mg(dbm)(eeac)]^+$ at *m/z* 374 and is displayed in Figure 3.19. The peaks at *m/z* 204 and *m/z* 160 are consistent with fragments from the dissociation of the (dbm) ligand.

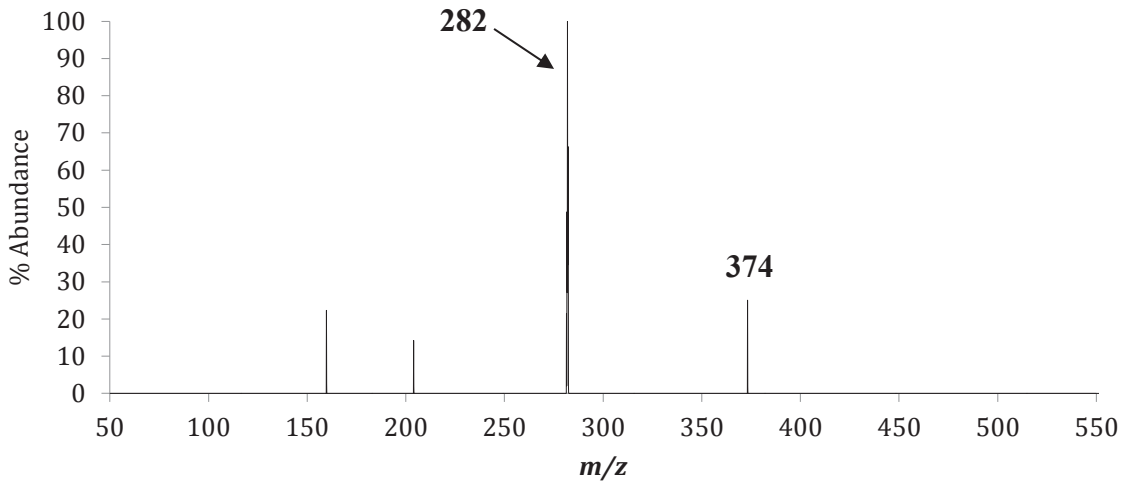

Figure 3.19: The positive mass spectrum obtained by scanning the third quadrupole following the selective reaction of *m/z* = 282 ($[Ni(dbm)]^+$) with neutral $Mg(eeac)_2$ to produce the mixed ligand exchange species $[Mg(dbm)(eeac)]^+$ at *m/z* 374.

The proposed mechanism for the gas-phase formation of the magnesium mixed ligand exchange product $[Mg(dbm)(eeac)]^+$ is presented in Equation 3.15.

$$[Ni(dbm)]^+ + Mg(eeac)(eeac) \rightarrow [Mg(dbm)(eeac)]^+ + Ni(eeac) \qquad \text{(Eqn 3.15)}$$

Although additional work is necessary, the spectra presented in Section 3.8 have provided much novel insight into the mechanism of gas-phase ligand exchange between $Mg(eeac)_2$ and $Ni(dbm)_2$.

Reactions of mass-selected $[Mg(eeac)_2]^+$ at *m/z* 278 and neutral $Ni(dbm)_2$ generated $[Ni(dbm)(eeac)]^+$ at *m/z* 407, while reactions involving mass-selected $[Mg(eeac\text{-}Et)(eeac)]^+$ with neutral $Ni(dbm)_2$ only generated $[Ni(eeac\text{-}Et)(eeac)]^+$ at *m/z* 283. No ligand exchange products were observed to occur when mass-selecting $[Mg(eeac\text{-}Et)(eeac\text{-}Et)+2H]^+$ at *m/z* 222, or $[Mg(eeac)]^+$ at *m/z* 151.

It also appears that mass-selected $[Ni(dbm)]^+$ and $[Ni(dbm)_2]^+$ are instrumental in the formation of magnesium ligand exchange products. Mass-selected $[Ni(dbm)_2]^+$ at *m/z*

504 reacting with neutral $Mg(eeac)_2$ was observed to produce $[Mg(dbm)(dbm\text{-}Ph)]^+$ at *m/z* 392. Mass-selected $[Ni(dbm)_2]^+$ at *m/*z 504 and $[Ni(dbm)]^+$ *m/*z 282 were both found to yield the magnesium mixed ligand exchange product $[Mg(dbm)(eeac)]^+$ at *m/z* 374 when reacted with neutral $Mg(eeac)_2$.

Chapter 4

The Co-Sublimation and Gas-Phase Ligand Exchange Reactions of Magnesium Bis-Diethylacetylacetonate ($Mg(eeac)_2$) with Copper Bis-Acetylacetonate ($Cu(acac)_2$), Copper Bis-Trifluorotrimethylacetylacetonate ($Cu(tftm)_2$), and Copper Bis-Dibenzoylmethane ($Cu(dbm)_2$)

4.1 Introduction

Presented herein is an in-depth analysis of gas-phase ligand exchange reactions between an alkaline earth metal β-diketonate complex and several transition metal β-diketonate complexes. $Mg(eeac)_2$ was once again selected as the alkaline earth metal β-diketonate complex of choice. However, in order to compare and contrast the possible reactions with nickel β-diketonates as described in Chapter 3, copper β-diketonate complexes were selected where the properties of the ligands chelated to the copper cation were varied in order to provide a more holistic view of the ensuing mechanisms. Copper bis-acetylacetonate ($Cu(acac)_2$) provided insight on how $Mg(eeac)_2$ exchanges ligands with a β-diketonate also possessing alkyl constituents; fluorinated $Cu(tftm)_2$ was selected to examine how $Mg(eeac)_2$ would exchange its ligands with a more volatile species; and steric effects from bulky ligands were evaluated using $Cu(dbm)_2$.

As introduced in Section 3, isotopic distributions within the chelating metals are a key factor in identifying ligand exchange products, particularly those which were isobaric, or possessing the same mass-to-charge (*m/z*) ratio. Magnesium possesses three naturally occurring isotopes; ^{24}Mg, which is present in 78.99% abundance, as well as ^{25}Mg and ^{26}Mg, present at 10.00% and 11.01%, respectively. Thus on a mass spectrum, a

species possessing a magnesium chelating metal will have one very prominent peak at the mass corresponding with that of ^{24}Mg, with two smaller peaks of virtually equal height to the immediate right, corresponding to masses ^{25}Mg and ^{26}Mg. Copper, however, exhibits only two stable isotopes; ^{63}Cu with 69.17% abundance and ^{65}Cu at 30.83% abundance. On a mass spectrum this would be reflected as a tall peak corresponding to ^{63}Cu, and a second peak about half its height at a slightly higher mass for ^{65}Cu. These signature-like patterns are an invaluable tool in identifying ligand exchange products when different metals are present in the experiment.

4.2 Magnesium Bis-Diethylacetylacetonate ($Mg(eeac)_2$)

For information regarding the positive EI mass spectrum of $Mg(eeac)_2$ and its corresponding fragmentation behavior, please refer to Section 3.2, specifically Figure 3.1. A cationic mass spectrum of $Mg(eeac)_2$ will be reproduced for all co-sublimation experiments described in this Chapter for purposes of clarity and comparison.

4.3 The Co-Sublimation of $Mg(eeac)_2$ and Copper Bis-Acetylacetonate ($Cu(acac)_2$)

Presented in Figure 4.1(a) and 4.1(b) are the positive EI mass spectra for $Mg(eeac)_2$ and copper bis-acetylacetonate ($Cu(acac)_2$). The mass spectrum describing the co-sublimation of these two compounds is displayed in Figure 4.1(c). Although each experimental scan had a range of *m/*z 50 to 650, the spectra presented are displayed from *m/*z 50 to 350 to highlight the distinct isotopic distribution patterns for each species. As mentioned in section 4.2, the positive EI mass spectrum for $Mg(eeac)_2$ is reproduced from Figure 3.1 and will not be discussed further. The positive EI mass spectrum for $Cu(acac)_2$ is displayed in Figure 4.1(b), where intact $[Cu(acac)_2]^+$ is displayed at the peak

of *m/z* 261. The loss of a methyl group to yield $[Cu(acac\text{-}CH_3)(acac)]^+$ is displayed at *m/z* 246, as is the loss of a second methyl group from the parent compound to form $[Cu(acac\text{-}CH_3)(acac\text{-}CH_3)]^+$ at *m/z* 231. The single ligand species $[Cu(acac)]^+$ is also present at *m/z* 162, as is the loss of a methyl group from the single ligand species to form $[Cu(acac\text{-}CH_3)]^+$ at *m/z* 147.

The co-sublimation mass spectrum of $Mg(eeac)_2$ and $Cu(acac)_2$ is displayed in Figure 4.1(c) where both copper and magnesium products are found to occur during co-sublimation. The copper complete ligand exchange species $[Cu(eeac)_2]^+$ is present at *m/z* 317 as well as the loss of one ethyl group from $[Cu(eeac)_2]^+$ to form $[Cu(eeac\text{-}Et)(eeac)]^+$ at *m/z* 288. Loss of another ethyl group from $[Cu(eeac\text{-}Et)(eeac)]^+$ to form $[Cu(eeac\text{-}Et)(eeac\text{-}Et)]^+$ is observed at *m/z* 259, as is the single ligand exchange species $[Cu(eeac)]^+$ at *m/z* 191. The loss of an ethyl group from the single ligand exchange species to form $[Cu(eeac\text{-}Et)]^+$ is clearly present at *m/z* 160 and the copper mixed ligand exchange species $[Cu(acac)(eeac)]^+$ can also be observed at *m/z* 289.

The complete magnesium ligand exchange product $[Mg(acac)_2]^+$ is also present in Figure 4.1(c) at *m/z* 222, as is the loss of a methyl group to form the fragment $[Mg(acac\text{-}CH_3)(acac)]^+$ at *m/z* 207. The magnesium single ligand exchange species $[Mg(acac)]^+$ is observed at *m/z* 123, as well as the magnesium mixed ligand exchange species $[Mg(acac)(eeac)]^+$ at *m/z* 250. However, it is important to note that the ion signal for $[Mg(acac)(eeac)]^+$ at *m/z* 250 and $[Mg(acac)_2]^+$ at *m/z* 222 overlap slightly with the magnesium baseline mass peaks for $[Mg(eeac\text{-}Et)(eeac)]^+$ at *m/z* 249 and $[Mg(eeac\text{-}Et)(eeac\text{-}Et)+2H]^+$ at *m/z* 222. However, the fragment $[Mg(acac\text{-}CH_3)(acac)]^+$ present at *m/z* 207 likely indicates that the complete ligand exchange product $[Mg(acac)_2]^+$ is indeed

present. The relative abundances of all species reported in Figure 4.1 are displayed in Table 4.1.

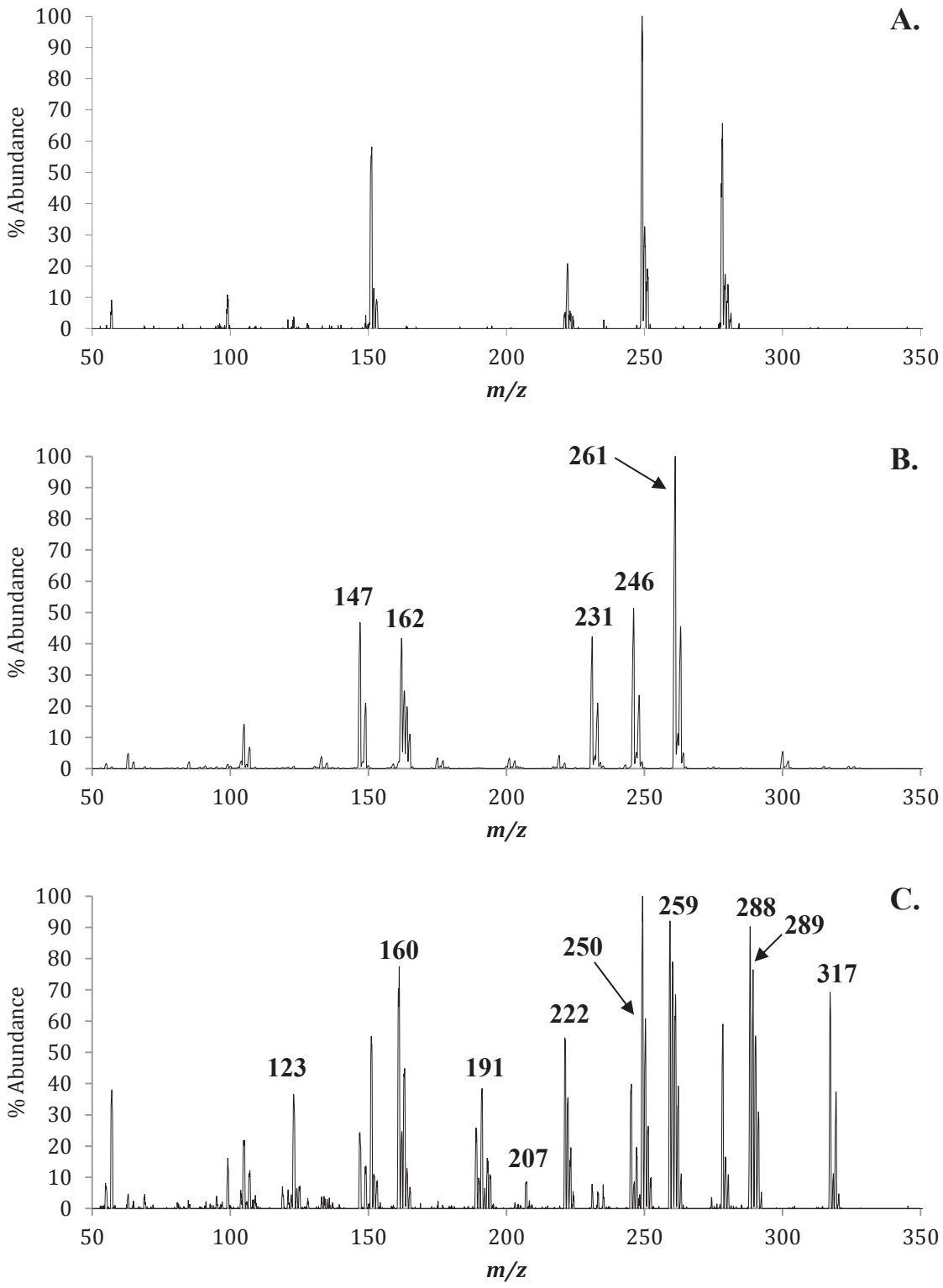

Figure 4.1: The positive EI mass spectra of (a) $Mg(eeac)_2$, (b) $Cu(acac)_2$, and (c) the gas-phase co-sublimation of $Mg(eeac)_2$ and $Cu(acac)_2$. The masses of parent compounds and fragments are labeled in (a) and (b). Masses of ligand exchange products and pertinent fragments are labeled in (c).

	Mass	Mass	MgL	CuL'	MgL & CuL'	MgL & CuL'
Species	**Mg**	**Cu**	**Mg**	**Cu**	**Mg**	**Cu**
$[ML_2]^+$	278	317	65		59	69
$[ML_2\text{-}C_2H_5]^+$	249	288	100		100	90
$[ML_2\text{-}2C_2H_5\text{+}2H]^+$	222	-	20		54	-
$[ML_2\text{-}2C_2H_5]^+$	-	259	0		-	92
$[ML]^+$	151	190	10		55	10
$[ML\text{-}C_2H_5]^+$	136	161	<1		1	70
$[ML'_2]^+$	222	261		100	35	68
$[ML'_2\text{-}CH_3]^+$	207	246		51	8	8
$[ML']^+$	123	162		42	36	24
$[ML'\text{-}CH_3]^+$	108	147		47	2	24
$[MLL'']^+$	250	289			60	76
$[M(L\text{-}C_2H_5)L'']^+$	221	260			54	78

Table 4.1: The relative mass spectrometric abundances of the $Mg(eeac)_2$ and $Cu(acac)_2$ β-diketonate complexes as well as the co-sublimation experiment, as presented in Figure 4.1. L = (eeac), L' = (acac).

4.4 The Selective Reactions of $Mg(eeac)_2$ and $Cu(acac)_2$

The most abundant species from the positive EI mass spectra of $Mg(eeac)_2$ and $Cu(acac)_2$ were also subjected to collision-induced reaction analysis using tandem mass spectrometry within a triple quadrupole mass spectrometer. For instance, $[Mg(eeac)_2]^+$ was mass-selected at *m/z* 278 using the first quadrupole and permitted to continue to the second quadrupole, containing an atmosphere of neutral $Cu(acac)_2$. The second quadrupole thus acted as a collision cell, and all resultant products were detected by scanning the third quadrupole from *m/z* 50 to 650. Each of the more abundant magnesium

containing species reported previously in Table 4.1 was mass-selected and subjected to CIR analysis.

The first product of interest following the reaction of mass-selected $[Mg(eeac)_2]^+$ at *m/z* 278 and neutral $Cu(acac)_2$ is presented in Figure 4.2, and produced the copper mixed ligand exchange product $[Cu(acac)(eeac)]^+$ at *m/z* 289.

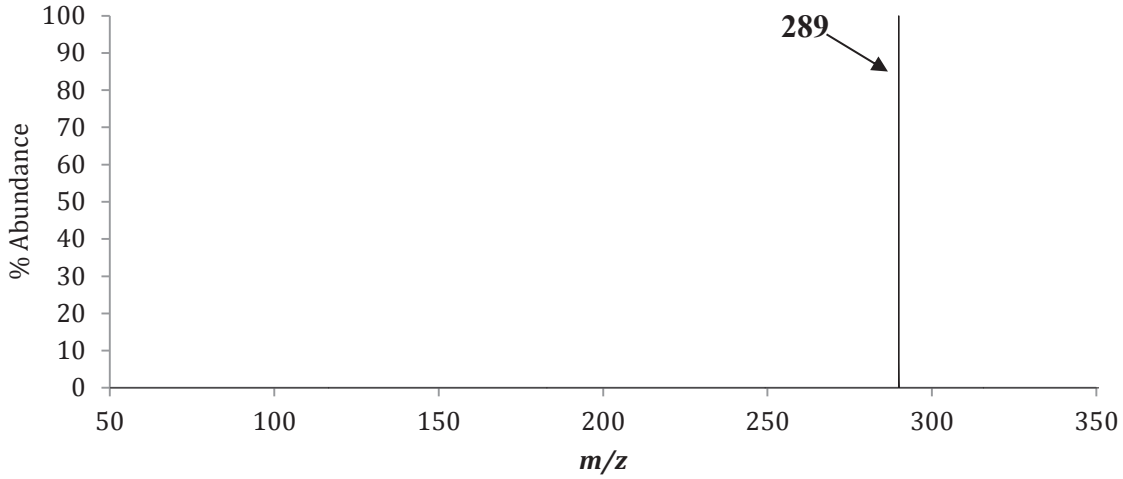

Figure 4.2: The positive mass spectrum obtained by scanning the third quadrupole following the selective reaction of *m/z* = 278 ($[Mg(eeac)_2]^+$) with neutral $Cu(acac)_2$ to produce the mixed ligand exchange product $[Cu(acac)(eeac)]^+$ at *m/z* 289.

The proposed mechanism for the gas-phase formation of the copper mixed ligand product $[Cu(acac)(eeac)]^+$ is presented in Equation 4.1.

$$[Mg(eeac)(eeac)]^+ + Cu(acac)(acac) \rightarrow [Cu(acac)(eeac)]^+ + Mg(acac)(eeac) \qquad \text{(Eqn 4.1)}$$

The second ligand exchange product of interest is presented in Figure 4.3 and was generated from mass-selected $[Mg(eeac)_2]^+$ at *m/z* 278 reacting with neutral $Cu(acac)_2$. Interestingly, only the mixed ligand exchange fragment $[Cu(acac)(eeac\text{-}Et)]^+$ was detected at *m/z* 260.

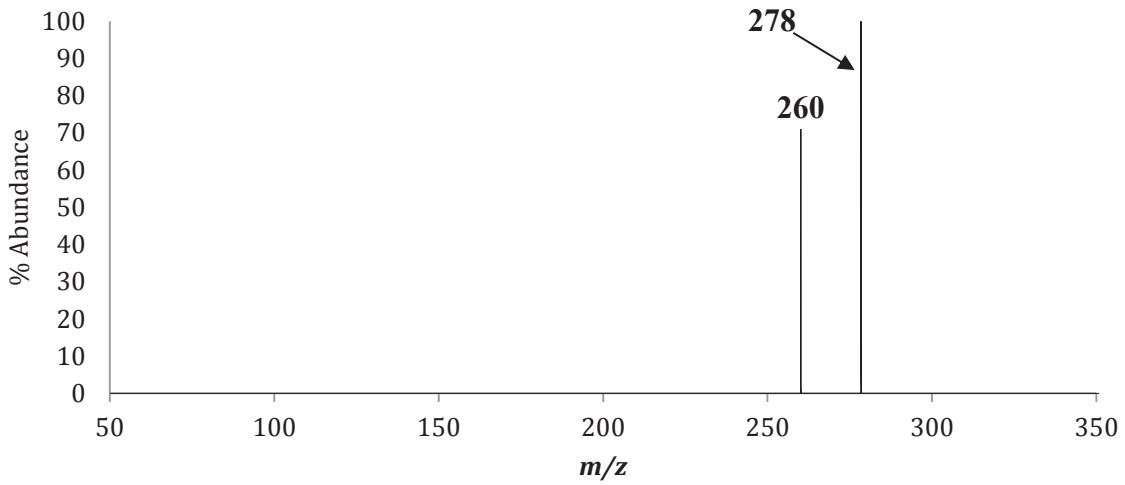

Figure 4.3: The positive mass spectrum obtained by scanning the third quadrupole following the selective reaction of *m/z* = 278 ($[Mg(eeac)_2]^+$) with neutral $Cu(acac)_2$ to produce the mixed ligand exchange fragment $[Cu(acac)(eeac\text{-}Et)]^+$ at *m/z* 260.

The proposed mechanism for the gas-phase formation of the copper mixed ligand fragment $[Cu(acac)(eeac\text{-}Et)]^+$ is displayed in Equation 4.2.

$$[Mg(eeac)(eeac)]^+ + Cu(acac)(acac) \rightarrow$$

$$[Cu(acac)(eeac\text{-}Et)]^+ + Mg(acac)(eeac) + Et \qquad \text{(Eqn 4.2)}$$

Another ligand exchange product generated from the collision-induced reaction of mass-selected $[Mg(eeac)_2]^+$ at *m/z* 278 and neutral $Cu(acac)_2$ is displayed in Figure 4.4 and corresponds to the single ligand exchange product $[Cu(eeac)]^+$ at *m/z* 191.

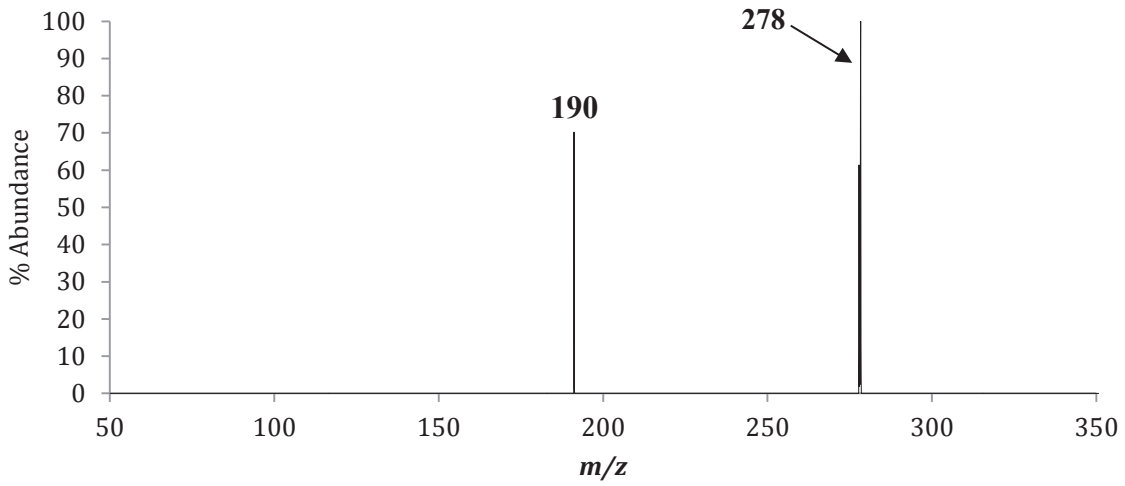

Figure 4.4: The positive mass spectrum obtained by scanning the third quadrupole following the selective reaction of *m/z* = 278 ($[Mg(eeac)_2]^+$) with neutral $Cu(acac)_2$ to produce the single ligand exchange product $[Cu(eeac)]^+$ at *m/z* 190.

The proposed mechanism for the gas-phase formation of the copper single ligand exchange product $[Cu(eeac)]^+$ is presented in Equation 4.3.

$$[Mg(eeac)(eeac)]^+ + Cu(acac)(acac) \rightarrow$$
$$[Cu(eeac)]^+ + Mg(acac)(eeac) + (acac) \qquad \text{(Eqn 4.3)}$$

The final product generated from the collision-induced reaction with $[Mg(eeac)_2]^+$ at *m/z* 278 and neutral $Cu(acac)_2$ was the single ligand exchange fragment $[Cu(eeac\text{-}Et)]^+$ at *m/z* 161, and is displayed in Figure 4.5.

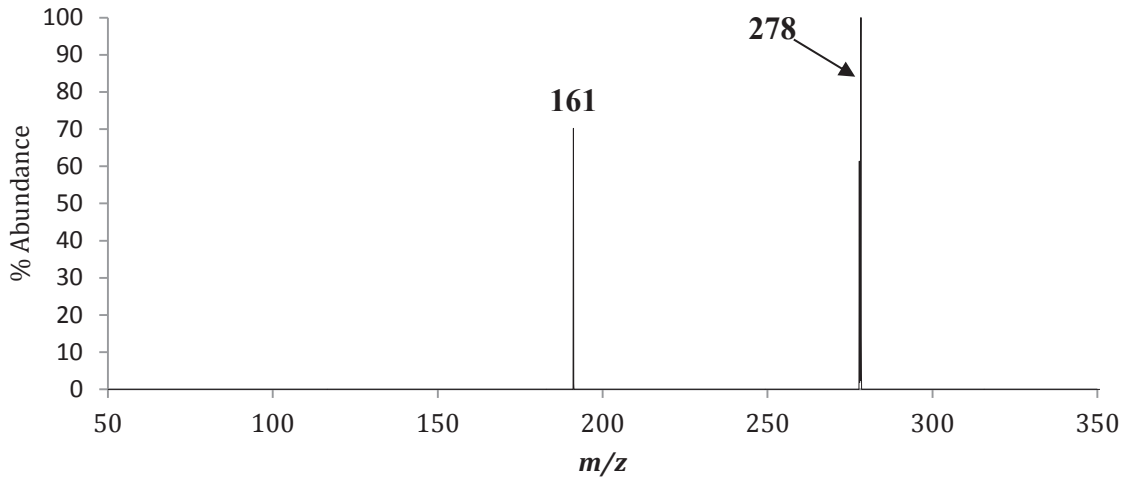

Figure 4.5: The positive mass spectrum obtained by scanning the third quadrupole following the selective reaction of *m/z* = 278 ($[Mg(eeac)_2]^+$) with neutral $Cu(acac)_2$ to produce the single ligand exchange fragment $[Cu(eeac\text{-}Et)]^+$ at *m/z* 161.

The proposed mechanism for the gas-phase formation of the copper single ligand exchange fragment $[Cu(eeac\text{-}Et)]^+$ is presented in Equation 4.4.

$$[Mg(eeac)(eeac)]^+ + Cu(acac)(acac) \rightarrow [Cu(eeac\text{-}Et)]^+ + Mg(acac)(eeac) + (acac) + Et \qquad \text{(Eqn 4.4)}$$

An additional ligand exchange product of interest was also generated by mass-selecting $[Mg(eeac\text{-}Et)(eeac)]^+$ at *m/z* 249 and allowing it to react with neutral $Cu(acac)_2$ to form $[Mg(acac\text{-}CH_3)]^+$ at *m/z* 207, as displayed in Figure 4.6.

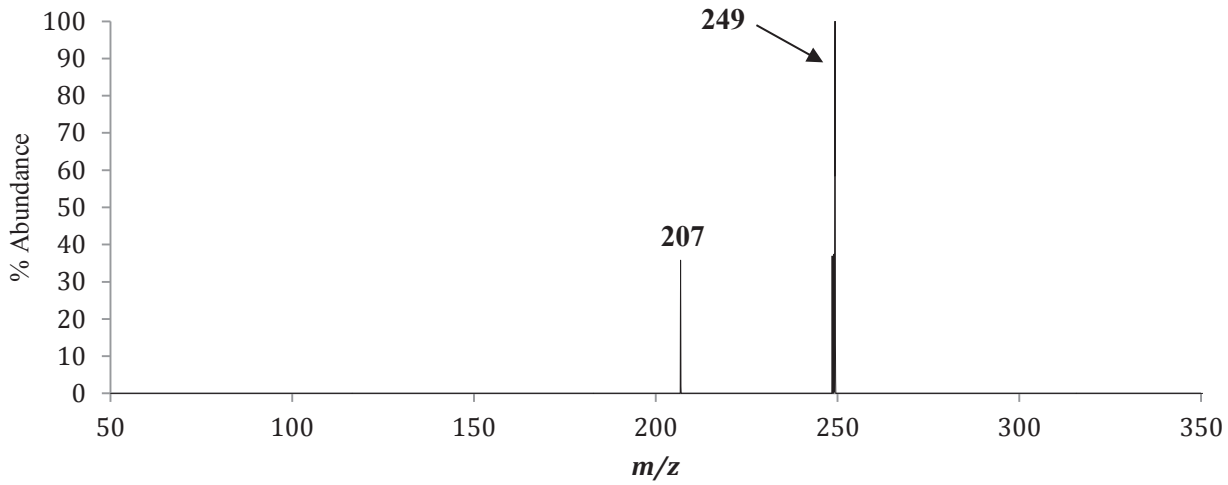

Figure 4.6: The positive mass spectrum obtained by scanning the third quadrupole following the selective reaction of *m/z* = 249 ($[Mg(eeac\text{-}Et)(eeac)]^+$) with neutral $Cu(acac)_2$ to produce the single ligand exchange fragment $[Mg(acac)(acac\text{-}CH_3)]^+$ at *m/z* 207.

The proposed mechanism for the gas-phase formation of the magnesium complete ligand exchange fragment $[Mg(acac\text{-}CH_3)(acac)]^+$ is presented in Equation 4.5.

$$[Mg(eeac\text{-}Et)(eeac)]^+ + Cu(acac)(acac) \rightarrow [Mg(acac\text{-}CH_3)(acac)]^+ + Cu(eeac\text{-}Et)(eeac) + CH_3 \quad \text{(Eqn 4.5)}$$

Mass-selected $[Mg(eeac\text{-}Et)(eeac\text{-}Et)+2H]^+$ at *m/z* 222 was also found to generate the magnesium single ligand exchange product $[Mg(acac\text{-}CH_3)]^+$ at *m/z* 207 when reacting with neutral $Cu(acac)_2$, and is depicted in Figure 4.7.

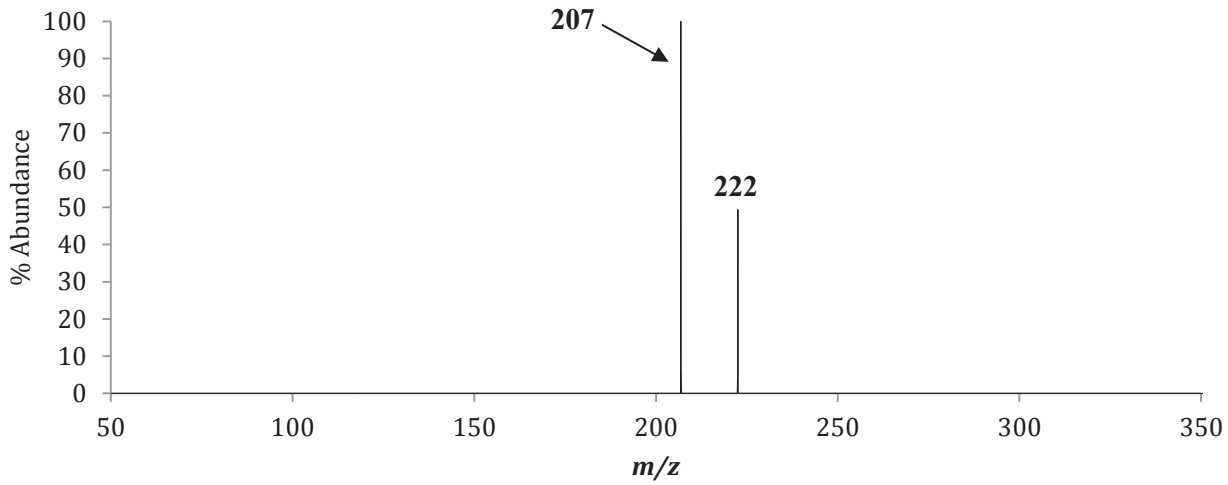

Figure 4.7: The positive mass spectrum obtained by scanning the third quadrupole following the selective reaction of *m/z* = 222 ([Mg(eeac-*Et*)(eeac-*Et*)+2H]$^+$) with neutral $Cu(acac)_2$ to produce the complete ligand exchange fragment [Mg(acac-CH_3)(acac)]$^+$ at *m/z* 207.

The proposed mechanism for the gas-phase formation of the magnesium complete ligand exchange fragment [Mg(acac-CH_3)(acac)]$^+$ is presented in Equation 4.6.

$$[Mg(eeac\text{-}Et)(eeac\text{-}Et)+2H]^+ + Cu(acac)(acac) \rightarrow$$
$$[Mg(acac\text{-}CH_3)(acac)]^+ + Cu(eeac)(eeac\text{-}Et) + CH_3 + 2H \qquad \text{(Eqn 4.6)}$$

No ligand exchange products were observed to form following the mass-selected reaction of [Mg(eeac-*Et*)]$^+$ at *m/z* 151 with neutral $Cu(acac)_2$.

Mass-selected copper ions were also investigated through specific collision-induced reaction analysis with neutral $Mg(eeac)_2$. The first product of interest generated from the collision-induced reaction of mass-selected [$Cu(acac)_2$]$^+$ at *m/z* 261 was the complete ligand exchange product [$Cu(eeac)_2$]$^+$ at *m/z* 317 and is presented in Figure 4.8.

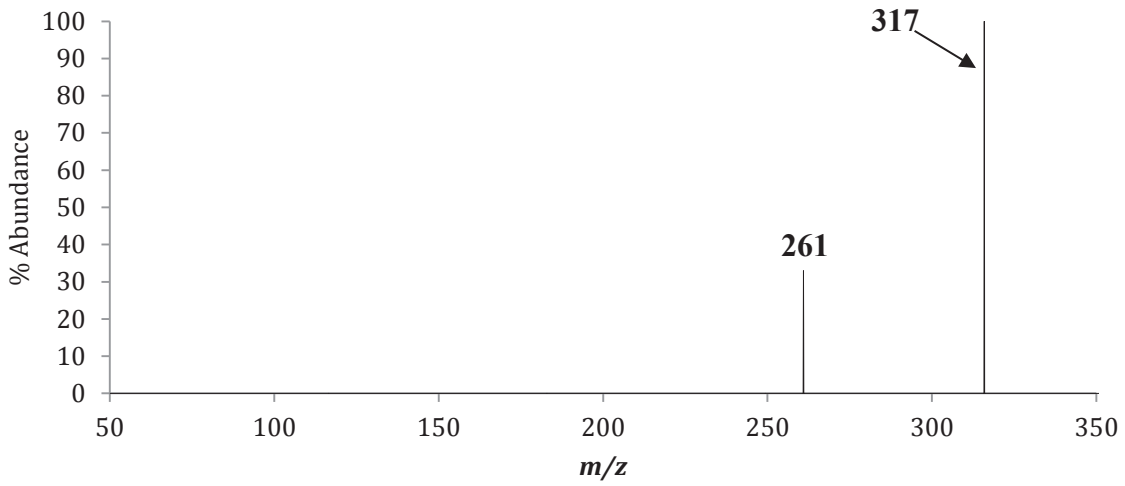

Figure 4.8: The positive mass spectrum obtained by scanning the third quadrupole following the selective reaction of *m/z* = 261 ($[Cu(acac)_2]^+$) with neutral $Mg(eeac)_2$ to produce the complete ligand exchange product $[Cu(eeac)_2]^+$ at *m/z* 317.

The proposed mechanism for the gas-phase formation of the copper complete ligand exchange product $[Cu(eeac)_2]^+$ is presented in Equation 4.7.

$$[Cu(acac)(acac)]^+ + Mg(eeac)(eeac) \rightarrow [Cu(eeac)(eeac)]^+ + Mg(acac)(acac) \qquad \text{(Eqn 4.7)}$$

The second product of interest generated by mass-selecting $[Cu(acac)_2]^+$ at *m/z* 261 and allowing it to react with neutral $Mg(eeac)_2$ is the complete ligand exchange product $[Cu(acac)(eeac)]^+$ at *m/z* 289 and is presented in Figure 4.9.

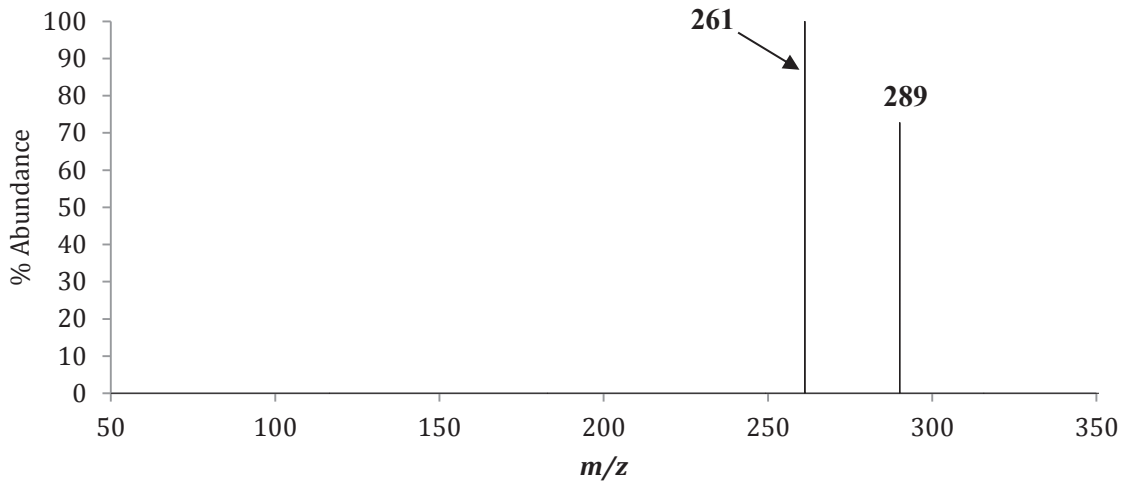

Figure 4.9: The positive mass spectrum obtained by scanning the third quadrupole following the selective reaction of *m/z* = 261 ($[Cu(acac)_2]^+$) with neutral $Mg(eeac)_2$ to produce the mixed ligand exchange product $[Cu(acac)(eeac)]^+$ at *m/z* 289.

The proposed mechanism for the gas-phase formation of the copper mixed ligand exchange product $[Cu(acac)(eeac)]^+$ is displayed in Equation 4.8.

$$[Cu(acac)(acac)]^+ + Mg(eeac)(eeac) \rightarrow [Cu(acac)(eeac)]^+ + Mg(acac)(eeac) \qquad \text{(Eqn 4.8)}$$

The mixed ligand exchange fragment $[Cu(acac)(eeac\text{-}Et)]^+$ at *m/z* 260 was generated from the reaction of mass-selected $[Cu(acac)_2]^+$ at *m/z* 261 and neutral $Mg(eeac)_2$ and is presented in Figure 4.10.

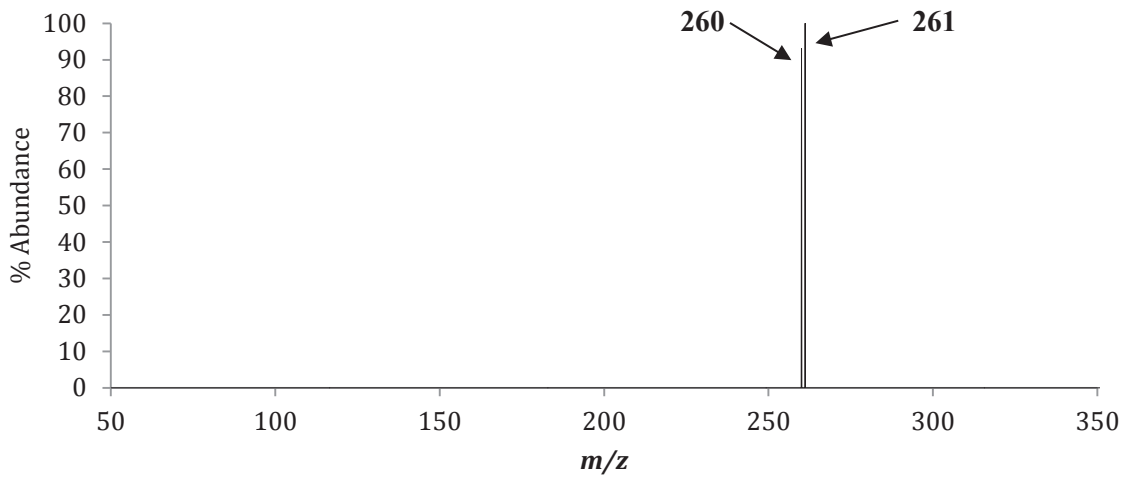

Figure 4.10: The positive mass spectrum obtained by scanning the third quadrupole following the selective reaction of *m/z* = 261 ($[Cu(acac)_2]^+$) with neutral $Mg(eeac)_2$ to produce the mixed ligand exchange fragment $[Cu(acac)(eeac\text{-}Et)]^+$ at *m/z* 260.

The proposed mechanism for the gas-phase formation of the copper mixed ligand exchange fragment $[Cu(acac)(eeac\text{-}Et)]^+$ is presented in Equation 4.9.

$$[Cu(acac)(acac)]^+ + Mg(eeac)(eeac) \rightarrow$$
$$[Cu(acac)(eeac\text{-}Et)]^+ + Mg(acac)(eeac) + Et \qquad \text{(Eqn 4.9)}$$

The mass-selected reaction of $[Cu(acac)_2]^+$ at *m/z* 261 with neutral $Mg(eeac)_2$ was also observed to participate in the formation of the single ligand exchange fragment $[Cu(eeac\text{-}Et)]^+$ at *m/z* 161, as depicted in Figure 4.11.

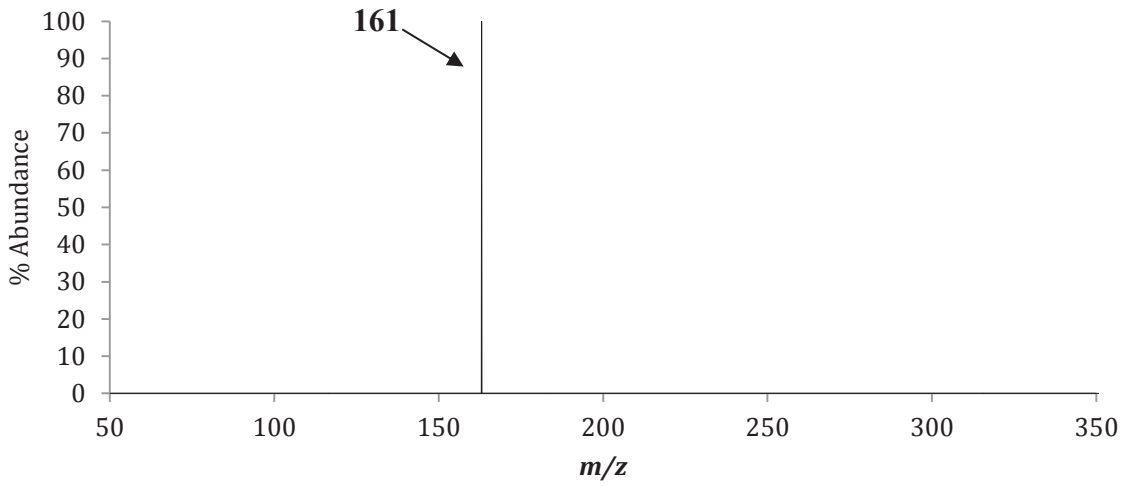

Figure 4.11: The positive mass spectrum obtained by scanning the third quadrupole following the selective reaction of m/z = 261 ($[Cu(acac)_2]^+$) with neutral $Mg(eeac)_2$ to produce the single ligand exchange fragment $[Cu(eeac\text{-}\mathit{Et})]^+$ at *m/z* 161.

The proposed mechanism for the gas-phase formation of copper single ligand exchange fragment $[Cu(eeac\text{-}\mathit{Et})]^+$ is presented in Equation 4.10.

$$[Cu(acac)(acac)]^+ + Mg(eeac)(eeac) \rightarrow$$
$$[Cu(eeac\text{-}\mathit{Et})]^+ + Mg(acac)(eeac) + (acac) + \mathit{Et} \qquad \text{(Eqn 4.10)}$$

Evidence for additional ligand exchange products is presented in Figure 4.12, where mass-selected $[Cu(acac\text{-}CH_3)(acac\text{-}CH_3)]^+$ at *m/z* 231 reacts with $Mg(eeac)_2$ to produce the complete ligand exchange product $[Cu(eeac)_2]^+$ at *m/z* 317.

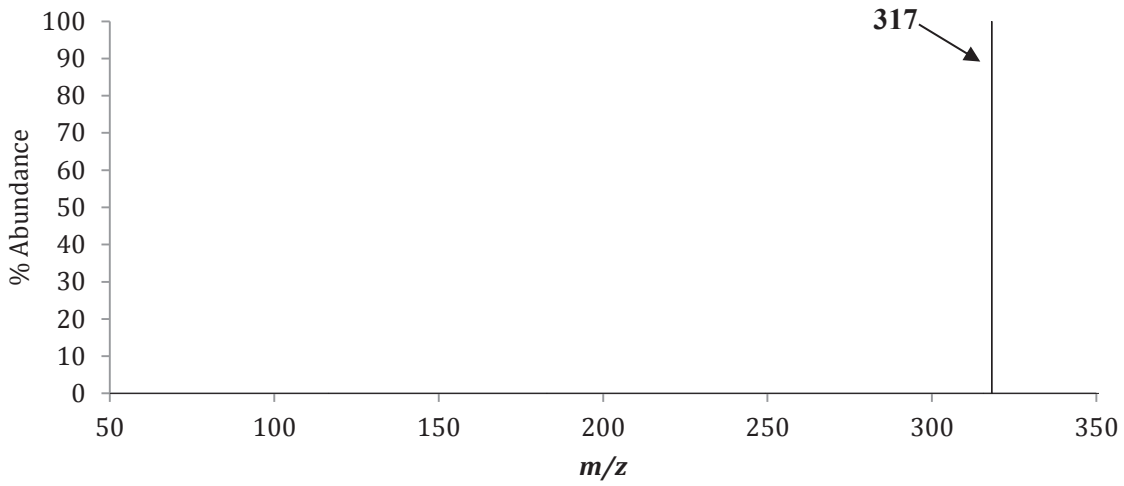

Figure 4.12: The positive mass spectrum obtained by scanning the third quadrupole following the selective reaction of *m/z* = 231 ($[Cu(acac\text{-}CH_3)(acac\text{-}CH_3)]^+$) with neutral $Mg(eeac)_2$ to produce the complete ligand exchange species $[Cu(eeac)_2]^+$ at *m/z* 317.

The proposed mechanism for the gas-phase formation of the copper complete ligand exchange product $[Cu(eeac)_2]^+$ is presented in Equation 4.11.

$$[Cu(acac\text{-}CH_3)(acac\text{-}CH_3)]^+ + Mg(eeac)(eeac) \rightarrow [Cu(eeac)(eeac)]^+ + Mg(acac\text{-}CH_3)(acac\text{-}CH_3) \qquad \text{(Eqn 4.11)}$$

Another product of interest generated by reacting mass-selected $[Cu(acac\text{-}CH_3)(acac\text{-}CH_3)]^+$ at *m/z* 231 with neutral $Mg(eeac)_2$ was $[Cu(eeac\text{-}Et)(eeac)]^+$ at *m/z* 288, and is displayed in Figure 4.13.

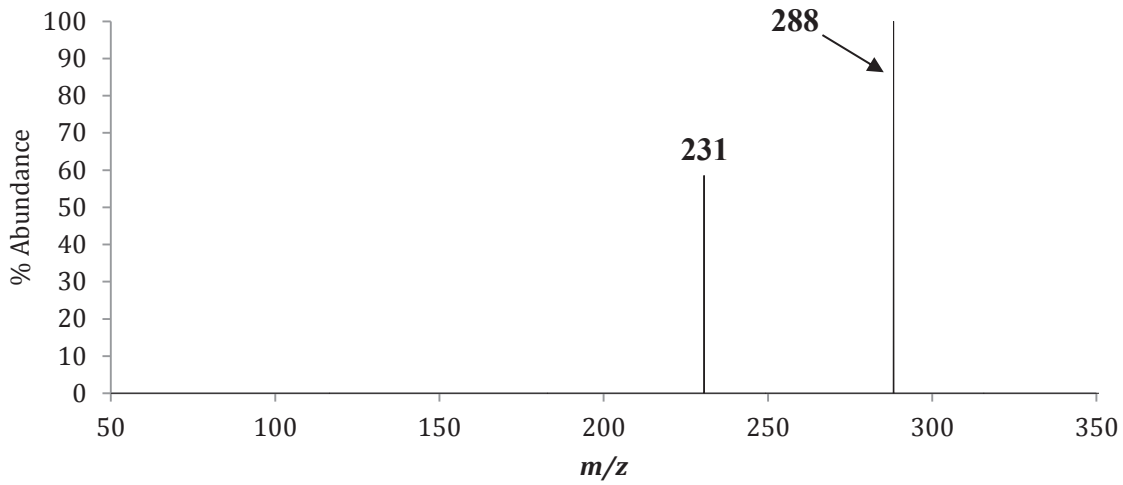

Figure 4.13: The positive mass spectrum obtained by scanning the third quadrupole following the selective reaction of *m/z* = 231 ($[Cu(acac\text{-}CH_3)(acac\text{-}CH_3)]^+$) with neutral $Mg(eeac)_2$ to produce the complete ligand exchange fragment $[Cu(eeac\text{-}Et)(eeac)]^+$ at *m/z* 288.

The proposed mechanism for the gas-phase formation of the copper complete ligand exchange fragment $[Cu(eeac\text{-}Et)(eeac)]^+$ is presented in Equation 4.12.

$$[Cu(acac\text{-}CH_3)(acac\text{-}CH_3)]^+ + Mg(eeac)(eeac) \rightarrow$$

$$[Cu(eeac\text{-}Et)(eeac)]^+ + Mg(acac\text{-}CH_3)(acac\text{-}CH_3) + Et \qquad \text{(Eqn 4.12)}$$

Mass-selected $[Cu(acac\text{-}CH_3)(acac\text{-}CH_3)]^+$ at *m/z* 231 was also observed to promote the formation of the mixed ligand exchange product fragment $[Cu(eeac\text{-}Et)(eeac\text{-}Et)]^+$ at *m/z* 259, which is displayed in Figure 4.14.

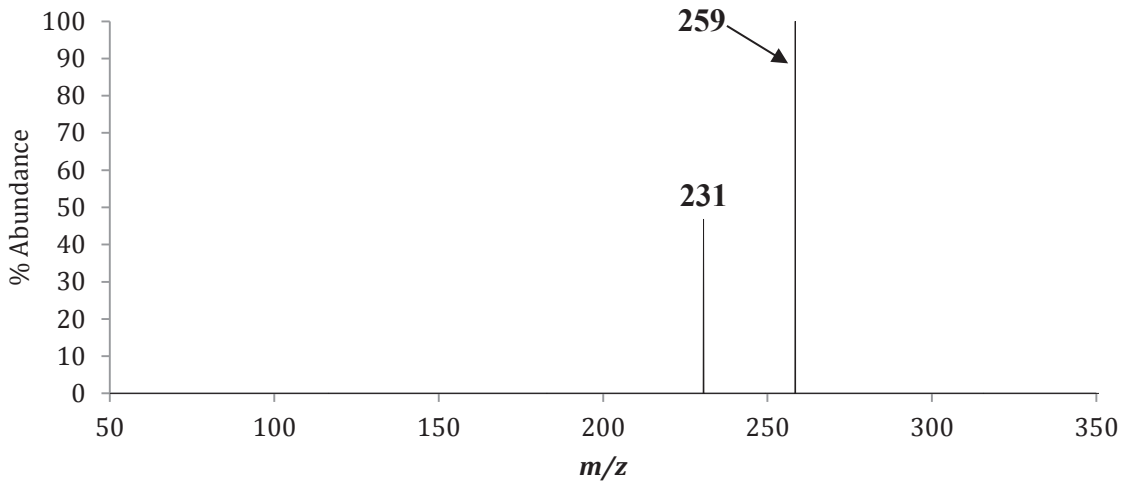

Figure 4.14: The positive mass spectrum obtained by scanning the third quadrupole following the selective reaction of *m/z* = 231 ($[Cu(acac\text{-}CH_3)(acac\text{-}CH_3)]^+$) with neutral $Mg(eeac)_2$ to produce the complete ligand exchange fragment $[Cu(eeac\text{-}Et)(eeac\text{-}Et)]^+$ at *m/z* 259.

The proposed mechanism for the gas-phase formation of the copper complete ligand exchange fragment $[Cu(eeac\text{-}Et)(eeac\text{-}Et)]^+$ is presented in Equation 4.13.

$$[Cu(acac\text{-}CH_3)(acac\text{-}CH_3)]^+ + Mg(eeac)(eeac) \rightarrow$$

$$[Cu(eeac\text{-}Et)(eeac\text{-}Et)]^+ + Mg(acac\text{-}CH_3)(acac\text{-}CH_3) + 2Et \qquad \text{(Eqn 4.13)}$$

Mass-selected $[Cu(eeac\text{-}Et)(eeac\text{-}Et)]^+$ at *m/z* 231 reacting with neutral $Mg(eeac)_2$ was observed to form the single ligand exchange product $[Cu(eeac)]^+$ at *m/z* 190, which is displayed in Figure 4.15.

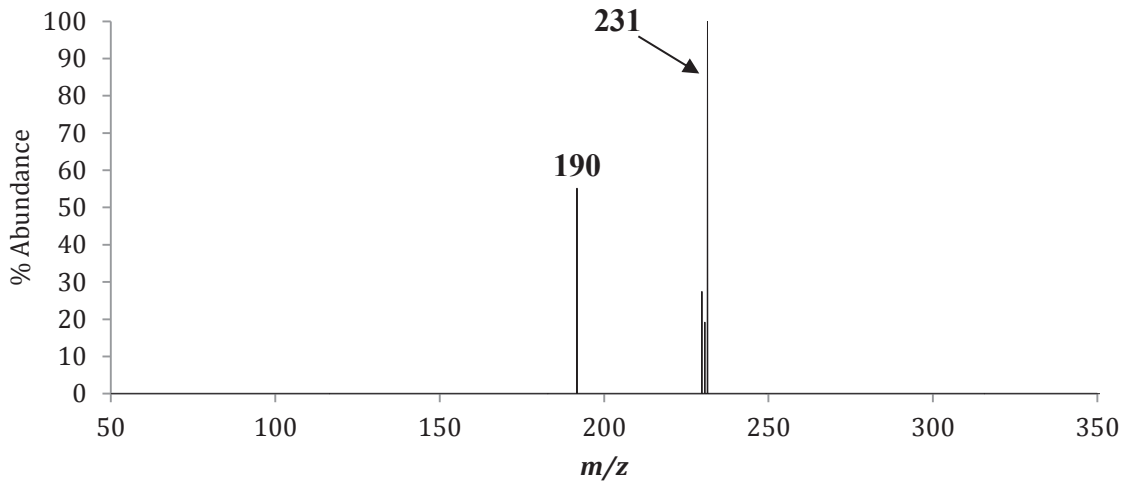

Figure 4.15: The positive mass spectrum obtained by scanning the third quadrupole following the selective reaction of *m/z* = 231 ($[Cu(acac\text{-}CH_3)(acac\text{-}CH_3)]^+$) with neutral $Mg(eeac)_2$ to produce the single ligand exchange product $[Cu(eeac)]^+$ at *m/z* 190.

The proposed mechanism for the gas-phase formation of the single ligand exchange product $[Cu(eeac)]^+$ is presented in Equation 4.14.

$$[Cu(acac\text{-}CH_3)(acac\text{-}CH_3)]^+ + Mg(eeac)(eeac) \rightarrow$$
$$[Cu(eeac)]^+ + Mg(acac\text{-}CH_3)(acac\text{-}CH_3) + (eeac) \qquad \text{(Eqn 4.14)}$$

Mass-selected $[Cu(eeac\text{-}Et)(eeac\text{-}Et)]^+$ at *m/z* 231 appears to be instrumental in the formation of the magnesium mixed ligand exchange product $[Mg(acac)(eeac)]^+$ at *m/z* 250, which is displayed in Figure 4.16, and must also incorporate ethyl groups to generate the intact species.

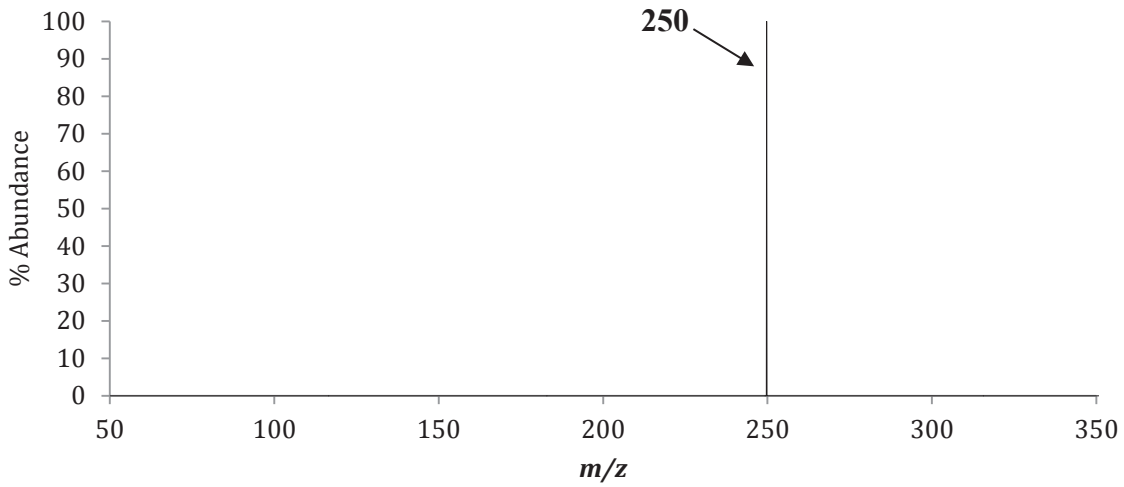

Figure 4.16: The positive mass spectrum obtained by scanning the third quadrupole following the selective reaction of m/z = 231 ($[Cu(acac\text{-}CH_3)(acac\text{-}CH_3)]^+$) with neutral $Mg(eeac)_2$ to produce the mixed ligand exchange product $[Mg(acac)(eeac)]^+$ at *m/z* 250.

The proposed mechanism for the gas-phase formation of the magnesium mixed ligand exchange product $[Mg(acac)(eeac)]^+$ is presented in Equation 4.15.

$$[Cu(acac\text{-}CH_3)(acac\text{-}CH_3)]^+ + Mg(eeac)(eeac) + CH_3 \rightarrow$$
$$[Mg(acac)(eeac)]^+ + Cu(acac\text{-}CH_3)(eeac) \qquad \text{(Eqn 4.15)}$$

A second magnesium ligand exchange product, $[Mg(acac\text{-}CH_3)(acac)]^+$ at *m/z* 207, was also generated from mass-selected $[Cu(acac\text{-}CH_3)(acac\text{-}CH_3)]^+$ at *m/z* 231, and is displayed in Figure 4.17.

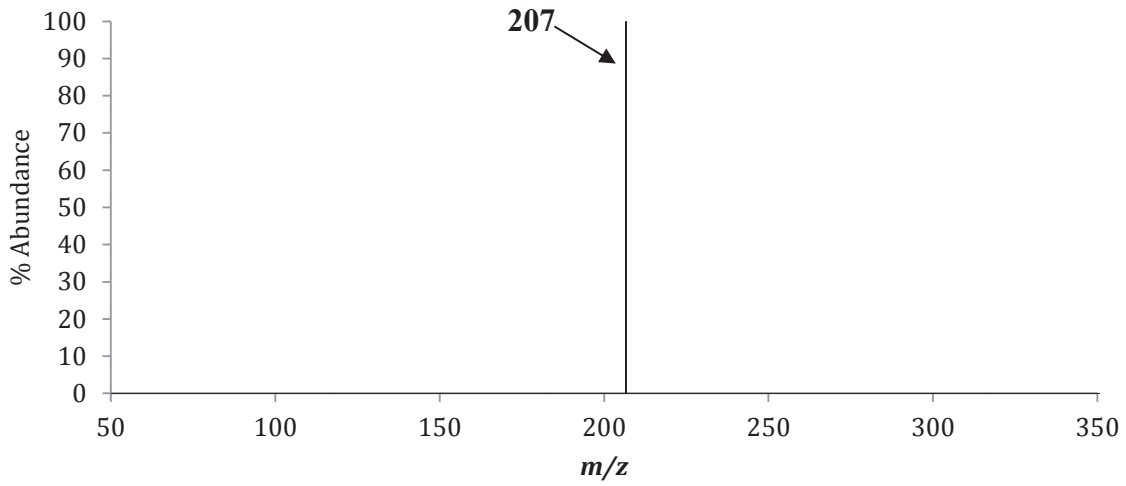

Figure 4.17: The positive mass spectrum obtained by scanning the third quadrupole following the selective reaction of *m/z* = 231 ($[Cu(acac\text{-}CH_3)(acac\text{-}CH_3)]^+$) with neutral $Mg(eeac)_2$ to produce the single ligand exchange fragment $[Mg(acac\text{-}CH_3)(acac)]^+$ at *m/z* 207.

The proposed mechanism for the gas-phase formation of the magnesium complete ligand exchange fragment $[Mg(acac\text{-}CH_3)(acac)]^+$ is displayed in Equation 4.16.

$$[Cu(acac\text{-}CH_3)(acac\text{-}CH_3)]^+ + Mg(eeac)(eeac) + CH_3 \rightarrow$$

$$[Mg(acac\text{-}CH_3)(acac)]^+ + Cu(eeac)(eeac) \qquad \text{(Eqn 4.16)}$$

Mass-selected $[Cu(acac\text{-}CH_3)]^+$ at *m/z* 147 reacting with neutral $Mg(eeac)_2$ appears instrumental in the formation of the complete magnesium ligand exchange product $[Mg(acac)_2]^+$ at *m/z* 222, which is displayed in Figure 4.18.

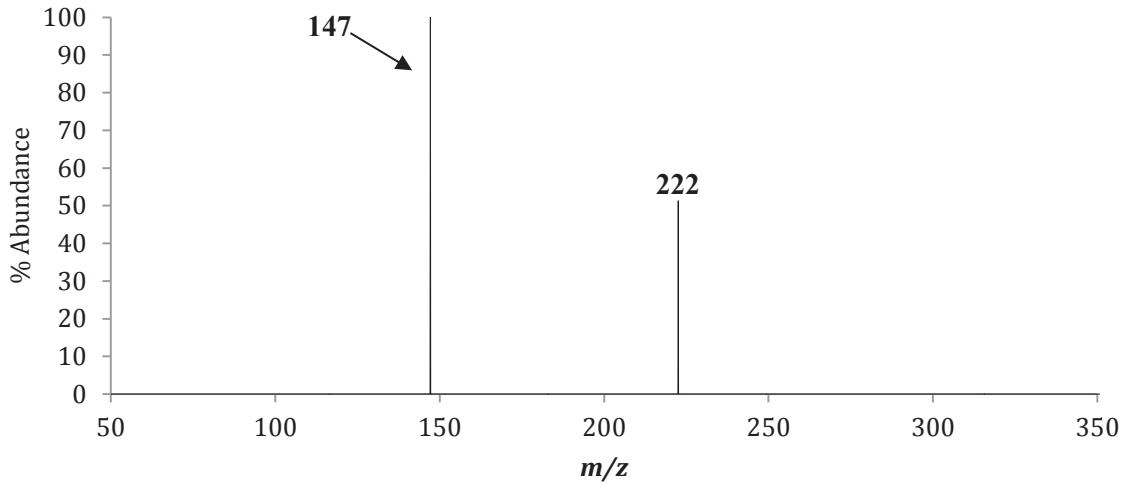

Figure 4.18: The positive mass spectrum obtained by scanning the third quadrupole following the selective reaction of *m/z* = 147 ($[Cu(acac\text{-}CH_3)]^+$) with neutral $Mg(eeac)_2$ to produce the complete ligand exchange product $[Mg(acac)_2]^+$ at *m/z* 222.

The proposed mechanism for the gas-phase formation of the magnesium complete ligand exchange product $[Mg(acac)_2]^+$ is displayed in Equation 4.17.

$$[Cu(acac\text{-}CH_3)]^+ + Mg(eeac)(eeac) + (acac) + CH_3 \rightarrow [Mg(acac)(acac)]^+ + Cu(eeac)(eeac) \qquad \text{(Eqn 4.17)}$$

The final product generated from collision-induced reaction of $[Cu(acac\text{-}CH_3)]^+$ at *m/z* 147 with neutral $Mg(eeac)_2$ was $[Mg(acac\text{-}CH_3)(acac)]^+$ at *m/z* 207, and is displayed in Figure 4.19.

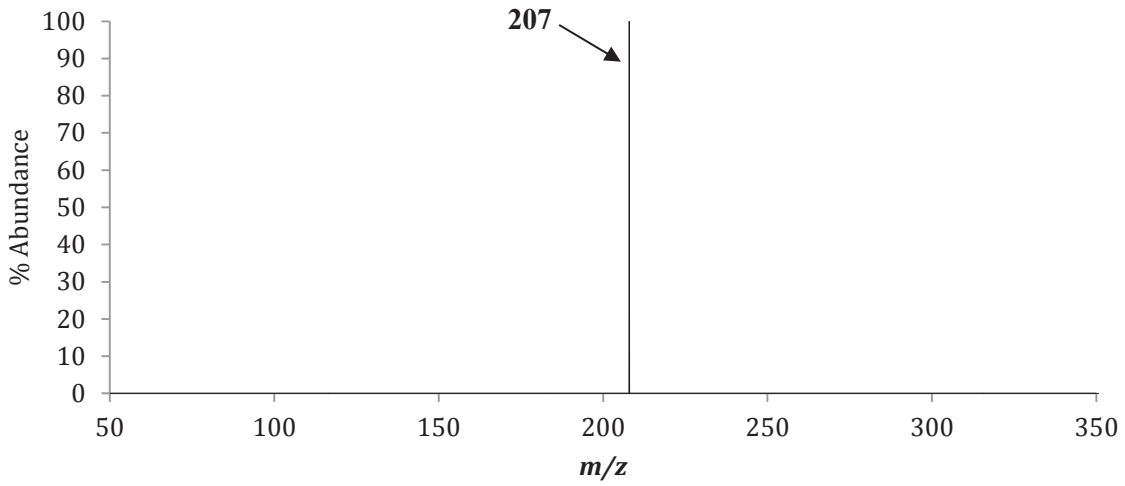

Figure 4.19: The positive mass spectrum obtained by scanning the third quadrupole following the selective reaction of *m/z* = 147 ($[Cu(acac\text{-}CH_3)]^+$) with neutral $Mg(eeac)_2$ to produce the complete ligand exchange fragment $[Mg(acac\text{-}CH_3)(acac)]^+$ at *m/z* 207.

The proposed mechanism for the gas-phase formation of the magnesium complete ligand exchange fragment $[Mg(acac\text{-}CH_3)(acac)]^+$ is presented in Figure 4.18.

$$[Cu(acac\text{-}CH_3)]^+ + Mg(eeac)(eeac) + (acac) \rightarrow$$
$$[Mg(acac\text{-}CH_3)(acac)]^+ + Cu(eeac)_2 \qquad \text{(Eqn 4.18)}$$

In conclusion, mass-selected $[Mg(eeac)_2]^+$ at *m/z* 278 generated several ligand exchange species when reacted with neutral $Cu(acac)_2$. The mixed ligand exchange product $[Cu(acac)(eeac)]^+$ was found at *m/z* 289, as was the mixed ligand exchange fragment $[Cu(acac)(eeac\text{-}Et)]^+$ at *m/z* 260. The single ligand exchange species $[Cu(eeac)]^+$ was also observed to form at *m/z* 190, as was its fragment $[Cu(eeac\text{-}Et)]^+$ at *m/z* 161.

Mass selected $[Mg(eeac\text{-}Et)(eeac)]^+$ at *m/z* 249 reacting with $Cu(acac)_2$ also yielded one ligand exchange product, namely $[Mg(acac\text{-}CH_3]^+$ at *m/z* 207. Mass-selected $[Mg(eeac\text{-}Et)(eeac\text{-}Et)+2H]^+$ also generated the same ligand exchange product, [Mg(acac-

$CH_3]^+$ at *m/z* 207. No ligand exchange products were generated from mass-selected $[Mg(eeac)]^+$ at *m/z* 151.

However, mass-selected copper ions provided many more ligand exchange products when reacting with neutral $Mg(eeac)_2$. Mass-selected $[Cu(acac)_2]^+$ at *m/z* 261 generated $[Cu(eeac)_2]^+$ at *m/z* 317, $[Cu(acac)(eeac)]^+$ at *m/z* 289, $[Cu(acac)(eeac\text{-}Et)]^+$ at *m/z* 260, and $[Cu(eeac\text{-}Et)]^+$ at *m/z* 161. Several ligand exchange products were also generated from mass-selected $[Cu(acac\text{-}CH_3)(acac\text{-}CH_3)]^+$ at *m/z* 231, including $[Cu(eeac)_2]^+$ at *m/z* 317, $[Cu(eeac\text{-}Et)(eeac)]^+$ at *m/z* 288, $[Cu(eeac\text{-}Et)(eeac\text{-}Et)]^+$ at *m/z* 259, and $[Cu(eeac)]^+$ at *m/z* 190. Magnesium ligand exchange products were also generated from $[Cu(acac\text{-}CH_3)(acac\text{-}CH_3)]^+$ at *m/z* 231, $[Mg(acac)(eeac)]^+$ at *m/z* 250 and $[Mg(acac\text{-}CH_3)(acac)]^+$ at *m/z* 207.

Finally, when conducting experiments with mass-selected $[Cu(acac\text{-}CH_3)]^+$ at *m/z* 147 reacting with neutral $Mg(eeac)_2$, two magnesium ligand exchange products, $[Mg(acac)_2]^+$ at *m/z* 222 and $[Mg(acac\text{-}CH_3)(acac)]^+$ at *m/z* 207, were found. Interestingly, no ligand exchange products were generated from mass-selected $[Cu(acac\text{-}CH_3)(acac)]^+$ at *m/z* 246 or $[Cu(acac)]^+$ at *m/z* 162. Although more work is necessary, the collision-induced reactions reported herein have elicited much novel information about the mechanism of gas-phase ligand exchange between $Mg(eeac)_2$ and $Cu(acac)_2$.

4.5 The Co-Sublimation of $Mg(eeac)_2$ and Copper Bis-Trifluorotrimethylacetylacetonate ($Cu(tftm)_2$)

Presented in Figure 4.20(a) and (b) are the positive EI mass spectra of $Mg(eeac)_2$ and copper bis-trifluorotrimethylacetylacetonate ($Cu(tftm)_2$). The co-sublimation

spectrum of $Mg(eeac)_2$ and $Cu(tftm)_2$ is presented in Figure 4.20(c). The spectra are stacked vertically for clarity and ease of comparison, as well as to highlight the formation of novel peaks, a strong indicator of gas-phase ligand exchange. Although scans were completed from *m/z* 50 to 650, the spectra presented are displayed from *m/z* 50 to 450 to highlight the distinct isotopic distributions of the products. The baseline mass spectrum of $Mg(eeac)_2$ is reproduced from Figure 3.1 and will not be discussed further. The baseline spectrum of $[Cu(tftm)_2]^+$ in Figure 4.20(b) displays several stable species, including intact $[Cu(tftm)_2]^+$ at *m/z* 453, $[Cu(tftm\text{-}tBu)(tftm)]^+$ *m/z* 396, as well as $[Cu(tftm\text{-}tBu)(tftm\text{-}tBu)]^+$ at *m/z* 339. The single ligand species $[Cu(tftm)]^+$ is also present at *m/z* 259, while the subsequent loss of one *tBu* to form $[Cu(tftm\text{-}tBu)]^+$ occurs at *m/z* 201.

The co-sublimation spectrum displayed in Figure 4.20(c) displays many novel peaks, including the peak at *m/z* 414 which corresponds to the mass of the complete ligand exchange product $[Mg(tftm)_2]^+$ and what appears to be loss of a *tBu* group to form $[Mg(tftm\text{-}tBu)(tftm)]^+$ at *m/z* 357. The mixed ligand exchange product $[Mg(eeac)(tftm)]^+$ is also present at *m/z* 346, as are several copper ligand exchange products including intact $[Cu(eeac)_2]^+$ at *m/z* 317, $[Cu(eeac\text{-}Et)(eeac)]^+$ at *m/z* 288, $[Cu(eeac\text{-}Et)(eeac\text{-}Et)]^+$ at *m/z* 259, $[Cu(eeac)]^+$ at *m/z* 190, and $[Cu(eeac\text{-}Et)]^+$ at *m/z* 161. The mixed ligand exchange product $[Cu(eeac)(tftm)]^+$ is also present at *m/z* 385, as is loss of one *tBu* group to form $[Cu(eeac)(tftm\text{-}tBu)]^+$ at *m/z* 328. The relative abundances of all observed species are displayed in Table 4.2

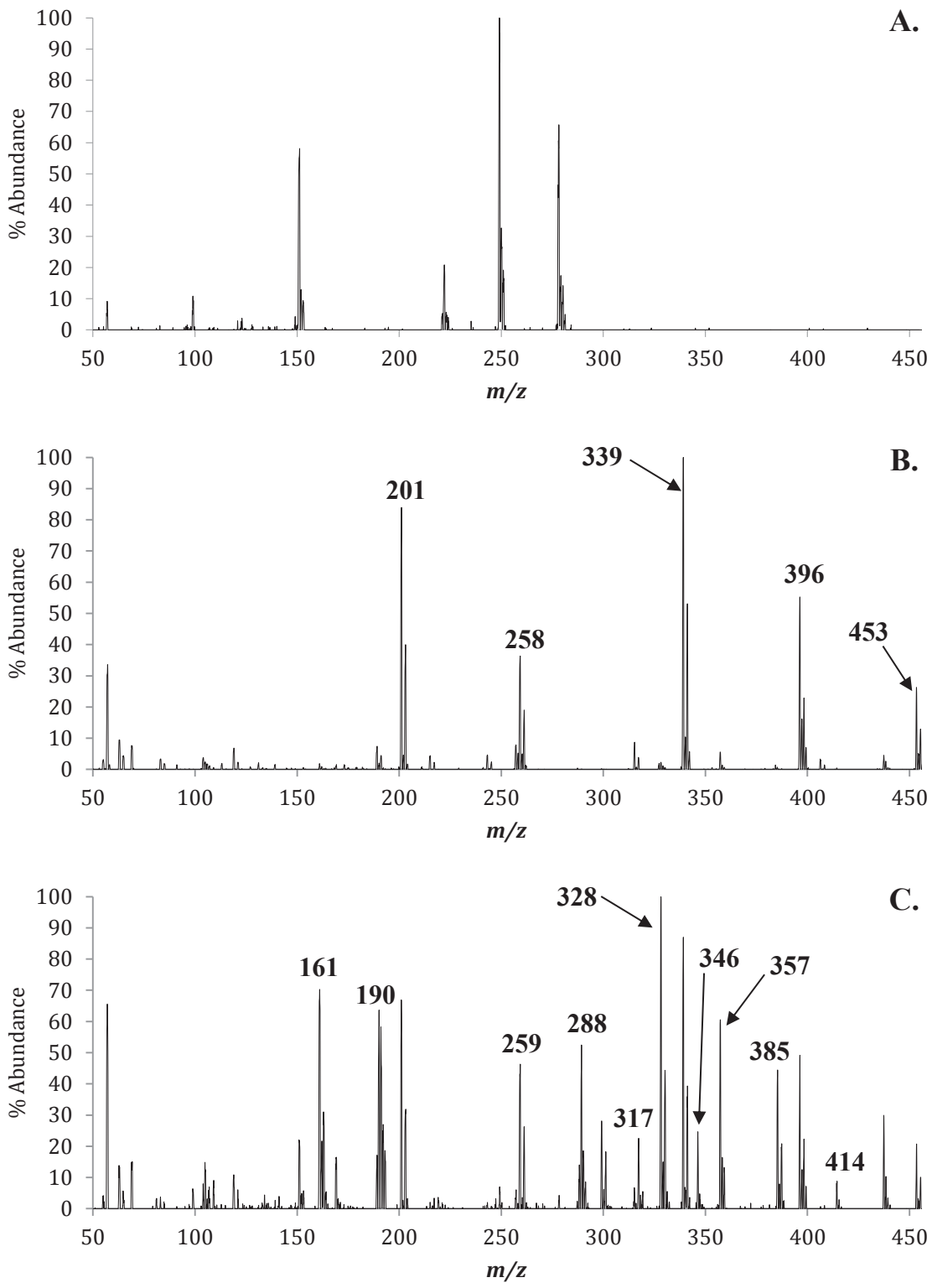

Figure 4.20: The positive EI mass spectra of (a) $Mg(eeac)_2$, (b) $Cu(tftm)_2$, and (c) the gas-phase co-sublimation of $Mg(eeac)_2$ and $Cu(tftm)_2$. The masses of parent compounds and fragments are labeled in (a) and (b). Masses of ligand exchange products and pertinent fragments are labeled in (c).

	Mass	Mass	MgL	CuL''	MgL & CuL''	MgL & CuL''
	Mg	Cu	Mg	Cu	Mg	Cu
$[ML_2]^+$	278	317	65		4	22
$[ML_2\text{-}C_2H_5]^+$	249	288	100		7	9
$[ML_2\text{-}2C_2H_5\text{+}2H]^+$	222	-	20		1	-
$[ML_2\text{-}2C_2H_5]^+$	-	259	0		-	43
$[ML]^+$	151	190	10		22	63
$[ML\text{-}C_2H_5]^+$	136	161	<1		<1	70
$[ML''_2]^+$	414	453		26	9	20
$[ML''_2\text{-}tBu]^+$	357	396		55	60	49
$[ML''_2\text{-}2tBu]^+$	300	339		100	6	86
$[ML'']^+$	219	258		36	2	1
$[ML''\text{-}tBu]^+$	162	201		83	21	66
$[ML''\text{-}CF_2]^+$	169	208		0	16	0
$[MLL'']^+$	346	385			24	44
$[M(L\text{-}C_2H_5)L'']^+$	317	356			22	<1
$[ML(L''\text{-}tBu)]^+$	289	328			52	100

Table 4.2: The relative mass spectrometric abundances of the $Mg(eeac)_2$ and $Cu(tftm)_2$ β-diketonate complexes as well as the co-sublimation experiment, as presented in Figure 4.20. L = (eeac) L'' = (tftm).

4.6 The Selective Reactions of $Mg(eeac)_2$ + $Cu(tftm)_2$

The most abundant species from the baseline mass spectra of $Mg(eeac)_2$ and $Cu(tftm)_2$ were subjected to collision-induced reaction analysis using tandem mass spectrometry within a triple quadrupole mass spectrometer. As discussed previously, a particular ion is mass-selected using the first quadrupole and permitted to continue to the second quadrupole containing a neutral β-diketonate; in this section $Cu(tftm)_2$ is the neutral species. The second quadrupole serves as a collision cell, where all resultant products are detected with the third quadrupole, following a scan from *m/z* 50 to 650.

Specific collision-induced reactions investigating the role of the most abundant species presented in Table 3.1 are described throughout this section.

The first ligand exchange product of interest generated from the collision-induced reaction of mass-selected $[Mg(eeac)_2]^+$ at *m/z* 278 reacting with $Cu(tftm)_2$ was the complete ligand exchange product $[Mg(tftm)_2]^+$ at *m/z* 414, and is depicted in Figure 4.21.

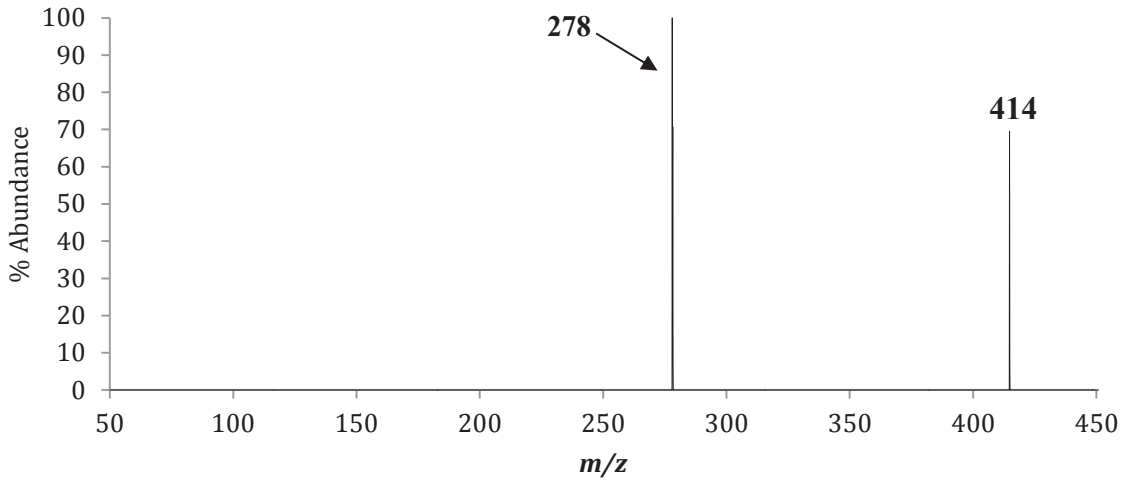

Figure 4.21: The positive mass spectrum obtained by scanning the third quadrupole following the selective reaction of *m/z* = 278 ($[Mg(eeac)_2]^+$) with neutral $Cu(tftm)_2$ to produce the complete ligand exchange product $[Mg(tftm)_2]^+$ at *m/z* 414.

The proposed mechanism for the gas-phase formation of the magnesium complete ligand exchange product $[Mg(tftm)_2]^+$ is presented in Equation 4.19.

$$[Mg(eeac)(eeac)]^+ + Cu(tftm)(tftm) \rightarrow [Mg(tftm)(tftm)]^+ + Cu(eeac)(eeac) \qquad \text{(Eqn 4.19)}$$

The complete ligand exchange fragment $[Mg(tftm\text{-}tBu)(tftm)]^+$ at *m/*z 357 was also observed to form from mass-selected $[Mg(eeac)_2]^+$ at *m/z* 278 reacting with neutral $Cu(tftm)_2$, and is presented in Figure 4.22.

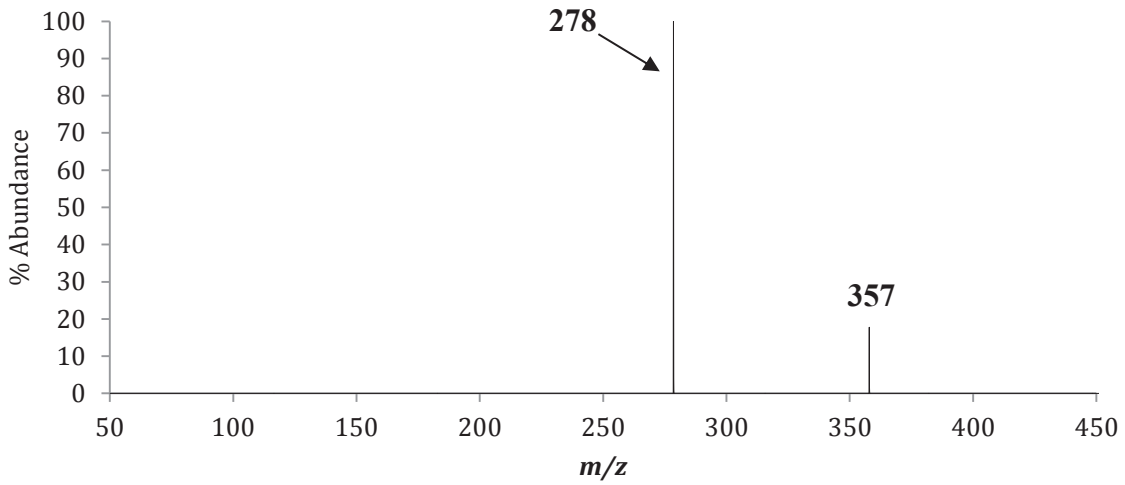

Figure 4.22: The positive mass spectrum obtained by scanning the third quadrupole following the selective reaction of *m/z* = 278 ($[Mg(eeac)_2]^+$) with neutral $Cu(tftm)_2$ to produce the complete ligand exchange fragment $[Mg(tftm\text{-}tBu)(tftm)]^+$ at *m/z* 357.

The proposed mechanism for the gas-phase formation of the magnesium complete ligand exchange fragment $[Mg(tftm\text{-}tBu)(tftm)]^+$ is presented in Equation 4.20.

$$[Mg(eeac)(eeac)]^+ + Cu(tftm)(tftm) \rightarrow [Mg(tftm\text{-}tBu)(tftm)]^+ + Cu(eeac)(eeac) + tBu \qquad \text{(Eqn 4.20)}$$

One final product of interest forming from the collision-induced reaction of mass-selected $[Mg(eeac)_2]^+$ at *m/z* 278 and neutral $Cu(tftm)_2$ corresponded to the formation of $[Mg(eeac)(tftm)]^+$ at *m/z* 346, and is displayed in Figure 4.23.

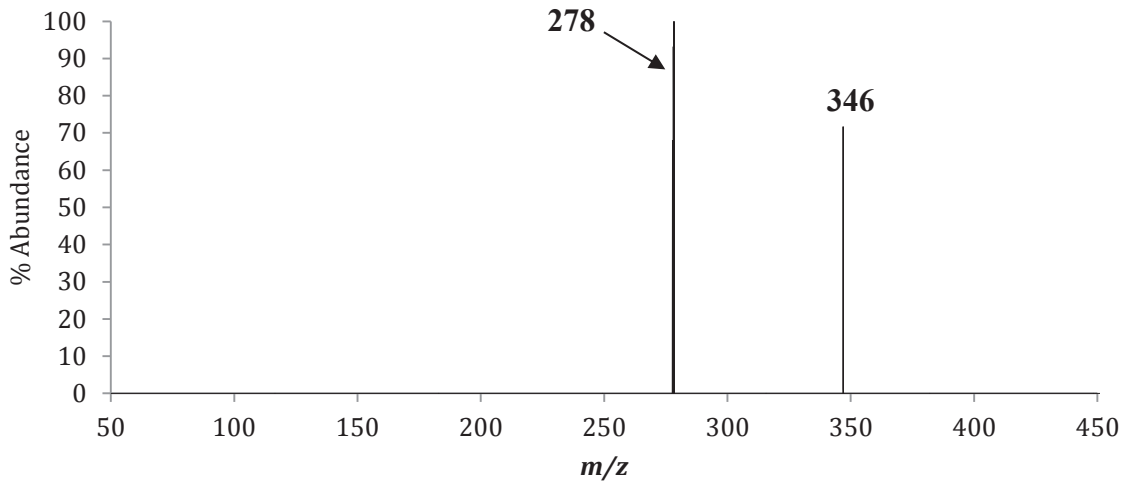

Figure 4.23: The positive mass spectrum obtained by scanning the third quadrupole following the selective reaction of *m/z* = 278 ($[Mg(eeac)_2]^+$) with neutral $Cu(tftm)_2$ to produce the mixed ligand exchange product $[Mg(eeac)(tftm)]^+$ at *m/z* 346.

The proposed mechanism for the gas-phase formation of the magnesium mixed ligand exchange product $[Mg(eeac)(tftm)]^+$ is displayed in Equation 4.21.

$$[Mg(eeac)(eeac)]^+ + Cu(tftm)(tftm) \rightarrow [Mg(eeac)(tftm)]^+ + Cu(eeac)(tftm) \qquad \text{(Eqn 4.21)}$$

The spectrum displayed in Figure 4.24 shows the results from mass-selected $[Mg(eeac\text{-}Et)(eeac)]^+$ at *m/z* 249 reacting with neutral $Cu(tftm)_2$ to yield the complete ligand exchange product $[Mg(tftm)_2]^+$ at *m/z* 414. The small peak at *m/z* 151 corresponds with $[Mg(eeac)]^+$, and is commonly observed in the spectra of several mass-selected $Mg(eeac)_2$ species.

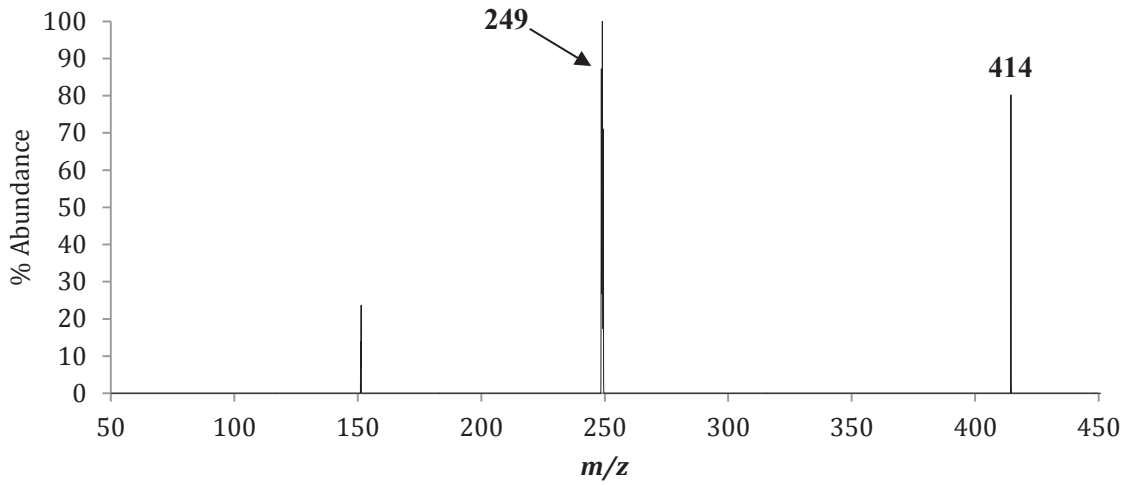

Figure 4.24: The positive mass spectrum obtained by scanning the third quadrupole following the selective reaction of *m/z* = 249 ($[Mg(eeac\text{-}Et)(eeac)]^+$) with neutral $Cu(tftm)_2$ to produce the complete ligand exchange product $[Mg(tftm)_2]^+$ at *m/z* 414.

The proposed mechanism for the gas-phase formation of the magnesium complete ligand exchange product $[Mg(tftm)_2]^+$ is presented in Equation 4.22.

$$[Mg(eeac\text{-}Et)(eeac)]^+ + Cu(tftm)(tftm) \rightarrow$$
$$[Mg(tftm)(tftm)]^+ + Cu(eeac\text{-}Et)(eeac) \qquad \text{(Eqn 4.22)}$$

The complete ligand exchange fragment $[Mg(tftm\text{-}tBu)(tftm)]^+$ at *m/z* 357 was also generated from reactions of mass-selected $[Mg(eeac\text{-}Et)(eeac)]^+$ at *m/z* 249 with $Cu(tftm)_2$, as depicted in Figure 4.25.

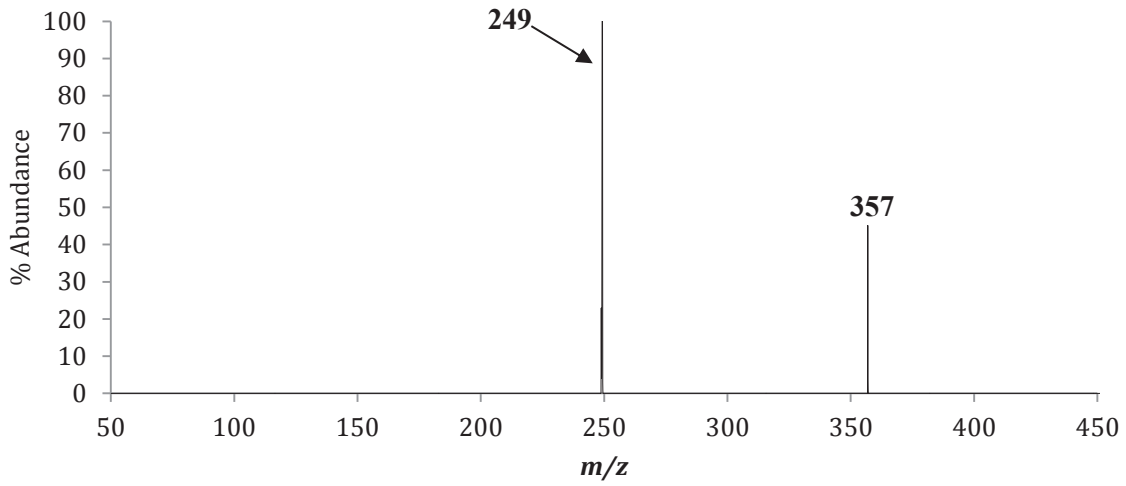

Figure 4.25: The positive mass spectrum obtained by scanning the third quadrupole following the selective reaction of *m/z* = 249 ($[Mg(eeac\text{-}Et)(eeac)]^+$) with neutral $Cu(tftm)_2$ to produce the complete ligand exchange fragment $[Mg(tftm\text{-}tBu)(tftm)]^+$ at *m/z* 357.

The proposed mechanism for the gas-phase formation of the magnesium complete ligand exchange fragment $[Mg(tftm\text{-}tBu)(tftm)]^+$ is presented in Equation 4.23.

$$[Mg(eeac\text{-}Et)(eeac)]^+ + Cu(tftm)(tftm) \rightarrow$$
$$[Mg(tftm\text{-}tBu)(tftm)]^+ + Cu(eeac\text{-}Et)(eeac) + tBu \qquad \text{(Eqn 4.23)}$$

A plethora of ligand exchange products of interest were generated from mass-selected $[Mg(eeac\text{-}Et)(eeac\text{-}Et)+2H]^+$ at *m/z* 222, the first of which was the magnesium complete ligand exchange product $[Mg(tftm)_2]^+$ at *m/z* 414, which is depicted in Figure 4.26. The peak at *m/z* 270 does not correspond to the mass of any ligand exchange products of interest and was not investigated further.

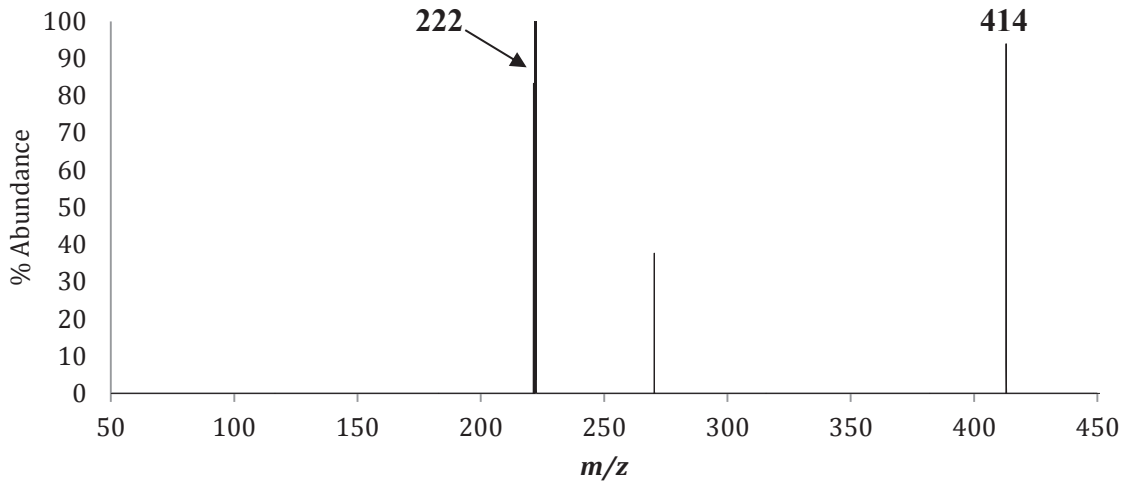

Figure 4.26: The positive mass spectrum obtained by scanning the third quadrupole following the selective reaction of *m/z* = 222 ([Mg(eeac-*Et*)(eeac-*Et*)+2H]$^+$) with neutral Cu(tftm)$_2$ to produce the complete ligand exchange product [Mg(tftm)$_2$]$^+$ at *m/z* 414.

The proposed mechanism for the gas-phase formation of the magnesium complete ligand exchange product [Mg(tftm)$_2$]$^+$ is presented in Equation 4.24.

$$[\text{Mg(eeac-}Et\text{)(eeac-}Et\text{)+2H}]^+ + \text{Cu(tftm)(tftm)} \rightarrow [\text{Mg(tftm)(tftm)}]^+ + \text{Cu(eeac-}Et\text{)(eeac-}Et\text{)} + 2\text{H} \qquad \text{(Eqn 4.24)}$$

The complete ligand exchange fragment [Mg(tftm-*tBu*)(tftm)]$^+$ at *m/*z 357 was also generated, as depicted in Figure 4.27, from the reaction between mass-selected [Mg(eeac-*Et*)(eeac-*Et*)+2H]$^+$ at *m/z* 222 and neutral Cu(tftm)$_2$.

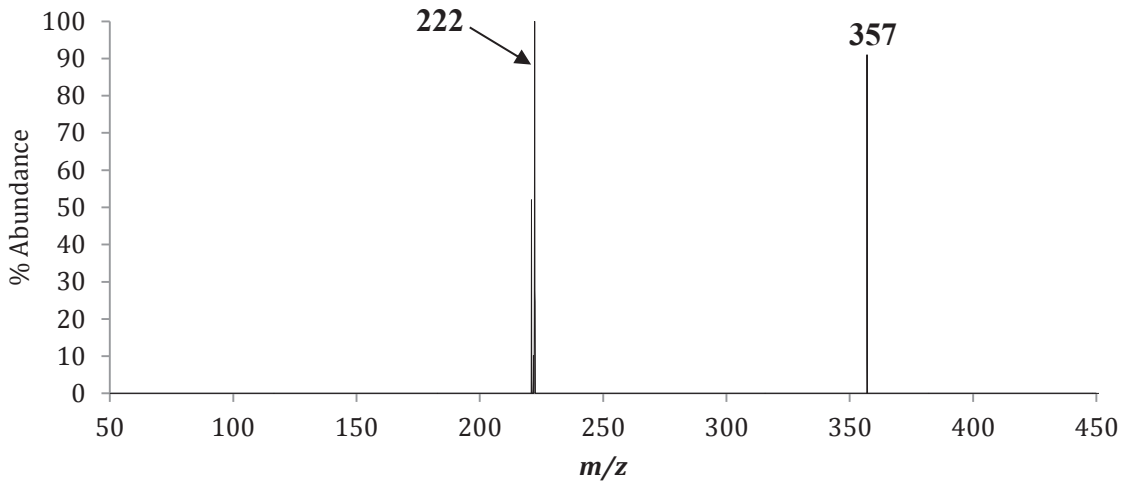

Figure 4.27: The positive mass spectrum obtained by scanning the third quadrupole following the selective reaction of *m/z* = 222 ([Mg(eeac-*Et*)(eeac-*Et*)+2H]$^+$) with neutral Cu(tftm)$_2$ to produce the complete ligand exchange fragment [Mg(tftm-*tBu*)(tftm)]$^+$ at *m/z* 357.

The proposed mechanism for the gas-phase formation of the magnesium complete ligand exchange fragment [Mg(tftm-*tBu*)(tftm)]$^+$ is presented in Equation 4.25.

$$[\text{Mg(eeac-}Et\text{)(eeac-}Et\text{)+2H}]^+ + \text{Cu(tftm)(tftm)} \rightarrow$$
$$[\text{Mg(tftm-}tBu\text{)(tftm)}]^+ + \text{Cu(eeac-}Et\text{)(eeac-}Et\text{)} + tBu + 2\text{H} \qquad \text{(Eqn 4.25)}$$

Mass-selected [Mg(eeac-*Et*)(eeac-*Et*)+2H]$^+$ at *m/z* 222 was also observed to form two additional products, which were coincidentally captured on the same mass spectrum; [Mg(eeac)(tftm-*tBu*)]$^+$ was detected at *m/*z 289 and [Mg(tftm-CF_2)]$^+$ was detected at *m/z* 169. Each of these ions is clearly displayed in Figure 4.28. The peak at *m/z* 151 is the single ligand species [Mg(eeac)]$^+$ and is a commonly observed fragment in other mass-selected magnesium species collision-induced reaction spectra.

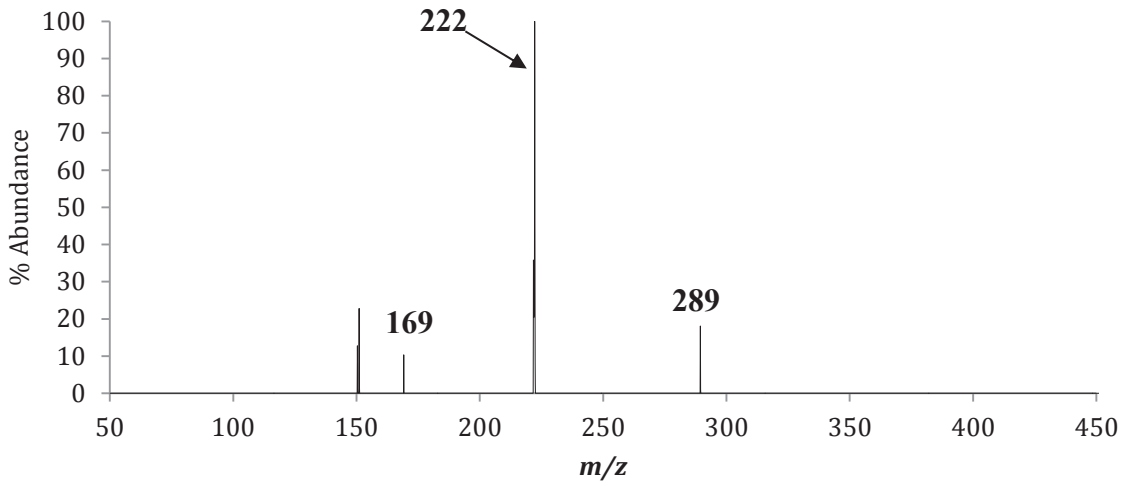

Figure 4.28: The positive mass spectrum obtained by scanning the third quadrupole following the selective reaction of *m/z* = 222 ([Mg(eeac-*Et*)(eeac-*Et*)+2H]$^+$) with neutral Cu(tftm)$_2$ to produce the mixed ligand exchange fragment [Mg(eeac)(tftm-*tBu*)]$^+$ at *m/z* 357 and the single ligand exchange fragment [Mg(tftm-CF_2)]$^+$ at *m/z* 169.

The proposed mechanisms for the gas-phase formation of the magnesium mixed ligand exchange fragment [Mg(eeac)(tftm-*tBu*)]$^+$ and the magnesium single ligand exchange fragment [Mg(tftm-CF_2)]$^+$ are presented in Equations 4.26 and 4.27, respectively.

$$[\text{Mg(eeac-}Et\text{)(eeac-}Et\text{)+2H}]^+ + \text{Cu(tftm)(tftm)} + Et \rightarrow$$
$$[\text{Mg(eeac)(tftm-}tBu\text{)}]^+ + \text{Cu(eeac-}Et\text{)(tftm)} + 2\text{H} \qquad \text{(Eqn 4.26)}$$

$$[\text{Mg(eeac-}Et\text{)(eeac-}Et\text{)+2H}]^+ + \text{Cu(tftm)(tftm)} \rightarrow$$
$$[\text{Mg(tftm-}CF_2\text{)}]^+ + \text{Cu(eeac-}Et\text{)(eeac-}Et\text{)} + \text{(tftm)} + CF_2 + 2\text{H} \qquad \text{(Eqn 4.27)}$$

Mass-selected [Mg(eeac-*Et*)(eeac-*Et*)+2H]$^+$ at *m/z* 222 also contributed to the formation of copper ligand exchange products, including [Cu(eeac)(tftm)]$^+$ at *m/z* 385 which is depicted in Figure 4.29. The peak at *m/z* 105 does not correspond with any particular ligand exchange product and is not considered further.

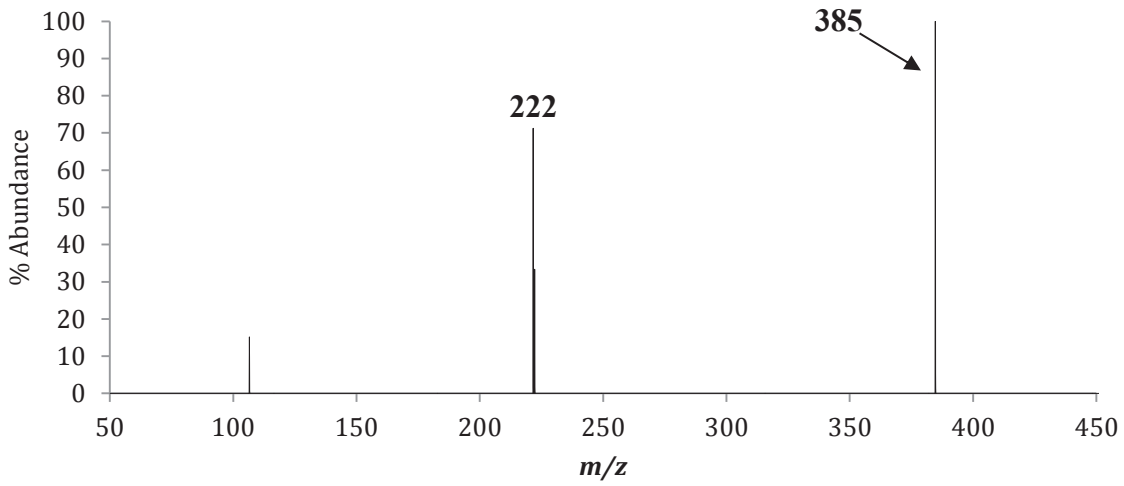

Figure 4.29: The positive mass spectrum obtained by scanning the third quadrupole following the selective reaction of *m/z* = 222 ([Mg(eeac-*Et*)(eeac-*Et*)+2H]$^+$) with neutral Cu(tftm)$_2$ to produce the mixed ligand exchange product [Cu(eeac)(tftm)]$^+$ at *m/z* 385.

The proposed mechanism for the gas-phase formation of the copper mixed ligand exchange product [Cu(eeac)(tftm)]$^+$ is presented in Equation 4.28.

$$[\text{Mg(eeac-}Et\text{)(eeac-}Et\text{)+2H}]^+ + \text{Cu(tftm)(tftm)} + Et \rightarrow$$
$$[\text{Cu(eeac)(tftm)}]^+ + \text{Mg(eeac-}Et\text{)(tftm)} + 2\text{H} \qquad \text{(Eqn 4.28)}$$

An additional copper ligand exchange product formed from the reaction of mass-selected [Mg(eeac-*Et*)(eeac-*Et*)+2H]$^+$ at *m/z* 222 and neutral Cu(tftm)$_2$ corresponds to the complete copper ligand exchange fragment [Cu(eeac-*Et*)(eeac)]$^+$ at *m/z* 288, and is presented in Figure 4.30.

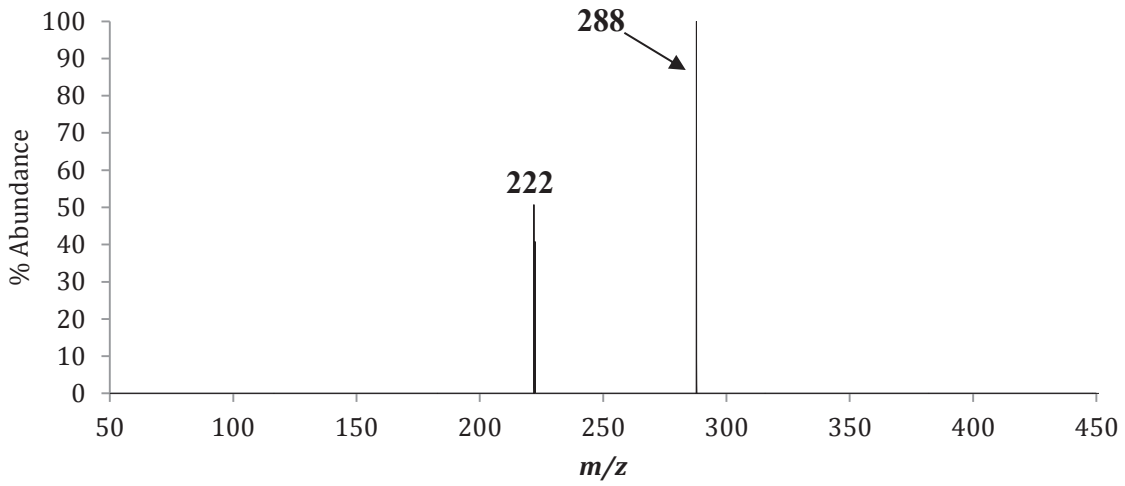

Figure 4.30: The positive mass spectrum obtained by scanning the third quadrupole following the selective reaction of *m/z* = 222 ([Mg(eeac-*Et*)(eeac-*Et*)+2H]$^+$) with neutral Cu(tftm)$_2$ to produce the complete ligand exchange fragment [Cu(eeac-*Et*)(eeac)]$^+$ at *m/z* 288.

The proposed mechanism for the gas-phase formation of the copper complete ligand exchange fragment [Cu(eeac-*Et*)(eeac)]$^+$ is displayed in Equation 4.29.

$$[\text{Mg(eeac-}Et\text{)(eeac-}Et\text{)+2H}]^+ + \text{Cu(tftm)(tftm)} + Et \rightarrow$$
$$[\text{Cu(eeac-}Et\text{)(eeac)}]^+ + \text{Mg(tftm)(tftm)} + 2\text{H} \qquad \text{(Eqn 4.29)}$$

The final ligand exchange product generated is displayed in Figure 4.31 from the reaction of mass-selected [Mg(eeac-*Et*)(eeac-*Et*)+2H]$^+$ at *m/z* 222 with Cu(tftm)$_2$, and was the copper complete ligand exchange fragment [Cu(eeac-*Et*)(eeac-*Et*)]$^+$ at *m/z* 259.

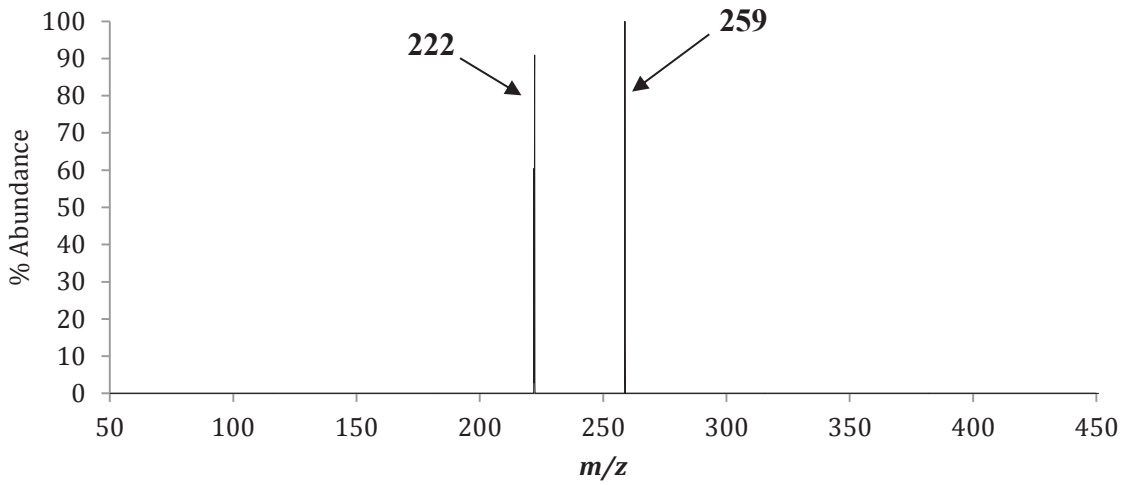

Figure 4.31: The positive mass spectrum obtained by scanning the third quadrupole following the selective reaction of *m/z* = 222 ([Mg(eeac-*Et*)(eeac-*Et*)+2H]$^+$) with neutral Cu(tftm)$_2$ to produce the complete ligand exchange fragment [Cu(eeac-*Et*)(eeac-*Et*)]$^+$ at *m/z* 259.

The proposed mechanism for the gas-phase formation of the copper complete ligand exchange fragment [Cu(eeac-*Et*)(eeac-*Et*)]$^+$ is presented in Equation 4.30.

$$[\text{Mg(eeac-}Et\text{)(eeac-}Et\text{)+2H}]^+ + \text{Cu(tftm)(tftm)} \rightarrow [\text{Cu(eeac-}Et\text{)(eeac-}Et\text{)}]^+ + \text{Mg(tftm)(tftm)} + 2\text{H} \qquad \text{(Eqn 4.30)}$$

The final species mass-selected for collision-induced reactions in this series was the single ligand species [Mg(eeac)]$^+$ at *m/z* 151. Upon reacting with Cu(tftm)$_2$ only one product of interest, [Cu(eeac-*Et*)(tftm)]$^+$ at *m/z* 356, was observed to form. The results of this reaction are displayed in Figure 4.32.

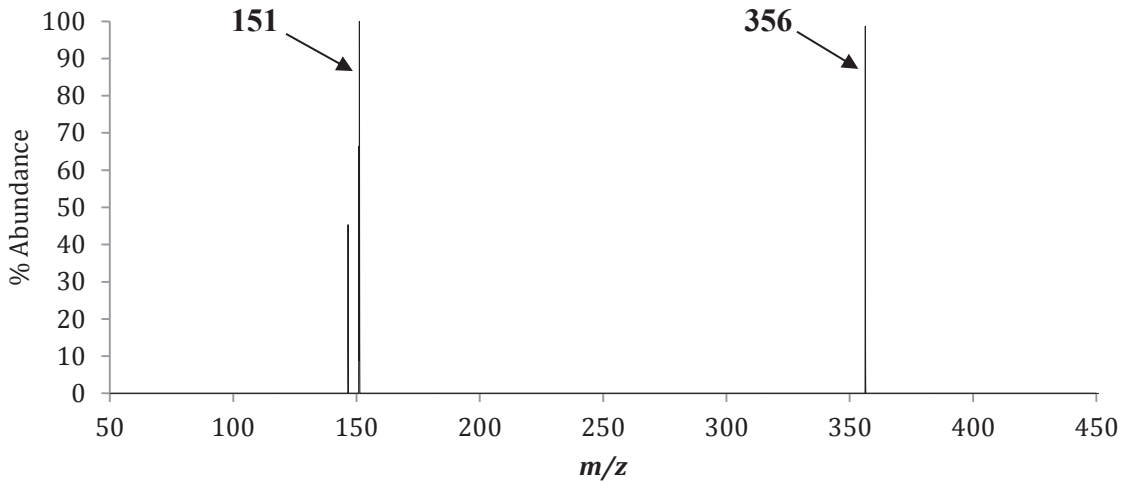

Figure 4.32: The positive mass spectrum obtained by scanning the third quadrupole following the selective reaction of *m/z* = 151 ($[Mg(eeac)]^+$) with neutral $Cu(tftm)_2$ to produce the mixed ligand exchange fragment $[Cu(eeac\text{-}Et)(tftm)]^+$ at *m/z* 356.

The proposed mechanism for the gas-phase formation of the copper mixed ligand exchange fragment $[Cu(eeac\text{-}Et)(tftm)]^+$ is presented in Equation 4.31.

$$[Mg(eeac)]^+ + Cu(tftm)(tftm) \rightarrow [Cu(eeac\text{-}Et)(tftm)]^+ + Mg(tftm) + Et \qquad \text{(Eqn 4.31)}$$

The most abundant species from the spectrum of $Cu(tftm)_2$ were also subjected to collision-induced reaction analysis. These species included mass-selected $[Cu(tftm)_2]^+$ at *m/z* 453, $[Cu(tftm\text{-}tBu)(tftm)]^+$ at *m/z* 396, $[Cu(tftm\text{-}tBu)(tftm\text{-}tBu)]^+$ at *m/z* 339, $[Cu(tftm)]^+$ at *m/z* 258, and $[Cu(tftm\text{-}tBu)]^+$ at *m/z* 201. As described previously, these fragments were individually selected using the first quadrupole and permitted to react with an atmosphere of neutral $Mg(eeac)_2$ in the second quadrupole. All resultant products were subsequently scanned in the third quadrupole from *m/z* 50 to 650.

The first mass-selected species that was subjected to a collision-induced reaction was $[Cu(tftm)_2]^+$ at *m/z* 453, which generated two ligand exchange products of interest;

$[Cu(eeac)_2]^+$ at *m/z* 317 and $[Cu(eeac)(tftm)]^+$ at *m/z* 385. Both of these ligand exchange products are clearly displayed in Figure 4.33.

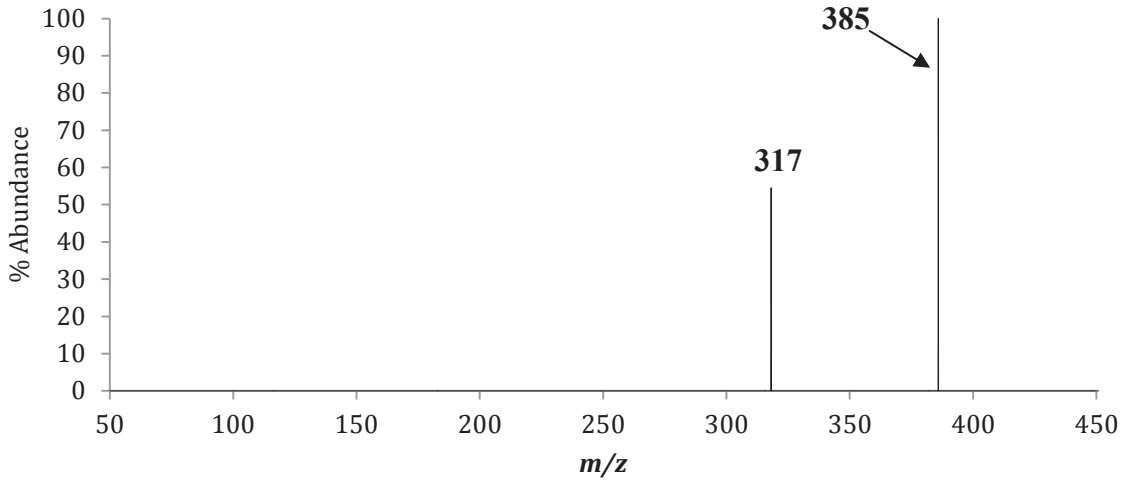

Figure 4.33: The positive mass spectrum obtained by scanning the third quadrupole following the selective reaction of *m/z* = 453 ($[Cu(tftm)_2]^+$) with neutral $Mg(eeac)_2$ to produce the complete ligand exchange product $[Cu(eeac)_2)]^+$ at *m/z* 317 and the mixed ligand exchange product $[Cu(eeac)(tftm)]^+$ at *m/z* 385.

The proposed mechanisms for the gas-phase formation of the copper complete ligand exchange product $[Cu(eeac)_2]^+$ and the copper mixed ligand exchange product $[Cu(eeac)(tftm)]^+$ are presented in Equations 4.32 and 4.33, respectively.

$$[Cu(tftm)(tftm)]^+ + Mg(eeac)(eeac) \rightarrow [Cu(eeac)(eeac)]^+ + Mg(tftm)(tftm) \qquad \text{(Eqn 4.32)}$$

$$[Cu(tftm)(tftm)]^+ + Mg(eeac)(eeac) \rightarrow [Cu(eeac)(tftm)]^+ + Mg(eeac)(tftm) \qquad \text{(Eqn 4.33)}$$

Ligand exchange products were also generated from mass-selected [Cu(tftm-*tBu*)(tftm-*tBu*)]$^+$ at *m/z* 339 reacting with neutral $Mg(eeac)_2$. The first observed ion was the complete ligand exchange product $[Mg(tftm)_2]^+$ at *m/z* 414, and is displayed in Figure 4.34.

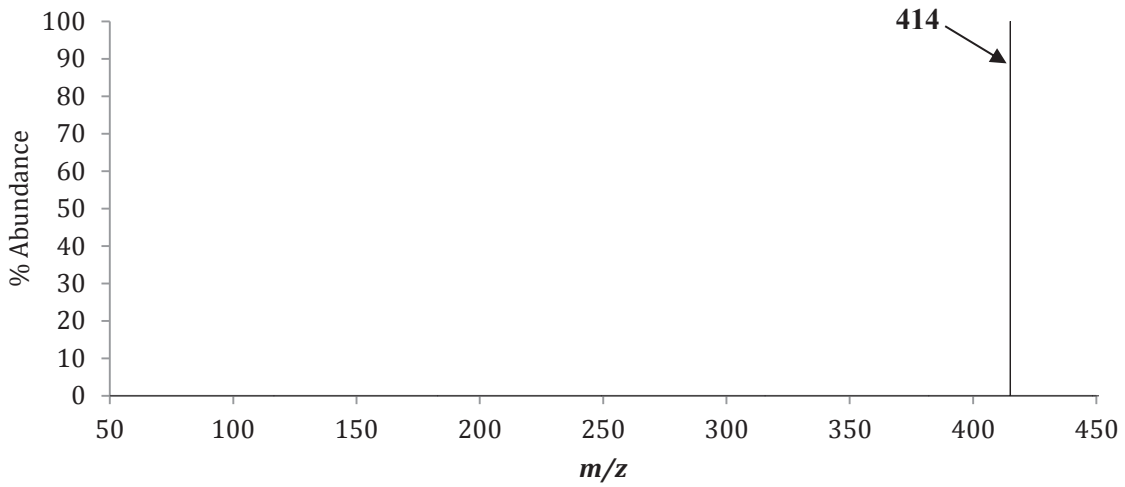

Figure 4.34: The positive mass spectrum obtained by scanning the third quadrupole following the selective reaction of *m/z* = 339 ([Cu(tftm-*tBu*)(tftm-*tBu*)]$^+$) with neutral Mg(eeac)$_2$ to produce the complete ligand exchange product [Mg(tftm)$_2$]$^+$ at *m/z* 414 .

The proposed mechanism for the gas-phase formation of the magnesium complete ligand exchange product [Mg(tftm)$_2$]$^+$ is presented in Equation 4.34.

$$[\text{Cu(tftm-}tBu\text{)(tftm-}tBu\text{)}]^+ + \text{Mg(eeac)(eeac)} + 2tBu \rightarrow [\text{Mg(tftm)(tftm)}]^+ + \text{Cu(eeac)(eeac)} \qquad \text{(Eqn 4.34)}$$

Mass-selected [Cu(tftm-*tBu*)(tftm-*tBu*)]$^+$ at *m/*z 339 reacting with Mg(eeac)$_2$ was also observed to produce the complete ligand exchange fragment [Mg(tftm-CF_2)(tftm)]$^+$ at *m/z* 364 and is displayed in Figure 4.35.

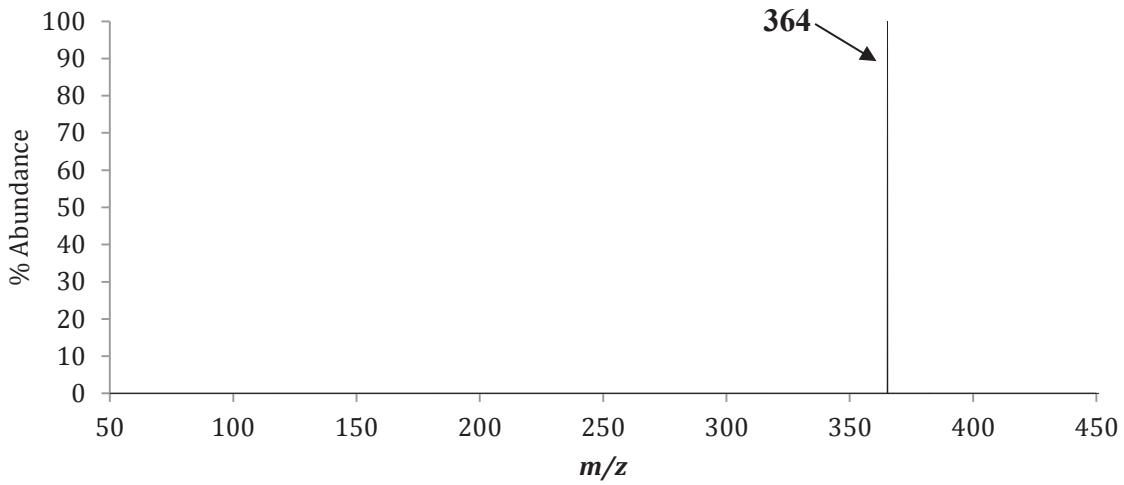

Figure 4.35: The positive mass spectrum obtained by scanning the third quadrupole following the selective reaction of *m/z* = 339 ([Cu(tftm-*tBu*)(tftm-*tBu*)]$^+$) with neutral Mg(eeac)$_2$ to produce the complete ligand exchange fragment [Mg(tftm-CF_2)(tftm)]$^+$ at *m/z* 364.

The proposed mechanism for the gas-phase formation of the magnesium complete ligand exchange fragment [Mg(tftm-CF_2)(tftm)]$^+$ is displayed in Equation 4.35.

$$[Cu(tftm\text{-}tBu)(tftm\text{-}tBu)]^+ + Mg(eeac)(eeac) + 2tBu \rightarrow$$
$$[Mg(tftm\text{-}CF_2)(tftm)]^+ + Cu(eeac)(eeac) + CF_2 \qquad \text{(Eqn 4.35)}$$

Mass-selected [Cu(tftm-*tBu*)(tftm-*tBu*)]$^+$ at *m/*z 339 reacting with Mg(eeac)$_2$ was found to also produce a second ligand exchange product of interest, [Mg(tftm-*tBu*)(tftm)]$^+$ at *m/z* 357, and is displayed in Figure 4.36.

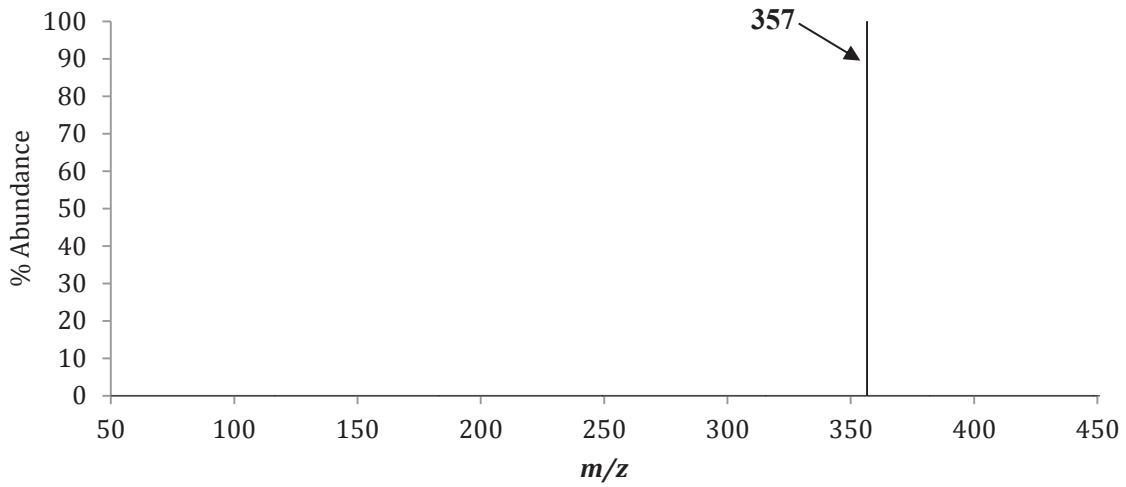

Figure 4.36: The positive mass spectrum obtained by scanning the third quadrupole following the selective reaction of *m/z* = 339 ([Cu(tftm-*tBu*)(tftm-*tBu*)]$^+$) with neutral Mg(eeac)$_2$ to produce the complete ligand exchange fragment [Mg(tftm-*tBu*)(tftm)]$^+$ at *m/z* 364.

The proposed mechanism for the gas-phase formation of the magnesium complete ligand exchange fragment [Mg(tftm-*tBu*)(tftm)]$^+$ is presented in Equation 4.36.

$$[Cu(tftm\text{-}tBu)(tftm\text{-}tBu)]^+ + Mg(eeac)(eeac) + tBu \rightarrow [Mg(tftm\text{-}tBu)(tftm)]^+ + Cu(eeac)(eeac) \quad \text{(Eqn 4.36)}$$

Two additional products were also generated from mass-selected [Cu(tftm-*tBu*)(tftm-*tBu*)]$^+$ at *m/z* 339 reacting with neutral Mg(eeac)$_2$. The first product is the magnesium single ligand exchange species [Mg(tftm-CF_2)]$^+$ at *m/z* 169; the second product was the copper mixed ligand exchange product [Cu(eeac)(tftm)]$^+$ at *m/z* 385. Each of the aforementioned products are displayed in Figure 4.37, where the peak at *m/z* 278 corresponds to the mass of the parent species [Mg(eeac)$_2$]$^+$.

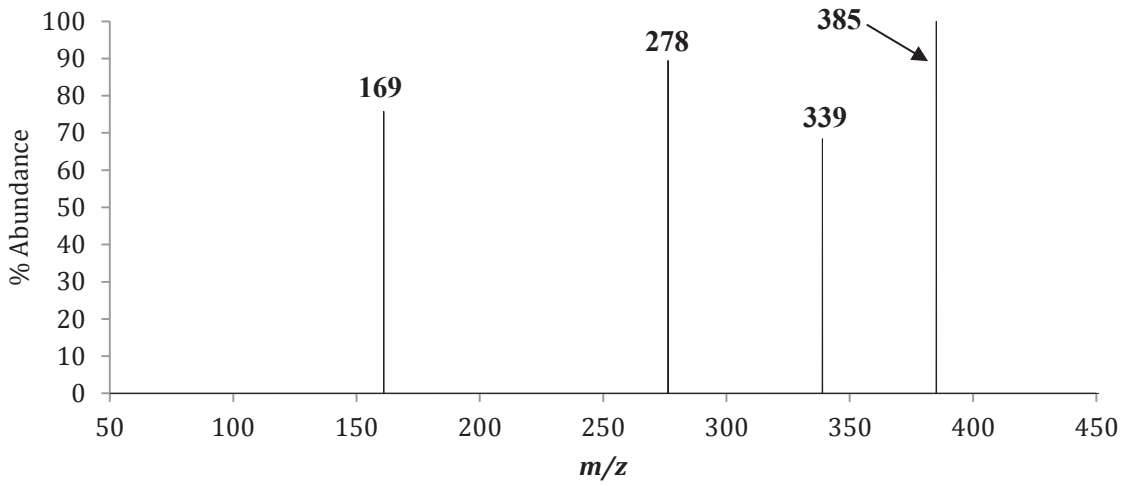

Figure 4.37: The positive mass spectrum obtained by scanning the third quadrupole following the selective reaction of *m/z* = 339 ([Cu(tftm-*tBu*)(tftm-*tBu*)]$^+$) with neutral Mg(eeac)$_2$ to produce the magnesium single ligand exchange fragment [Mg(tftm-CF_2)]$^+$ at *m/z* 169 and the copper mixed ligand exchange species [Cu(eeac)(tftm)]$^+$ at *m/z* 385.

The proposed mechanism for the gas-phase formation of the magnesium single ligand exchange fragment [Mg(tftm-CF_2)]$^+$ and the copper mixed ligand exchange product [Cu(eeac)(tftm)]$^+$ are presented in Equation 4.37 and 4.38, respectively.

$$[\text{Cu(tftm-}tBu\text{)(tftm-}tBu\text{)}]^+ + \text{Mg(eeac)(eeac)} + tBu \rightarrow$$
$$[\text{Mg(tftm-CF}_2\text{)}]^+ + \text{Cu(eeac)(tftm-}tBu\text{)} + \text{(eeac)} + CF_2 \qquad \text{(Eqn 4.37)}$$

$$[\text{Cu(tftm-}tBu\text{)(tftm-}tBu\text{)}]^+ + \text{Mg(eeac)(eeac)} + tBu \rightarrow$$
$$[\text{Cu(eeac)(tftm)}]^+ + \text{Mg(eeac)(tftm-}tBu\text{)} \qquad \text{(Eqn 4.38)}$$

One product, [Cu(eeac)$_2$]$^+$ at *m/z* 317, was observed to form from the mass-selected single ligand species [Cu(tftm)]$^+$ at *m/z* 258 reacting with Mg(eeac)$_2$ and is displayed in Figure 4.38.

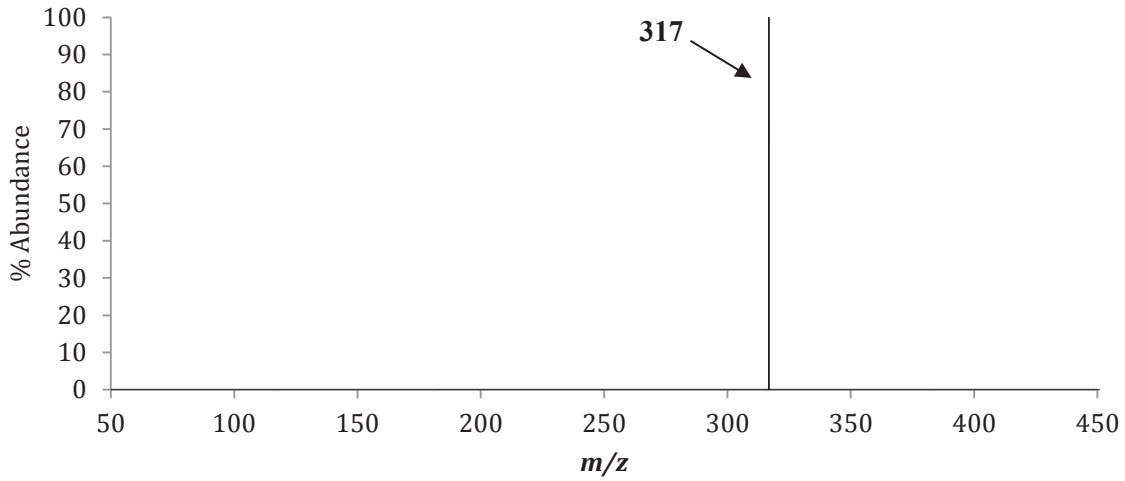

Figure 4.38: The positive mass spectrum obtained by scanning the third quadrupole following the selective reaction of *m/z* = 258 ($[Cu(tftm)]^+$) with neutral $Mg(eeac)_2$ to produce the copper complete ligand exchange product $[Cu(eeac)_2]^+$ at *m/z* 317.

The proposed mechanism for the gas-phase formation of the copper complete ligand exchange product $[Cu(eeac)_2]^+$ is presented in Equation 4.39.

$$[Cu(tftm)]^+ + Mg(eeac)(eeac) \rightarrow [Cu(eeac)(eeac)]^+ + Mg(tftm) \qquad \text{(Eqn 4.39)}$$

Additional ligand exchange products of interest were also generated from the mass-selected copper single ligand fragment $[Cu(tftm\text{-}tBu)]^+$ at *m/z* 201 reacting with $Mg(eeac)_2$. The first product of interest is $[Cu(eeac)(tftm)]^+$ at *m/z* 385 which is depicted in Figure 4.39.

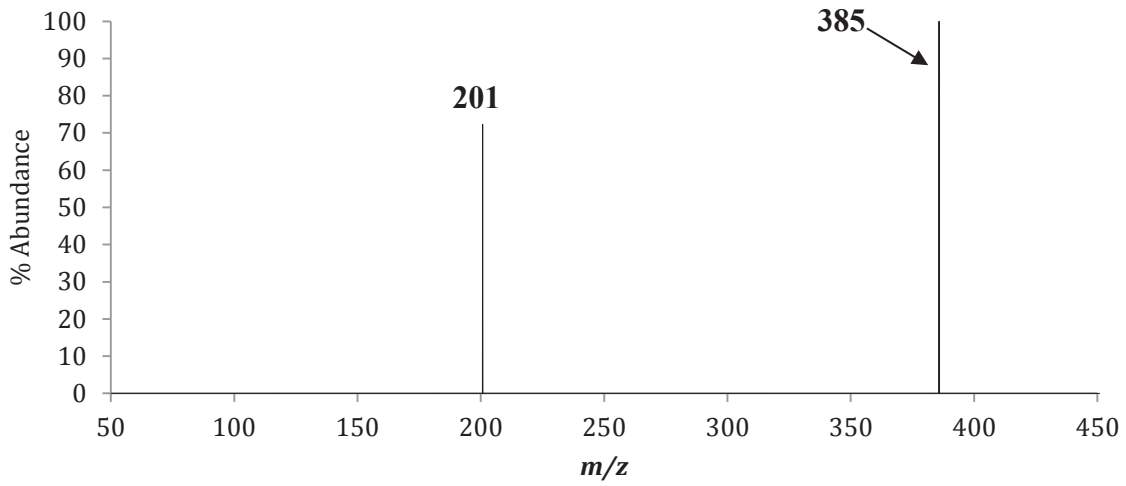

Figure 4.39: The positive mass spectrum obtained by scanning the third quadrupole following the selective reaction of *m/z* = 201 ($[Cu(tftm\text{-}tBu)]^+$) with neutral $Mg(eeac)_2$ to produce the copper mixed ligand exchange product $[Cu(eeac)(tftm)]^+$ at *m/z* 385.

The proposed mechanism for the gas-phase formation of the copper complete mixed ligand exchange product $[Cu(eeac)(tftm)]^+$ is presented in Equation 4.40.

$$[Cu(tftm\text{-}tBu)]^+ + Mg(eeac)(eeac) + tBu \rightarrow [Cu(eeac)(tftm)]^+ + Mg(eeac) \qquad \text{(Eqn 4.40)}$$

Mass-selected $[Cu(tftm\text{-}tBu)]^+$ at *m/z* 201 reacting with $Mg(eeac)_2$ was also observed to contribute to the formation of two magnesium ligand exchange products, the first of which is the complete ligand exchange product $[Mg(tftm)_2]^+$ at *m/z* 414, which is displayed in Figure 4.40.

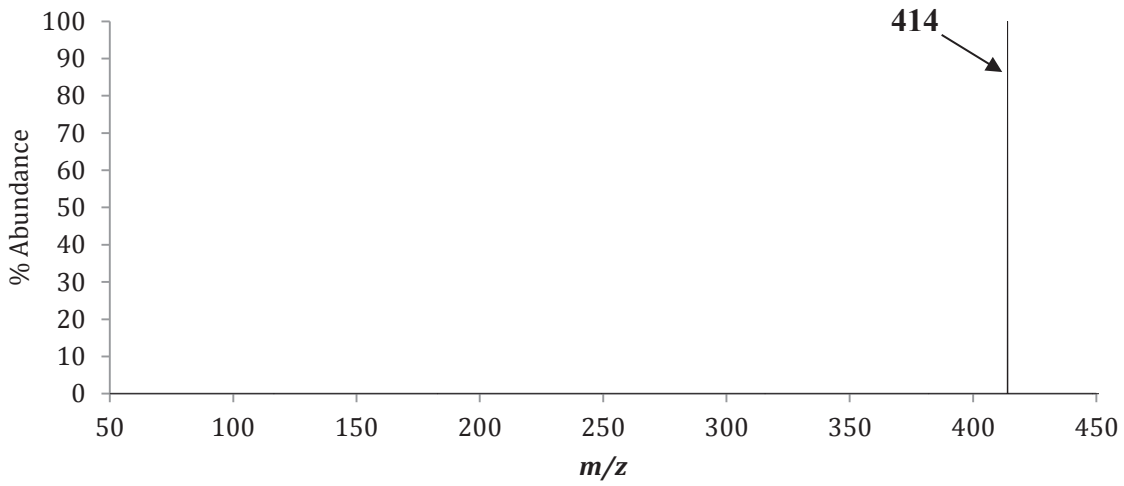

Figure 4.40: The positive mass spectrum obtained by scanning the third quadrupole following the selective reaction of *m/z* = 201 ($[Cu(tftm\text{-}tBu)]^+$) with neutral $Mg(eeac)_2$ to produce the magnesium complete ligand exchange product $[Mg(tftm)_2]^+$ at *m/z* 414.

The proposed mechanism for the gas-phase formation of the magnesium complete ligand exchange product $[Mg(tftm)_2]^+$ is presented in Equation 4.41.

$$[Cu(tftm\text{-}tBu)]^+ + Mg(eeac)(eeac) + (tftm) + tBu \rightarrow [Mg(tftm)(tftm)]^+ + Cu(eeac)(eeac) \qquad \text{(Eqn 4.41)}$$

The final product generated from mass-selected $[Cu(tftm\text{-}tBu)]^+$ at *m/z* 201 with $Mg(eeac)_2$ was the magnesium complete ligand exchange fragment $[Mg(tftm\text{-}CF_2)(tftm)]^+$ at *m/z* 364 and is displayed in Figure 4.41. The peak at *m/z* 73 does not correspond to any ligand exchange products and is not considered further.

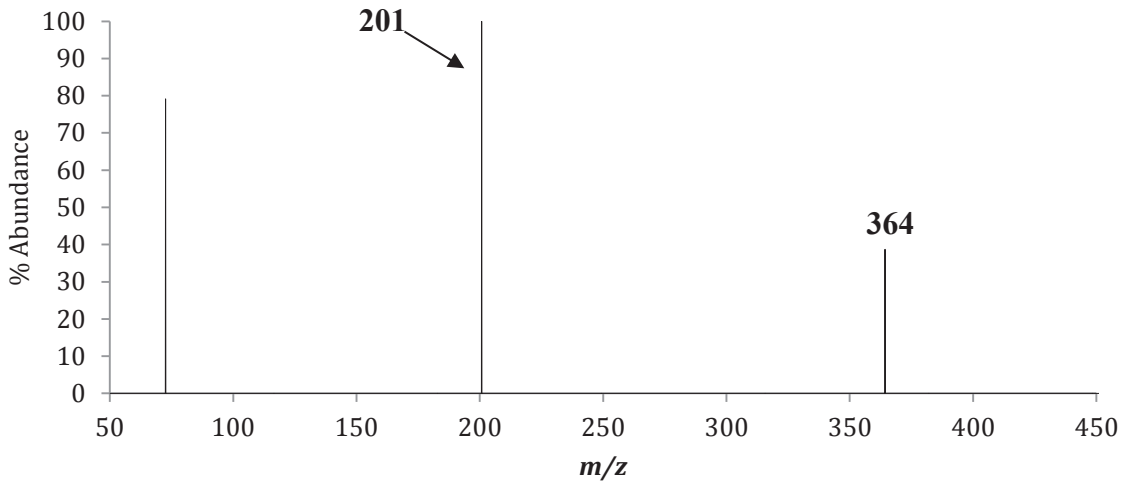

Figure 4.41: The positive mass spectrum obtained by scanning the third quadrupole following the selective reaction of *m/z* = 201 ($[Cu(tftm\text{-}tBu)]^+$) with neutral $Mg(eeac)_2$ to produce the magnesium complete ligand exchange product $[Mg(tftm\text{-}CF_2)(tftm)]^+$ at *m/z* 364.

The proposed mechanism for the gas-phase formation of the magnesium complete ligand exchange fragment $[Mg(tftm\text{-}CF_2)(tftm)]^+$ is presented in Equation 4.42.

$$[Cu(tftm\text{-}tBu)]^+ + Mg(eeac)(eeac) + (tftm) + tBu \rightarrow [Mg(tftm\text{-}CF_2)(tftm)]^+ + Cu(eeac)(eeac) + CF_2 \qquad \text{(Eqn 4.42)}$$

In conclusion, both mass-selected magnesium and copper species were found to contribute to the formation of many different ligand exchange products. Although the proposed mechanisms shed new light onto the mechanism of ligand exchange, additional work is necessary. Mass-selected $[Mg(eeac)_2]^+$ at *m/z* 278 reacting with $Cu(tftm)_2$ was observed to lead to the formation of the magnesium mixed ligand exchange product $[Mg(eeac)(tftm)]^+$ at *m/z* 346, the complete ligand exchange product $[Mg(tftm)_2]^+$ at *m/z* 414, as well as the complete ligand exchange fragment $[Mg(tftm\text{-}tBu)(tftm)]^+$ at *m/z* 357.

Mass-selected $[Mg(eeac\text{-}Et)(eeac)]^+$ at *m/z* 249 reacting with $Cu(tftm)_2$ promoted the formation of two ligand exchange product, the complete ligand exchange product

$[Mg(tftm)_2]^+$ at *m/z* 414 and the complete ligand exchange fragment [Mg(tftm-*tBu*)(tftm)]$^+$ at *m/z* 357.

Mass-selected [Mg(eeac-*Et*)(eeac-*Et*)+2H]$^+$ at *m/z* 222 was observed to generate several ligand exchange products when reacting with $Cu(tftm)_2$ including the magnesium complete ligand exchange product $[Mg(tftm)_2]^+$ at *m/z* 414 and the complete ligand exchange fragment [Mg(tftm-*tBu*)(tftm)]$^+$ at *m/z* 357. [Mg(eeac-*Et*)(eeac-*Et*)+2H]$^+$ was also observed to promote the formation of the magnesium ligand exchange fragments [Mg(eeac)(tftm-*tBu*)]$^+$ at *m/z* 289 and $[Mg(tftm\text{-}CF_2]^+$ at *m/z* 169. Several stable copper ligand exchange products were generated from mass-selected [Mg(eeac-*Et*)(eeac-*Et*)+2H]$^+$, including the copper mixed ligand exchange species [Cu(eeac)(tftm)]$^+$ at *m/z* 385 and the complete ligand exchange product $[Cu(eeac)_2]^+$ at *m/z* 317. Multiple copper ligand exchange fragments were also formed; [Cu(eeac-*Et*)(eeac)]$^+$ was formed at *m/z* 288, [Cu(eeac-*Et*)(eeac-*Et*)]$^+$ at *m/z* 259, and [Cu(eeac-*Et*)]$^+$ at *m/z* 161. [Mg(eeac)]$^+$ was also mass-selected at *m/z* 151 and generated one ligand exchange product, the copper mixed ligand exchange fragment [Cu(eeac-*Et*)(tftm)]$^+$ at *m/z* 356.

Mass-selected $[Cu(tftm)_2]^+$ at *m/z* 453 reacting with $Mg(eeac)_2$ was also found to yield two ligand exchange products; the complete ligand exchange product $[Cu(eeac)_2]^+$ at *m/z* 317 and the copper mixed ligand exchange product [Cu(eeac)(tftm)]$^+$ at *m/z* 385. Mass-selected [Cu(tftm-*tBu*)(tftm)]$^+$ reacting with $Mg(eeac)_2$ was observed to not yield any ligand exchange products while mass-selected [Cu(tftm-*tBu*)(tftm-*tBu*)]$^+$ at *m/z* 339 was found to generate several ligand exchange products. The magnesium complete ligand exchange product $[Mg(tftm)_2]^+$ at *m/z* 414 and the fragment [Mg(tftm-*tBu*)(tftm)]$^+$ at *m/z* 357 were both detected. A copper mixed ligand exchange product, [Cu(eeac)(tftm)]$^+$, was

also detected at *m/z* 385. Mass-selected $[Cu(tftm)]^+$ at *m/z* 258 appeared to contribute to the formation of only one ligand exchange product, the copper complete ligand exchange product $[Cu(eeac)_2]^+$. Three ligand exchange products were generated from the mass-selected reaction of the copper fragment $[Cu(tftm\text{-}tBu)]^+$ at *m/z* 201 with $Mg(eeac)_2$. The copper mixed ligand exchange product $[Cu(eeac)(tftm)]^+$ was present at *m/z* 385 as was the magnesium complete ligand exchange product $[Mg(tftm)_2]^+$ at *m/z* 414 and the magnesium complete ligand exchange fragment $[Mg(tftm\text{-}CF_2)(tftm)]^+$ at *m/z* 364.

4.7 The Co-Sublimation of $Mg(eeac)_2$ and Copper Bis-Dibenzoylmethane ($Cu(dbm)_2$)

Copper bis-dibenzoylmethane ($Cu(dbm)_2$) was also selected for co-sublimation and collision-induced reactions with $Mg(eeac)_2$. Presented in Figure 4.42(a) and (b) are the positive EI mass spectra of $Mg(eeac)_2$ and $Cu(dbm)_2$ with the co-sublimation spectrum of $Mg(eeac)_2$ and $Cu(dbm)_2$ presented in Figure 4.42(c). The spectra are stacked vertically for clarity and ease of comparison, and to demonstrate the formation of novel peaks, a strong indicator of ligand exchange. Although scans were completed from *m/z* 50 to 650, the spectra are displayed from *m/z* 50 to 550 to highlight the distinct isotopic distributions of the products. The baseline spectrum of $Mg(eeac)_2$ is reproduced from Figure 3.1 and will not be discussed further. The positive EI mass spectrum of $Cu(dbm)_2$ displays two key peaks; intact $[Cu(dbm)_2]^+$ at *m/z* 509 and the single ligand species $[Cu(dbm)]^+$ at *m/z* 286. The co-sublimation spectrum displayed in Figure 4.42(c) yields two key ligand exchange peaks; the magnesium complete ligand exchange product $[Mg(dbm)_2]^+$ at *m/z* 470 and the magnesium single ligand exchange product $[Mg(dbm)]^+$ at *m/z* 247. No copper ligand exchange products were detected following the co-

sublimation of $Mg(eeac)_2$ and $Cu(dbm)_2$. The relative abundances of the aforementioned species are displayed in Table 4.3.

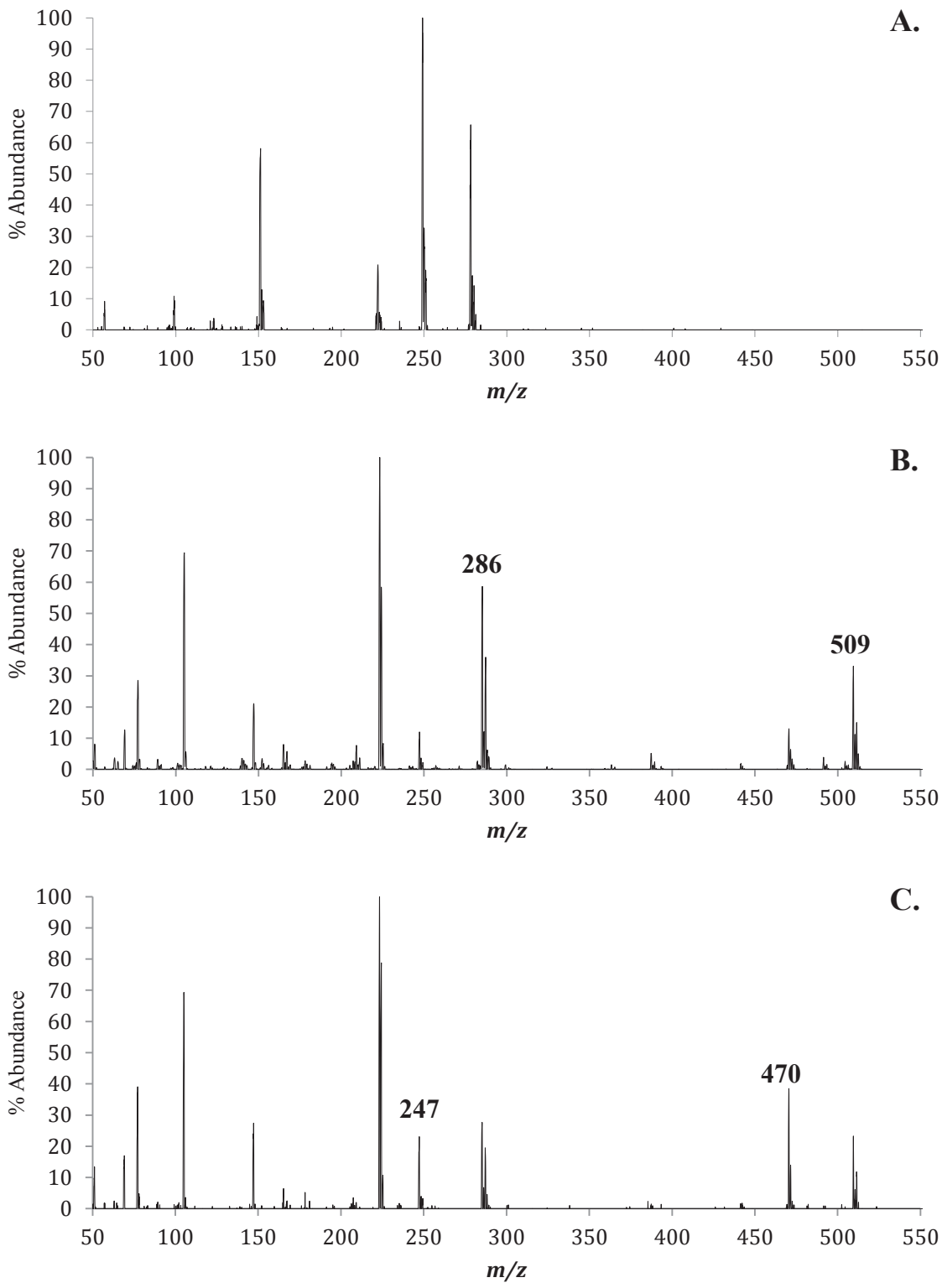

Figure 4.42: The positive EI mass spectra of (a) $Mg(eeac)_2$, (b) $Cu(dbm)_2$, and (c) the gas-phase co-sublimation of $Mg(eeac)_2$ and $Cu(dbm)_2$. The masses of parent compounds and fragments are labeled in (a) and (b). Masses of ligand exchange products and pertinent fragments are labeled in (c).

	Mass	Mass	MgL_2	CuL'''_2	MgL_2 & CuL'''_2	MgL_2 & CuL'''_2
Species	**Mg**	**Cu**	**Mg**	**Cu**	**Mg**	**Cu**
$[ML_2]^+$	278	317	65		0	0
$[ML_2\text{-}C_2H_5]^+$	249	288	100		2	5
$[ML_2\text{-}2C_2H_5\text{+}2H]^+$	222	-	20		0	-
$[ML_2\text{-}2C_2H_5]^+$	-	259	0		-	<1
$[ML]^+$	151	191	10		0	<1
$[ML\text{-}C_2H_5]^+$	136	160	<1		0	0
$[ML'''_2]^+$	470	509		33	38	23
$[ML''']^+$	247	286		12	23	7
$[MLL''']^+$	374	413			<1	0
$[M(L'\text{-}C_2H_5)L''']^+$	345	384			0	0

Table 4.3: The relative mass spectrometric abundances of the $Mg(eeac)_2$ and $Cu(dbm)_2$ β-diketonate complexes as well as the co-sublimation experiment, as presented in Figure 4.42. L = (eeac) L''' = (dbm).

4.7 The Selective Reactions of $Mg(eeac)_2$ and $Cu(dbm)_2$

The most abundant species detected from the positive EI mass spectrum of $Mg(eeac)_2$ were subjected to collision-induced reactions. As described previously, each species was mass-selected and isolated using the first quadrupole and permitted to continue to the second quadrupole wherein it encountered an atmosphere of neutral $Cu(dbm)_2$. All resulting products were subsequently scanned in the third quadrupole from *m/z* 50 to 650.

The first magnesium species mass-selected for collision-induced reaction was $[Mg(eeac)_2]^+$ at *m/z* 278, and according to Figure 4.43 produced the complete ligand exchange species $[Mg(dbm)_2]^+$ at *m/z* 470. The peak at *m/z* 222 corresponds to the mass

of [Mg(eeac-*Et*)(eeac-*Et*)+2H]$^+$, an accessory fragment from the original mass-selected parent species [Mg(eeac)$_2$]$^+$.

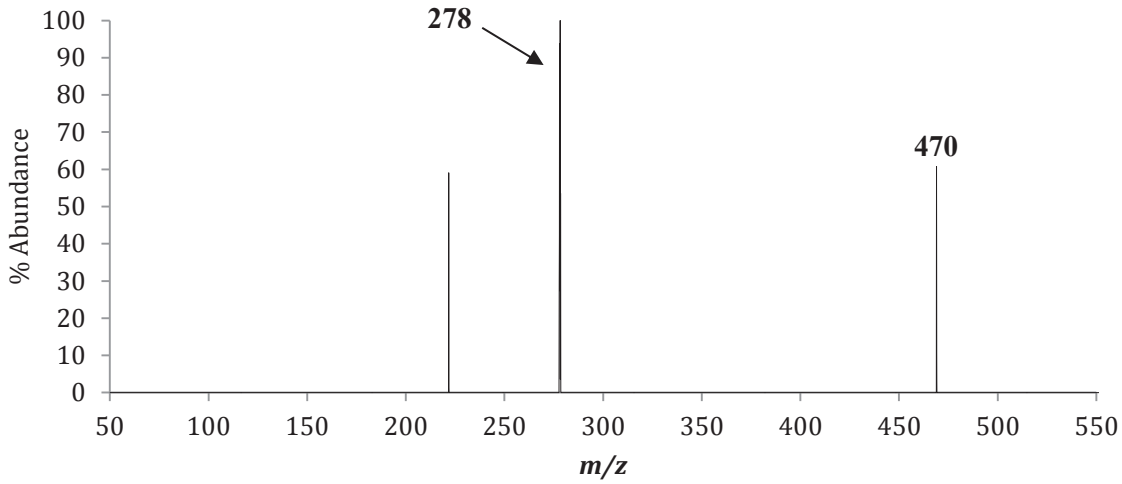

Figure 4.43: The positive mass spectrum obtained by scanning the third quadrupole following the selective reaction of *m/z* = 278 ([Mg(eeac)$_2$]$^+$) with neutral Cu(dbm)$_2$ to produce the magnesium complete ligand exchange product [Mg(dbm)$_2$]$^+$ at *m/z* 470.

The proposed mechanism for the gas-phase formation of the magnesium complete ligand exchange product [Mg(dbm)$_2$]$^+$ is presented in Equation 4.43.

$$[Mg(eeac)(eeac)]^+ + Cu(dbm)(dbm) \rightarrow [Mg(dbm)(dbm)]^+ + Cu(eeac)(eeac) \quad \text{(Eqn 4.43)}$$

The second mass-selected magnesium species that generated a ligand exchange product was [Mg(eeac-*Et*)(eeac)]$^+$ at *m/z* 249, which also generated [Mg(dbm)$_2$]$^+$ at *m/z* 470. Both of these species are displayed in Figure 4.44, where the peak at *m/z* 151 corresponds to the mass of [Mg(eeac)]$^+$, which is an accessory fragment from the original mass-selected parent species.

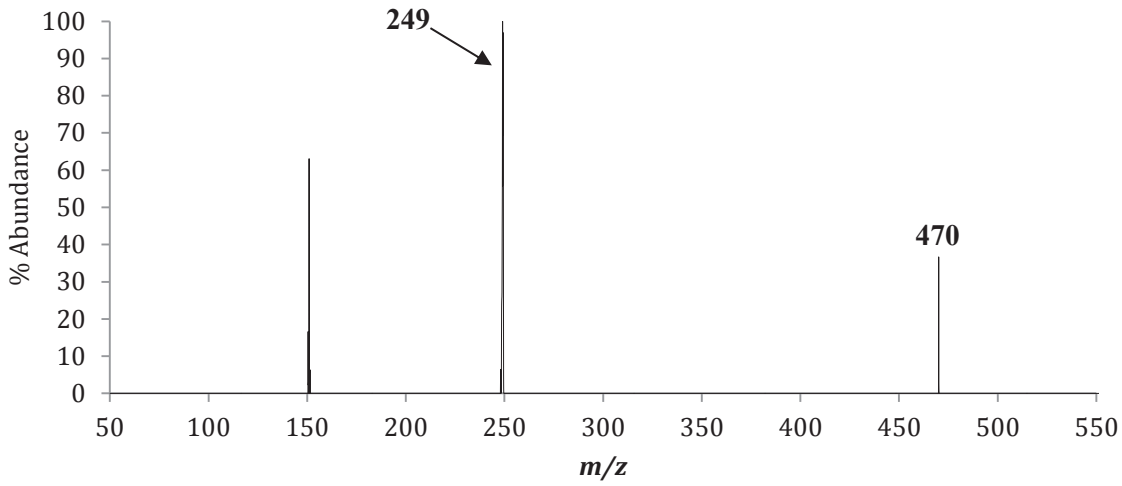

Figure 4.44: The positive mass spectrum obtained by scanning the third quadrupole following the selective reaction of *m/z* = 249 ($[Mg(eeac\text{-}Et)(eeac)]^+$) with neutral $Cu(dbm)_2$ to produce the magnesium complete ligand exchange product $[Mg(dbm)_2]^+$ at *m/z* 470.

The proposed mechanism for the gas-phase formation of the magnesium complete ligand exchange product $[Mg(dbm)_2]^+$ is displayed in Equation 4.44.

$$[Mg(eeac\text{-}Et)(eeac)]^+ + Cu(dbm)(dbm) \rightarrow [Mg(dbm)(dbm)]^+ + Cu(eeac\text{-}Et)(eeac) \quad \text{(Eqn 4.44)}$$

The mass-selected magnesium fragment $[Mg(eeac\text{-}Et)(eeac\text{-}Et)+2H]^+$ at *m/z* 222 after reacting with $Cu(dbm)_2$ generated the single ligand exchange product $[Mg(dbm)]^+$ at *m/z* 247 as demonstrated by Figure 4.45. The peak at *m/z* 478 does not correspond to the mass of any predicted ligand exchange product and is not considered any further.

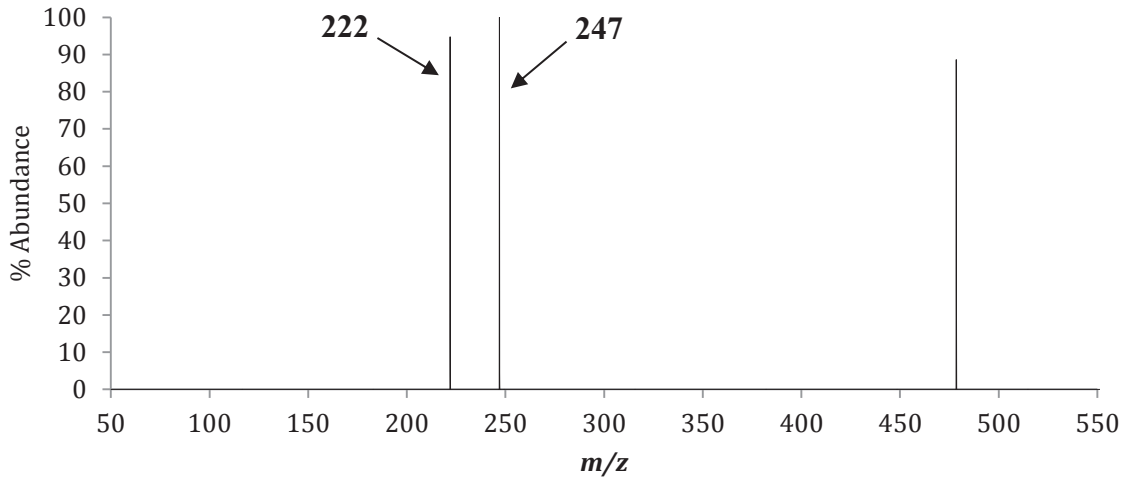

Figure 4.45: The positive mass spectrum obtained by scanning the third quadrupole following the selective reaction of *m/z* = 222 ([Mg(eeac-*Et*)(eeac-*Et*)+2H]$^+$) with neutral Cu(dbm)$_2$ to produce the magnesium single ligand exchange product [Mg(dbm)]$^+$ at *m/z* 247.

The proposed mechanism for the gas-phase formation of the magnesium single ligand exchange product [Mg(dbm)]$^+$ is presented in Equation 4.45.

$$[\text{Mg(eeac-}Et\text{)(eeac-}Et\text{)+2H}]^+ + \text{Cu(dbm)(dbm)} \rightarrow$$

$$[\text{Mg(dbm)}]^+ + \text{Cu(eeac-}Et\text{)(eeac-}Et\text{)} + \text{(dbm)+ 2H} \qquad \text{(Eqn 4.45)}$$

The mass-selected magnesium species [Mg(eeac)]$^+$ at *m/z* 151, after reacting with neutral Cu(dbm)$_2$, was observed to form [Mg(dbm)$_2$]$^+$ at *m/z* 470 and is presented in Figure 4.46.

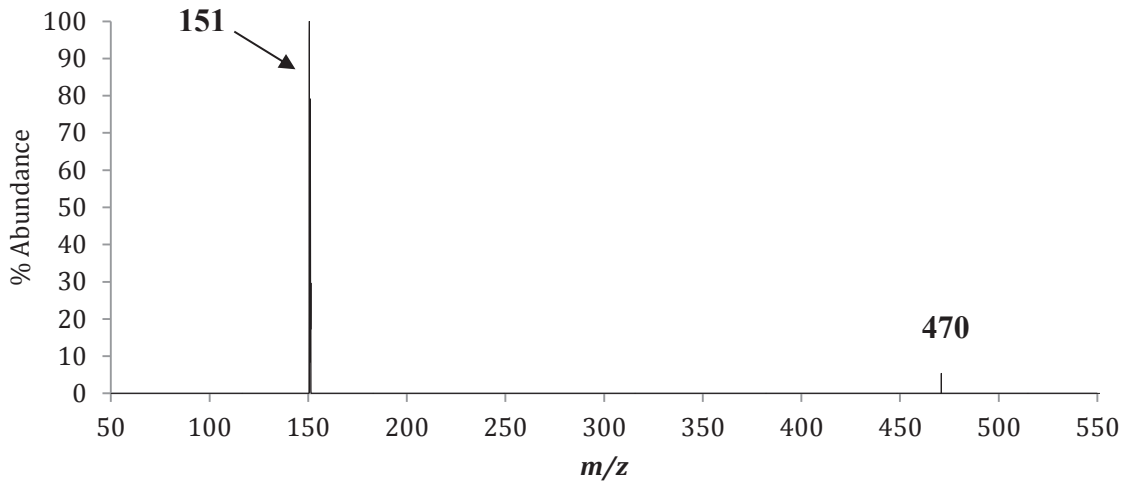

Figure 4.46: The positive mass spectrum obtained by scanning the third quadrupole following the selective reaction of *m/z* = 151 ($[Mg(eeac)]^+$) with neutral $Cu(dbm)_2$ to produce the magnesium complete ligand exchange product $[Mg(dbm)_2]^+$ at *m/z* 470.

The proposed mechanism for the gas-phase formation of the magnesium complete ligand exchange product $[Mg(dbm)_2]^+$ is presented in Equation 4.46.

$$[Mg(eeac)]^+ + Cu(dbm)(dbm) \rightarrow [Mg(dbm)(dbm)]^+ + Cu(eeac) \qquad \text{(Eqn 4.46)}$$

Mass-selected copper species were also isolated and allowed to react with an atmosphere of neutral $Mg(eeac)_2$. Only one product, mass-selected $[Cu(dbm)]^+$ at *m/z* 286 reacting with neutral $Mg(eeac)_2$, generated the ligand exchange product $[Mg(dbm)]^+$ at *m/z* 247 and is displayed in Figure 4.47.

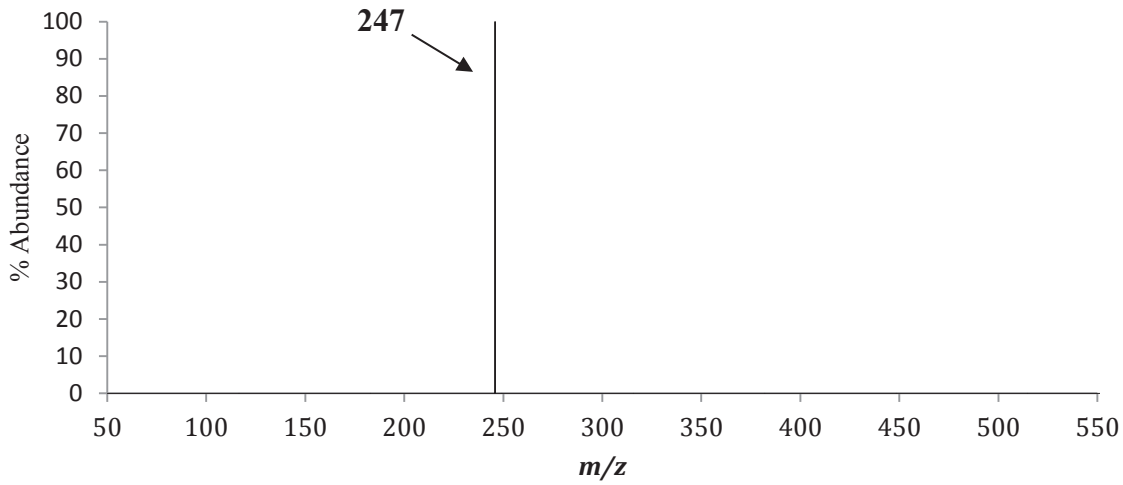

Figure 4.47: The positive mass spectrum obtained by scanning the third quadrupole following the selective reaction of *m/z* = 286 ($[Cu(dbm)]^+$) with neutral $Mg(eeac)_2$ to produce the magnesium single ligand exchange product $[Mg(dbm)]^+$ at *m/z* 247.

The proposed mechanism for the gas-phase formation of the magnesium single ligand exchange product $[Mg(dbm)]^+$ is presented in Equation 4.47.

$$[Cu(dbm)]^+ + Mg(eeac)(eeac) \rightarrow [Mg(dbm)]^+ + Cu(eeac)(eeac) \qquad \text{(Eqn 4.47)}$$

The single ligand species $[Cu(dbm)]^+$ also appears to contribute to the formation of the magnesium single ligand exchange product and interestingly, no ligand exchange products were generated from mass-selected $[Cu(dbm)_2]^+$ at *m/z* 509. The spectra presented in Section 4.7 have contributed much novel information to the mechanism of ligand exchange between $Mg(eeac)_2$ and $Cu(dbm)_2$. Although these mechanisms require further inspection, they have shed new light onto how the process of ligand exchange transpires in the gas phase.

Mass-selected $[Mg(eeac)_2]^+$ at *m/z* 278, $[Mg(eeac\text{-}Et)(eeac)]^+$ at *m/z* 249, and $[Mg(eeac)]^+$ at *m/z* 151 all appear to promote the formation of the complete ligand exchange product $[Mg(dbm)_2]^+$ when reacting with neutral $Cu(dbm)_2$, while [Mg(eeac-

Et)(eeac-*Et*)+2H]$^+$ at *m/z* 222 was observed to lead to the formation of the single ligand exchange product [Mg(dbm)]$^+$.

The only ligand exchange product generated from mass-selected copper species was from [Cu(dbm)]$^+$ at *m/z* 286, which promoted the formation of the single ligand exchange product [Mg(dbm)]$^+$. No ligand exchange products were generated from reacting mass-selected [Cu(dbm)$_2$]$^+$ at *m/z* 509 with neutral Mg(eeac)$_2$.

Chapter 5

The Co-Sublimation and Gas-Phase Ligand Exchange Reactions of Magnesium Bis-Trifluorotrimethylacetylacetonate ($Mg(tftm)_2$) with Nickel Bis-Acetylacetonate ($Ni(acac)_2$), Nickel Bis-Diethylacetylacetonate ($Ni(eeac)_2$), and Nickel Bis-Dibenzoylmethane ($Ni(dbm)_2$)

5.1 Introduction

Within this Chapter is the first analysis of gas-phase ligand exchange reactions utilizing magnesium β-diketonate complexes coordinated with trifluorotrimethylacetylaetonate (tftm) ligands. Previous examinations of gas-phase ligand exchange focused on transition metal β-diketonates, but not alkaline earth metals. Magnesium carries the same valency as many other transition metals, yet with a much smaller atomic radius, and exhibits novel patterns of ligand exchange not previously observed in other, much larger, transition metal complexes. Aiding in this discussion is a comparison of the isotopic distributions of each metal. Magnesium and nickel exhibit distinct isotopic patterns, which are reflected in the relative heights of the individual peaks on an EI mass spectrum. A list of the respective naturally occurring isotopic abundances of both magnesium and nickel are provided in Section 3.1. These differences in abundances are quite obvious in the mass spectrum and the signature-like patterns greatly aid in identifying potential ligand exchange products, particularly in cases wherein products are isobaric, or carrying the same *m/z* ratio.

After co-sublimation reactions verified the occurrence of novel peaks (and thus, ligand exchange), collision-induced reaction analysis (CIR) of mass-selected ions were

used to identify possible mechanisms of ligand exchange. Previous examinations into gas-phase ligand exchange reactions using CIR have elucidated that not all fragments are likely to equally contribute to the formation of ligand exchange products. While one particular mass-selected fragment may form several different ligand exchange products, other fragments may not participate at all in the formation of any ligand exchange products. The experimental conditions employed here closely match the CIR experiments described in earlier sections, where this Chapter details $Mg(tftm)_2$ for the first time.

5.2 Magnesium Trifluorotrimethylacetylacetonate ($Mg(tftm)_2$)

The reactions presented herein all involve magnesium bis-trifluorotrimethylacetylacetonate, or $Mg(tftm)_2$. A baseline positive EI mass spectrum for $Mg(tftm)_2$ is presented in Figure 5.1 where the most abundant peaks have been labeled. The peak at *m/z* 414 correlates with the mass of intact $[Mg(tftm)_2]^+$, with the loss of a tertiary-butyl, or *tBu*, group from the parent compound to form $[Mg(tftm\text{-}tBu)(tftm)]^+$ is also observed at *m/z* 357. The third peak on the spectrum is $[Mg(tftm\text{-}CF_2)]^+$ at *m/z* 169, which corresponds to the fluorine migration product, as discussed earlier. Although a complete scan was performed from *m/z* 50 to 650, the spectrum presented herein is only shown from *m/z* 100 to 450 to highlight the distinct isotopic distributions of the magnesium compounds. The relative abundances of all detected ions are organized in Table 5.1.

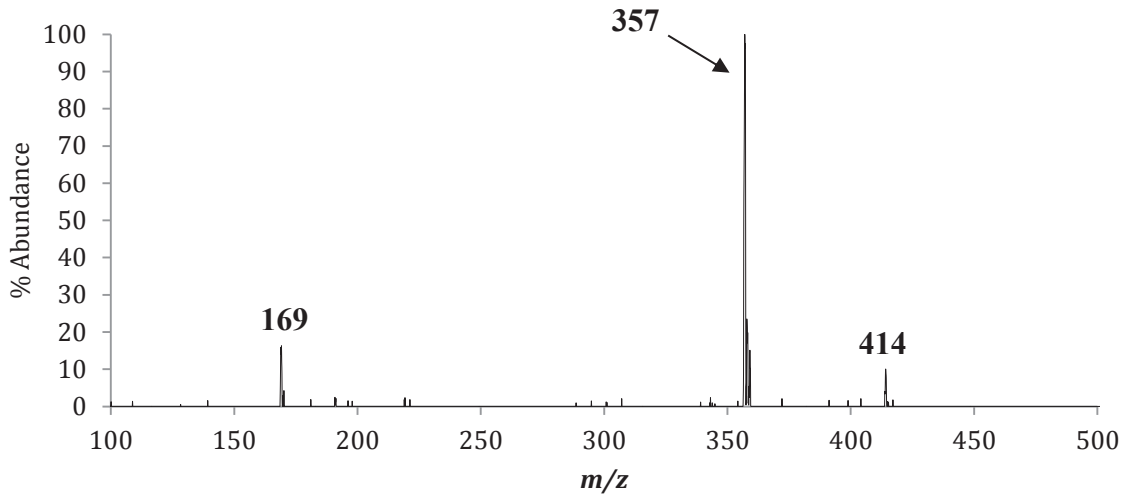

Figure 5.1: The 70 eV positive electron impact (EI) mass spectra of magnesium bis-trifluorotrimethylacetylacetonate, or $[Mg(tftm)_2]^+$, and its corresponding fragmentation pattern.

Species	*m/z*	Relative Abundance
$[Mg(tftm)_2]^+$	414	10
$[Mg(tftm\text{-}tBu)(tftm)]^+$	357	100
$[Mg(tftm\text{-}CF_2)]^+$	169	16

Table 5.1: Fragmentation species and relative positive ion intensities of the mass spectral analysis of $Mg(tftm)_2$ presented in Figure 5.1.

5.3 The Co-Sublimation of $Mg(tftm)_2$ and Nickel Bis-Acetylacetonate ($Ni(acac)_2$)

The positive EI mass spectra presented in Figure 5.2 (a)-(c) display the baseline spectra of $Mg(tftm)_2$, $Ni(acac)_2$, and the results following co-sublimation. Each spectrum is stacked vertically, and pertinent peaks are labeled for purposes of clarity and comparison. Figure 5.2(a) is reproduced from Figure 3.1 and will not be discussed further. Likewise, the baseline mass spectrum for $Ni(acac)_2$ in Figure 5.1(b) is reproduced from Figure 3.2(b). The co-sublimation spectrum in Figure 5.2(c) displays numerous novel peaks, a clear indicator that ligand exchange has occurred. The resultant peaks correspond to the formation of both magnesium and nickel ligand exchange products,

which were verified by evaluating isotopic abundances. The complete, intact ligand exchange product $[Ni(tftm)_2]^+$ is present at *m/z* 448, and loss of a *tBu* group to form $[Ni(tftm\text{-}tBu)(tftm)]^+$ is visible at *m/z* 391. The heteroleptic, or mixed ligand, product, $[Ni(tftm)(acac)]^+$, is displayed at *m/*z 352, as is the loss of a *tBu* group to form $[Ni(tftm\text{-}tBu)(acac)]^+$ at *m/z* 295. Although the complete, intact magnesium ligand exchange product was not detected in Figure 5.2(c), the mixed ligand exchange product $[Mg(acac)(tftm)]^+$ is present at *m/z* 318. $[Mg(acac)(tftm\text{-}tBu)]^+$ is present in high abundance at *m/z* 261, and the partial ligand exchange product $[Mg(acac)]^+$ is also quite prevalent at *m/z* 123.

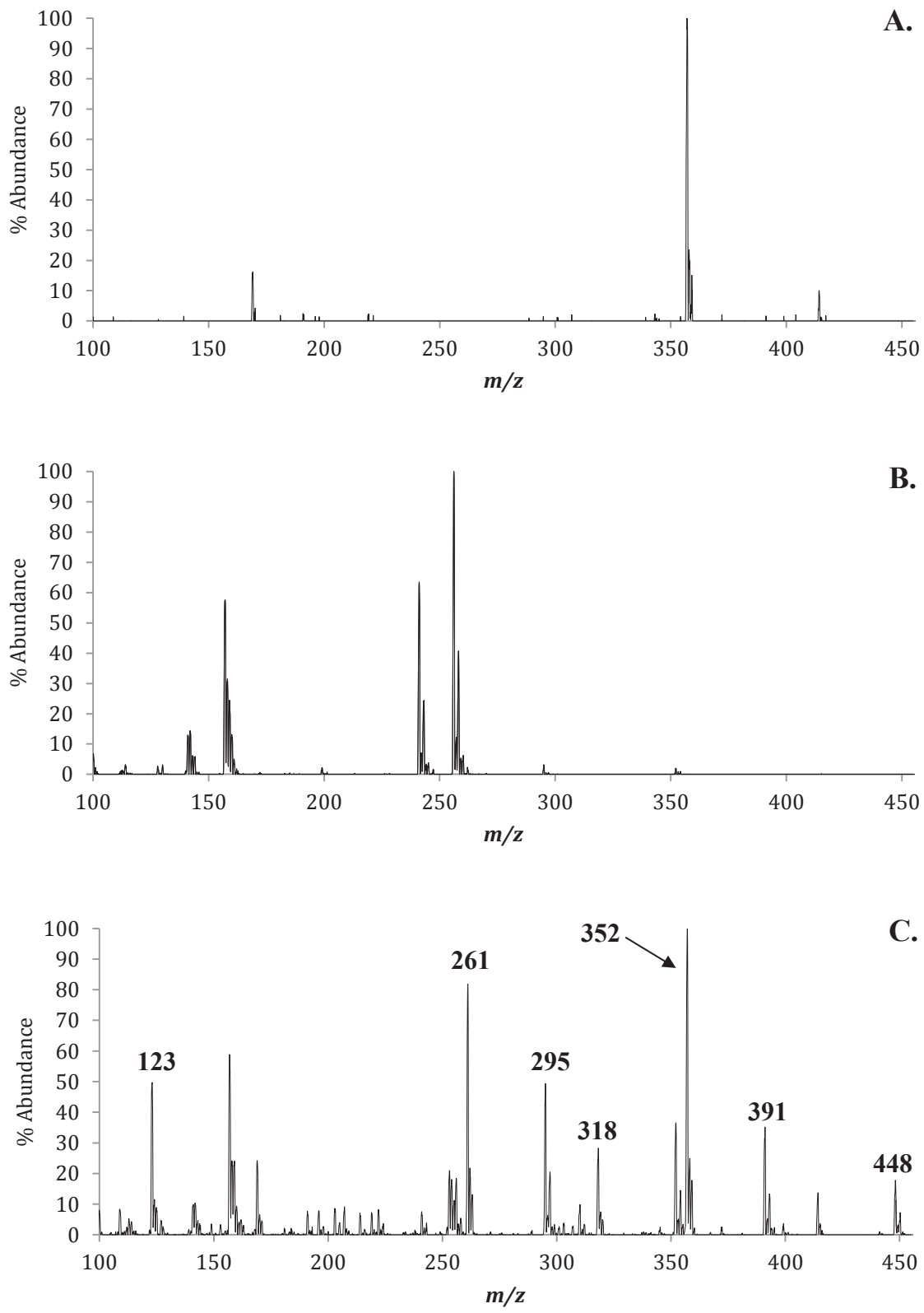

Figure 5.2(a)-(c): The positive EI mass spectra of (a) $Mg(tftm)_2$, (b) $Ni(acac)_2$, and (c) the gas-phase co-sublimation of $Mg(tftm)_2$ and $Ni(acac)_2$. The masses of parent compounds and fragments are labeled in (a) and (b). Masses of ligand exchange products and pertinent fragments are labeled in (c).

	Mass	Mass	MgL_2	NiL'_2	MgL_2 & NiL'_2	MgL & NiL'_2
Species	Mg	Ni	Mg	Ni	Mg	Ni
$[ML_2]^+$	414	448	10		14	18
$[ML_2\text{-}tBu]^+$	357	391	100		100	35
$[ML_2\text{-}CF_3]^+$	345	379	<1		<1	<1
$[ML_2\text{-}CF_2]^+$	364	398	0		0	<1
$[ML]^+$	219	253	2		7	21
$[ML\text{-}tBu]^+$	162	196	0		5	8
$[ML\text{-}CF_2]^+$	169	203	16		7	8
$[ML'_2]^+$	222	256		100	8	18
$[ML'_2\text{-}CH_3]^+$	207	241		63	9	7
$[ML']^+$	123	157		57	50	59
$[ML'\text{-}CH_3]^+$	108	142		14	8	10
$[MLL']^+$	318	352			28	37
$[M(L\text{-}tBu)L']^+$	261	295			81	49
$[ML(L'\text{-}CH_3]^+$	303	337			4	<1

Table 5.2: The relative mass spectrometric abundances of the $Mg(tftm)_2$ and $Ni(acac)_2$ β-diketonate complexes as well as the co-sublimation experiment, as presented in Figure 5.2. L = (tftm); L' = (acac).

5.4 The Selective Reactions of $Mg(tftm)_2$ and $Ni(acac)_2$

Since the peaks present in Figure 5.2(c) indicate the occurrence of ligand exchange, mass-selected fragments of both compounds were subjected to collision-induced reaction analysis, and similar protocols as those followed in Chapter 3 and Chapter 4 were used here to generate the ligand exchange products of interest.

The first product formed from collision-induced reaction was [Ni(tftm-*tBu*)(acac)]$^+$ at *m/z* 295, which was produced after mass-selecting [Mg(tftm-*tBu*)(tftm)]$^+$ at *m/z* 357. The spectrum displaying this exchange is presented in Figure 5.3.

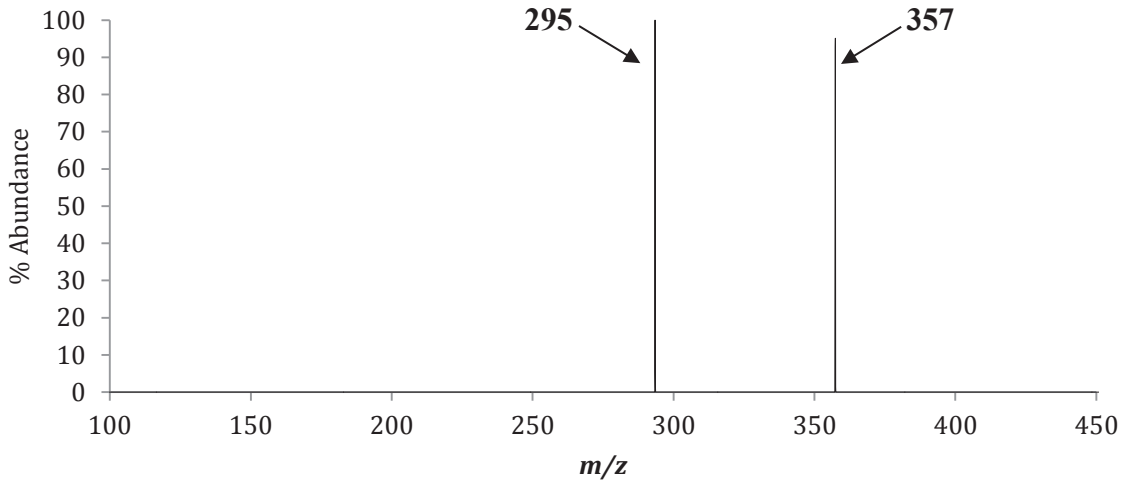

Figure 5.3: The positive mass spectrum obtained by scanning the third quadrupole following the selective reaction of *m/z* = 357 ([Mg(tftm-*tBu*)(tftm)]$^+$) with neutral Ni(acac)$_2$ to produce the mixed ligand exchange product [Ni(acac)(tftm-*tBu*)]$^+$ at *m/z* 295.

The proposed mechanism for the gas-phase formation of the nickel mixed ligand exchange fragment [Ni(acac)(tftm-*tBu*)]$^+$ is displayed in Equation 5.1.

$$[Mg(tftm\text{-}tBu)(tftm)]^+ + Ni(acac)(acac) \rightarrow [Ni(acac)(tftm\text{-}tBu)]^+ + Mg(acac)(tftm) \qquad \text{(Eqn 5.1)}$$

Another ligand exchange product of interest generated from collision-induced reaction with [Mg(tftm-CF_2)]$^+$ at *m/z* 169 reacting with neutral Ni(acac)$_2$ was the mixed ligand product [Ni(acac)(tftm)]$^+$ at *m/*z 352, which is displayed in Figure 5.4. The small peak at *m/*z 428 does not correlate with a predicted ligand exchange species and is not considered further.

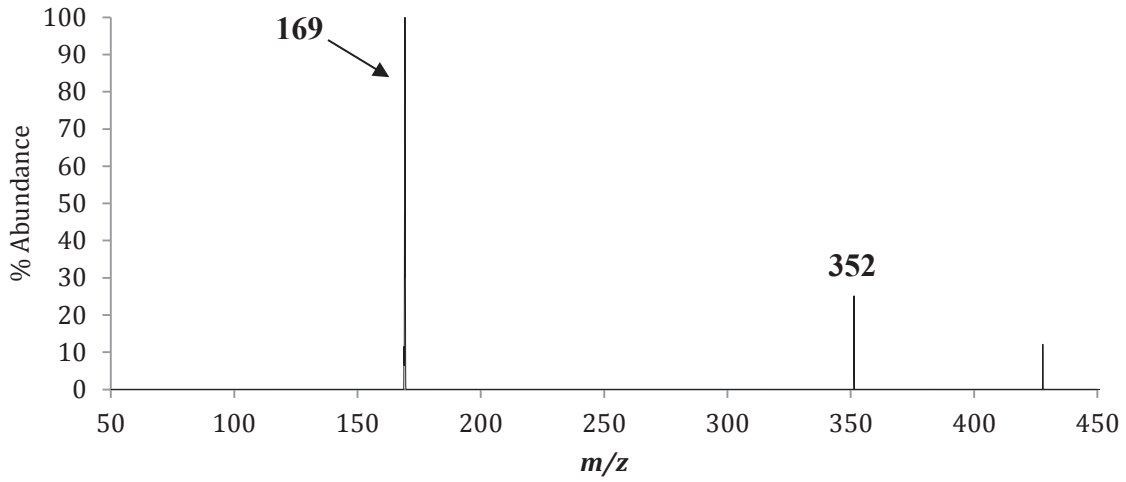

Figure 5.4: The positive mass spectrum obtained by scanning the third quadrupole following the selective reaction of *m/z* = 169 ($[Mg(tftm\text{-}CF_2]^+$) with neutral $Ni(acac)_2$ to produce the mixed ligand exchange product $[Ni(acac)(tftm)]^+$ *at m/z* 352.

The proposed mechanism for the gas-phase formation of the nickel mixed ligand exchange product $[Ni(acac)(tftm)]^+$ is presented in Equation 5.2

$$[Mg(tftm\text{-}CF_2)]^+ + Ni(acac)(acac) + CF_2 \rightarrow [Ni(acac)(tftm)]^+ + Mg(acac) \qquad \text{(Eqn. 5.2)}$$

The final ligand exchange product of interest produced from collision-induced reaction was also generated from mass-selected $[Mg(tftm\text{-}CF_2)]^+$ at *m/z* 169. The product, $[Ni(tftm\text{-}CF_3)(tftm)]^+$ at *m/z* 379 is displayed in Figure 5.5.

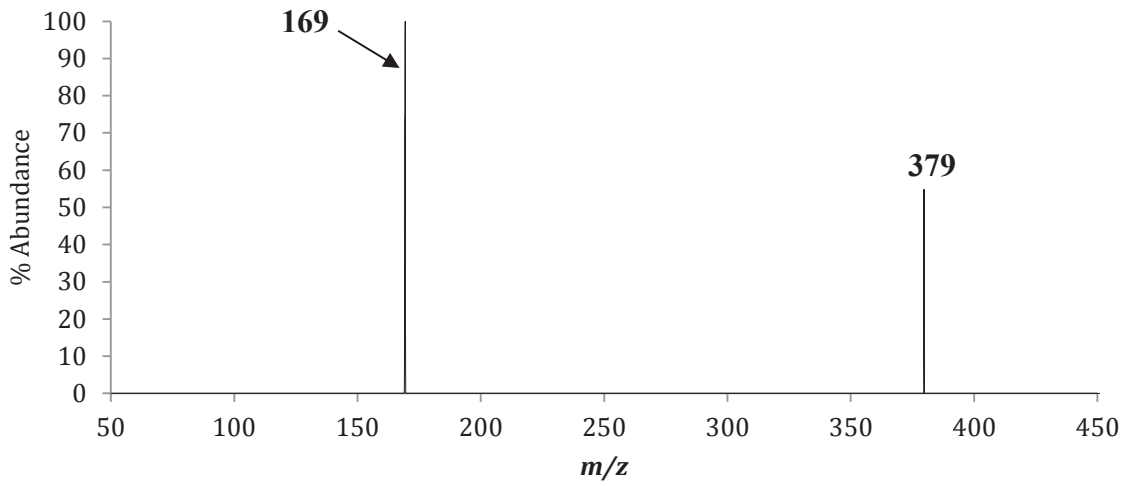

Figure 5.5: The positive mass spectrum obtained by scanning the third quadrupole following the selective reaction of *m/z* = 169 ($[Mg(tftm\text{-}CF_2)]^+$) with neutral $Ni(acac)_2$ to produce the mixed ligand exchange product $[Ni(tftm\text{-}CF_3)(tftm)]^+$ at *m/z* 379.

The proposed mechanism for the gas-phase formation of the nickel complete ligand exchange fragment $[Ni(tftm\text{-}CF_3)(tftm)]^+$ is presented in Equation 5.3.

$$[Mg(tftm\text{-}CF_2)]^+ + Ni(acac)(acac) + CF_2 \rightarrow [Ni(tftm\text{-}CF_3)(tftm)]^+ + Mg(acac) + CF_3 \quad \text{(Eqn 5.3)}$$

Mass-selected nickel species also generated several ligand exchange products of interest. Mass-selected $[Ni(acac)_2]^+$ at *m/z* 256 when reacting with neutral $Mg(tftm)_2$ generated the complete ligand exchange product $[Mg(acac)_2]^+$ at *m/z* 222, which is displayed in Figure 5.6.

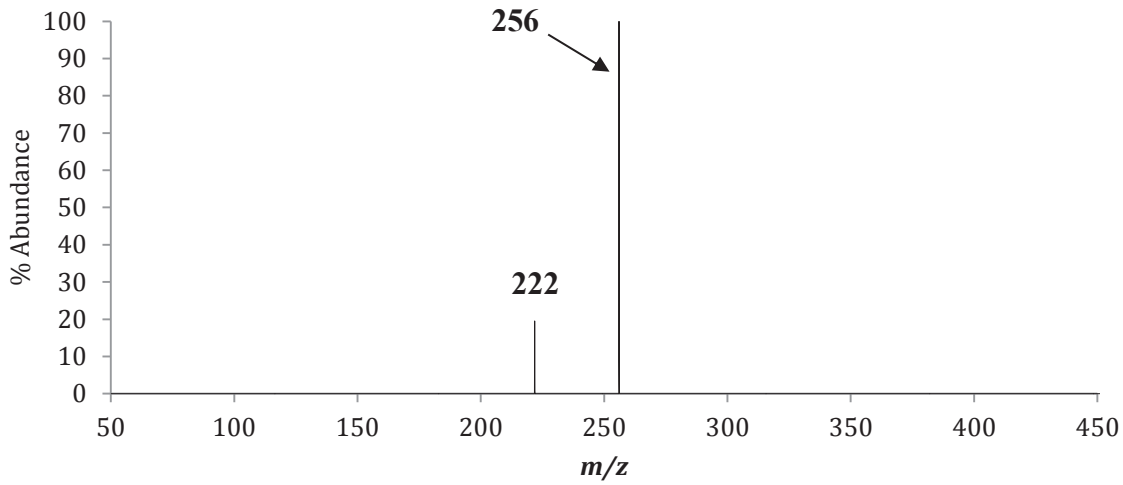

Figure 5.6: The positive mass spectrum obtained by scanning the third quadrupole following the selective reaction of *m/z* = 256 ($[Ni(acac)_2]^+$) with neutral $Mg(tftm)_2$ to produce the complete ligand exchange product $[Mg(acac)_2]^+$ at *m/z* 222.

The proposed mechanism for the gas-phase formation of the magnesium complete ligand exchange product $[Mg(acac)_2]^+$ is presented in Equation 5.4.

$$[Ni(acac)(acac)]^+ + Mg(tftm)(tftm) \rightarrow [Mg(acac)(acac)]^+ + Ni(tftm)(tftm) \qquad \text{(Eqn 5.4)}$$

Mass-selected $[Ni(acac\text{-}CH_3)(acac)]^+$ at *m/z* 241 also observed to generate ligand exchange products of interest when reacting with neutral $Mg(tftm)_2$, the first of which was $[Ni(acac\text{-}CH_3)(tftm)]^+$ at *m/z* 337, and is displayed in Figure 5.7.

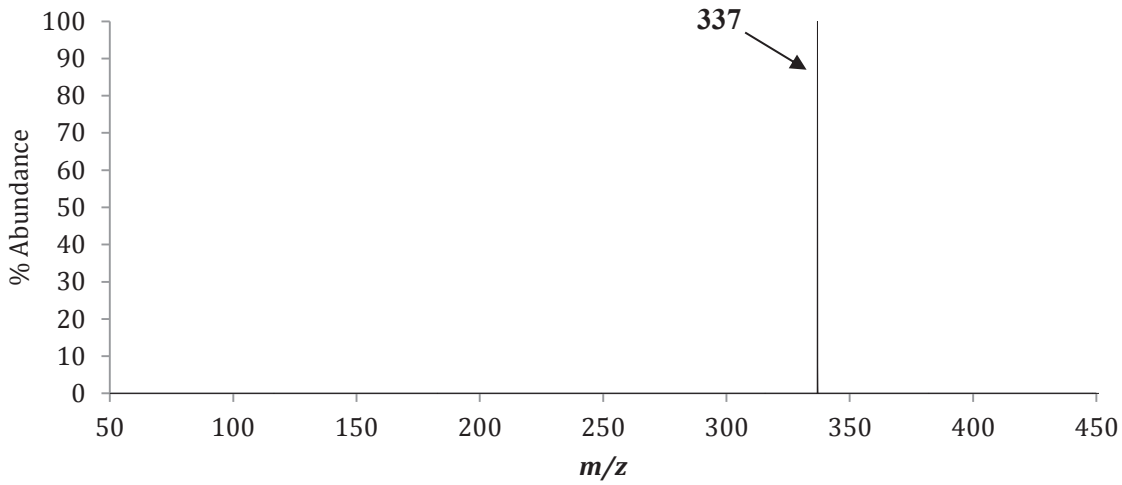

Figure 5.7: The positive mass spectrum obtained by scanning the third quadrupole following the selective reaction of *m/z* = 241 ($[Ni(acac\text{-}CH_3)(acac)]^+$) with neutral $Mg(tftm)_2$ to produce the complete ligand exchange product $[Ni(acac\text{-}CH_3)(tftm)]^+$ at *m/z* 337.

The proposed mechanism for the gas-phase formation of the nickel mixed ligand exchange fragment $[Ni(acac\text{-}CH_3)(tftm)]^+$ is presented in Equation 5.5.

$$[Ni(acac\text{-}CH_3)(acac)]^+ + Mg(tftm)(tftm) \rightarrow [Ni(acac\text{-}CH_3)(tftm)]^+ + Mg(acac)(tftm) \quad \text{(Eqn 5.5)}$$

Mass-selected $[Ni(acac\text{-}CH_3)(acac)]^+$ at *m/z* 241 was also observed to generate a product when reacting with neutral $Mg(tftm)_2$, this time the single ligand exchange product $[Ni(tftm)]^+$ at *m/z* 253 and is displayed in Figure 5.8.

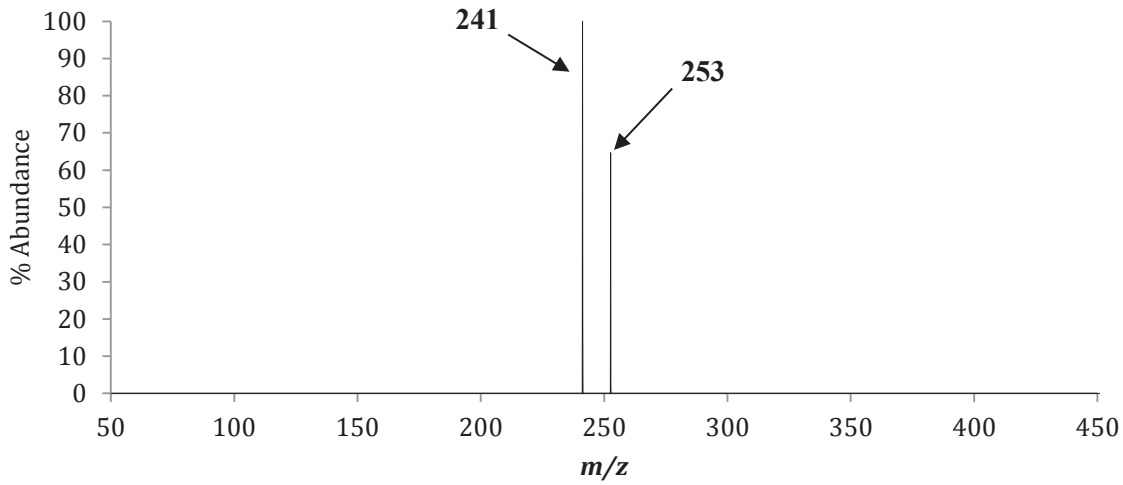

Figure 5.8: The positive mass spectrum obtained by scanning the third quadrupole following the selective reaction of *m/z* = 241 ($[Ni(acac\text{-}CH_3)(acac)]^+$) with neutral $Mg(tftm)_2$ to produce the complete ligand exchange product $[Ni(tftm)]^+$ at *m/z* 253.

The proposed mechanism for the gas-phase formation of the nickel single ligand exchange product $[Ni(tftm)]^+$ is presented in Equation 5.6.

$$[Ni(acac\text{-}CH_3)(acac)]^+ + Mg(tftm)_2 \rightarrow$$

$$[Ni(tftm)]^+ + Mg(acac)(tftm) + (acac\text{-}CH_3) \qquad \text{(Eqn 5.6)}$$

Mass-selected $[Ni(acac\text{-}CH_3)]^+$ at *m/z* 142 also yielded two ligand exchange products of interest when reacting with neutral $Mg(tftm)_2$, the first of which is $[Mg(acac\text{-}CH_3)(tftm)]^+$ at *m/z* 303 and is presented in Figure 5.9.

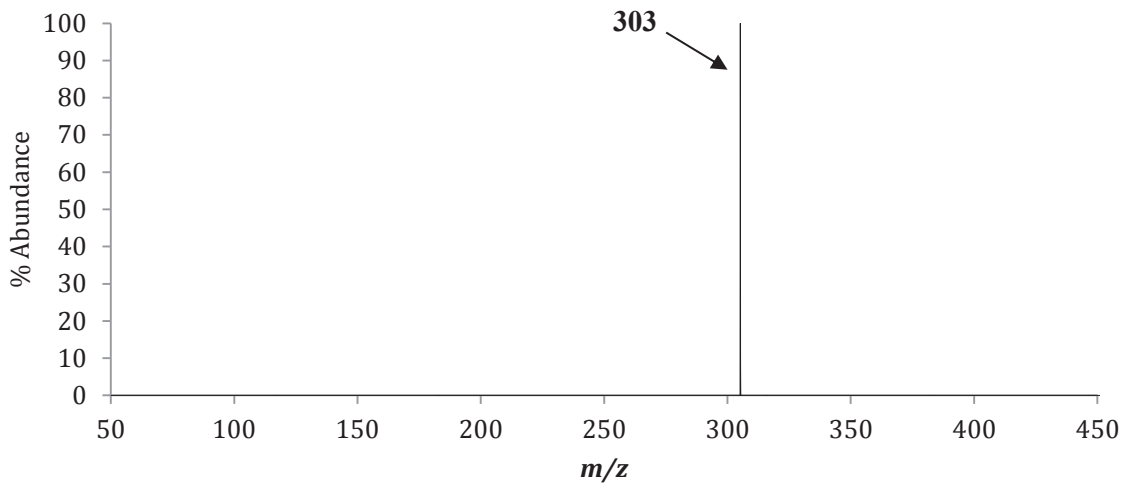

Figure 5.9: The positive mass spectrum obtained by scanning the third quadrupole following the selective reaction of *m/z* = 142 ($[Ni(acac\text{-}CH_3)]^+$) with neutral $Mg(tftm)_2$ to produce the mixed ligand exchange fragment $[Mg(acac\text{-}CH_3)(tftm)]^+$ at *m/z* 303.

The proposed mechanism for the gas-phase formation of the magnesium mixed ligand exchange fragment $[Mg(acac\text{-}CH_3)(tftm)]^+$ is presented in Equation 5.7.

$$[Ni(acac\text{-}CH_3)]^+ + Mg(tftm)(tftm) \rightarrow [Mg(acac\text{-}CH_3)(tftm)]^+ + (tftm) \qquad \text{(Eqn 5.7)}$$

The final product generated from mass-selected nickel species originated from $[Ni(acac\text{-}CH_3)]^+$ at *m/z* 142 reacting with $Mg(tftm)_2$ to form $[Ni(acac)(tftm)]^+$ at *m/z* 352, which is clearly displayed in Figure 5.10.

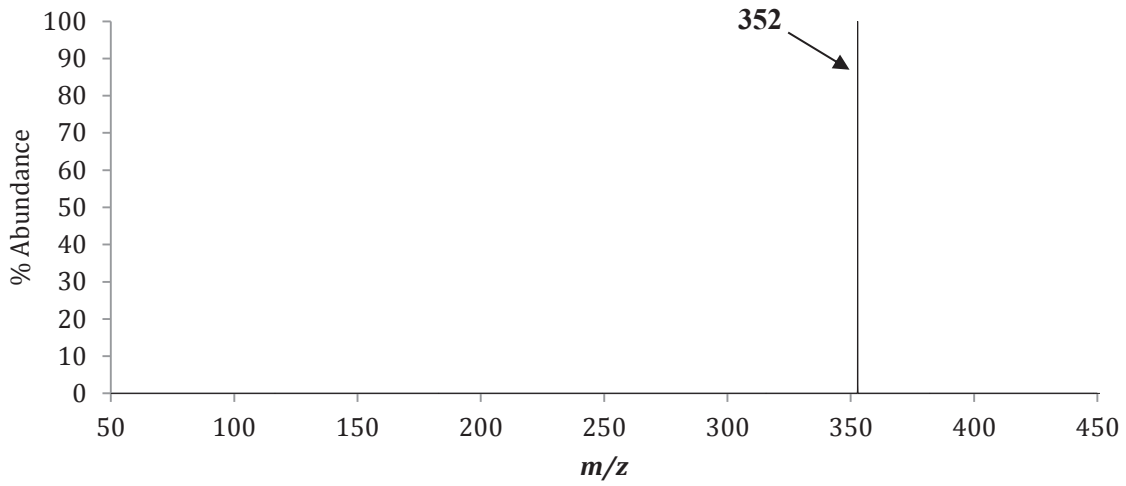

Figure 5.10: The positive mass spectrum obtained by scanning the third quadrupole following the selective reaction of *m/z* = 142 ($[Ni(acac\text{-}CH_3)]^+$) with neutral $Mg(tftm)_2$ to produce the complete ligand exchange product $[Ni(acac)(tftm)]^+$ at *m/z* 352.

The proposed mechanism for the gas-phase formation of the nickel mixed ligand exchange product $[Ni(acac)(tftm)]^+$ is presented in Equation 5.8.

$$[Ni(acac\text{-}CH_3)]^+ + Mg(tftm)(tftm) + CH_3 \rightarrow [Ni(acac)(tftm)]^+ + Mg(tftm) \qquad \text{(Eqn 5.8)}$$

The novel equations presented herein have provided much insight into the mechanism of ligand exchange between $Mg(tftm)_2$ and $Ni(acac)_2$. Although additional work is necessary, these equations have helped establish a foundation for others to expand upon.

Mass-selected $[Mg(tftm\text{-}tBu)(tftm)]^+$ at *m/z* 357 when reacted with neutral $Ni(acac)_2$ was observed to initiate the formation of the mixed ligand exchange fragment $[Ni(tftm\text{-}tBu)(acac)]^+$ at *m/z* 295. Mass-selected $[Mg(tftm\text{-}CF_2)]^+$ at *m/z* 169 was found to yield the mixed ligand exchange product $[Ni(acac)(tftm)]^+$ at *m/z* 352, as well as the complete ligand exchange fragment $[Ni(tftm\text{-}CF_3)(tftm)]^+$ at *m/z* 379 reacting with neutral $Ni(acac)_2$. No ligand exchange products were generated from mass-selected $[Mg(tftm)_2]^+$ at *m/z* 414 reacting with neutral $Ni(acac)_2$.

Mass-selected nickel species when reacted with neutral $Mg(tftm)_2$ also generated several ligand exchange products, the first of which was mass-selected $[Ni(acac)_2]^+$ at *m/z* 261, which produced $[Mg(acac)_2]^+$ at *m/z* 222. Mass-selected $[Ni(acac\text{-}CH_3)(acac)]^+$ at *m/z* 241 was observed to generate two ligand exchange products when reacting with neutral $Mg(tftm)_2$, $[Ni(acac\text{-}CH_3)(tftm)]^+$ at *m/z* 337 and $[Ni(tftm)]^+$ at *m/z* 253 while mass-selected $[Ni(acac\text{-}CH_3)]^+$ at *m/z* 142 generated both $[Mg(acac\text{-}CH_3)(tftm)]^+$ at *m/z* 303 and $[Ni(acac)(tftm)]^+$ at *m/z* 352. No ligand exchange products were generated from mass-selected $[Ni(acac)]^+$ at *m/z* 157 reacting with neutral $Mg(tftm)_2$.

5.5 The Co-Sublimation of $Mg(tftm)_2$ and Nickel Bis-Diethylacetylacetonate ($Ni(eeac)_2$)

Presented in Figure 5.11(a)-(c) are the positive EI mass spectra of $Mg(tftm)_2$ and $Ni(eeac)_2$, and their co-sublimation mass spectrum, stacked vertically for ease of clarity and comparison. The mass spectrum of $Mg(tftm)_2$ is reproduced from Figure 5.1 and will not be further discussed. The positive EI mass spectrum of $Ni(eeac)_2$ is displayed in Figure 5.11(b), where intact $[Ni(eeac)_2]^+$ is present at *m/z* 312 and the loss of an ethyl group to form $[Ni(eeac\text{-}Et)(eeac)]^+$ is observed at *m/z* 283. The single ligand species $[Ni(eeac)]^+$ is observed at *m/z* 185, and loss of an ethyl group to form $[Ni(eeac\text{-}Et)]^+$ is displayed at *m/z* 156.

The resulting co-sublimation spectrum of $Mg(tftm)_2$ and $Ni(eeac)_2$ is displayed in Figure 5.11(c). The spectrum is largely dominated by nickel ligand exchange products, but a few magnesium ligand products are displayed as well. The complete ligand exchange product, $[Ni(tftm)_2]^+$, is displayed at *m/z* 448, and loss of a *tBu* group to form

[Ni(tftm-*tBu*)(tftm)]$^+$ is displayed at *m/*z 391. The peak at *m/z* 380 corresponds to the mixed ligand product [Ni(eeac)(tftm)]$^+$, with the subsequent loss of a *tBu* group to form [Ni(eeac)(tftm-*tBu*)]$^+$ is displayed at *m/z* 323. A few magnesium ligand exchange products were also generated. The peak at *m/z* 346 represents the magnesium mixed ligand exchange product [Mg(eeac)(tftm)]$^+$, with loss of a *tBu* group to form [Mg(eeac)(tftm-*tBu*)]$^+$ at *m/z* 289.

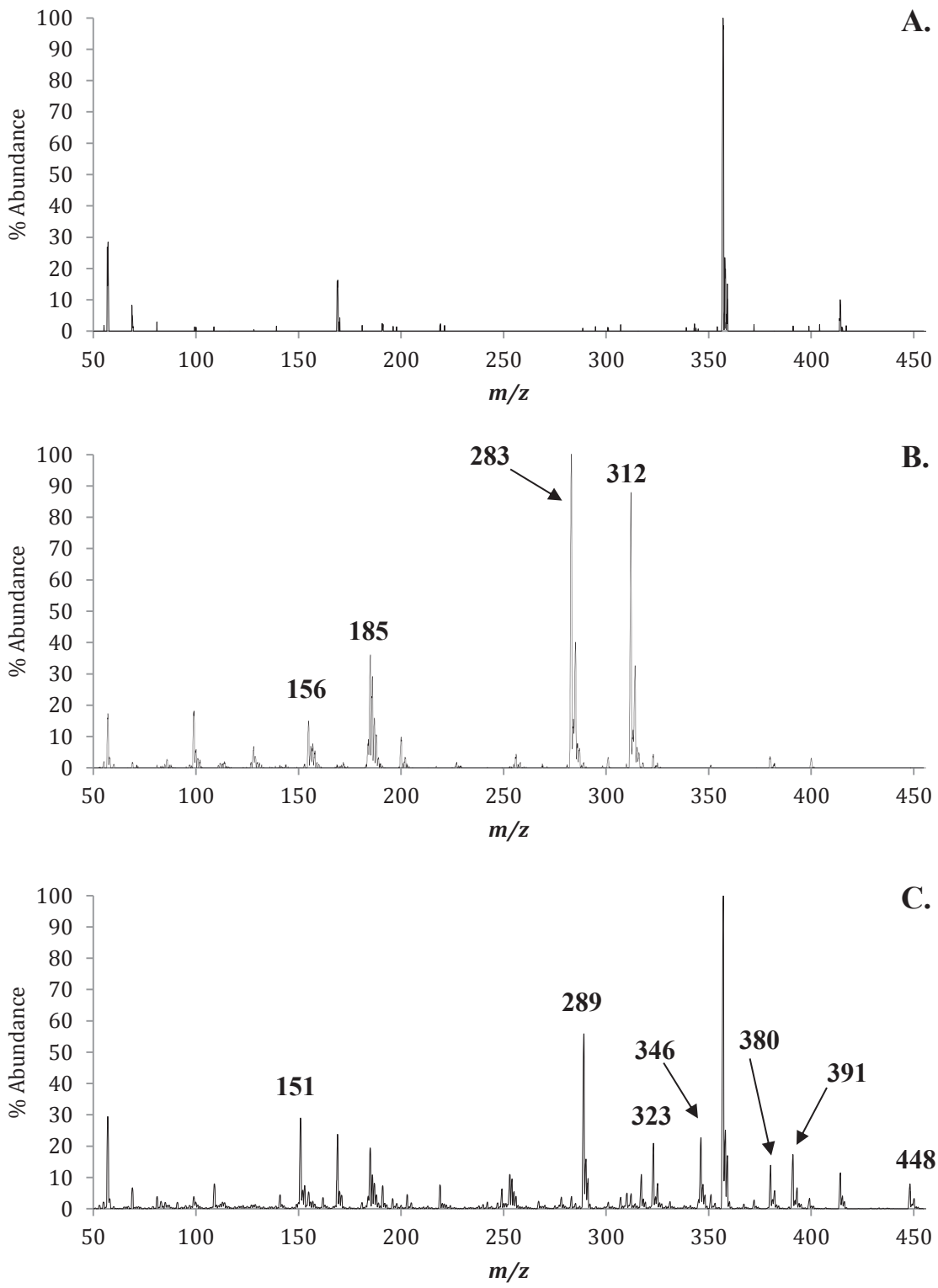

Figure 5.11(a)-(c): The positive EI mass spectra of (a) $Mg(tftm)_2$, (b) $Ni(eeac)_2$, and (c) the gas-phase co-sublimation of $Mg(tftm)_2$ and $Ni(eeac)_2$. The masses of parent compounds and fragments are labeled in (a) and (b). Masses of ligand exchange products and pertinent fragments are labeled in (c).

	Mass	Mass	MgL	NiL'	MgL_2 & NiL''_2	MgL & NiL''_2
Species	Mg	Ni	Mg	Ni	Mg	Ni
$[ML_2]^+$	414	448	10		12	8
$[ML_2\text{-}tBu]^+$	357	391	100		100	17
$[ML]^+$	219	253	2		7	11
$[ML\text{-}CF_2]^+$	169	203	16		24	5
$[ML''_2]^+$	278	312		88	4	5
$[ML''_2\text{-}C_2H_5]^+$	249	283		100	6	4
$[ML'']^+$	151	185		36	29	19
$[ML''\text{-}C_2H_5]^+$	122	156		7	<1	2
$[MLL'']^+$	346	380			23	14
$[M(L\text{-}tBu)L'']^+$	289	323			56	20
$[M(L\text{-}CF_3)L'']^+$	277	311			1	1
$[M(L\text{-}CF_2)L'']^+$	296	330			<1	<1

Table 5.3: The relative mass spectrometric abundances of the $Mg(tftm)_2$ and $Ni(eeac)_2$ β-diketonate complexes as well as the co-sublimation experiment, as presented in Figure 5.11(a)-(c). L = (tftm); L'' = (eeac).

5.6 The Selective Reactions of $Mg(tftm)_2$ and $Ni(eeac)_2$

The first ligand exchange product of interest generated following CIR analysis was $[Ni(tftm\text{-}tBu)(tftm)]^+$ at *m/z* 391, which was generated from mass-selected $[Mg(tftm\text{-}tBu)(tftm)]^+$ at *m/z* 357 reacting with neutral $Ni(eeac)_2$. The spectrum displaying this exchange is presented in Figure 5.12.

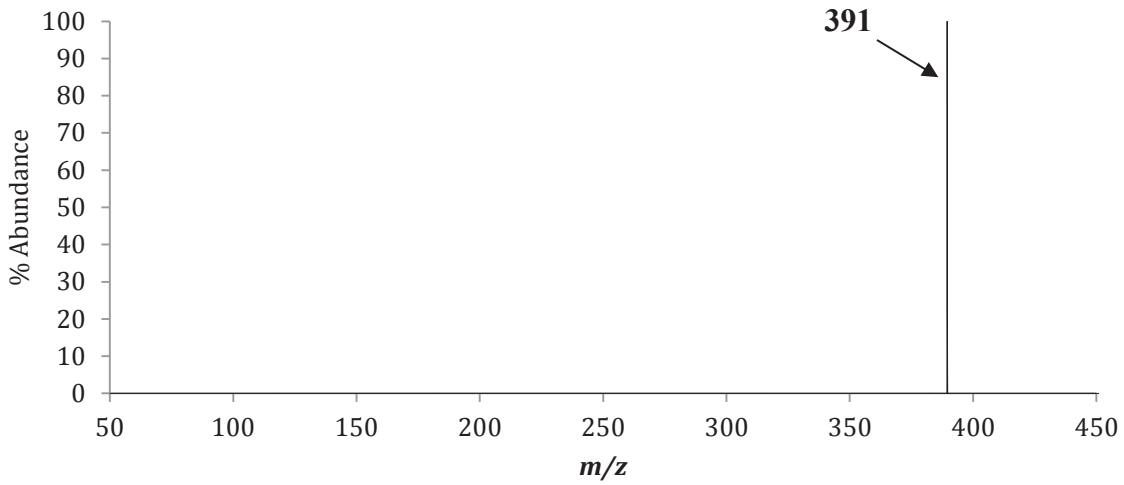

Figure 5.12: The positive mass spectrum obtained by scanning the third quadrupole following the selective reaction of *m/z* = 357 ($[Mg(tftm\text{-}CF_3)(tftm)]^+$) with neutral $Ni(acac)_2$ to produce the complete ligand exchange fragment $[Ni(tftm\text{-}tBu)(tftm)]^+$ at *m/z* 391.

The proposed mechanism for the gas-phase formation of the nickel complete ligand exchange fragment $[Ni(tftm\text{-}tBu)(tftm)]^+$ is presented in Equation 5.9.

$$[Mg(tftm\text{-}tBu)(tftm)]^+ + Ni(eeac)(eeac) \rightarrow [Ni(tftm\text{-}tBu)(tftm)]^+ + Mg(eeac)(eeac) \qquad \text{(Eqn 5.9)}$$

Another ligand exchange product of interest was $[Ni(tftm\text{-}CF_2)(eeac)]^+$ at *m/z* 330, which was generated from mass-selected $[Mg(tftm\text{-}CF_2)]^+$ at *m/z* 169 reacting with neutral $Ni(eeac)_2$. The spectrum displaying the formation of $[Ni(tftm\text{-}CF_2)(eeac)]^+$ is displayed in Figure 5.13.

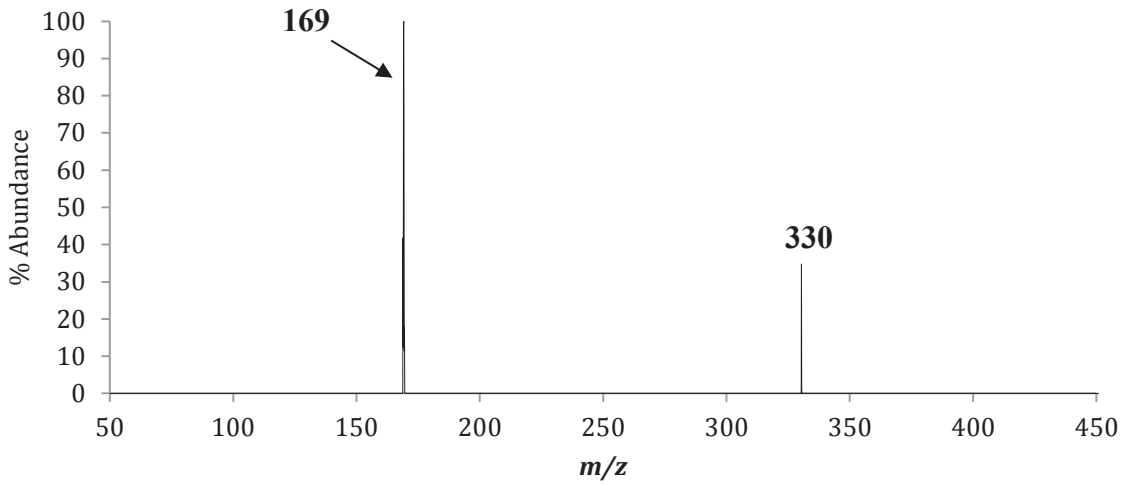

Figure 5.13: The positive mass spectrum obtained by scanning the third quadrupole following the selective reaction of *m/z* = 169 ($[Mg(tftm\text{-}CF_2)]^+$) with neutral $Ni(acac)_2$ to produce the complete ligand exchange fragment $[Ni(tftm\text{-}CF_2)(eeac)]^+$ at *m/z* 330.

The proposed mechanism for the gas-phase formation of the nickel mixed ligand exchange fragment $[Ni(tftm\text{-}CF_2)(eeac)]^+$ is presented in Equation 5.10.

$$[Mg(tftm\text{-}CF_2)]^+ + Ni(eeac)(eeac) \rightarrow [Ni(tftm\text{-}CF_2)(eeac)]^+ + Mg(eeac) \qquad \text{(Eqn 5.10)}$$

Mass-selected $[Mg(tftm\text{-}CF_2)]^+$ at *m/z* 169 when reacting with neutral $Ni(eeac)_2$ was observed to form $[Ni(tftm\text{-}CF_3)(eeac)]^+$ at *m/z* 311, which is displayed in Figure 5.14.

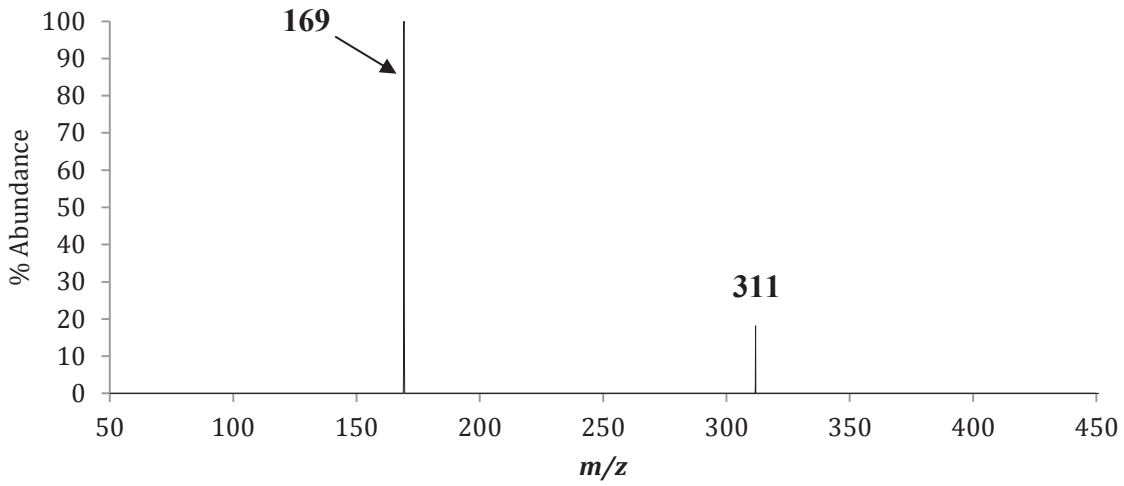

Figure 5.14: The positive mass spectrum obtained by scanning the third quadrupole following the selective reaction of *m/z* = 169 ($[Mg(tftm\text{-}CF_2)]^+$) with neutral $Ni(acac)_2$ to produce the complete ligand exchange fragment $[Ni(tftm\text{-}CF_3)(eeac)]^+$ at *m/z* 311.

The proposed mechanism for the gas-phase formation of the nickel mixed ligand exchange fragment $[Ni(eeac)(tftm\text{-}CF_3)]^+$ is presented in Equation 5.11.

$$[Mg(tftm\text{-}CF_2)]^+ + Ni(eeac)(eeac) + CF_2 \rightarrow [Ni(eeac)(tftm\text{-}CF_3]^+ + Mg(eeac) + CF_3 \quad \text{(Eqn 5.11)}$$

Mass-selected nickel compounds was also observed to produce ligand exchange products of interest. $[Ni(eeac\text{-}Et)(eeac\text{-}Et)]^+$ at *m/z* 254, when reacted with $Mg(tftm)_2$, was found to produce the mixed ligand exchange product $[Mg(eeac)(tftm)]^+$ at *m/z* 346, which is displayed in Figure 5.15.

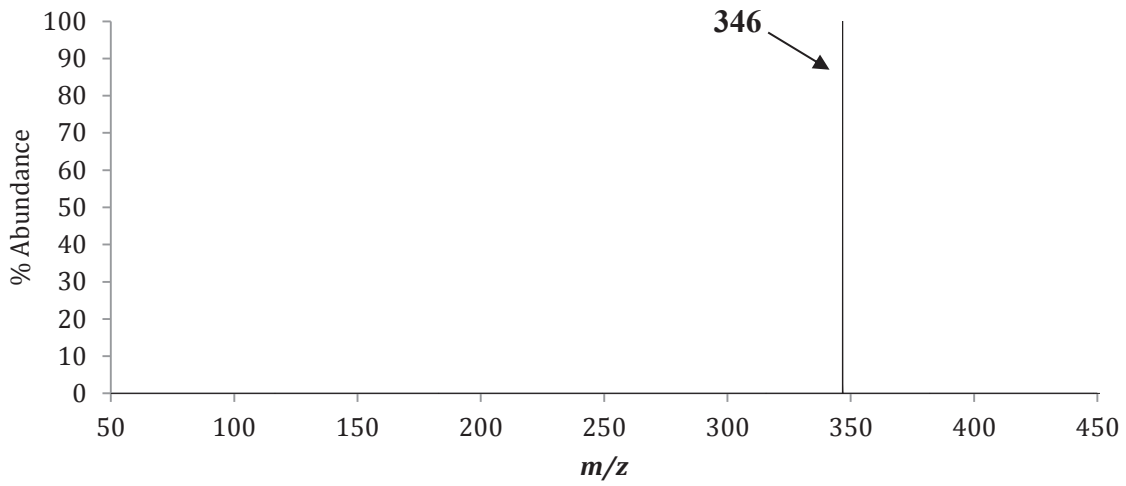

Figure 5.15: The positive mass spectrum obtained by scanning the third quadrupole following the selective reaction of *m/z* = 254 ([Ni(eeac-*Et*)(eeac-*Et*)]$^+$) with neutral $Mg(tftm)_2$ to produce the mixed ligand exchange product $[Mg(eeac)(tftm)]^+$ at *m/z* 346.

The proposed mechanism for the gas-phase formation of the magnesium mixed ligand exchange product $[Mg(eeac)(tftm)]^+$ is presented in Equation 5.12.

$$[Ni(eeac\text{-}Et)(eeac\text{-}Et)]^+ + Mg(tftm)(tftm) + Et \rightarrow [Mg(eeac)(tftm)]^+ + Ni(eeac\text{-}Et)(tftm) \qquad \text{(Eqn 5.12)}$$

The final ligand exchange product that was produced during CIR was the mixed ligand exchange fragment $[Mg(eeac\text{-}Et)(tftm)]^+$ at *m/z* 317. It was produced during the reaction of mass-selected $[Ni(eeac\text{-}Et)]^+$ at *m/z* 128 and the spectrum depicting the exchange is presented in Figure 5.16.

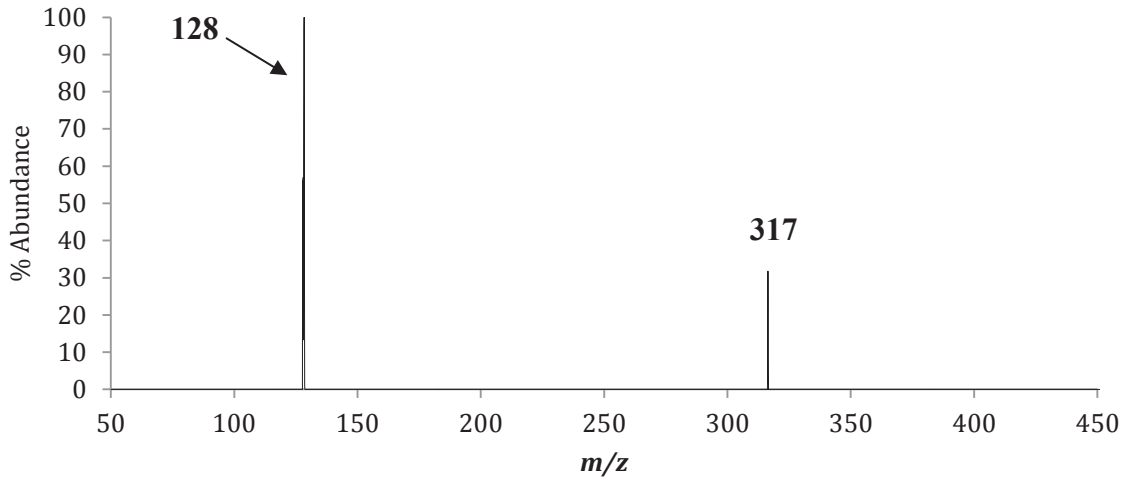

Figure 5.16: The positive mass spectrum obtained by scanning the third quadrupole following the selective reaction of *m/z* = 128 ($[Ni(eeac\text{-}Et)]^+$) with neutral $Mg(tftm)_2$ to produce the mixed ligand exchange product $[Mg(eeac\text{-}Et)(tftm)]^+$ at *m/z* 317.

The proposed mechanism for the gas-phase formation of the magnesium mixed ligand exchange fragment $[Mg(eeac\text{-}Et)(tftm)]^+$ is presented in Equation 5.13.

$$[Ni(eeac\text{-}Et)]^+ + Mg(tftm)(tftm) \rightarrow [Mg(eeac\text{-}Et)(tftm)]^+ + Ni(tftm) \qquad \text{(Eqn 5.13)}$$

The proposed mechanisms presented herein have provided much novel information on the mechanism of gas-phase ligand exchange between $Mg(tftm)_2$ and $Ni(eeac)_2$.

When reacting with neutral $Ni(eeac)_2$, mass-selected $[Mg(tftm\text{-}tBu)(tftm)]^+$ at *m/z* 357 was found to produce the complete ligand exchange fragment $[Ni(tftm\text{-}tBu)(tftm)]^+$ at *m/z* 391, whereas mass-selected $[Mg(tftm\text{-}CF_2)]^+$ at *m/z* 169 yielded $[Ni(tftm\text{-}CF_2)(eeac)]^+$ at *m/z* 330 and $[Ni(tftm\text{-}CF_3)(eeac)]^+$ at *m/z* 311. No ligand exchange products of interest were generated from mass-selected $[Mg(tftm)_2]^+$ at *m/z* 414 reacting with neutral $Ni(eeac)_2$.

Mass-selected nickel products also generated ligand exchange products of interest. Mass-selected $[Ni(eeac\text{-}Et)(eeac\text{-}Et)]^+$ at *m/z* 254 generated the mixed ligand exchange product $[Mg(eeac)(tftm)]^+$ at *m/z* 346 when reacted with neutral $Mg(tftm)_2$. Mass-selected $[Ni(eeac\text{-}Et)]^+$ at *m/z* 128 was observed to generate $[Mg(eeac\text{-}Et)(tftm)]^+$ at *m/z* 317. Interestingly, no ligand products of interest were generated from mass-selected $[Ni(eeac)_2]^+$ at *m/z* 312, $[Ni(eeac\text{-}Et)(eeac)]^+$ at *m/z* 283, or $[Ni(eeac)]^+$ at *m/z* 185 when reacting with neutral $Mg(tftm)_2$.

5.7 The Co-Sublimation of $Mg(tftm)_2$ and Nickel Bis-Dibenzoylmethane ($Ni(dbm)_2$)

Presented in Figures 5.17(a)-(c) are the positive EI mass spectra of $Mg(tftm)_2$, $Ni(dbm)_2$, and their co-sublimation. The spectra of $Mg(tftm)_2$ has been reproduced from Section 5.2 and will not be elaborated upon further. Figure 5.17(b) displays the baseline spectra of $Ni(dbm)_2$, which has also been reproduced from Figure 3.12(c) and will not be elaborated upon further. Figure 5.12(c) displays the positive EI co-sublimation mass spectra of $Mg(tftm)_2$ and $Ni(dbm)_2$, which produced exclusively magnesium ligand exchange products. The homoleptic ligand exchange product $[Mg(dbm)_2]^+$ is displayed at *m/z* 442, while the heteroleptic product $[Mg(dbm)(tftm)]^+$ is presented at *m/z* 447. Loss of a *tBu* functionality from $[Mg(dbm)(tftm)]^+$ to form $[Mg(dbm)(tftm\text{-}tBu)]^+$ is displayed at *m/z* 385, while the single ligand exchange product $[Mg(dbm)]^+$ is present at *m/z* 247. The novel peaks at *m/z* 442, *m/z* 385, and *m/*z 247 are clear indicators of ligand exchange. No nickel ligand exchange products were detected during co-sublimation experiments.

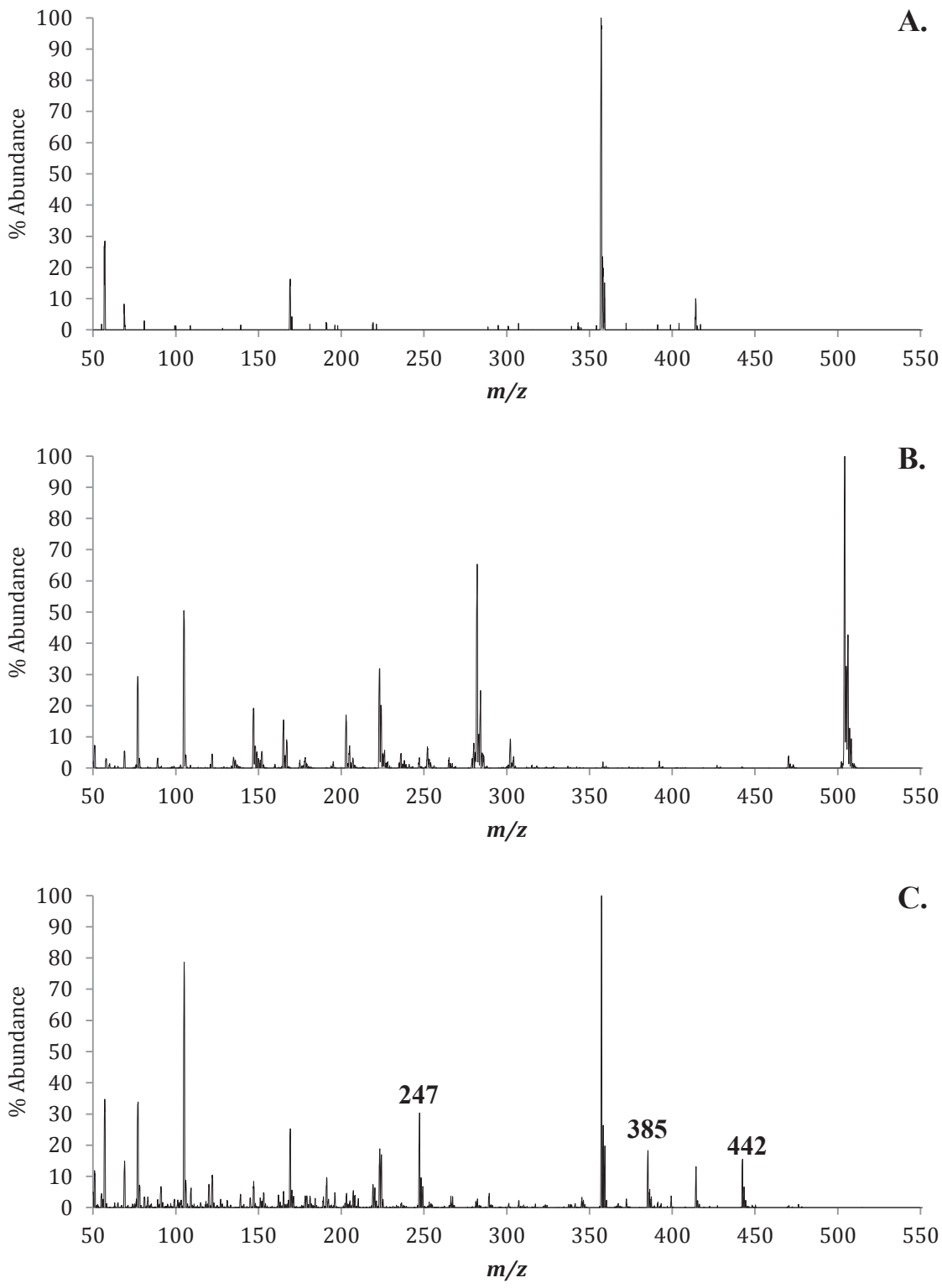

Figure 5.17: The positive EI mass spectra of (a) $Mg(tftm)_2$, (b) $Ni(dbm)_2$, and (c) the gas-phase co-sublimation of $Mg(tftm)_2$ and $Ni(dbm)_2$. The masses of parent compounds and fragments are labeled in (a) and (b). Masses of ligand exchange products and pertinent fragments are labeled in (c).

	Mass	Mass	MgL_2	NiL'''_2	MgL_2 & NiL'''_2	MgL & NiL'''_2
Species	Mg	Ni	Mg	Ni	Mg	Ni
$[ML_2]^+$	414	448	10		13	<1
$[ML_2\text{-}tBu]^+$	357	391	100		100	2
$[ML_2\text{-}CF_3]^+$	345	379	<1		2	<1
$[ML_2\text{-}CF_2]^+$	364	398	0		0	0
$[ML]^+$	219	253	2		7	1
$[ML\text{-}tBu]^+$	162	196	0		4	5
$[ML\text{-}CF_2]^+$	169	203	16		25	5
$[ML'''_2]^+$	470	504		100	<1	0
$[ML'''_2\text{-}Ph]^+$	393	427		<1	<1	<1
$[ML'''+tBu]^+$	304	339		-	0	<1
$[ML''']^+$	247	282		65	30	2
$[ML'''\text{-}Ph]^+$	170	204		7	6	<1
$[MLL''']^+$	442	476			15	1

Table 5.4: The relative mass spectrometric abundances of the $Mg(tftm)_2$ and $Ni(dbm)_2$ β-diketonate complexes as well as the co-sublimation experiment, as presented in Figure 5.17(a)-(c). L = (tftm); L''' = (dbm).

5.8 The Selective Reactions of $Mg(tftm)_2$ and $Ni(dbm)_2$

After co-sublimation confirmed that ligand exchange had indeed occurred between $Mg(tftm)_2$ and $Ni(dbm)_2$, CIR analysis was completed using the most abundant species from the baseline spectra. The ligand exchange products generated from these reactions and the proposed mechanisms for their exchange will be discussed in greater detail herein.

The first product that was generated was produced from mass-selected [Mg(tftm-CF_2)]$^+$ at *m/z* 169 reacting with neutral Ni(dbm)$_2$ to produce the single ligand exchange product, [Mg(dbm)]$^+$ at *m/z* 247, displayed in Figure 5.18.

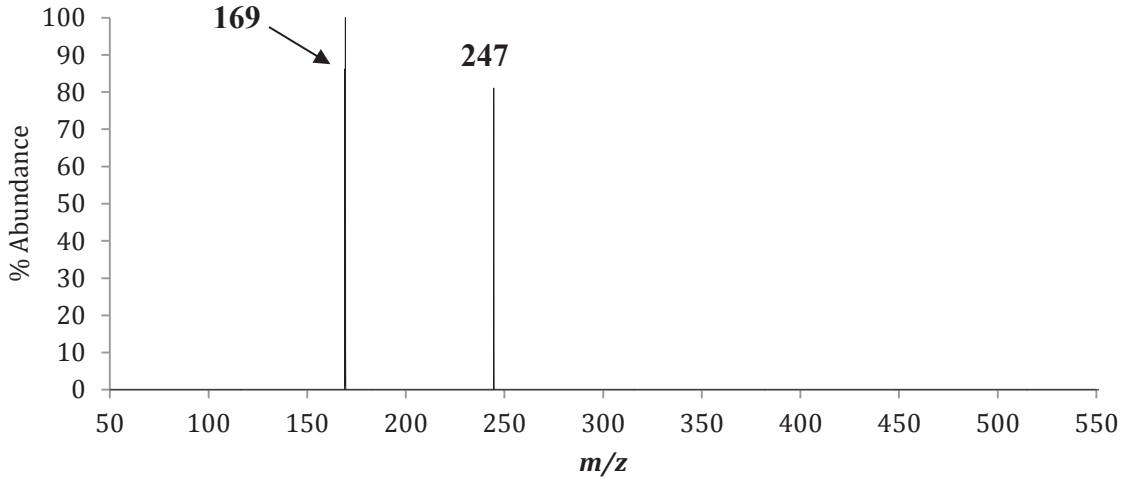

Figure 5.18: The positive mass spectrum obtained by scanning the third quadrupole following the selective reaction of *m/z* = 169 ([Mg (tftm-CF_2)]$^+$) with neutral Ni(dbm)$_2$ to produce the single ligand exchange product [Mg(dbm)]$^+$ at *m/z* 247.

The proposed mechanism for the gas-phase formation of the magnesium single ligand exchange product [Mg(dbm)]$^+$ is presented in Equation 5.14.

$$[Mg(tftm\text{-}CF_2)]^+ + Ni(dbm)(dbm) \rightarrow [Mg(dbm)]^+ + Ni(tftm\text{-}CF_2) + (dbm) \qquad \text{(Eqn 5.14)}$$

Mass-selected nickel species also generated ligand exchange products of interest. Mass-selected [Ni(dbm)]$^+$ at *m/z* 282 generated the magnesium ligand exchange fragment [Mg(dbm)+*tBu*]$^+$ at *m/z* 305, which is displayed in Figure 5.19.

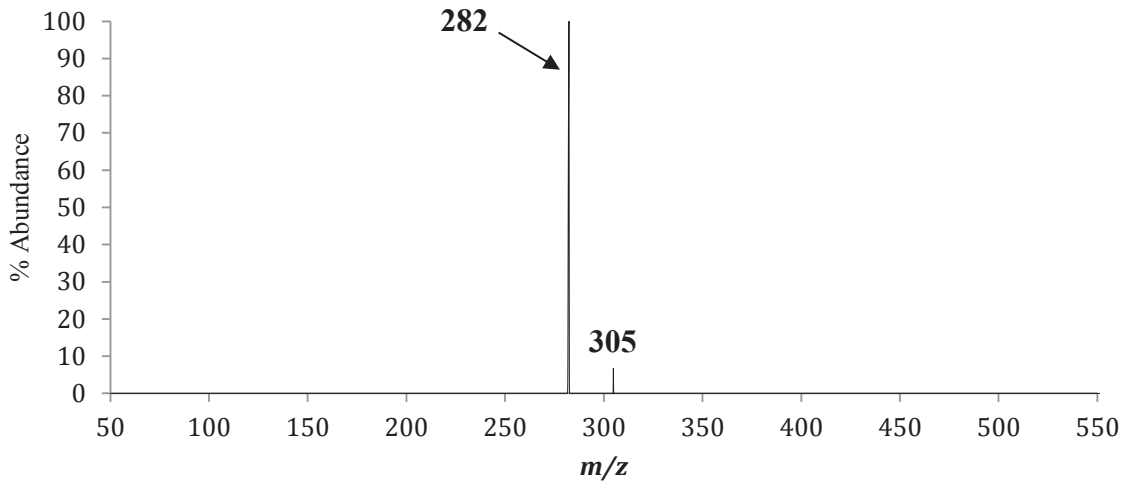

Figure 5.19: The positive mass spectrum obtained by scanning the third quadrupole following the selective reaction of *m/z* = 282 ($[Ni(dbm)]^+$) with neutral $Mg(tftm)_2$ to produce the single ligand exchange species $[Mg(dbm)+tBu]^+$ at *m/z* 305.

The proposed mechanism for the gas-phase formation of the magnesium single ligand exchange species $[Mg(dbm)+tBu]^+$ is presented in Equation 5.15.

$$[Ni(dbm)]^+ + Mg(tftm)(tftm) + tBu \rightarrow [Mg(dbm)+tBu]^+ + Ni(tftm)(tftm) \qquad \text{(Eqn 5.15)}$$

The final ligand exchange product that was generated by collision-induced reaction was also generated from mass-selected $[Ni(dbm)]^+$ at *m/z* 282. The product, $[Ni(tftm\text{-}CF_3)(tftm)]^+$ at *m/z* 379 is presented in Figure 5.20.

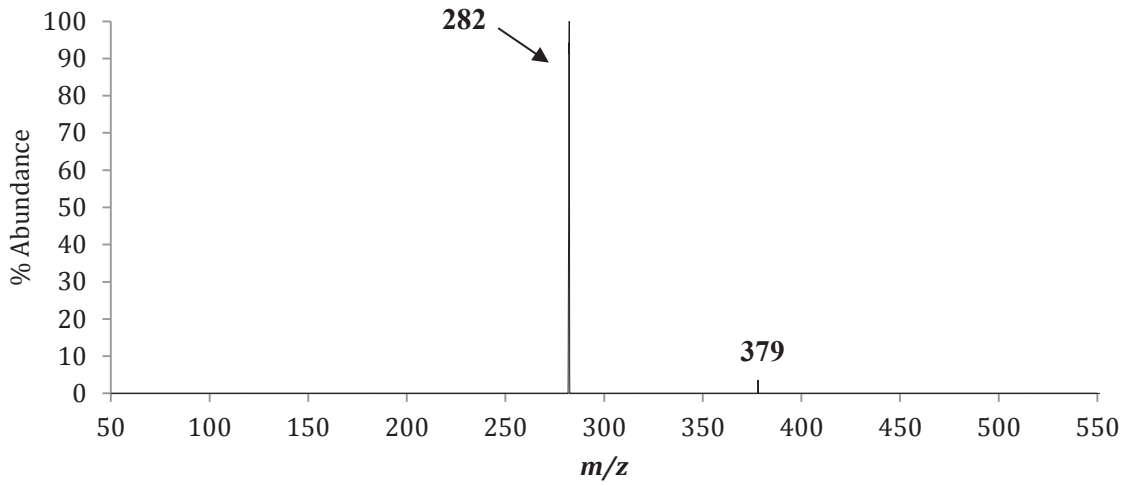

Figure 5.20: The positive mass spectrum obtained by scanning the third quadrupole following the selective reaction of *m/z* = 282 ($[Ni(dbm)]^+$) with neutral $Mg(tftm)_2$ to produce the complete ligand exchange fragment $[Ni(tftm\text{-}CF_3)(tftm)]^+$ at *m/z* 379.

The proposed mechanism for the gas-phase formation of the nickel complete ligand exchange fragment $[Ni(tftm\text{-}CF_3)(tftm)]^+$ is displayed in Equation 5.16.

$$[Ni(dbm)]^+ + Mg(tftm)(tftm) \rightarrow [Ni(tftm\text{-}CF_3)(tftm)]^+ + Mg(dbm) + CF_3 \qquad \text{(Eqn 5.16)}$$

After careful examination of the collision-induced reaction spectra, three mechanisms were proposed to help explain how ligand exchange occurs between $Mg(tftm)_2$ and $Ni(dbm)_2$. Although much work is still left to be done, these mechanisms do shed new light onto the process of ligand exchange between $Mg(tftm)_2$ and $Ni(dbm)_2$.

Mass-selected $[Mg(tftm\text{-}CF_2)]^+$ at *m/z* 169 when reacted with neutral $Ni(dbm)_2$ was found to generate the single magnesium ligand exchange product $[Mg(dbm)]^+$ at *m/z* 247. No ligand exchange products were generated from reactions involving mass-selected $[Mg(tftm)_2]^+$ at *m/z* 414 or $[Mg(tftm\text{-}tBu)(tftm)]^+$ at *m/z* 357.

The key contributor to the formation of both magnesium and nickel ligand exchange products appears to be $[Ni(dbm)]^+$ at *m/z* 282, which generated

$[Mg(dbm)+tBu]^+$ at *m/*z 304 and $[Ni(tftm\text{-}CF_3)(tftm)]^+$ at *m/z* 379 when reacting with neutral $Mg(tftm)_2$. No ligand exchange products were generated from mass-selected $[Ni(dbm)_2]^+$ at *m/z* 504 reacting with neutral $Mg(tftm)_2$.

Chapter 6

The Co-Sublimation and Gas-Phase Ligand Exchange Reactions of Magnesium Bis-Trifluorotrimethylacetylacetonate ($Mg(tftm)_2$) with Copper Bis-Acetylacetonate ($Cu(acac)_2$), Copper Bis-Diethylacetylacetonate ($Cu(eeac)_2$), and Copper Bis-Dibenzoylmethane ($Cu(dbm)_2$)

6.1 Introduction

Presented within this Chapter is novel information regarding the gas-phase ligand exchange of $Mg(tftm)_2$ with copper β-diketonate complexes. To expand upon the examinations of $Mg(tftm)_2$ with nickel β-diketonates, $Mg(tftm)_2$ was subject to co-sublimation and collision-induced reaction analysis with copper bis-acetylacetonate ($Cu(acac)_2$), copper bis-diethylacetylacetonate ($Cu(eeac)_2$), and copper bis-dibenzoylmethane ($Cu(dbm)_2$). Naturally occurring isotopic distributions of each metal are an integral part of the discussion of potential ligand exchange products. A list of the naturally occurring isotopic distributions of magnesium and copper is provided in Section 4.1. Distinct isotopic patterns aid in the identification of ligand exchange products of interest, particularly in cases in which products are isobaric, or possessing the same *m/z* ratio.

Collision-induced reaction (CIR) of mass-selected ions and fragments was used to supplement co-sublimation analysis through the use of a triple quadrupole mass spectrometer. Previous examinations into gas-phase ligand exchange has identified that not all ions and ion fragments contribute equally to ligand exchange processes, thus exhibiting a precursor-product relationship. The research presented within this Chapter further substantiates this notion. Oftentimes, one mass-selected ion will promote

formation of several different ligand exchange products, whereas another mass-selected ion will not generate any products at all. Targeting specific species, and identifying which products are produced from that species, provides a basis for a mechanistic explanation of ligand exchange. Thus, while co-sublimation reactions prove that ligand exchange does in fact occur, the collision-induced reaction analysis examines how these reactions may proceed. The experimental conditions utilized herein closely match those described earlier, and provide new information into the gas phase ligand exchange between $Mg(tftm)_2$ and several copper β-diketonates.

6.2 Magnesium Bis-Trifluorotrimethylacetylacetonate ($Mg(tftm)_2$)

For information regarding the positive EI mass spectrum of $Mg(tftm)_2$ and its corresponding fragmentation behavior, please refer Figure 5.1. A positive mass spectrum of $Mg(tftm)_2$ will be reproduced for all co-sublimation discussions in this Chapter for purposes of clarity and comparison.

6.3 The Co-Sublimation of $Mg(tftm)_2$ and Copper Bis-Acetylacetonate ($Cu(acac)_2$)

The positive EI mass spectra presented in Figure 6.1(a)-(c) display the positive EI mass spectra of $Mg(tftm)_2$, $Cu(acac)_2$, and the results following co-sublimation. Each spectrum is stacked vertically, and peaks of interest are labeled for purposes of clarity and comparison. Figure 6.1(a), the baseline mass spectrum of $Mg(tftm)_2$ is reproduced from Figure 5.1 and will not be discussed in further detail. Likewise, the spectrum of $Cu(acac)_2$ is reproduced from Figure 4.1(a) and will also not be discussed further.

The co-sublimation spectrum of $Mg(tftm)_2$ and $Cu(acac)_2$ is presented in Figure 6.1(c). The incidence of novel peaks is a clear indicator that ligand exchange did, in fact,

occur. Complete ligand exchange was observed for both magnesium and copper, albeit in low abundance. The peak at *m/z* 453 demonstrates the formation of $[Cu(tftm)_2]^+$, and loss of a first, and then a second, *tBu* group to form $[Cu(tftm\text{-}tBu)(tftm)]^+$ and $[Cu(tftm\text{-}tBu)(tftm)]^+$ at *m/z* 396 and *m/z* 339, respectively. The magnesium complete ligand exchange product $[Mg(acac)_2]^+$ is displayed at *m/z* 222 with subsequent loss of a methyl group to form $[Mg(acac\text{-}CH_3)(acac)]^+$ at *m/z* 207. The partial ligand exchange product $[Mg(acac)]^+$ is also present at *m/z* 123.

The mixed ligand product $[Mg(acac)(tftm)]^+$ is observed at *m/z* 318, as is the loss of a *tBu* group to form $[Mg(acac)(tftm\text{-}tBu)]^+$ at *m/z* 261. This peak possesses the same *m/z* ratio, or is isobaric with, $[Cu(acac)_2]^+$. The formation of isobaric peaks necessitates analysis of the isotopic abundances of the metal present in the product. The isotopic abundances of these metals correlates with the relative heights of the peaks on a mass spectum, which can help identify the product.

Upon examining the co-sublimation spectra in Figure 6.1(c), the peak at *m/z* 261 lacks the distinct shoulder that identifies copper compounds, thus it is likely the mixed ligand exchange fragment $[Mg(acac)(tftm\text{-}tBu)]^+$. A similar problem is encountered when observing the copper mixed ligand exchange product $[Cu(acac)(tftm)]^+$ at *m/z* 357, which is by far the most abundant ion in the $Mg(tftm)_2$ mass spectrum. However, while *m/z* 300 is consistent with the loss of a *tBu* from $[Cu(acac)(tftm)]^+$ to form $[Cu(acac)(tftm\text{-}tBu)]^+$, the spectrum does not adequately reflect the predicted isotopic abundances of copper. The peak at *m/z* 357 does not display the characteristic shoulder of copper compounds, indicating there is likely overlap of $[Mg(tftm\text{-}tBu)(tftm)]^+$ and $[Cu(acac)(tftm)]^+$ at this particular *m/z* region.

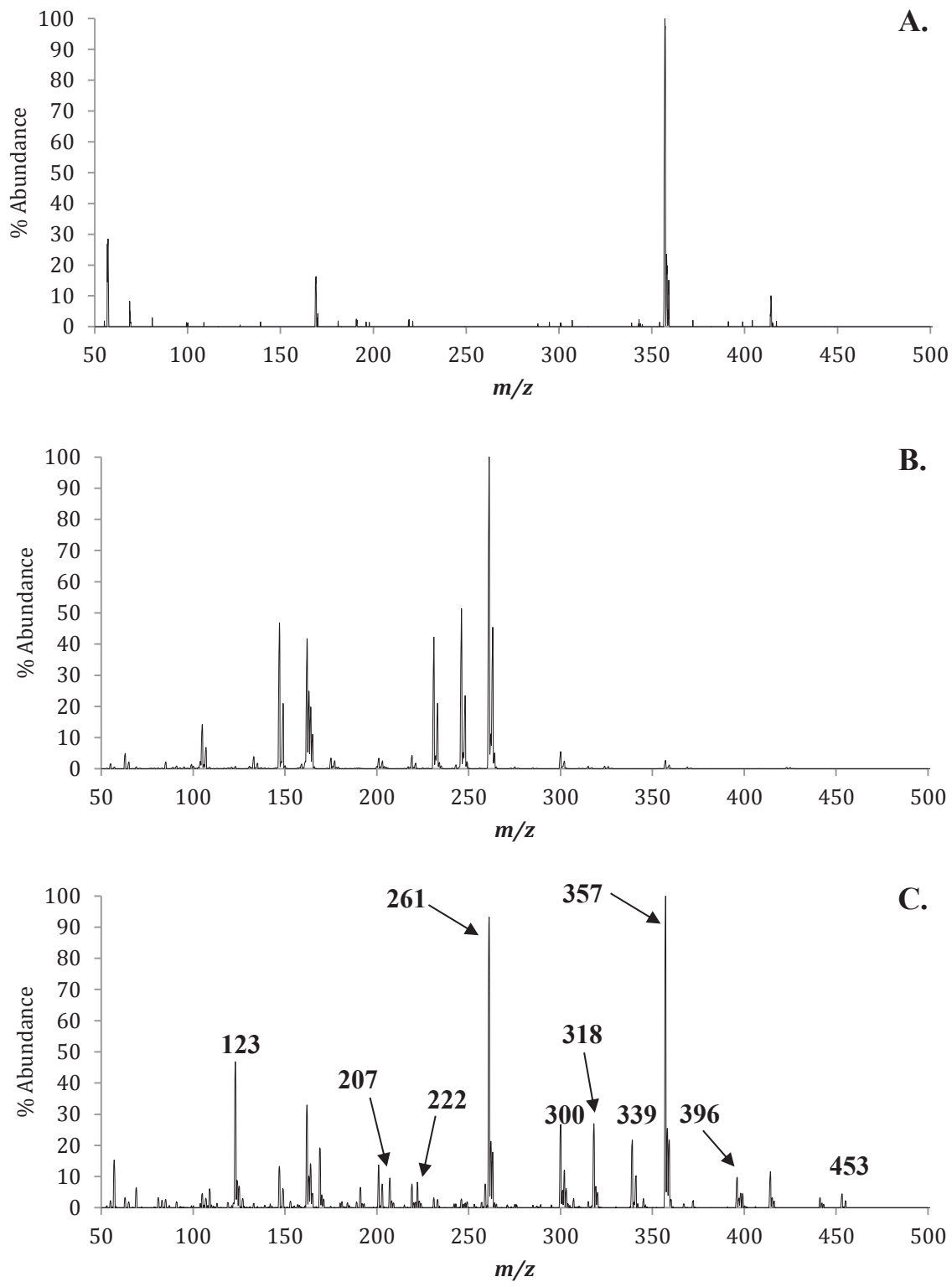

Figure 6.1: The positive EI mass spectra of (a) $Mg(tftm)_2$, (b) $Cu(acac)_2$, and (c) the gas-phase co-sublimation of $Mg(tftm)_2$ and $Ni(acac)_2$. The masses of parent compounds and fragments are labeled in (a) and (b). Masses of ligand exchange products and pertinent fragments are labeled in (c).

	Mass	Mass	MgL_2	CuL'_2	MgL_2 & CuL'_2	MgL_2 & CuL'_2
Species	Mg	Cu	Mg	Cu	Mg	Cu
$[ML_2]^+$	414	453	10		12	4
$[ML_2\text{-}tBu]^+$	*357*	396	100		*100*	10
$[ML_2\text{-}CF_3]^+$	345	384	<1		3	0
$[ML]^+$	219	258	2		8	<1
$[ML\text{-}tBu]^+$	162	201	0		33	14
$[ML\text{-}CF_2]^+$	169	208	16		19	2
$[ML'_2]^+$	222	*261*		100	8	*93*
$[ML'_2\text{-}CH_3]^+$	207	246		51	10	3
$[ML'_2\text{-}2CH_3]^+$	192	231		42	1	3
$[ML']^+$	123	162		42	47	33
$[ML'\text{-}CH_3]^+$	108	147		47	<1	13
$[MLL']^+$	318	*357*			27	*100*
$[M(L\text{-}tBu)L']^+$	*261*	300			*93*	27
$[M(L\text{-}CF_3)L']^+$	249	288			<1	0

Table 6.1: The mass spectrometric relative abundances of $Mg(tftm)_2$ and $Cu(acac)_2$ metal β-diketonate complexes as well as their co-sublimation experiment, as presented in Figure 6.1. L = (tftm), L' = (acac).

6.4 The Selective Reactions of $Mg(tftm)_2$ and $Cu(acac)_2$

Since the peaks present in Figure 6.2(c) indicate that ligand exchange did indeed occur, mass-selected fragments from both compounds were subjected to CIR analysis. Similar protocols to those employed in Chapter 3, Chapter 4, and Chapter 5 were followed to obtain the spectra presented herein. The only ligand exchange products observed from mass-selected magnesium ions are displayed in Figure 6.2 and were generated from $[Mg(tftm\text{-}CF_2)]^+$ at *m/z* 169 reacting with neutral $Cu(acac)_2$ to form $[Mg(acac)(tftm\text{-}CF_3)]^+$ at *m/z* 249.

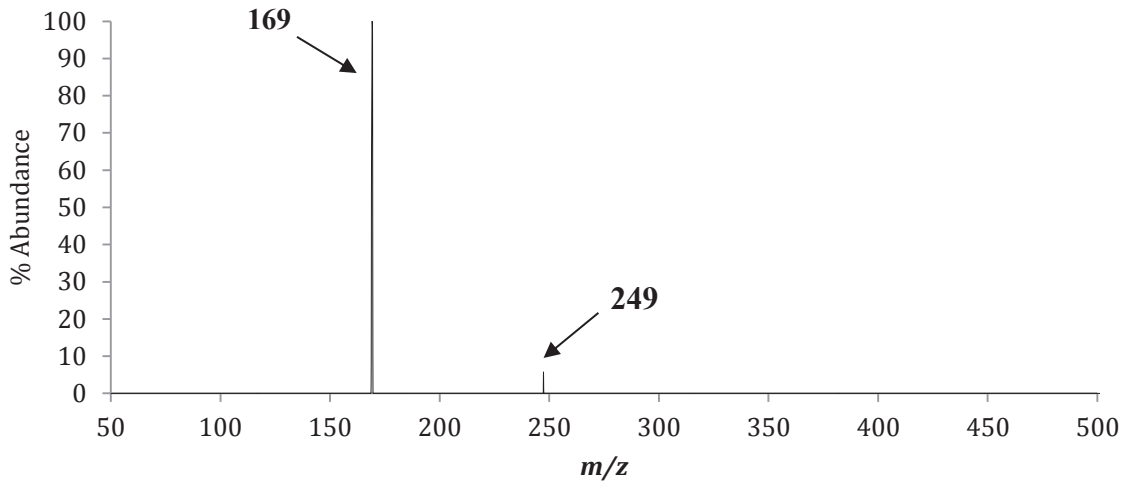

Figure 6.2: The positive mass spectrum obtained by scanning the third quadrupole following the selective reaction of *m/z* = 169 ($[Mg(tftm\text{-}CF_2)]^+$) with neutral $Cu(acac)_2$ to produce the mixed ligand exchange fragment $[Mg(acac)(tftm\text{-}CF_3)]^+$ at *m/z* 249.

The proposed mechanism for the gas-phase formation of the magnesium mixed ligand exchange fragment $[Mg(acac)(tftm\text{-}CF_3)]^+$ is displayed in Equation 6.1.

$$[Mg(tftm\text{-}CF_2)]^+ + Cu(acac)(acac) + CF_2 \rightarrow [Mg(acac)(tftm\text{-}CF_3)]^+ + Cu(acac) + CF_3 \quad \text{(Eqn 6.1)}$$

The second product generated from mass-selected $[Mg(tftm\text{-}CF_2)]^+$ at *m/z* 169 reacting with neutral $Cu(acac)_2$ is $[Cu(tftm)_2]^+$ at *m/z* 453, which is displayed in Figure 6.3.

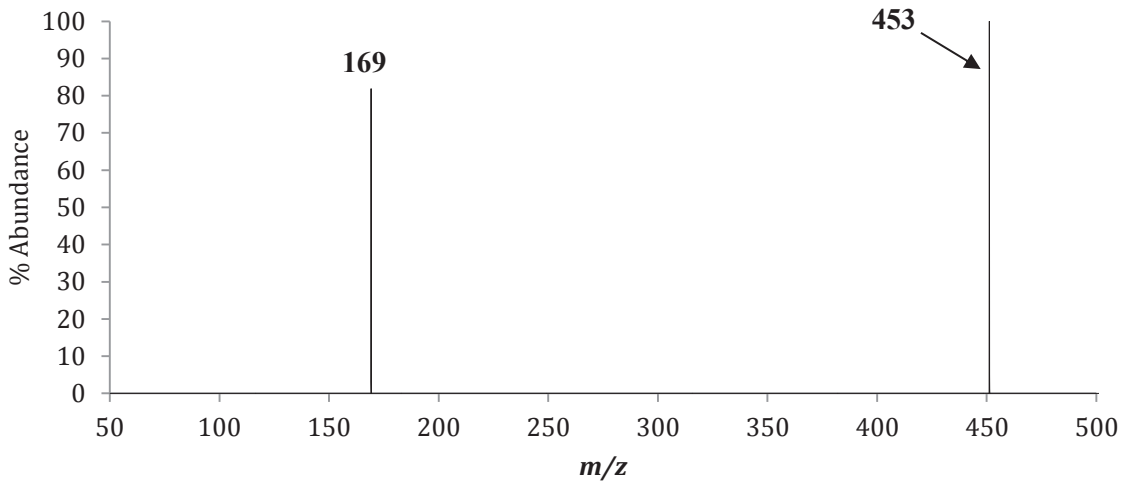

Figure 6.3: The positive mass spectrum obtained by scanning the third quadrupole following the selective reaction of *m/z* = 169 ($[Mg(tftm\text{-}CF_2)]^+$) with neutral $Cu(acac)_2$ to produce the complete exchange product $[Cu(tftm)_2]^+$ at *m/z* 453.

The proposed mechanism for the gas-phase formation of the copper complete ligand exchange product $[Cu(tftm)_2]^+$ is presented in Equation 6.2.

$$[Mg(tftm\text{-}CF_2)]^+ + Cu(acac)(acac) + CF_2 + (tftm) \rightarrow [Cu(tftm)(tftm)]^+ + Mg(acac)(acac) \qquad \text{(Eqn 6.2)}$$

The first ligand exchange product of interest generated from mass-selected $[Cu(acac)_2]^+$ at *m/z* 261 reacting with neutral $Mg(tftm)_2$ was $[Cu(tftm)_2]^+$ at *m/z* 453 and is displayed in Figure 6.4. There is also a much smaller peak at m/z 113, which does not correlate to a ligand exchange product and is not further considered.

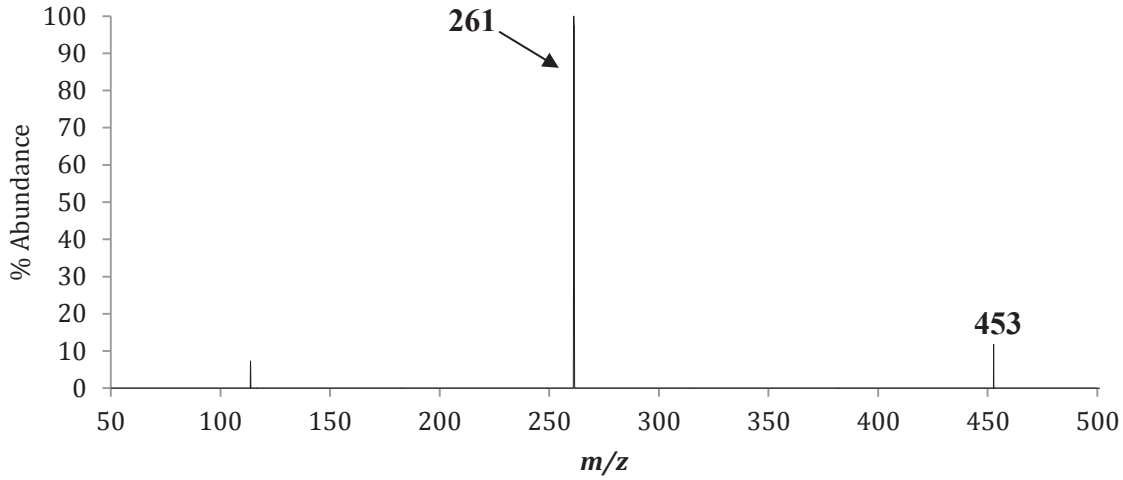

Figure 6.4: The positive mass spectrum obtained by scanning the third quadrupole following the selective reaction of *m/z* = 261 ($[Cu(acac)_2]^+$) with neutral $Mg(tftm)_2$ to produce the complete exchange product $[Cu(tftm)_2]$+ at *m/z* 453.

The proposed mechanism for the gas-phase formation of the copper complete ligand exchange product $[Cu(tftm)_2]^+$ is presented in Equation 6.3.

$$[Cu(acac)(acac)]^+ + Mg(tftm)(tftm) \rightarrow [Cu(tftm)(tftm)]^+ + Mg(acac)(acac) \qquad \text{(Eqn 6.3)}$$

Mass-selected $[Cu(acac)_2]^+$ at *m/z* 261 when reacted with neutral $Mg(tftm)_2$ also generated the mixed ligand exchange product $[Cu(acac)(tftm)]^+$ at *m/z* 357, which is displayed in Figure 6.5.

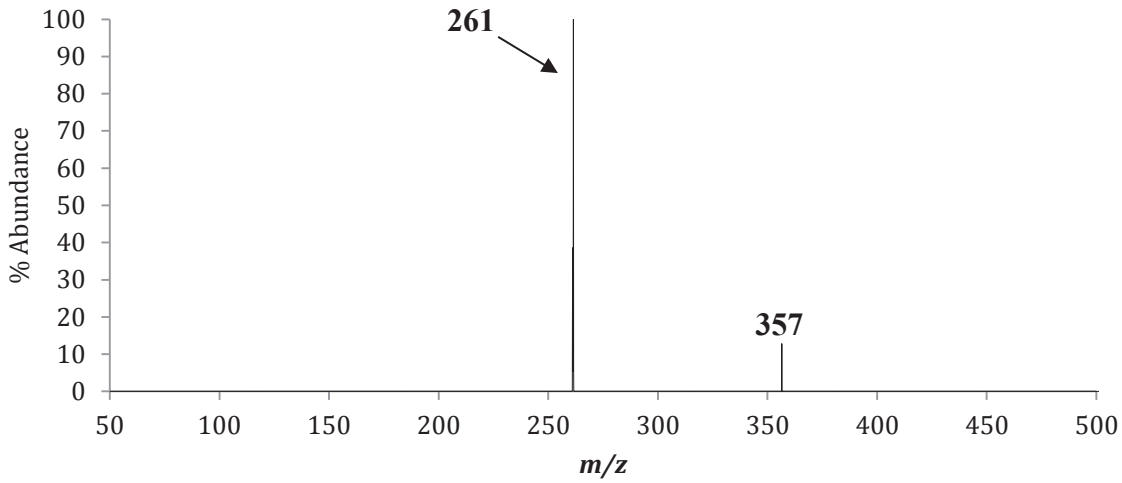

Figure 6.5: The positive mass spectrum obtained by scanning the third quadrupole following the selective reaction of *m/z* = 261 ($[Cu(acac)_2]^+$) with neutral $Mg(tftm)_2$ to produce the mixed ligand exchange product $[Cu(acac)(tftm)]^+$ at *m/z* 357.

The proposed mechanism for the gas-phase formation of the copper mixed ligand exchange product $[Cu(acac)(tftm)]^+$ is presented in Equation 6.4.

$$[Cu(acac)(acac)]^+ + Mg(tftm)(tftm) \rightarrow [Cu(acac)(tftm)]^+ + Mg(acac)(tftm) \qquad \text{(Eqn 6.4)}$$

The final ligand exchange product generated by a collision-induced reaction was also formed by the reaction of neutral $Mg(tftm)_2$ and mass-selected $[Cu(acac)_2]^+$ at *m/z* 261 was the complete ligand exchange fragment $[Cu(tftm\text{-}CF_2)(tftm)]^+$ at *m/z* 403. The spectrum depicting this exchange is presented in Figure 6.6.

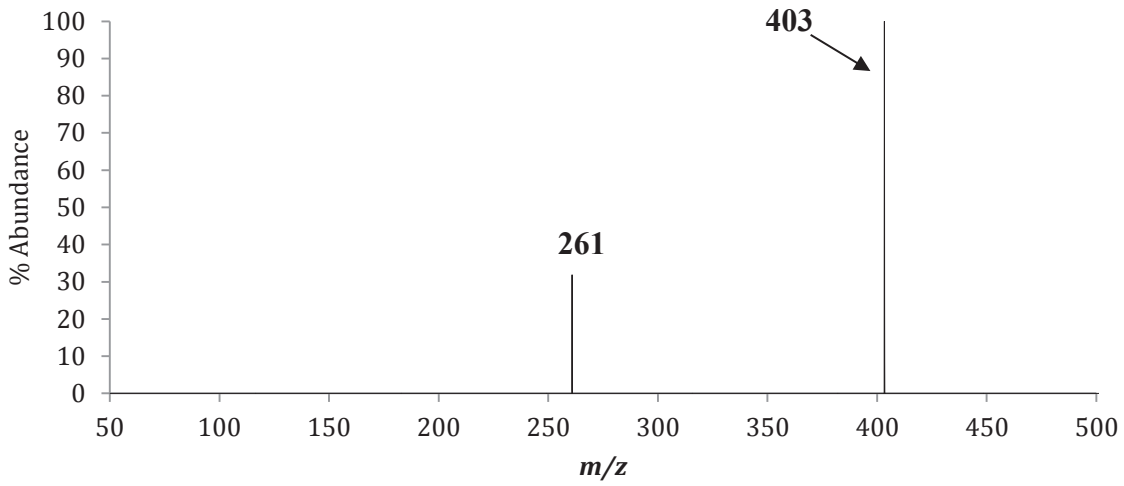

Figure 6.6: The positive mass spectrum obtained by scanning the third quadrupole following the selective reaction of *m/z* = 261 ($[Cu(acac)_2]^+$) with neutral $Mg(tftm)_2$ to produce the complete ligand exchange fragment $[Cu(tftm\text{-}CF_2)(tftm)]^+$ at *m/z* 403.

The proposed mechanism for the gas-phase formation of the copper complete ligand exchange fragment $[Cu(tftm\text{-}CF_2)(tftm)]^+$ is presented in Equation 6.5.

$$[Cu(acac)(acac)]^+ + Mg(tftm\text{-}CF_2)(tftm) \rightarrow [Cu(tftm\text{-}CF_2)(tftm)]^+ + Mg(acac)(acac) \quad \text{(Eqn 6.5)}$$

The spectra presented herein have provided much novel information about the mechanism of ligand exchange between $Mg(tftm)_2$ and $Cu(acac)_2$. Although additional work is necessary, the new information still provides insight into how ligand exchange occurs between these two compounds.

The key contributor to the formation of copper ligand exchange products appears to be mass-selected $[Cu(acac)_2]^+$ at *m/z* 261, which lead to the formation of $[Cu(tftm)_2]^+$ at *m/z* 453, $[Cu(acac)(tftm)]^+$ at *m/z* 357, and $[Cu(tftm\text{-}tBu)(tftm)]^+$ at *m/z* 403 when reacted with neutral $Mg(tftm)_2$. No ligand exchange products of interest were observed to form from $[Cu(acac\text{-}CH_3)(acac)]^+$ at *m/z* 246, $[Cu(acac\text{-}CH_3)(acac\text{-}CH_3)]^+$ at *m/z* 231,

$[Cu(acac)]^+$ at *m/z* 162, or $[Cu(acac\text{-}CH_3)]^+$ at *m/z* 147 when reacted with neutral $Mg(tftm)_2$.

The only ligand exchange products of interest generated from mass-selected magnesium species were $[Mg(acac)(tftm\text{-}CF_3)]^+$ at *m/z* 249 and $[Ni(tftm)_2]^+$ at *m/z* 453, both of which were isolated from mass-selected $[Mg(tftm\text{-}CF_2)]^+$ at *m/z* 169. No ligand exchange products were generated from mass-selected $[Mg(tftm)_2]^+$ at *m/z* 414 or $[Mg(tftm\text{-}tBu)(tftm)]^+$ at *m/z* 357 reacting with neutral $Ni(acac)_2$.

6.5 The Co-Sublimation of $Mg(tftm)_2$ and Copper Bis-Diethylacetylacetonate ($Cu(eeac)_2$)

The positive EI mass spectra presented in Figure 6.7(a)-(c) display the baseline spectra of $Mg(tftm)_2$ and $Cu(eeac)_2$, followed by the spectrum resulting from their co-sublimation in the gas phase. The spectra are all stacked vertically, which aids in clarity and ease of comparison. Although the original spectra were scanned from *m/z* 50 to 650, the spectra presented herein have a range of *m/z* 100 to 500 to better display isotopic abundances of the parent β-diketonates and ligand exchange products. Figure 6.7(a) is reproduced from Figure 5.1 and will not be elaborated upon further. Figure 6.7(b) displays the positive EI mass spectra of $Cu(eeac)_2$, where the peak at *m/z* 317 corresponds to intact $[Cu(eeac)_2]^+$, followed by loss of a first and then a second ethyl group to form $[Cu(eeac\text{-}Et)(eeac)]^+$ and $[Cu(eeac\text{-}Et)(eeac\text{-}Et)]^+$ at *m/z* 288 and *m/z* 259, respectively. The single ligand species $[Cu(eeac)]^+$ is present at *m/z* 190, as is the loss of one ethyl group at *m/z* 161.

Figure 6.7(c) displays the products formed from the co-sublimation of $Mg(tftm)_2$ and $Cu(eeac)_2$, and demonstrate the formation of partial, mixed, and complete ligand exchange products for both magnesium and copper. The peak at *m/z* 453 corresponds to the mass of $[Cu(tftm)_2]^+$, with loss of a *tBu* group to form $[Cu(tftm\text{-}tBu)(tftm)]^+$ at *m/z* 396. Loss of a second *tBu* group to form $[Cu(tftm\text{-}tBu)(tftm\text{-}tBu)]^+$ is depicted at *m/z* 339. The single ligand product $[Cu(tftm)]^+$ is displayed in low abundance at *m/z* 258, with the loss of a *tBu* to form $[Cu(tftm\text{-}tBu)]^+$ is displayed in much higher abundance at *m/z* 201. Also, loss of a trifluoromethyl group, CF_3 from $[Cu(tftm)]^+$ to form $[Cu(tftm\text{-}CF_3)]^+$ is present at *m/z* 190. The copper mixed ligand exchange product $[Cu(eeac)(tftm)]^+$ is displayed at *m/z* 385 with loss of a *tBu* group to form $[Cu(eeac)(tftm\text{-}tBu)]^+$ at *m/z* 328. Partial, mixed, and complete ligand exchange is also evident for magnesium β-diketonates. The complete ligand exchange product $[Mg(eeac)_2]^+$ is displayed at *m/z* 278, with the single ligand exchange product $[Mg(eeac)]^+$ displayed at *m/z* 151. All of these novel peaks correlate with the previously elucidated fragmentation pathways for copper and magnesium β-diketonates, yet provide compelling evidence that ligand exchange is occurring between these two previously unexamined compounds.

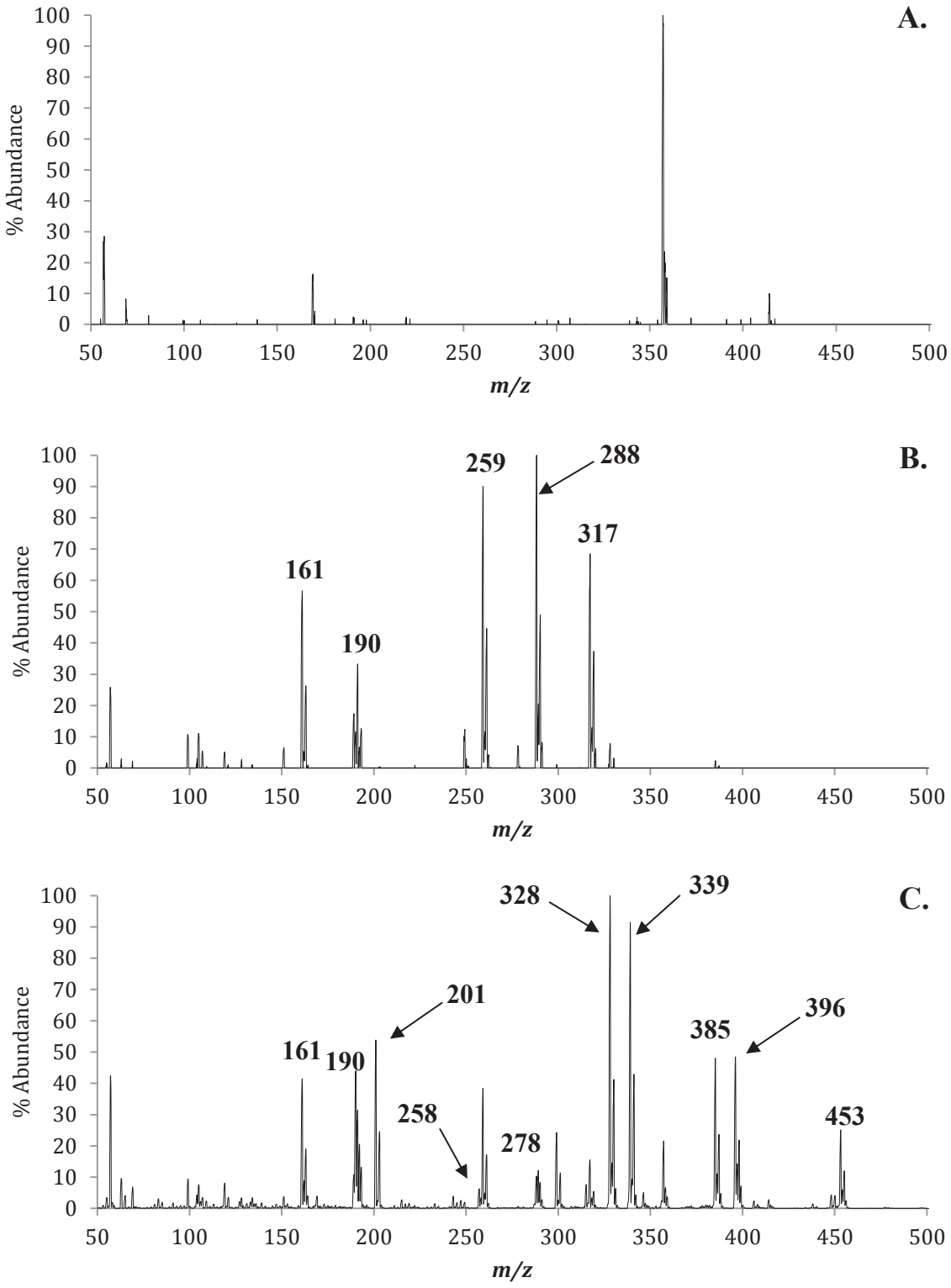

Figure 6.7: The positive EI mass spectra of (a) $Mg(tftm)_2$, (b) $Cu(eeac)_2$, and (c) the gas-phase co-sublimation of $Mg(tftm)_2$ and $Cu(eeac)_2$. The masses of parent compounds and fragments are labeled in (a) and (b). Masses of ligand exchange products and pertinent fragments are labeled in (c).

	Mass	Mass	MgL_2	CuL''_2	MgL_2 & CuL''_2	MgL_2 & CuL''_2
Species	Mg	Cu	Mg	Cu	Mg	Cu
$[ML_2]^+$	414	453	10		3	25
$[ML_2\text{-}tBu]^+$	357	396	100		21	48
$[ML_2\text{-}2tBu]^+$	300	339	1		2	91
$[ML_2\text{-}CF_3]^+$	345	384	<1		<1	1
$[ML_2\text{-}CF_2]^+$	364	403	0		0	<1
$[ML]^+$	219	258	2		1	3
$[ML\text{-}tBu]^+$	162	201	0		8	53
$[ML\text{-}CF_3]^+$	150	189	0		<1	10
$[ML\text{-}CF_2]^+$	169	208	16		4	<1
$[ML''_2]^+$	278	317		69	<1	15
$[ML''_2\text{-}Et]^+$	249	288		100	2	10
$[ML''_2\text{-}2Et\text{+}2H]^+$	222	-		-	<1	-
$[ML''_2\text{-}2Et]^+$	-	259		90	-	38
$[ML'']^+$	151	190		11	3	43
$[ML''\text{-}Et]^+$	122	161		57	<1	41
$[MLL'']^+$	346	385			5	48
$[M(L\text{-}tBu)L'']^+$	289	328			12	100
$[M(L\text{-}CF_3)L'']^+$	277	316			<1	2
$[ML(L''\text{-}Et)]^+$	317	356			15	2

Table 6.2: The relative mass spectrometric abundances of the $Mg(tftm)_2$ and $Cu(eeac)_2$ β-diketonate complexes as well as the co-sublimation experiment, as presented in Figure 6.2. L = (tftm), L'' = (eeac).

6.6 Selective Reaction of $Mg(tftm)_2$ and $Cu(eeac)_2$

Once co-sublimation reactions verified the occurrence of gas-phase ligand exchange, mass-selected fragments of both $Mg(tftm)_2$ and $Cu(eeac)_2$ were subjected to CIR analysis using the triple quadrupole mass spectrometer. The reaction conditions

described in this Chapter closely match those described earlier and focus on the formation of new products.

The first ligand exchange product of interest was generated from mass-selected $[Mg(tftm\text{-}tBu)(tftm)]^+$ at *m/z* 357. The product, $[Cu(tftm)_2]^+$, is displayed at *m/z* 453 in Figure 6.8.

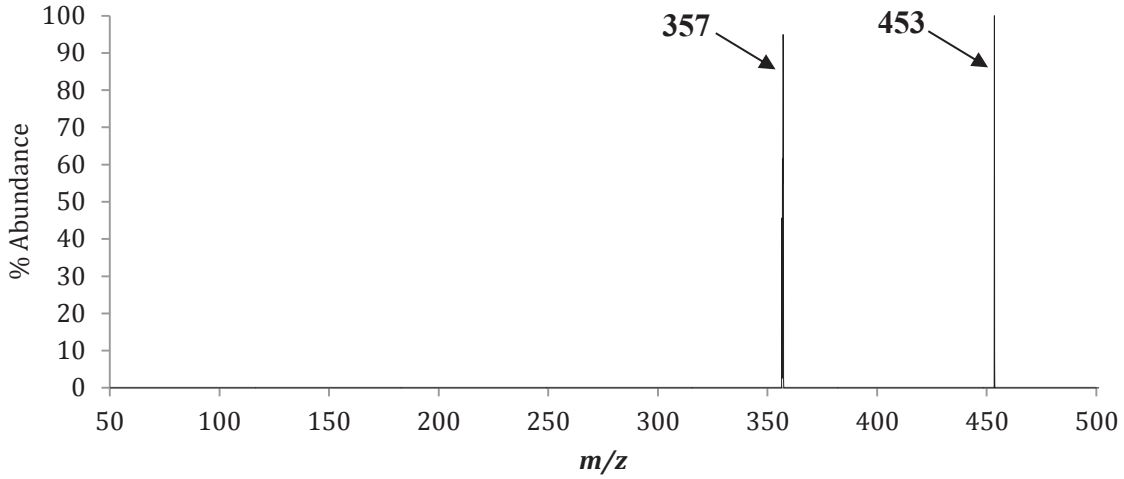

Figure 6.8: The positive mass spectrum obtained by scanning the third quadrupole following the selective reaction of *m/z* = 357 ($[Mg(tftm\text{-}tBu)(tftm)]^+$) with neutral $Cu(eeac)_2$ to produce the complete exchange product $[Cu(tftm)_2]^+$ at *m/z* 453.

The proposed mechanism for the gas-phase formation of the copper complete ligand exchange product $[Cu(tftm)_2]^+$ is displayed in Equation 6.6.

$$[Mg(tftm\text{-}tBu)(tftm)]^+ + Cu(eeac)(eeac) + tBu \rightarrow [Cu(tftm)(tftm)]^+ + Mg(eeac)(eeac) \qquad \text{(Eqn 6.6)}$$

Mass-selecting $[Mg(tftm\text{-}tBu)(tftm)]^+$ at *m/z* 357 and reacting it with neutral $Cu(eeac)_2$ also yielded a second ligand exchange product, $[Cu(tftm\text{-}tBu)(tftm\text{-}tBu)]^+$ at *m/z* 339, which is displayed in Figure 6.9.

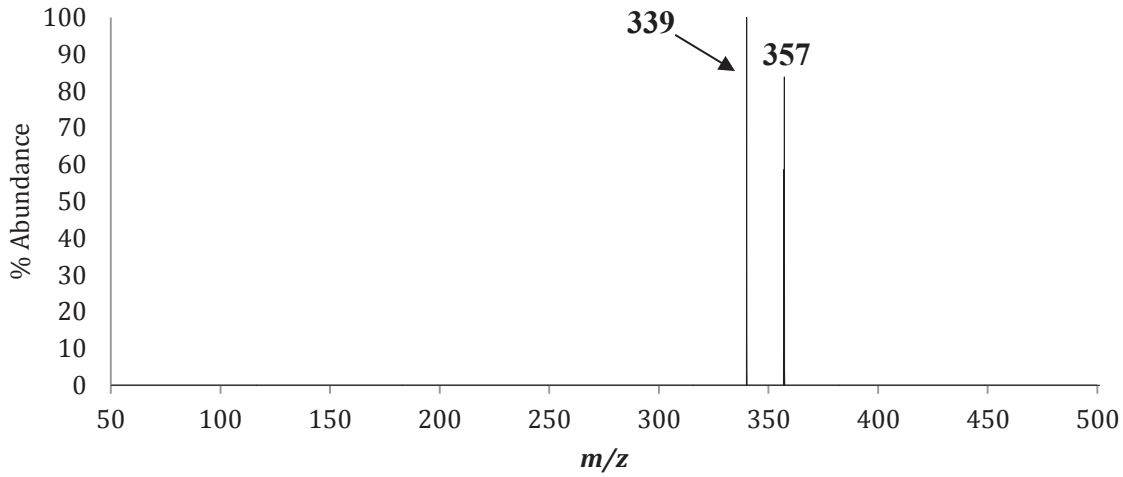

Figure 6.9: The positive mass spectrum obtained by scanning the third quadrupole following the selective reaction of *m/z* = 357 ([Mg(tftm-*tBu*)(tftm)]$^+$) with neutral Cu(eeac)$_2$ to produce the complete exchange fragment [Cu(tftm-*tBu*)(tftm-*tBu*)]$^+$ at *m/z* 339.

The proposed mechanism for the gas-phase formation of the copper complete ligand exchange fragment [Cu(tftm-*tBu*)(tftm-*tBu*)]$^+$ is presented in Equation 6.7.

$$[\text{Mg(tftm-}tBu\text{)(tftm)}]^+ + \text{Cu(eeac)(eeac)} \rightarrow [\text{Cu(tftm-}tBu\text{)(tftm-}tBu\text{)}]^+ + \text{Mg(eeac)(eeac)} + tBu \qquad \text{(Eqn 6.7)}$$

The final product that was generated from collision-induced reaction resulted from mass-selecting [Mg(tftm-CF_2)]$^+$ at *m/z* 169 reacting with neutral Cu(eeac)$_2$ was the complete ligand exchange fragment [Mg(eeac-*Et*)(eeac)]$^+$ at *m/z* 249, which is presented in Figure 6.10.

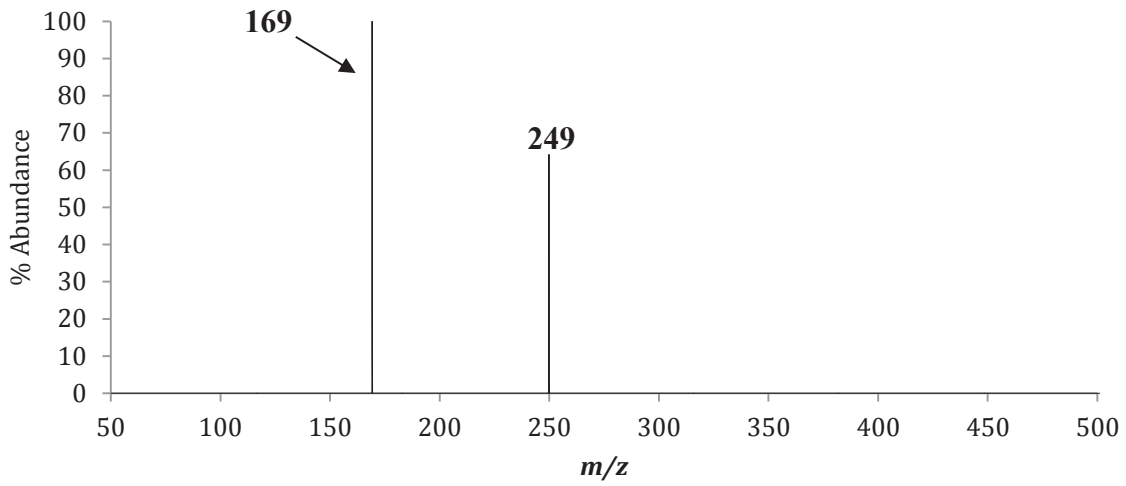

Figure 6.10: The positive mass spectrum obtained by scanning the third quadrupole following the selective reaction of *m/z* = 169 ($[Mg(tftm\text{-}CF_2)]^+$) with neutral $Cu(eeac)_2$ to produce the complete exchange fragment $[Mg(eeac\text{-}Et)(eeac))]^+$ at *m/z* 249.

The proposed mechanism for the gas-phase formation of the magnesium complete ligand exchange fragment $[Mg(eeac\text{-}Et)(eeac)]^+$ is presented in Equation 6.8.

$$[Mg(tftm\text{-}CF_2)]^+ + Cu(eeac)(eeac) \rightarrow [Mg(eeac\text{-}Et)(eeac)]^+ + Cu(tftm\text{-}CF_2) + Et \qquad \text{(Eqn 6.8)}$$

Mass-selected copper ions were also observed to generate a ligand exchange product. Specifically, mass-selected $[Cu(eeac\text{-}Et)(eeac)]^+$ at *m/z* 288 reacting with neutral $Mg(tftm)_2$ generated the complete ligand exchange product $[Mg(eeac)(eeac)]^+$ at *m/z* 278. The results of this reaction are depicted in Figure 6.11, where $[Cu(eeac)_2]^+$ is also observed at *m/z* 317.

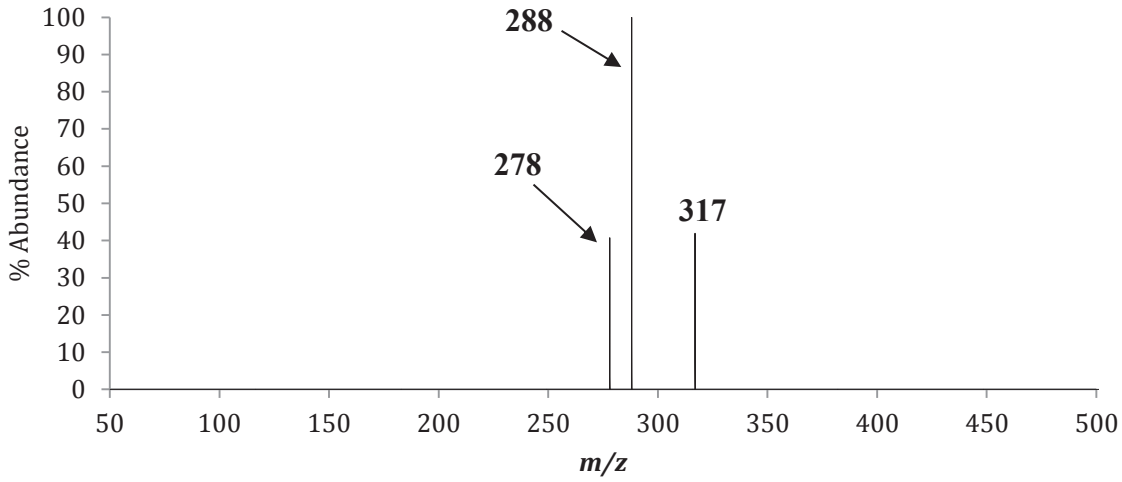

Figure 6.11: The positive mass spectrum obtained by scanning the third quadrupole following the selective reaction of *m/z* = 288 ([Cu(eeac-*Et*)(eeac)]$^+$) with neutral Mg(tftm)$_2$ to produce the complete exchange product [Mg(eeac)$_2$]$^+$ at *m/z* 278.

The proposed mechanism for the gas-phase formation of the magnesium complete ligand exchange product [Mg(eeac)$_2$]$^+$ is presented in Equation 6.9.

$$[\text{Cu(eeac-}Et\text{)(eeac)}]^+ + \text{Mg(tftm)(tftm)} + Et \rightarrow [\text{Mg(eeac)(eeac)}]^+ + \text{Cu(tftm)(tftm)} \qquad \text{(Eqn 6.9)}$$

The mechanisms reported herein have shed light on the mechanism of ligand exchange between Mg(tftm)$_2$ and Cu(eeac)$_2$. While much work must still be completed to provide a more holistic picture, these new mechanisms have helped establish a strong foundation for future research.

Mass-selected [Mg(tftm-*tBu*)(tftm)]$^+$ at *m/z* 357 reacting with neutral Cu(eeac)$_2$ was observed to lead to the formation of two ligand exchange products of interest; [Cu(tftm)$_2$]$^+$ at *m/z* 453 and [Cu(tftm-*tBu*)(tftm-*tBu*)]$^+$ at *m/z* 339. Mass-selected [Mg(tftm-CF$_2$)]$^+$ also yielded a new product, namely [Mg(eeac-*Et*)(eeac)]$^+$ at *m/z* 249. No ligand exchange products of interest were generated from mass-selected [Mg(tftm)$_2$]$^+$ at *m/z* 414 reacting with neutral Cu(eeac)$_2$.

The CIR analysis of copper products was observed to yield only one ligand exchange product. Mass-selected $[Cu(eeac\text{-}Et)(eeac)]^+$ at *m/z* 283 reacting with neutral $Mg(tftm)_2$ promoted the formation of the complete magnesium ligand exchange product $[Mg(eeac)_2]^+$ at *m/z* 278. Interestingly, no ligand exchange products of interest were generated from mass-selected $[Cu(eeac)_2]^+$ at *m/z* 317, $[Cu(eeac\text{-}Et)(eeac\text{-}Et)]^+$ at *m/z* 259, $[Cu(eeac)]^+$ at *m/z* 190, or $[Cu(eeac\text{-}Et)]^+$ at *m/z* 161 reacting with neutral $Mg(tftm)_2$.

6.7 The Co-Sublimation of $Mg(tftm)_2$ and Copper Bis-Dibenzoylmethane ($Cu(dbm)_2$)

Presented in Figure 6.12(a)-(c) are the baseline positive EI mass spectra of $Mg(tftm)_2$, $Cu(dbm)_2$, and the resultant co-sublimation mass spectrum. The $Mg(tftm)_2$ spectra displayed in Figure 6.12(a) is reproduced from Section 5.2 and will not be further elaborated upon. Similarly, Figure 6.12(b) displays the mass spectrum of $Cu(dbm)_2$ and is reproduced from Figure 4.42(c) and will also not be discussed further. The co-sublimation reaction is presented in Figure 6.12(c), where the complete ligand exchange product $[Mg(dbm)_2]^+$ at *m/z* 470 and $[Mg(dbm)]^+$ at *m/z* 247 are both clearly present. The mixed ligand exchange product $[Mg(dbm)(tftm)]^+$ also appears to readily form at *m/z* 442, with loss of a *tBu* group to form $[Mg(dbm)(tftm\text{-}tBu)]^+$ at *m/z* 385. Interestingly, no copper ligand exchange products were formed during the co-sublimation experiment.

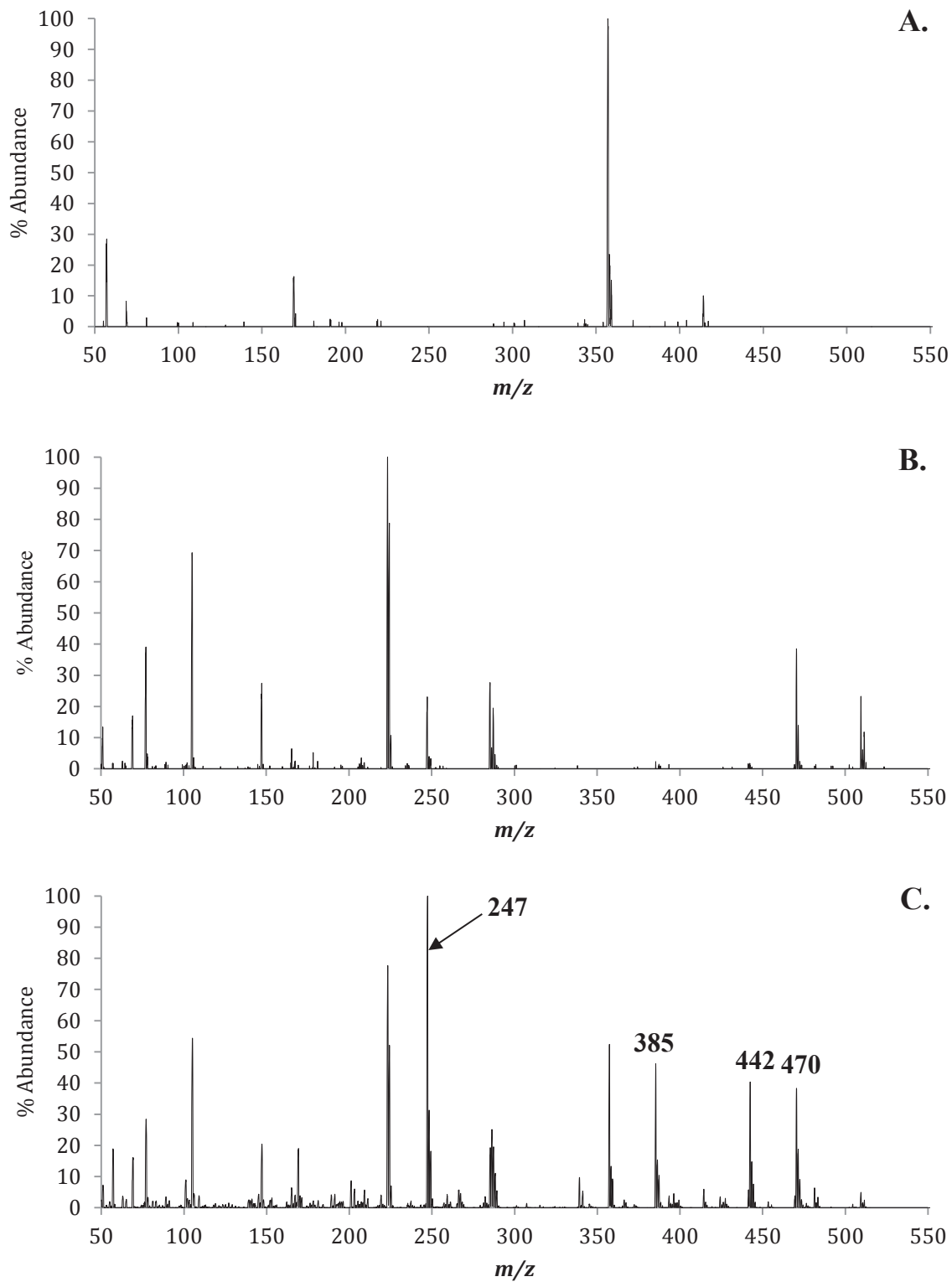

Figure 6.12: The positive EI mass spectra of (a) $Mg(tftm)_2$, (b) $Cu(dbm)_2$, and (c) the gas-phase co-sublimation of $Mg(tftm)_2$ and $Cu(dbm)_2$. The masses of parent compounds and fragments are labeled in (a) and (b). Masses of ligand exchange products and pertinent fragments are labeled in (c).

	Mass	Mass	MgL_2	CuL'''_2	MgL_2 & CuL'''_2	MgL_2 & CuL'''_2
Species	**Mg**	**Cu**	**Mg**	**Cu**	**Mg**	**Cu**
$[ML_2]^+$	414	453	10		6	2
$[ML_2\text{-}tBu]^+$	357	396	100		38	5
$[ML_2\text{-}CF_3]^+$	345	384	<1		1	<1
$[ML_2\text{-}CF_2]^+$	364	403	0		0	0
$[ML]^+$	219	258	2		4	1
$[ML\text{-}tBu]^+$	162	201	0		2	9
$[ML\text{-}CF_3]^+$	150	189	0		0	4
$[ML\text{-}CF_2]^+$	169	208	16		19	2
$[ML'''_2]^+$	470	509		33	38	5
$[ML'''_2\text{-}Ph]^+$	393	432		<1	4	0
$[ML''']^+$	247	286		12	100	25
$[ML'''\text{-}Ph]^+$	170	209		8	4	6
$[MLL''']^+$	442	481			40	6
$[M(L\text{-}tBu)L''']^+$	385	424			46	4

Table 6.3: The relative mass spectrometric abundances of $Mg(tftm)_2$ and $Cu(dbm)_2$ β-diketonate complexes as well as the co-sublimation experiment, as presented in Figure 6.12. L = (tftm), L''' = (dbm).

6.8 The Selective Reactions of $Mg(tftm)_2$ and $Cu(dbm)_2$

To better understand the mechanism of ligand exchange, mass-selected reactions were completed for the most abundant species present in the $Mg(tftm)_2$ and $Cu(dbm)_2$ mass spectra using the collision cell of a triple quadrupole mass spectrometer as described previously. Both mass-selected copper and magnesium species generated ligand exchange products of interest and will be discussed herein.

The first product of interest generated from the collision-induced reaction of mass-selected $[Mg(tftm)_2]^+$ at *m/z* 414 and neutral $Cu(dbm)_2$ was $[Mg(dbm)(tftm\text{-}tBu)]^+$ at *m/z* 385, which is displayed in Figure 6.13.

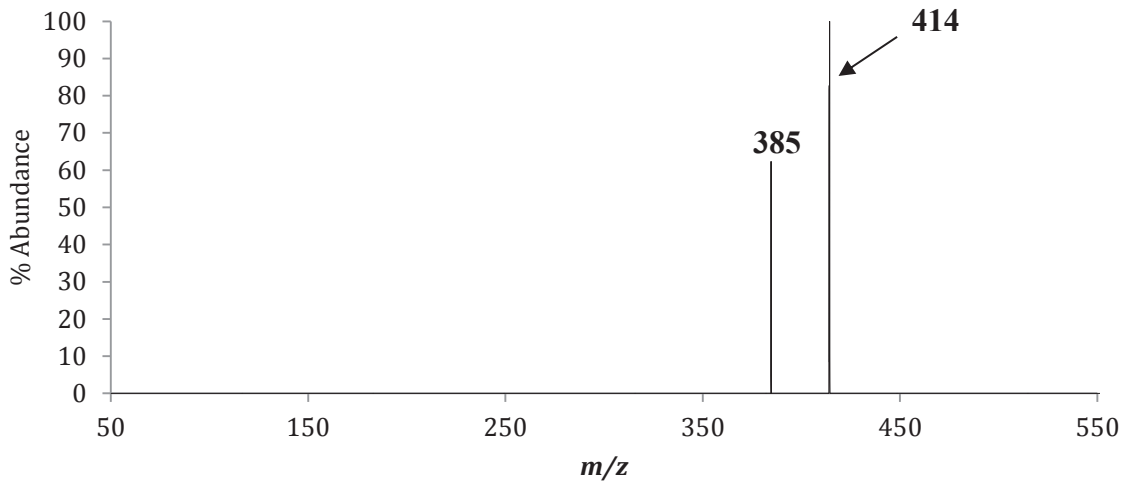

Figure 6.13: The positive mass spectrum obtained by scanning the third quadrupole following the selective reaction of *m/z* = 414 ($[Mg(tftm)_2]^+$) with neutral $Cu(dbm)_2$ to produce the mixed ligand exchange fragment $[Mg(tftm\text{-}tBu)(dbm)]^+$ at *m/z* 385.

The proposed mechanism for the gas-phase formation of the magnesium mixed ligand exchange fragment $[Mg(dbm)(tftm\text{-}tBu)]^+$ is displayed in Equation 6.10.

$$[Mg(tftm)(tftm)]^+ + Cu(dbm)(dbm) \rightarrow [Mg(dbm)(tftm\text{-}tBu)]^+ + Cu(dbm)(tftm) + tBu \qquad \text{(Eqn 6.10)}$$

Mass-selected $[Cu(dbm)_2]^+$ at *m/z* 509 reacting with neutral $Mg(tftm)_2$ also yielded a ligand exchange product of interest, $[Mg(dbm)]^+$ at *m/z* 247 and is displayed in Figure 6.14.

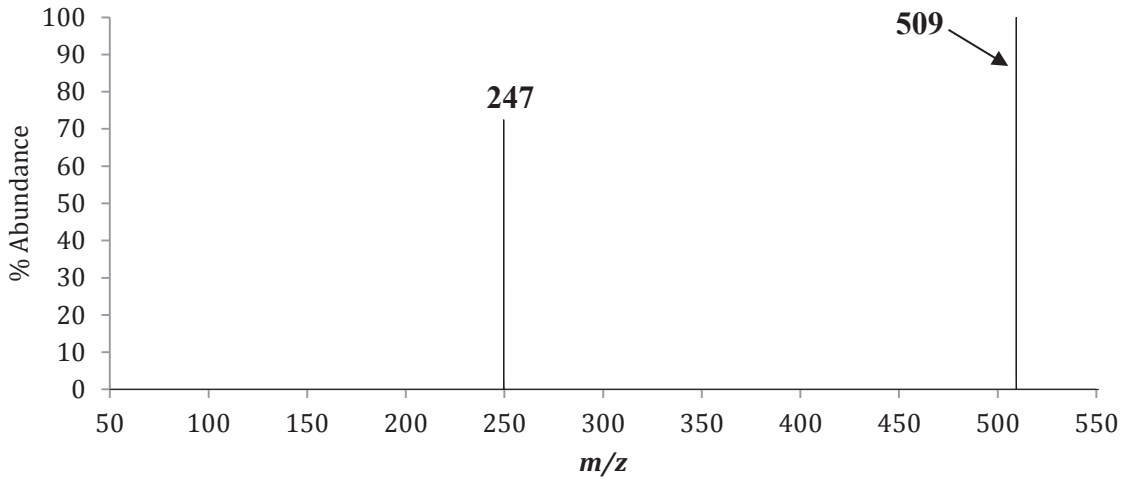

Figure 6.14: The positive mass spectrum obtained by scanning the third quadrupole following the selective reaction of *m/z* = 509 ($[Cu(dbm)_2]^+$) with neutral $Mg(tftm)_2$ to produce the complete exchange fragment $[Mg(dbm)]^+$ at *m/z* 247.

The proposed mechanism for the gas-phase formation of the magnesium single ligand exchange product $[Mg(dbm)]^+$ is presented in Equation 6.11.

$$[Cu(dbm)(dbm)]^+ + Mg(tftm)(tftm) \rightarrow$$

$$[Mg(dbm)]^+ + Cu(dbm)(tftm) + (tftm) \qquad \text{(Eqn 6.11)}$$

Mass-selected $[Cu(dbm)_2]^+$ at *m/z* 509 reacting with neutral $Mg(tftm)_2$ was also observed to form a second ligand exchange product, $[Mg(dbm\text{-}Ph)(dbm)]^+$ at *m/z* 393, which is displayed in Figure 6.15.

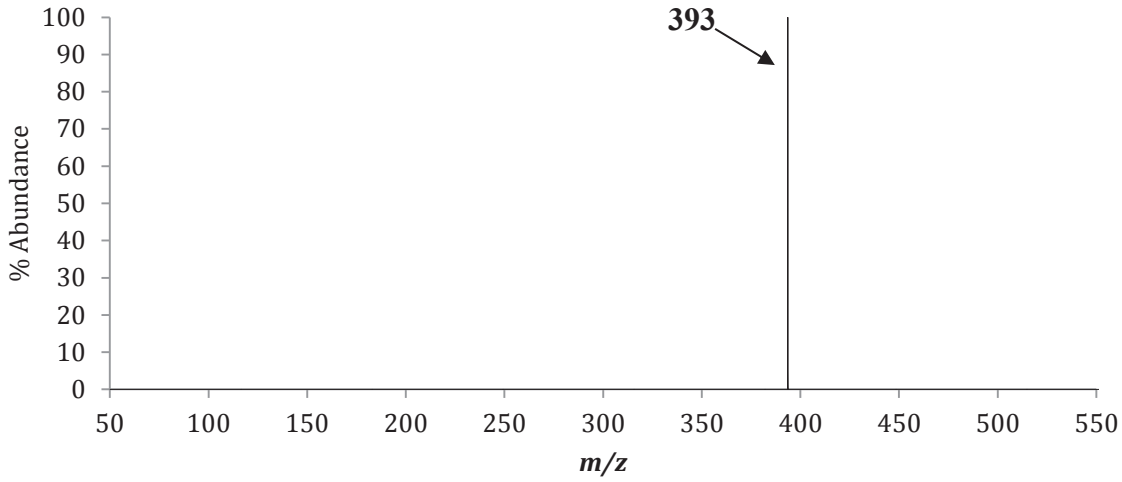

Figure 6.15: The positive mass spectrum obtained by scanning the third quadrupole following the selective reaction of *m/z* = 509 ($[Cu(dbm)_2]^+$) with neutral $Mg(tftm)_2$ to produce the complete exchange fragment $[Mg(dbm\text{-}Ph)(dbm)]^+$ at *m/z* 393.

The proposed mechanism for the gas-phase formation of the magnesium complete ligand exchange fragment $[Mg(dbm\text{-}Ph)(dbm)]^+$ is displayed in Equation 6.12.

$$[Cu(dbm)(dbm)]^+ + Mg(tftm)(tftm) \rightarrow [Mg(dbm\text{-}Ph)(dbm)]^+ + Cu(tftm)(tftm) + Ph \qquad \text{(Eqn 6.12)}$$

The collision-induced reactions of $[Mg(tftm)_2]^+$ and $[Cu(dbm)_2]^+$ have shed much light on the mechanism of ligand exchange for these two compounds. Although additional work is necessary, these reactions have helped establish the underlying gas-phase ligand exchange reactions between $Mg(tftm)_2$ and $Cu(dbm)_2$.

Mass-selecting for $[Cu(dbm)_2]^+$ at *m/z* 509 and reacting it with neutral $Mg(tftm)_2$ produced two appreciable ligand exchange products, $[Mg(dbm)]^+$ at *m/z* 247 and $[Mg(dbm\text{-}Ph)(dbm)]^+$ at *m/z* 393. No ligand exchange products of interest were observed for reactions involving $[Cu(dbm)]^+$ at *m/z* 286 reacting with neutral $Mg(tftm)_2$.

The selective reaction of $[Mg(tftm)_2]^+$ at *m/*z 414 also appears to be an active participant in the formation of the mixed ligand exchange fragment [Mg(dbm)(tftm-*tBu*)]$^+$ at *m/z* 285. No ligand exchange products of interest were generated from reactions involving mass-selected [Mg(tftm-*tBu*)(tftm)]$^+$ at *m/z* 357 or $[Mg(tftm\text{-}CF_2)]^+$ at *m/z* 169 reacting with neutral $Cu(dbm)_2$.

Chapter 7

The Co-Sublimation and Gas-Phase Ligand Exchange Reactions of Palladium Bis-Trifluorotrimethylacetylacetonate ($Pd(tftm)_2$) with Nickel Bis-Acetylacetonate ($Ni(acac)_2$), Nickel Bis-Diethylacetylacetonate ($Ni(eeac)_2$), and Nickel Bis-Trifluoroacetylacetonate ($Ni(tfac)_2$)

7.1 Introduction

Presented within this Chapter is a follow up investigation focusing on the ligand exchange mechanisms involving palladium bis-trifluorotrimethylacetylacetonate ($Pd(tftm)_2$) and three nickel compounds, nickel bis-acetylacetonate ($Ni(acac)_2$), nickel bis-diethylacetylacetonate ($Ni(eeac)_2$), and nickel bis-trifluoroacetylaceonate ($Ni(tfac)_2$). These reactions were first examined by Youngstown State University Master's student Jennifer Pekar, who explored the ligand exchange products from the reaction of mass-selected palladium species with neutral nickel compounds. Spectra involving palladium compounds are complicated by the presence of six naturally occurring palladium isotopes; ^{102}Pd is present at 1.02% abundance, ^{104}Pd is present at 11.14% abundance, ^{105}Pd is present at 22.33% abundance, ^{106}Pd at 27.33% abundance, ^{108}Pd at 26.46% abundance, and ^{110}Pd is present at 11.72% abundance. This oftentimes makes the spectra more crowded and difficult to interpret. Similarly, nickel possesses five stable isotopes, which have been outlined in Section 3.1. To briefly review, the five naturally occurring isotopes are ^{58}Ni at 68.08% abundance, ^{60}Ni at 26.22% abundance, ^{61}Ni at 1.14% abundance, ^{62}Ni at 3.63% abundance, and ^{64}Ni at about 0.93% abundance. While palladium compounds appear as small finger-like peaks on a mass spectrum, nickel

products are distinguished by one tall peak with a small shoulder at a slightly higher mass. Isotopic abundances help assist in the identification of isobaric peaks, or species possessing the same *m/z* ratio.

Similar to the reactions discussed in Chapters 3, 4, 5, and 6, collision-induced reaction analysis was used to elucidate mechanisms of ligand exchange. After baseline spectra were obtained for both $Pd(tftm)_2$ and the respective nickel reactant, a co-sublimation reaction was run. The appearance of novel peaks on the co-sublimation spectra clearly indicated that ligand exchange had occurred. Since not all fragments contribute equally to ligand exchange processes, each of the most stable palladium and nickel species were mass-selected and reacted with a second, neutral β-diketonate. Pekar completed the first half of this process by mass-selecting for the most abundant palladium species and allowing them to react with an atmosphere of the desired nickel compounds[38]. The results presented herein display the ligand exchange products generated from mass-selecting the nickel species and allowing them to react with neutral $Pd(tftm)_2$. Careful analysis and comparison with the previously reported results provides insight to the reverse reaction, and establishes a more complete picture of the gas-phase ligand exchange mechanism of $Pd(tftm)_2$ with $Ni(acac)_2$, $Ni(eeac)_2$, and $Ni(tfac)_2$.

7.2 Palladium Bis-Trifluorotrimethylacetylacetonate ($Pd(tftm)_2$)

All co-sublimation and collision-induced reactions discussed in this Chapter involve palladium bis-trifluorotrimethylacetylacetonate ($Pd(tftm)_2$), the positive mass spectrum for which is presented in Figure 7.1. Although the original scan was completed from *m/z* 50 to 650, the presented spectrum has a range of *m/z* 100 to 525 to better

highlight the distinct isotopic distributions of palladium. Intact $[Pd(tftm)_2]^+$ is displayed at *m/z* 496, with loss of a *tBu* group to form $[Pd(tftm\text{-}tBu)(tftm)]^+$ at *m/z* 439. The single ligand species $[Pd(tftm)]^+$ is displayed at *m/z* 301, and subsequent loss of a *tBu* group to form $[Pd(tftm\text{-}tBu)]^+$ is displayed at *m/z* 244. The single ligand species also appears to lose a trifluoromethyl (CF_3) group to form $[Pd(tftm\text{-}CF_3)]^+$ at *m/z* 232. The relative abundances of the most prominent ions are also presented in Table 7.1.

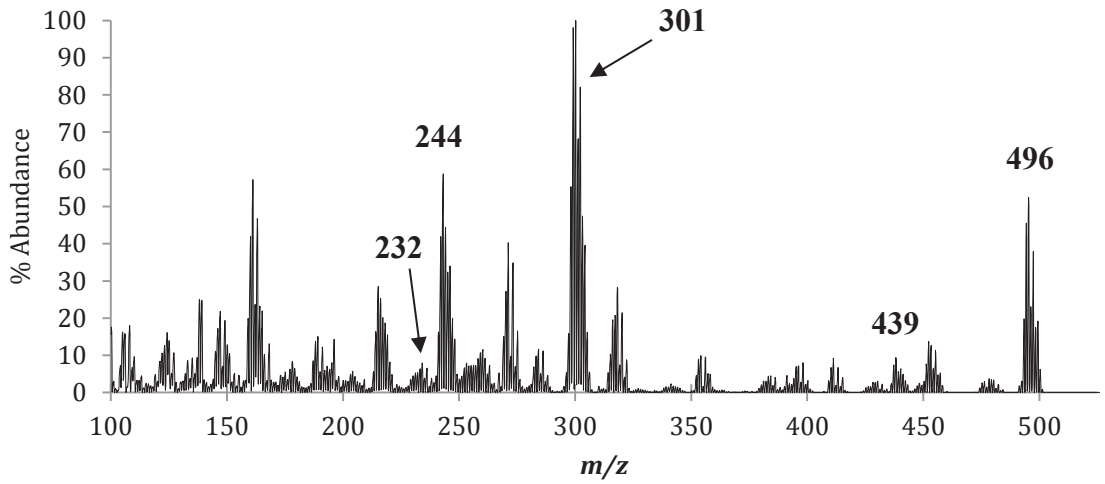

Figure 7.1: The 70 eV positive electron impact (EI) mass spectra of palladium bis-trifluorotrimethylacetylacetonate, or $[Pd(tftm)_2]^+$, and its corresponding fragmentation pattern.

Species	*m/z*	Relative Abundance
$[Pd(tftm)_2]^+$	496	52
[Pd (tftm-*tBu*)(tftm)]$^+$	439	9
$[Pd(tftm)]^+$	301	100
$[Pd(tftm\text{-}tBu)]^+$	244	59
$[Pd(tftm\text{-}CF_3)]^+$	232	8

Table 7.1: Fragmentation species and relative abundances of the mass spectral analysis of $Pd(tftm)_2$ presented in Figure 7.1.

7.3 The Co-Sublimation of $Pd(tftm)_2$ and Nickel Bis-Acetylacetonate ($Ni(acac)_2$)

Presented in Figure 7.2 (a)-(c) are the positive EI mass spectra for $Pd(tftm)_2$ and $Ni(acac)_2$, as well as the co-sublimation spectrum. The spectra are stacked vertically for purposes of clarity and comparison. Although the samples were originally scanned from *m/z* 50 to 650, the spectra presented below display peaks from *m/z* 100 to 525, to better highlight the distinct isotopic abundances of the products. Figure 7.2(a) depicts the spectrum for $Pd(tftm)_2$, which is reproduced from Figure 7.1 and will not be discussed further. Figure 7.2(b) displays the most abundant species for the fragmentation of $Ni(acac)_2$, which is reproduced from Figure 3.2(b) and will also not be discussed further.

The co-sublimation spectrum is represented in Figure 7.2(c), and pertinent ligand exchange products are labeled. The complete ligand exchange product $[Ni(tftm)_2]^+$ is displayed at *m/z* 448 while $[Pd(acac)_2]^+$ is displayed at *m/z* 304. Loss of an (acac) ligand to form $[Pd(acac)]^+$ is observed at *m/z* 205. Both heteroleptic, or mixed ligand, products are also displayed; $[Pd(acac)(tftm)]^+$ at *m/z* 400 and $[Ni(acac)(tftm)]^+$ at *m/z* 352. The heteroleptic palladium product also loses a *tBu* group to form $[Pd(acac)(tftm\text{-}tBu)]^+$ at *m/z* 342.

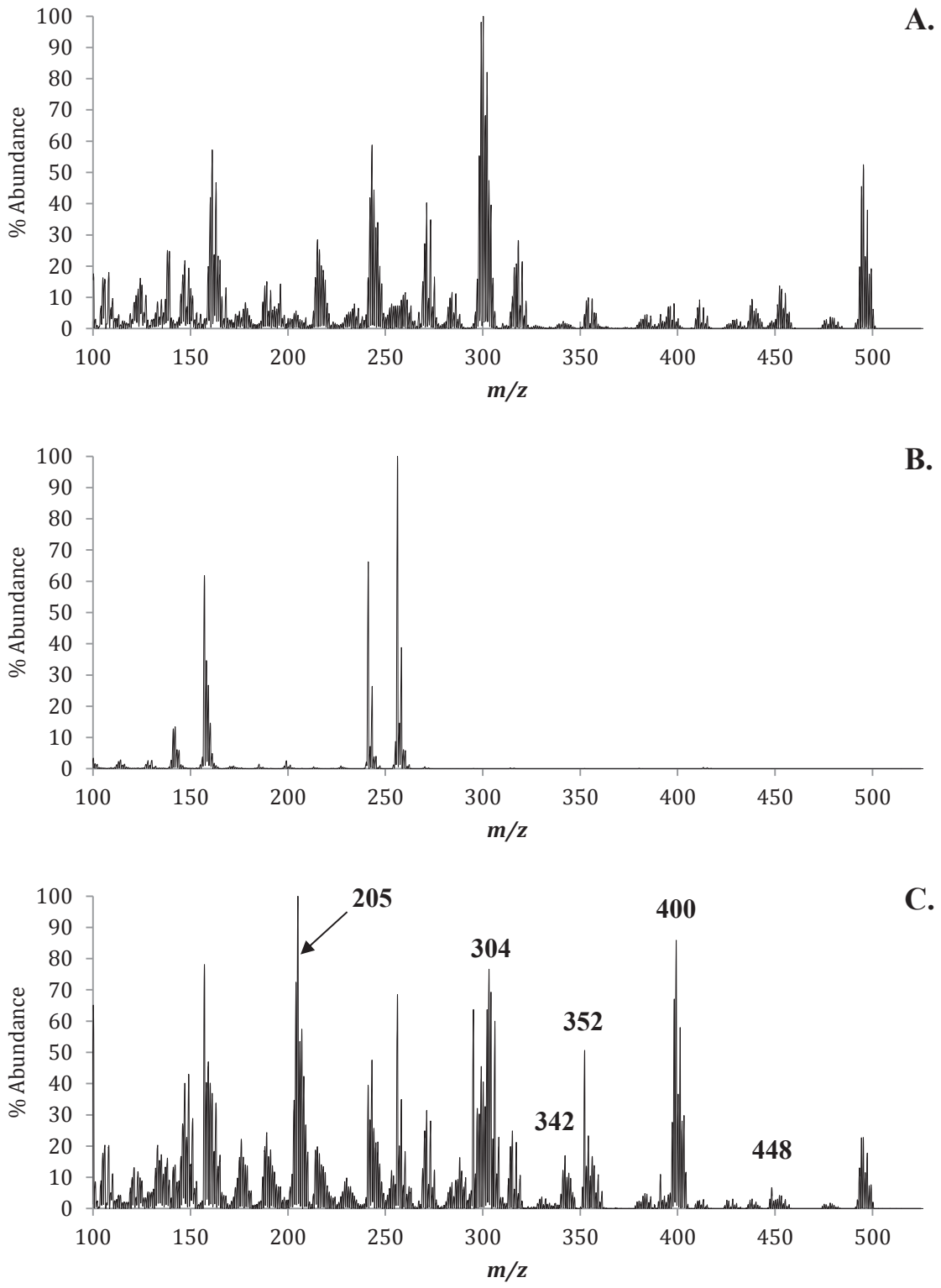

Figure 7.2: The positive EI mass spectra of (a) $Pd(tftm)_2$, (b) $Ni(acac)_2$, and (c) the gas-phase co-sublimation of $Pd(tftm)_2$ and $Ni(acac)_2$. The masses of parent compounds and fragments are labeled in (a) and (b). Masses of ligand exchange products and pertinent fragments are labeled in (c).

	Mass	Mass	PdL_2	NiL'_2	PdL_2 & NiL'_2	PdL_2 & NiL'_2
Species	Pd	Ni	Pd	Ni	Pd	Ni
$[ML_2]^+$	496	448	20		10	6
$[ML_2\text{-}t\text{Bu}]^+$	439	391	2		<1	8
$[ML]^+$	300	253	40		36	10
$[ML\text{-}t\text{Bu}]^+$	243	196	23		43	6
$[ML\text{-}CF_3]^+$	231	184	2		6	1
$[ML'_2]^+$	304	256		100	61	62
$[ML'_2\text{-}CH_3]^+$	289	241		66	10	33
$[ML'_2\text{-}2CH_3]^+$	275	226		<1	10	2
$[ML']^+$	205	157		61	100	72
$[ML'\text{-}CH_3]^+$	190	142		13	17	13
$[MLL']^+$	400	352			33	43
$[M(L\text{-}t\text{Bu})L']^+$	343	295			35	55
$[M(L\text{-}tBu)(L'\text{-}CH_3)^+$	328	280			1	<1

Table 7.2: The relative mass spectrometric abundances of the $Mg(tftm)_2$ and $Ni(acac)_2$ β-diketonate complexes as well as the co-sublimation experiment, as presented in Figure 7.2 L = (tftm) L' = (acac).

7.4 The Selective Reactions of $Pd(tftm)_2$ and $Ni(acac)_2$

The most abundant species from the $Ni(acac)_2$ positive EI mass spectrum, ($[Ni(acac)_2]^+$ at *m/z* 256, $[Ni(acac\text{-}CH_3)(acac)]^+$ at *m/z* 241, $[Ni(acac)]^+$ at *m/z* 157, and $[Ni(acac\text{-}CH_3)]^+$ at *m/z* 142) were subjected to collision-induced reaction analysis with neutral $Pd(tftm)_2$. A complete scan from *m/*z 50 to 650 was performed in the third quadrupole, and the products were evaluated as possible contributors to the ligand exchange processes observed in the co-sublimation spectrum.

The first mass-selected species that yielded a ligand exchange product was $[Ni(acac\text{-}CH_3)(acac)]^+$ at *m/z* 241 reacting with neutral $Pd(tftm)_2$ to form $[Pd(acac\text{-}CH_3)(tftm\text{-}CF_2)]^+$ at *m/z* 328 and is displayed in Figure 7.3.

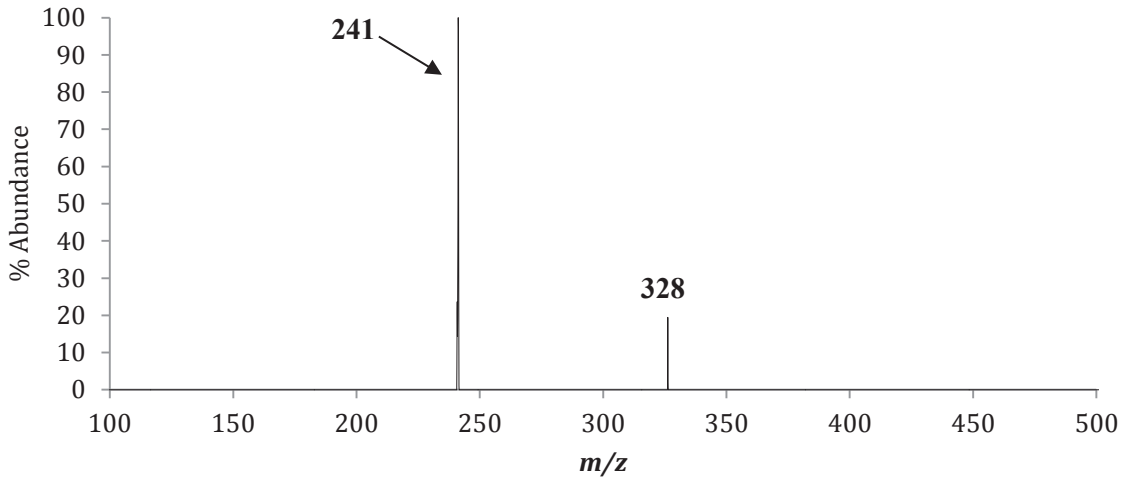

Figure 7.3: The positive mass spectrum obtained by scanning the third quadrupole following the selective reaction of *m/z* = 241 ($[Ni(acac\text{-}CH_3)(acac)]^+$) with neutral $Pd(tftm)_2$ to produce the mixed ligand exchange product $[Pd(acac\text{-}CH_3)(tftm\text{-}tBu)]^+$ at *m/z* 328.

The proposed mechanism for the gas-phase formation of the palladium mixed ligand exchange fragment $[Pd(acac\text{-}CH_3)(tftm\text{-}CF_2)]^+$ is presented in Equation 7.1.

$$[Ni(acac\text{-}CH_3)(acac)]^+ + Pd(tftm)(tftm) \rightarrow [Pd(acac\text{-}CH_3)(tftm\text{-}tBu)]^+ + Ni(acac)(tftm) + tBu \qquad \text{(Eqn 7.1)}$$

The second ligand exchange product generated from mass-selecting the single ligand species $[Ni(acac)]^+$ at *m/z* 157 and reacting it with neutral $Pd(tftm)_2$, which formed the complete ligand exchange product $[Ni(tftm)_2]^+$ at *m/z* 448 and is displayed in Figure 7.4. The third peak on the spectrum, at *m/z* 256, corresponds to the bis-chelated parent species $[Ni(acac)_2]^+$, and was not further examined.

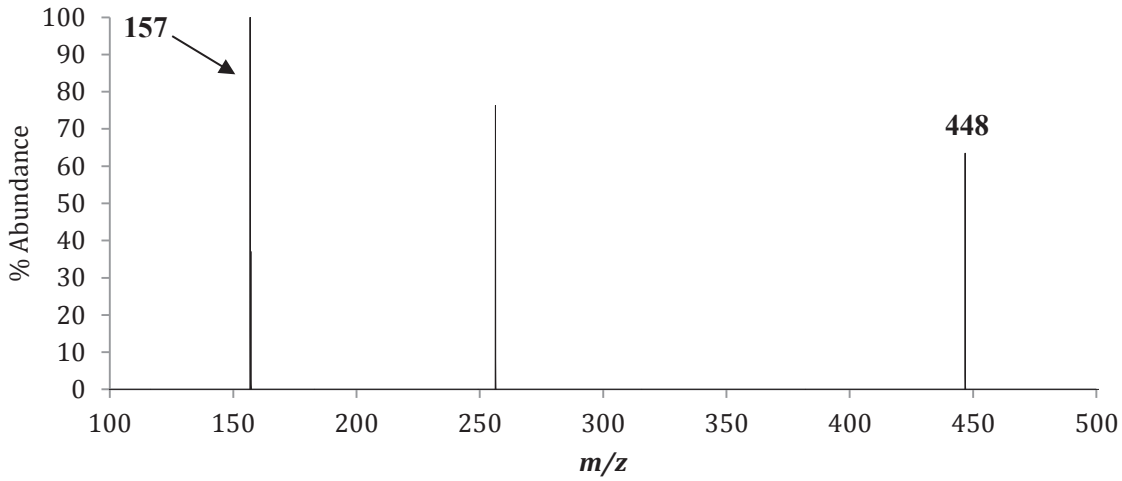

Figure 7.4: The positive mass spectrum obtained by scanning the third quadrupole following the selective reaction of *m/z* = 241 ($[Ni(acac)]^+$) with neutral $Pd(tftm)_2$ to produce the complete ligand exchange product $[Ni(tftm)_2]^+$ at *m/z* 448.

The proposed mechanism for the gas-phase formation of the nickel complete ligand exchange product $[Ni(tftm)_2]^+$ is presented in Equation 7.2.

$$[Ni(acac)]^+ + Pd(tftm)(tftm) \rightarrow [Ni(tftm)(tftm)]^+ + Pd(acac) \qquad \text{(Eqn 7.2)}$$

The final ligand exchange product generated from mass-selected nickel species was also generated from mass-selected $[Ni(acac)]^+$ at *m/z* 157 reacting with neutral $Pd(tftm)_2$, which formed $[Ni(acac)(tftm\text{-}tBu)]^+$ at *m/*z 295 and is displayed in Figure 7.5.

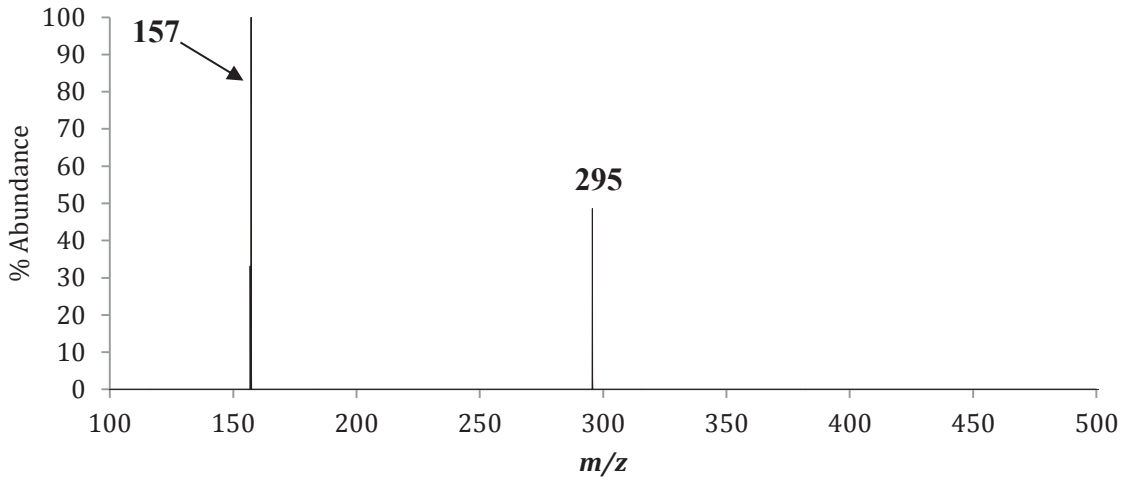

Figure 7.5: The positive mass spectrum obtained by scanning the third quadrupole following the selective reaction of *m/z* = 241 ($[Ni(acac)]^+$) with neutral $Pd(tftm)_2$ to produce the mixed ligand exchange fragment $[Ni(acac)(tftm\text{-}tBu)]^+$ at *m/z* 295.

The proposed mechanism for the gas-phase formation of the nickel mixed ligand fragment $[Ni(acac)(tftm\text{-}tBu)]^+$ is displayed in Equation 7.3.

$$[Ni(acac)]^+ + Pd(tftm)(tftm) \rightarrow [Ni(acac)(tftm\text{-}tBu)]^+ + Pd(tftm) + tBu \qquad \text{(Eqn 7.3)}$$

The spectra displayed in this Chapter provide much novel insight into the mechanism of ligand exchange between $Pd(tftm)_2$ and $Ni(acac)_2$. Although additional work is necessary, the mechanisms reported herein have contributed new information into the process of ligand exchange between these two β-diketonates.

The key contributor to the formation of palladium ligand exchange products appears to be $[Ni(acac\text{-}CH_3)(acac)]^+$ at *m/z* 241 and produced $[Pd(acac\text{-}CH_3)(tftm\text{-}CF_2)]^+$ at *m/z* 326 when reacted with neutral $Pd(tftm)_2$. Moreover, mass-selecting for $[Ni(acac)]^+$ at *m/*z 162 and reacting it with neutral $Pd(tftm)_2$ yielded two nickel ligand exchange products; $[Ni(tftm)_2]^+$ at *m/z* 448 and $[Ni(acac)(tftm\text{-}tBu)]^+$ at *m/z* 295. Interestingly, no ligand exchange products of interest were generated from mass-selected $[Ni(acac)_2]^+$ at *m/z* 256 or $[Ni(acac\text{-}CH_3)]^+$ at *m/z* 142.

7.5 The Co-Sublimation of $Pd(tftm)_2$ and Nickel Bis-Diethylacetylacetonate ($Ni(eeac)_2$)

To provide a more in-depth analysis on the mechanism of ligand exchange of $Pd(tftm)_2$ with nickel β-diketonates, the co-sublimation of $Pd(tftm)_2$ was examined with $Ni(eeac)_2$. The positive EI mass spectra of $Pd(tftm)_2$ and $Ni(eeac)_2$ are presented in Figure 7.6(a) and 7.6(b) respectively, while the co-sublimation spectrum is presented in Figure 7.6(c), which is displayed below the baseline spectra to aid in comparison. The presented spectra display a range from *m/z* 100 to 525 to highlight the isotopic abundances of each species. The spectrum for $Pd(tftm)_2$ is reproduced from Figure 7.1, and will not be further discussed. Figure 7.6(b) is reproduced from Figure 5.2(b) and will also not be discussed further.

The co-sublimation spectrum of $Pd(tftm)_2$ and $Ni(eeac)_2$ is presented in Figure 7.6(c). A plethora of novel peaks are now present, which is a clear indication that ligand exchange occurred. Interestingly, both nickel and palladium ligand exchange products are generated. The peak at *m/z* 448 corresponds to the nickel ligand exchange product $[Ni(tftm)_2)]^+$ with loss of a *t-Bu* group forming $[Ni(tftm\text{-}tBu)(tftm)]^+$ at *m/z* 391. The single ligand exchange species $[Ni(tftm)]^+$ was also generated at *m/z* 253. The homoleptic palladium ligand exchange product $[Pd(eeac)_2]^+$ is clearly displayed at *m/z* 360, and the single ligand species $[Pd(eeac)]^+$ is present at *m/z* 232. The nickel mixed ligand exchange product $[Ni(eeac)(tftm)]^+$ is present at *m/z* 380, as is the loss of a *t-Bu* group forming $[Ni(eeac)(tftm\text{-}tBu)]^+$ at *m/z* 323. The relative abundances of all spectra reported herein are presented in Table 7.3.

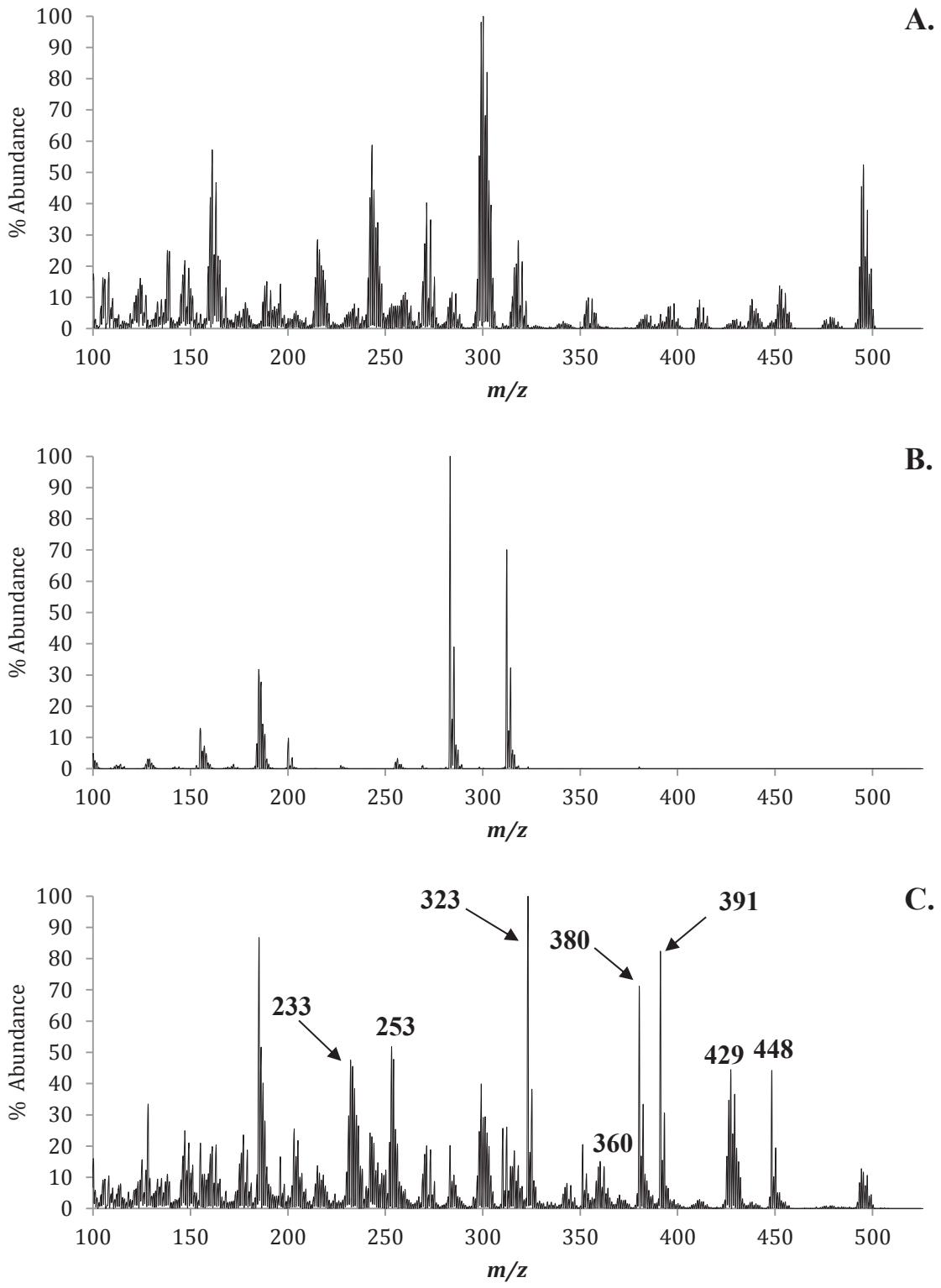

Figure 7.6: The positive EI mass spectra of (a) $Pd(tftm)_2$, (b) $Ni(eeac)_2$, and (c) the gas-phase co-sublimation of $Pd(tftm)_2$ and $Ni(eeac)_2$. The masses of parent compounds and fragments are labeled in (a) and (b). Masses of ligand exchange products and pertinent fragments are labeled in (c).

	Mass	Mass	PdL_2	NiL''_2	PdL_2 & NiL''_2	PdL_2 & NiL''_2
Species	Pd	Ni	Pd	Ni	Pd	Ni
$[ML_2]^+$	496	448	20		7	44
$[ML2\text{-}tBu]^+$	439	391	2		<1	82
$[ML]^+$	300	253	40		29	51
$[ML\text{-}tBu]^+$	243	196	23		23	16
$[ML\text{-}CF_3]^+$	231	184	2		29	10
$[ML''_2]^+$	360	312		67	15	26
$[ML''_2\text{-}Et]^+$	331	283		100	2	20
$[ML'']^+$	233	185		30	45	86
$[ML''\text{-}Et]^+$	205	156		5	21	10
$[MLL'']^+$	429	380			36	71
$[M(L\text{-}tBu)L'']^+$	371	323			2	100
$[M(L\text{-}CF_3)L'']^+$	359	311			13	5
$[ML(L''\text{-}Et)]^+$	399	351			1	20

Table 7.3: The relative mass spectrometric abundances of the nickel and palladium β-diketonate complexes as well as the co-sublimation experiment, as presented in Figure 7.6. L = (tftm); L'' = (eeac).

7.6 The Selective Reactions of $Pd(tftm)_2$ and $Ni(eeac)_2$

The four most abundant species from the positive EI mass spectrum of $Ni(eeac)_2$, including ($[Ni(eeac)_2]^+$ at *m/z* 312, $[Ni(eeac\text{-}Et)(eeac)]^+$ at *m/z* 283, $[Ni(eeac)]^+$ at *m/z* 185, and $[Ni(eeac\text{-}Et)]^+$ at *m/z* 156, were each mass-selected and subjected to collision-induced reaction analysis with neutral $Pd(tftm)_2$. A full scan from *m/z* 50 to 650 was completed in the third quadrupole, and all of the observed complete, partial, and mixed palladium and nickel ligand exchange products are reported herein.

The first ligand exchange product of interest was $[Pd(eeac)]^+$ at *m/z* 233, generated from mass-selected $[Ni(eeac\text{-}Et)(eeac)]^+$ at *m/z* 283 reacting with neutral $Pd(tftm)_2$ and is presented in Figure 7.7.

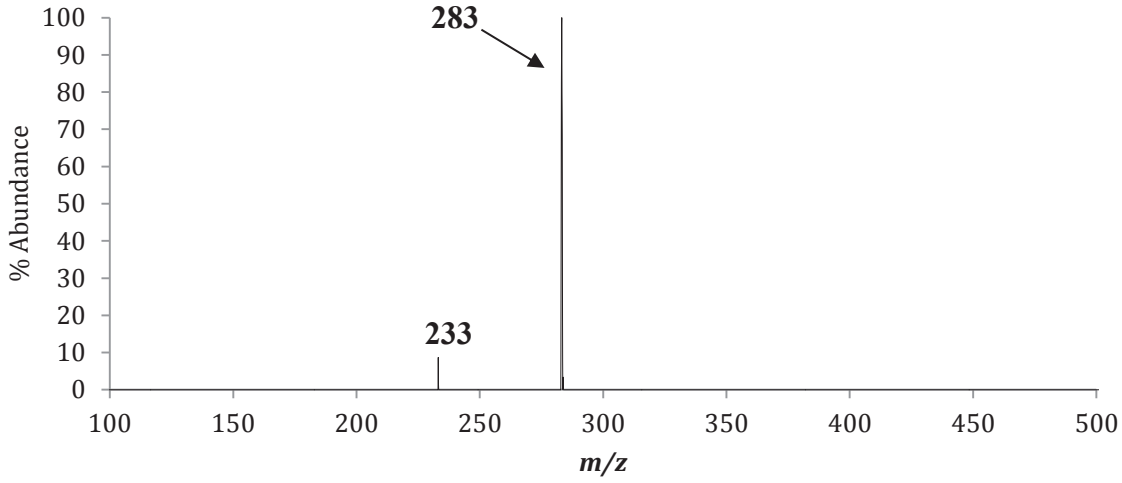

Figure 7.7: The positive mass spectrum obtained by scanning the third quadrupole following the selective reaction of *m/z* = 283 ($[Ni(eeac\text{-}Et)(eeac)]^+$) with neutral $Pd(tftm)_2$ to produce the partial ligand exchange product $[Pd(eeac)]^+$ at *m/z* 233.

The proposed mechanism for the gas-phase formation of the palladium single ligand exchange product $[Pd(eeac)]^+$ is displayed in Equation 7.4.

$$[Ni(eeac\text{-}Et)(eeac)]^+ + Pd(tftm)(tftm) \rightarrow$$
$$[Pd(eeac)]^+ + Ni(eeac\text{-}Et)(tftm) + (tftm) \qquad \text{(Eqn 7.4)}$$

The second ligand exchange product generated from collision-induced reaction was the mixed ligand exchange fragment $[Ni(eeac)(tftm\text{-}tBu)]^+$ at *m/z* 323, which was produced from mass-selecting $[Ni(eeac)]^+$ at *m/z* 185 reacting with neutral $Pd(tftm)_2$ and is displayed in Figure 7.8.

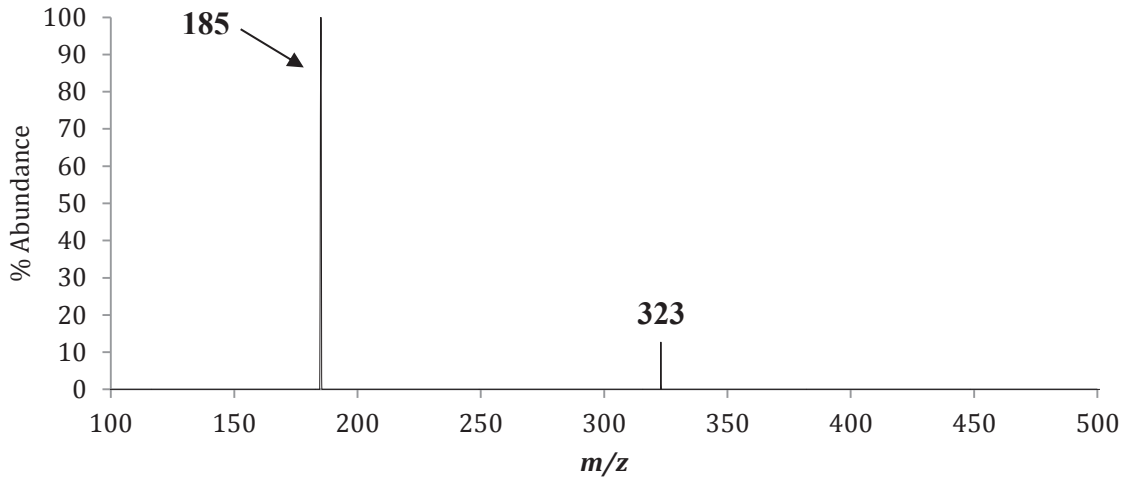

Figure 7.8: The positive mass spectrum obtained by scanning the third quadrupole following the selective reaction of *m/z* = 185 ($[Ni(eeac)]^+$) with neutral $Pd(tftm)_2$ to produce the mixed ligand exchange fragment $[Ni(eeac)(tftm\text{-}tBu)]^+$ at *m/z* 323.

The proposed mechanism for the gas-phase formation of the nickel mixed ligand exchange fragment $[Ni(eeac)(tftm\text{-}tBu)]^+$ is presented in Equation 7.5.

$$[Ni(eeac)]^+ + Pd(tftm)(tftm) \rightarrow [Ni(eeac)(tftm\text{-}tBu)]^+ + Pd(tftm) + tBu \qquad \text{(Eqn 7.5)}$$

The third product generated from collision-induced reaction was the nickel single ligand exchange product, $[Ni(tftm)]^+$ at *m/z* 253 which was produced from the mass-selected parent fragment $[Ni(eeac\text{-}Et)]^+$ at *m/z* 156 reacting with neutral $Pd(tftm)_2$, and is displayed in Figure 7.9

.

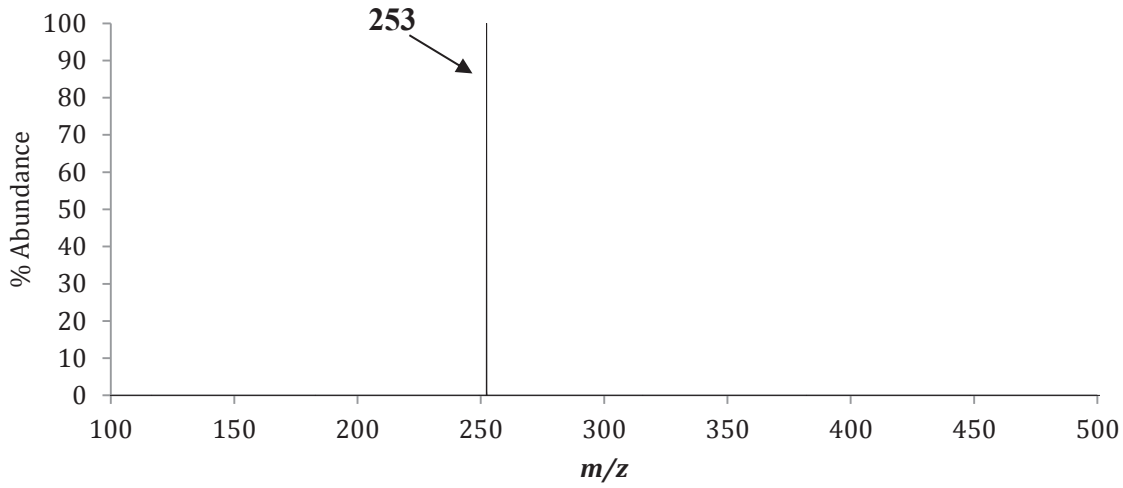

Figure 7.9: The positive mass spectrum obtained by scanning the third quadrupole following the selective reaction of *m/z* = 156 ([Ni(eeac-*Et*)]$^+$) with neutral Pd(tftm)$_2$ to produce the single ligand exchange product [Ni(tftm)]$^+$ at *m/z* 253.

The proposed mechanism for the gas-phase formation of the nickel single ligand exchange product [Ni(tftm)]$^+$ is presented in Equation 7.6.

$$[\text{Ni(eeac-}Et\text{)}]^+ + \text{Pd(tftm)(tftm)} \rightarrow [\text{Ni(tftm)}]^+ + \text{Pd(eeac-}Et\text{)(tftm)} \qquad \text{(Eqn 7.6)}$$

The fourth ligand exchange product generated from the collision-induced reaction was the mixed ligand exchange fragment [Ni(eeac)(tftm-*tBu*)]$^+$ at *m/z* 323, which was also generated from mass selecting [Ni(eeac-*Et*)]$^+$ at *m/z* 156 reacting with neutral Pd(tftm)$_2$ and is displayed in Figure 7.10.

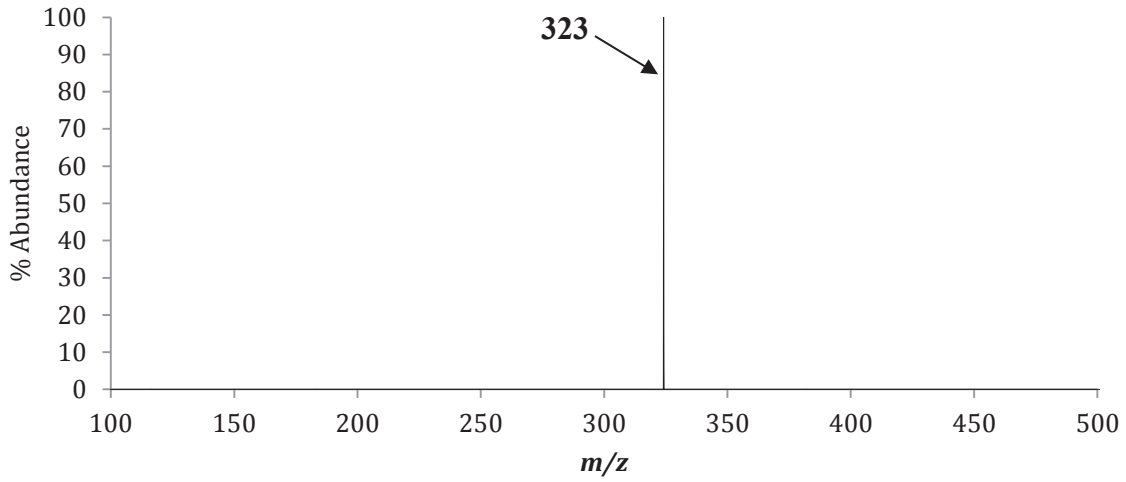

Figure 7.10: The positive mass spectrum obtained by scanning the third quadrupole following the selective reaction of *m/z* = 156 ([Ni(eeac-*Et*)]$^+$) with neutral Pd(tftm)$_2$ to produce the mixed ligand exchange fragment [Ni(eeac)(tftm-*tBu*)]$^+$ at *m/z* 323.

The proposed mechanism for the gas-phase formation of the nickel mixed ligand exchange fragment [Ni(eeac)(tftm-*tBu*)]$^+$ is presented in Equation 7.7.

$$[\text{Ni(eeac-}Et\text{)}]^+ + \text{Pd(tftm)(tftm)} + Et \rightarrow [\text{Ni(eeac)(tftm-}tBu\text{)}]^+ + \text{Pd(tftm)} + tBu \quad \text{(Eqn 7.7)}$$

The final product generated from the collision-induced reaction of mass-selected nickel species was the complete ligand exchange fragment [Ni(tftm-*tBu*)(tftm)]$^+$ at *m/z* 391, which was formed from reacting [Ni(eeac-*Et*)]$^+$ at *m/z* 156 with neutral Pd(tftm)$_2$, and is displayed in Figure 7.11.

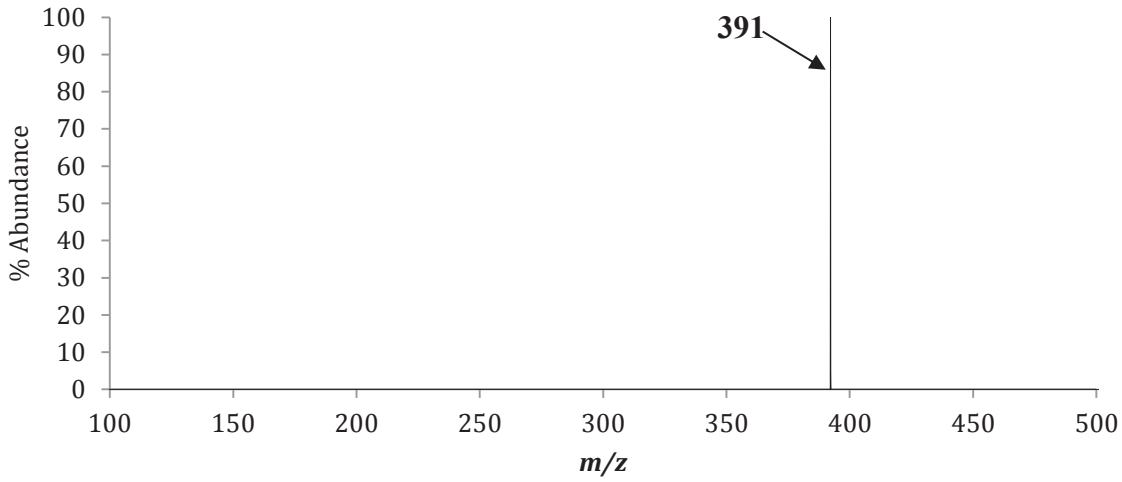

Figure 7.11: The positive mass spectrum obtained by scanning the third quadrupole following the selective reaction of *m/z* = 156 ([Ni(eeac-*Et*)]$^+$) with neutral Pd(tftm)$_2$ to produce the mixed ligand exchange fragment [Ni(tftm-*tBu*)(tftm)]$^+$ at *m/z* 391.

The proposed mechanism for the gas-phase formation of the nickel complete ligand exchange fragment [Ni(tftm-*tBu*)(tftm)]$^+$ is presented in Equation 7.8.

$$[\text{Ni(eeac-}Et\text{)}]^+ + \text{Pd(tftm)(tftm)} \rightarrow [\text{Ni(tftm-}tBu\text{)(tftm)}]^+ + \text{Pd(eeac-}Et\text{)} + tBu \qquad \text{(Eqn 7.8)}$$

The spectra displayed in this Chapter provide much novel insight into the mechanism of ligand exchange between Pd(tftm)$_2$ and Ni(eeac)$_2$. Although additional work is necessary, the mechanisms reported herein have contributed new information into the process of ligand exchange between these two β-diketonates.

Ionized nickel β-diketonate species were observed to be key contributors to ligand exchange processes. Mass-selected [Ni(eeac-*Et*)(eeac)]$^+$ at *m/z* 283 when reacted with neutral Pd(tftm)$_2$ was found to generate [Pd(eeac)]$^+$ at *m/z* 233, while mass-selected [Ni(eeac)]$^+$ at *m/z* 185 generated [Ni(eeac)(tftm-*tBu*)]$^+$ at *m/z* 323. The key contributor to ligand exchange appears to be mass-selected [Ni(eeac-*Et*)]$^+$ at *m/z* 156, which promoted the formation of three nickel ligand exchange products: [Ni(tftm)]$^+$ at *m/z* 253, [Ni(eeac)(tftm-*tBu*)]$^+$ at *m/z* 323, and [Ni(tftm-*tBu*)(tftm)]$^+$ at *m/z* 392. Interestingly, no

ligand exchange products were generated from the reaction between neutral $Pd(tftm)_2$ and mass-selected $[Ni(eeac)_2]^+$ at *m/z* 312.

7.7 The Co-Sublimation of $Pd(tftm)_2$ and Nickel Bis-Trifluoroacetylacetonate ($Ni(tfac)_2$)

The final nickel species evaluated by collision-induced reaction with $Pd(tftm)_2$ was nickel bis-trifluoroacetylacetonate, or $Ni(tfac)_2$. Presented in Figure 7.12 (a)-(c) are the positive EI mass spectra of $Pd(tftm)_2$ and $Ni(tfac)_2$, and their respective co-sublimation spectrum. Although the scans were run between *m/z* 50 to 650, the spectra were displayed between *m/z* 100 to 525 to highlight the isotopic abundances of the products. The positive EI mass spectrum of $Pd(tftm)_2$ is reproduced from Figure 7.1 and will not be discussed further. Presented in Figure 7.12(b) is the positive EI mass spectrum of $Ni(tfac)_2$, which displays four prominent species. Intact $[Ni(tfac)_2]^+$ is displayed at *m/z* 364, with the subsequent loss of a trifluoromethyl (CF_3) group to form $[Ni(tfac\text{-}CF_3)(tfac)]^+$ at *m/z* 295. Intact $[Ni(tfac)]^+$ is observed to be present at *m/z* 211, and loss of a trifluoromethyl group with subsequent fluorine migration to form $[Ni(tfac\text{-}CF_2)]^+$ is displayed at *m/z* 161.

The co-sublimation spectra of $Pd(tftm)_2$ and $Ni(tfac)_2$ is displayed in Figure 7.12(c) and clearly shows evidence for gas-phase ligand exchange. The peak at *m/z* 448 correlates with the mass of $[Ni(tftm)_2]^+$, while loss of a *tBu* group to form $[Ni(tftm\text{-}tBu)(tftm)]^+$ is displayed at *m/z* 391. The heteroleptic nickel ligand exchange product, $[Ni(tfac)(tftm)]^+$ is displayed at *m/z* 406, with subsequent loss of a methyl group to form $[Ni(tfac\text{-}CH_3)(tftm)]^+$ at *m/z* 391. The peak at *m/z* 391 is isobaric for [Ni(tfac-

CH_3)(tftm)]$^+$ and [Ni(tftm-*tBu*)(tftm)]$^+$, and since both are nickel-containing products where both intact species are formed during co-sublimation, it is difficult to determine whether it is the fragment of the homoleptic or heteroleptic species. The single ligand nickel species [Ni(tftm)]$^+$ is also displayed at *m/z* 253. The only palladium product observed to form was the heteroleptic species [Pd(tfac)(tftm)]$^+$ at *m/z* 453. The relative abundances of all species reported herein are presented in Table 7.4, and isobaric peaks have been italicized.

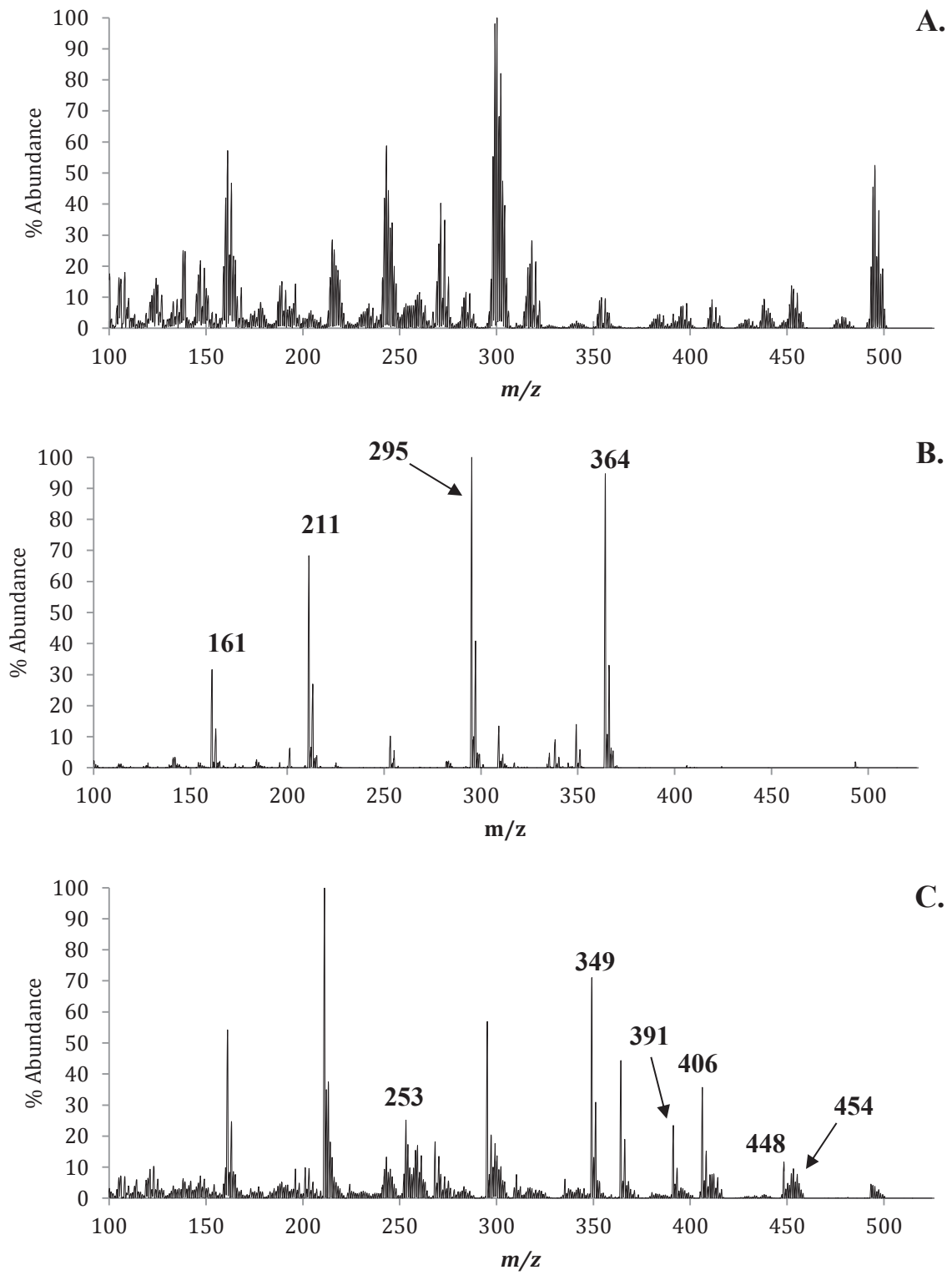

Figure 7.12: The positive EI mass spectra of (a) $Pd(tftm)_2$, (b) $Ni(tfac)_2$, and (c) the gas-phase co-sublimation of $Pd(tftm)_2$ and $Ni(tfac)_2$. The masses of parent compounds and fragments are labeled in (a) and (b). Masses of ligand exchange products and pertinent fragments are labeled in (c).

	Mass	Mass	PdL_2	NiL'''_2	PdL_2 & NiL'''_2	PdL_2 & NiL'''_2
Species	Pd	Ni	Pd	Ni	Pd	Ni
$[ML_2]^+$	496	448	20		2	11
$[ML_2\text{-}tBu]^+$	*439*	*391*	2		*<1*	*23*
$[ML]^+$	300	253	40		13	25
$[ML\text{-}CF_2]^+$	250	203	1		<1	9
$[ML\text{-}tBu]^+$	243	196	23		12	9
$[ML\text{-}CF_3]^+$	231	184	2		2	1
$[ML'''_2]^+$	414	364		95	7	44
$[ML'''_2\text{-}CF_3]^+$	345	295		100	3	56
$[ML''']^+$	260	211		66	8	100
$[ML'''\text{-}CF_2]^+$	209	161		32	2	54
$[MLL''']^+$	454	406			6	35
$[ML(L'''\text{-}CH_3)]^+$	*439*	*391*			*<1*	*23*
$[M(L\text{-}tBu)L''']^+$	397	349			2	71
$[MLL'''\text{-}CF_3]^+$	385	337			<1	3

Table 7.4: The relative mass spectrometric abundances of the nickel and palladium β-diketonate complexes as well as the co-sublimation experiment, as presented in Figure 7.12. L = (tftm); L''' = (tfac).

7.8 The Selective Reactions of $Pd(tftm)_2$ and $Ni(tfac)_2$

Presented herein are the ligand exchange products resulting from the reaction of neutral $Pd(tftm)_2$ and the most abundant $Ni(tfac)_2$ species from the positive EI mass spectrum, including ($[Ni(tfac)_2]^+$ at *m/z* 364, $[Ni(tfac\text{-}CF_3)(tfac)]^+$ at *m/z* 295, $[Ni(tfac)]^+$ at *m/z* 211, and $[Ni(tfac\text{-}CF_2)]^+$ at *m/z* 161). The first product of interest generated from mass-selecting the intact species $[Ni(tfac)_2]^+$ at *m/z* 364 and reacting it with neutral $Pd(tftm)_2$ was observed to generate $[Ni(tftm)_2]^+$ at *m/z* 448 and is displayed in Figure 7.13.

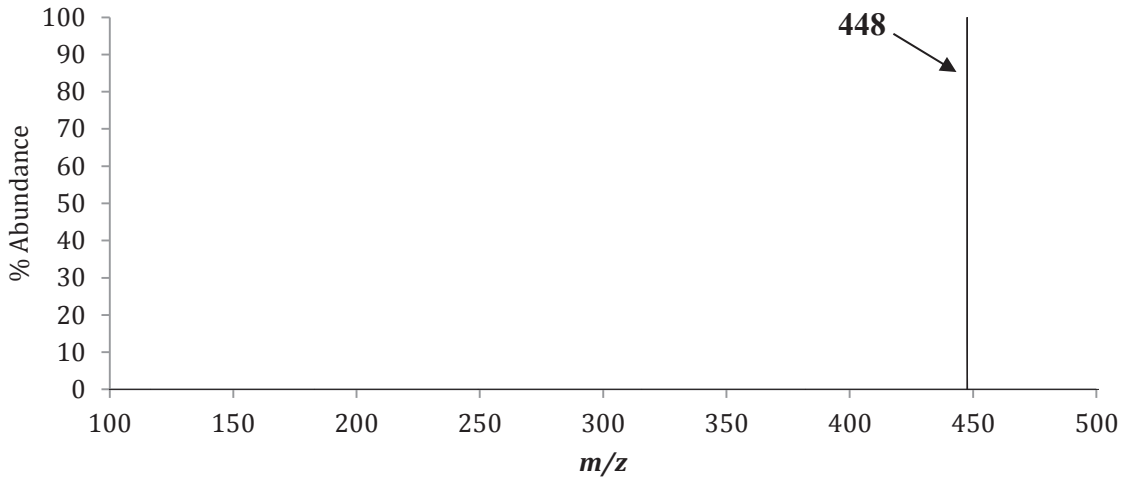

Figure 7.13: The positive mass spectrum obtained by scanning the third quadrupole following the selective reaction of *m/z* = 364 ($[Ni(tfac)_2]^+$) with neutral $Pd(tftm)_2$ to produce the complete ligand exchange product $[Ni(tftm)_2]^+$ at *m/z* 448.

The proposed mechanism for the gas-phase formation of the nickel complete ligand exchange product $[Ni(tftm)_2]^+$ is presented in Equation 7.9.

$$[Ni(tfac)(tfac)]^+ + Pd(tftm)(tftm) \rightarrow [Ni(tftm)(tftm)]^+ + Pd(tfac)(tfac) \qquad \text{(Eqn 7.9)}$$

The single ligand exchange species $[Ni(tftm)]^+$ at *m/z* 253 was also formed from mass-selecting $[Ni(tfac)_2]^+$ at *m/z* 364 reacting with neutral $Pd(tftm)_2$, and is displayed in Figure 7.14.

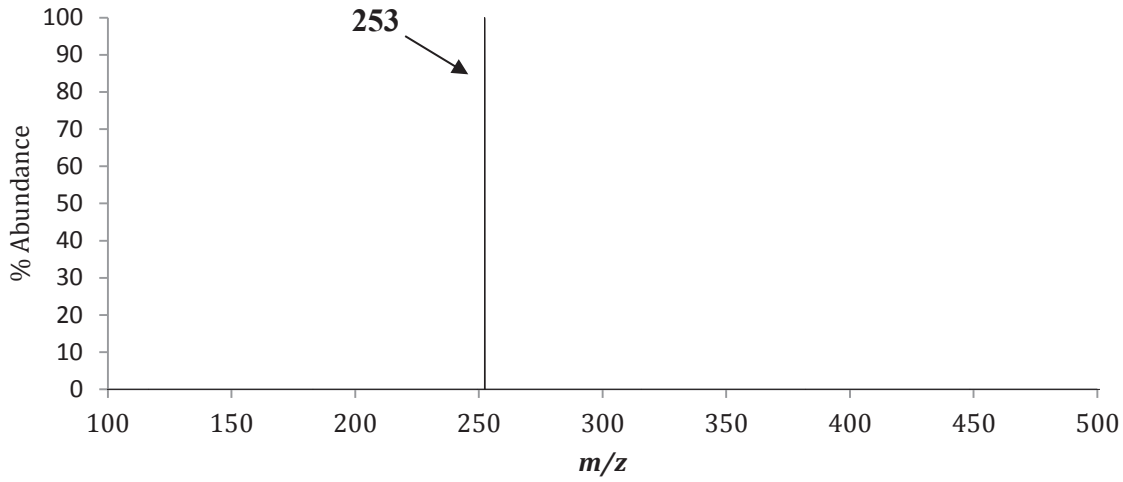

Figure 7.14: The positive mass spectrum obtained by scanning the third quadrupole following the selective reaction of *m/z* = 364 ($[Ni(tfac)_2]^+$) with neutral $Pd(tftm)_2$ to produce the partial ligand exchange product $[Ni(tftm)]^+$ at *m/z* 253.

The proposed mechanism for the gas-phase formation of the nickel single ligand exchange product $[Ni(tftm)]^+$ is presented in Equation 7.10.

$$[Ni(tfac)(tfac)]^+ + Pd(tftm)(tftm) \rightarrow [Ni(tftm)]^+ + Pd(tfac)(tfac) + (tftm) \qquad \text{(Eqn 7.10)}$$

A third product of interest was generated following the reaction of neutral $Pd(tftm)_2$ with mass-selected $[Ni(tfac)]^+$ at *m/z* 211. The product, $[Ni(tfac)(tftm\text{-}tBu)]^+$, is present at *m/z* 349 and is displayed in Figure 7.15.

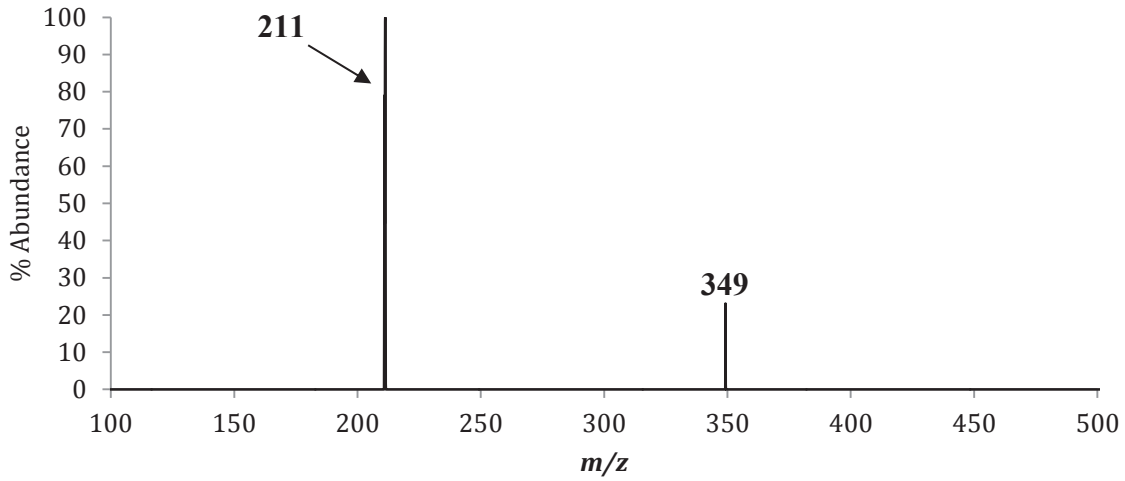

Figure 7.15: The positive mass spectrum obtained by scanning the third quadrupole following the selective reaction of *m/z* = 211 ($[Ni(tfac)]^+$) with neutral $Pd(tftm)_2$ to produce the mixed ligand exchange fragment $[Ni(tfac)(tftm\text{-}tBu)]^+$ at *m/z* 349.

The proposed mechanism for the gas-phase formation of the nickel mixed ligand exchange fragment $[Ni(tfac)(tftm\text{-}tBu)]^+$ is presented in Equation 7.11.

$$[Ni(tfac)]^+ + Pd(tftm)(tftm) \rightarrow [Ni(tfac)(tftm\text{-}tBu)]^+ + Pd(tftm) + tBu \qquad \text{(Eqn 7.11)}$$

Other products generated following the mass-selected reaction of $[Ni(tfac)]^+$ at *m/z* 211 with neutral $Pd(tftm)_2$ include $[Ni(tftm)]^+$ and $[Ni(tftm\text{-}CF_2)]^+$ at *m/z* 253 and 203, respectively, and are displayed in Figure 7.16.

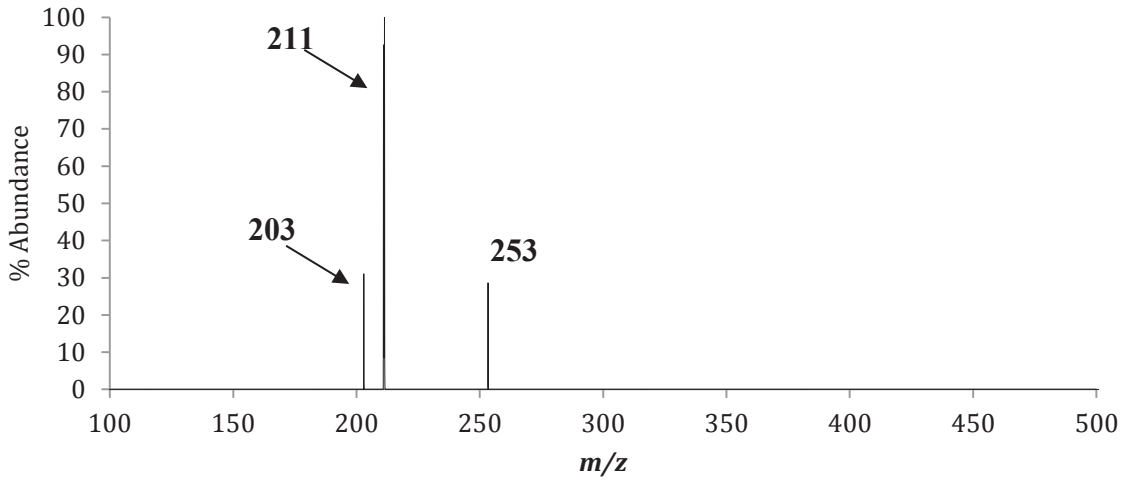

Figure 7.16: The positive mass spectrum obtained by scanning the third quadrupole following the selective reaction of *m/z* = 211 ($[Ni(tfac)]^+$) with neutral $Pd(tftm)_2$ to produce the partial ligand exchange product $[Ni(tftm)]^+$ at *m/z* 253 and the partial ligand exchange fragment $[Ni(tftm\text{-}CF_2)]^+$at *m/z* 203.

The proposed mechanisms for the gas-phase formation of the nickel single ligand exchange product $[Ni(tftm)]^+$ and the nickel single ligand exchange fragment $[Ni(tftm\text{-}CF_2)]^+$ are displayed in Equations 7.12 and 7.13.

$$[Ni(tfac)]^+ + Pd(tftm)(tftm) \rightarrow [Ni(tftm)]^+ + Pd(tfac)(tftm) \qquad \text{(Eqn 7.12)}$$

$$[Ni(tfac)]^+ + Pd(tftm)(tftm) \rightarrow [Ni(tftm\text{-}CF_2)]^+ + Pd(tfac)(tftm) + CF_2 \qquad \text{(Eqn 7.13)}$$

The final product generated from collision-induced reaction was $[Pd(tfac)(tftm)]^+$ at *m/z* 453, which was produced following the reaction of neutral $Pd(tftm)_2$ and $[Ni(tfac\text{-}CF_2)]^+$ at *m/z* 161 and is displayed in Figure 7.17.

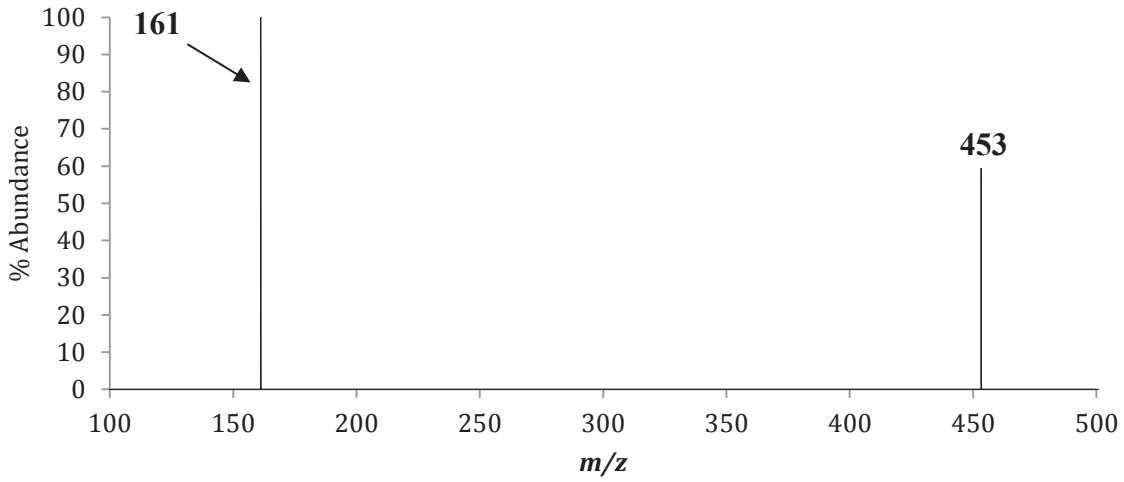

Figure 7.17: The positive mass spectrum obtained by scanning the third quadrupole following the selective reaction of *m/z* = 161 ($[Ni(tfac\text{-}CF_2)]^+$) with neutral $Pd(tftm)_2$ to produce the mixed ligand exchange product $[Pd(tfac)(tftm)]^+$ at *m/z* 453.

The proposed mechanism for the gas-phase formation of the palladium mixed ligand exchange product $[Pd(tfac)(tftm)]^+$ is presented in Equation 7.14.

$$[Ni(tfac\text{-}CF_2)]^+ + Pd(tftm)(tftm) + CF_2 \rightarrow [Pd(tfac)(tftm)]^+ + Ni(tftm) \qquad \text{(Eqn 7.14)}$$

The spectra displayed in this Chapter provide much novel insight into the mechanism of ligand exchange between $Pd(tftm)_2$ and $Ni(tfac)_2$. Although additional work is necessary, the mechanisms reported herein have contributed new information into the process of ligand exchange between these two β-diketonates.

It was found that mass-selected $[Ni(tfac)_2]^+$ at *m/z* 364 promoted the formation of $[Ni(tftm)]^+$ at *m/z* 253 when reacted with neutral $Pd(tftm)_2$, while mass-selected $[Ni(tfac)]^+$ at *m/*z 211 contributed to the formation of three ligand exchange products, $[Ni(tfac)(tftm\text{-}tBu)]^+$ at *m/z* 349, $[Ni(tftm)]^+$ at *m/z* 253, and $[Ni(tftm\text{-}CF_2)]^+$ at *m/z* 203. Finally, mass-selected $[Ni(tfac\text{-}CF_2)]^+$ at *m/*z 161 reacting with neutral $Pd(tftm)_2$ appears

to promote the formation of $[Pd(tfac)(tftm)]^+$ at *m/z* 453. Interestingly, no pertinent ligand exchange products were detected from mass-selecting $[Ni(tftm\text{-}CF_3)(tftm)]^+$ at *m/z* 295.

Chapter 8

The Co-Sublimation Reactions of Calcium Bis-Acetylacetonate Complexes ($Ca(acac)_2$)

8.1 Introduction

Although much work has been done to evaluate ligand exchange between transition metal β-diketonate complexes, additional experiments are still necessary to understand the ligand exchange mechanisms of alkaline earth metal β-diketonate complexes. The previous Chapters have demonstrated ligand exchange between magnesium β-diketonate complexes and other selected transition metal β-diketonate complexes. In order to expand upon this growing body of knowledge, co-sublimation reactions were initiated using another alkaline earth metal, calcium, as the chelating metal of interest. Calcium maintains the same valency as magnesium (II) and like magnesium, also lacks occupied *d*-orbitals. However, calcium is much larger in comparison to magnesium and appears to undergo nucleation as well as additional ligand exchange processes.

Calcium, like the other metals described in earlier Chapters, exhibits a distinct isotopic pattern, which is easily recognizable on a mass spectrum. Only one naturally occurring isotope, ^{40}Ca, is observed with an abundance of 96.94%. Four other isotopes (^{42}Ca, ^{43}Ca, ^{44}Ca, and ^{46}Ca) are stable but observed at very low abundance. Therefore, calcium complexes are easily distinguished on a mass spectrum, making it an ideal candidate for co-sublimation exchange reactions.

8.2 Calcium Bis-Acetylacetonate ($Ca(acac)_2$)

The positive EI mass spectrum of calcium bis-acetylacetonate ($Ca(acac)_2$) is presented in Figure 8.1 and is reported for the first time. The intact $[Ca(acac)_2]^+$ species is present at *m/z* 238, as is $[Ca(acac)]^+$ at *m/z* 139. Only one fragmented ion, $[Ca(acac\text{-}CH_3)(acac)]^+$, is observed at *m/z* 223. Otherwise, $Ca(acac)_2$ does not readily fragment but instead forms larger cluster ions. Cluster ions are complexes in which more than one metal center is chelated to two or more ligands and are clearly displayed as separate peaks. In Figure 8.1, the peak at *m/z* 278 corresponds to the cluster ion $[Ca_2(acac)_2]^+$ while the peak at *m/z* 377 corresponds to $[Ca_2(acac)_3]^+$. The peak at *m/z* 476 is consistent with the assignment of $[Ca_2(acac)_4]^+$, as is $[Ca_3(acac)_5]^+$ at *m/z* 615. The relative abundances of these species are reported in Table 8.1.

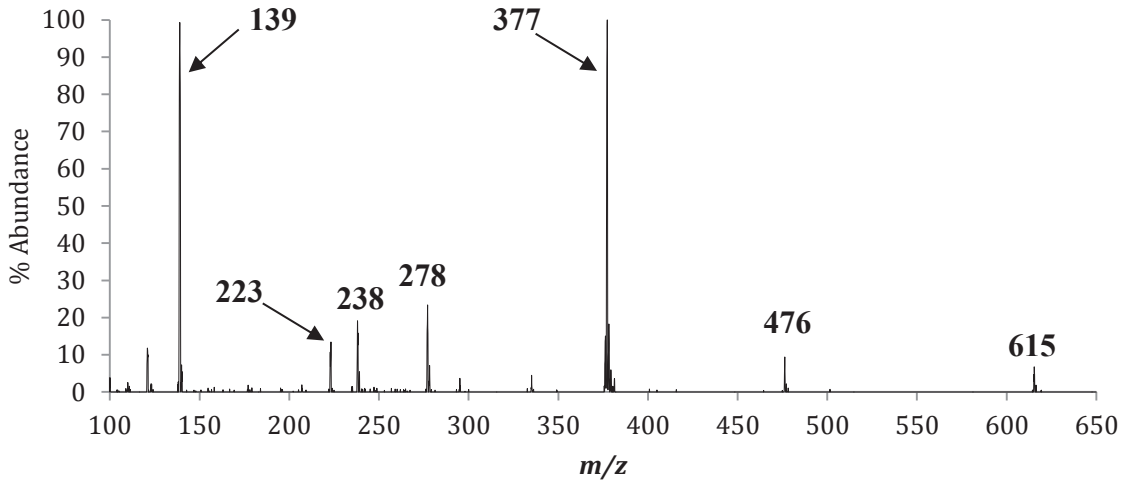

Figure 8.1: The 70 eV positive electron impact (EI) mass spectra of calcium bis-acetylacetonate, or $Ca(acac)_2$, and its corresponding clustering and fragmentation pattern.

Species	*m/z*	Relative Abundance
$[Ca(acac)]^+$	139	99
$[Ca(acac\text{-}CH_3)(acac)]^+$	223	13
$[Ca(acac)_2]^+$	238	16
$[Ca_2(acac)_2]^+$	278	23
$[Ca_2(acac)_3]^+$	377	100
$[Ca_2(acac)_4]^+$	476	9
$[Ca_3(acac)_5]^+$	615	7

Table 8.1: Clusters and relative positive ion intensities of the mass spectral analysis of $Ca(acac)_2$, as displayed in Figure 8.1.

8.3 The Co-Sublimation of $Ca(acac)_2$ and $Ni(eeac)_2$

The first transition metal β-diketonate subjected to co-sublimation reactions with $Ca(acac)_2$ was nickel bis-diethylacetylacetonate, or $Ni(eeac)_2$. The baseline spectra of $Ca(acac)_2$ and $Ni(eeac)_2$, and their respective co-sublimation spectrum is presented in Figure 8.2 (a)-(c). The spectrum in Figure 8.2(a) is reproduced from Figure 8.1, and will not be discussed further. The spectrum of $Ni(eeac)_2$ is reproduced from Figure 5.2(b) and will also not be discussed further.

The spectrum presented in Figure 8.3(c) displays the co-sublimation of $Ca(acac)_2$ and $Ni(eeac)_2$. The appearance of novel peaks is a clear indicator that gas-phase ligand exchange has indeed transpired. Both nickel and calcium ligand exchange species were identified. The peak at *m/z* 256 corresponds to the mass of the complete ligand exchange product $[Ni(acac)_2]^+$ and the peak at *m/z* 157 corresponds to the mass of the single ligand exchange product $[Ni(acac)]^+$. The nickel mixed ligand exchange product $[Ni(acac)(eeac)]^+$ is also present at *m/z* 283, but is isobaric with the parent species $[Ni(eeac\text{-}Et)(eeac)]^+$. Multiple calcium products were also generated during co-sublimation experiments, including $[Ca_2(eeac)_2]^+$ at *m/z* 334 and $[Ca_2(eeac)_3]^+$ at *m/z* 461.

Unlike the mass spectrum, fragmentation of the ligand is present at *m/z* 432, which corresponds to $[Ca_2(eeac\text{-}Et)(eeac)(eeac)]^+$. Curiously, a mixed ligand exchange cluster is also present at *m/z* 405, which corresponds to $[Ca_2(acac)_2(eeac)]^+$. Although the relative intensities are small, the peak at *m/z* 504 is consistent with the mixed ligand exchange cluster $[Ca_2(acac)_3(eeac)]^+$ and the peak at *m/z* 643 matches the expected mass for the mixed ligand exchange cluster $[Ca_3(acac)_4(eeac)]^+$. The relative abundances of each mass spectrum and the respective co-sublimation products are displayed in Table 8.2. Isobaric masses have been designated by italics.

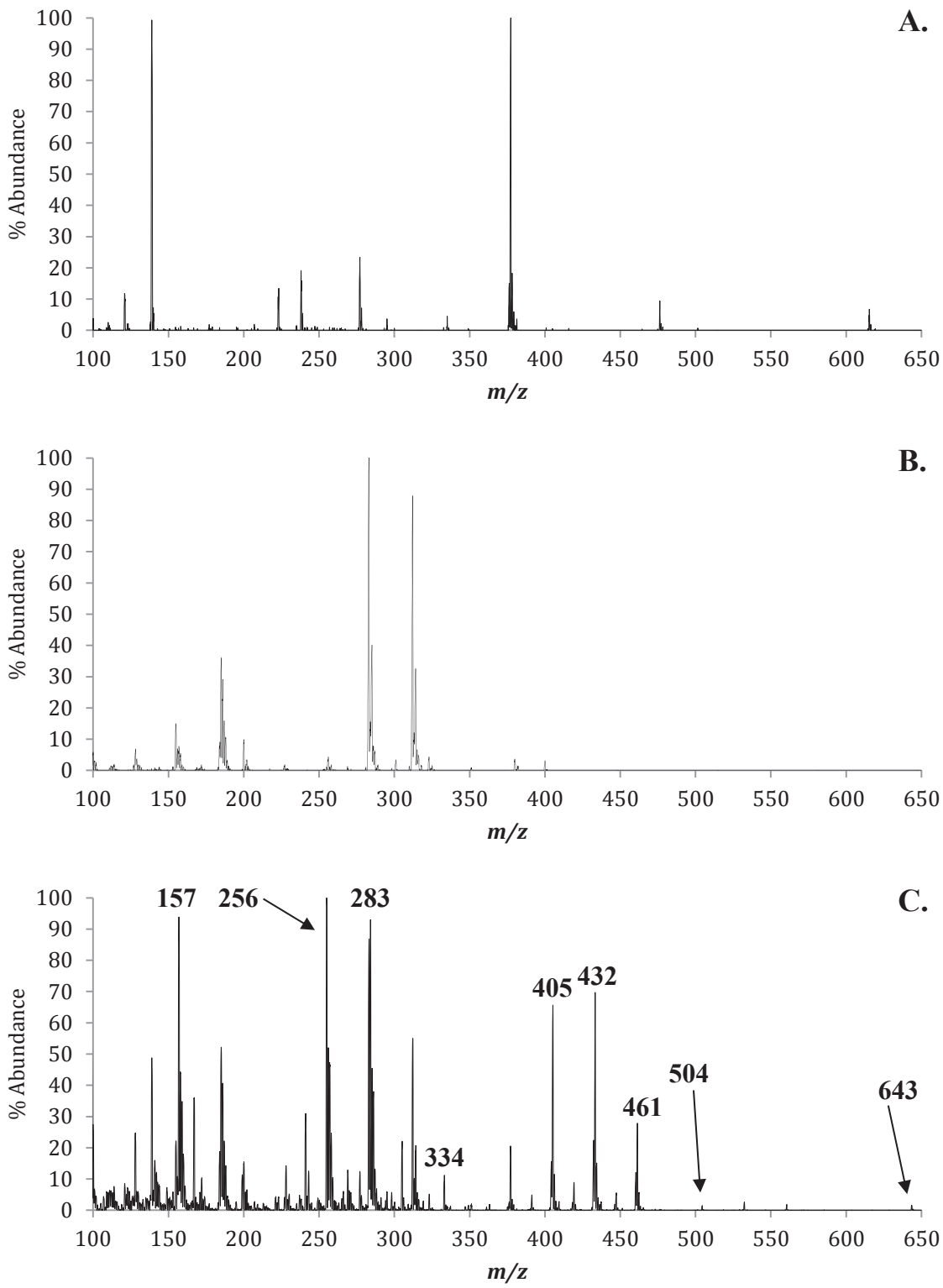

Figure 8.2(a)-(c): The positive EI mass spectra of (a) $Ca(acac)_2$, (b) $Ni(eeac)_2$, and (c) the gas-phase co-sublimation of $Ca(acac)_2$ and $Ni(eeac)_2$. The masses of parent compounds and fragments are labeled in (a) and (b). Masses of ligand exchange products and pertinent fragments and clusters are labeled in (c).

Species	Mass	Mass	CaL_2	NiL'_2	CaL & NiL'_2	CaL & NiL'_2
	Ca	Ni	Ca	Ni	Ca	Ni
$[ML]^+$	139	157	99		48	93
$[ML_2\text{-}CH_3]^+$	223	241	13		4	31
$[ML_2]^+$	238	256	16		3	52
$[M_2L_2]^+$	278	314	23		4	20
$[M_2L_3]^+$	377	413	100		20	<1
$[M_2L_4]^+$	476	512	9		<1	0
$[M_3L_5]^+$	615	-	7		0	-
$[ML']^+$	167	185		52	36	52
$[ML'\text{-}C_2H_5]^+$	138	156		10	4	10
$[ML'_2]^+$	294	312		74	3	55
$[ML'_2\text{-}C_2H_5]^+$	265	*283*		100	3	*86*
$[ML'_2\text{-}2C_2H_5]^+$	236	254		3	0	<1
$[M_2L'_2]^+$	334	372			1	0
$[M_2L_2L']^+$	405	443			65	<1
$[M_2L'_3]^+$	461	499			27	<1
$[M_2L'_3\text{-}C_2H_5]^+$	432	470			70	0
$[M_2L_3L']^+$	504	542			1	0
$[M_3L_4L']^+$	643	-			2	-
$[MLL']^+$	266	*283*			6	*86*

Table 8.2: The relative mass spectrometric abundances of the $Ca(acac)_2$ and $Ni(eeac)_2$ β-diketonate complexes as well as the co-sublimation experiment, as presented in Figure 8.2(a)-(c). L = (acac); L' = (eeac).

8.4 The Co-Sublimation of $Ca(acac)_2$ and $Mg(eeac)_2$

The next compound selected for co-sublimation with $Ca(acac)_2$ was another alkaline earth metal β-diketonate, magnesium bis-diethylacetylacetonate, or $Mg(eeac)_2$. The positive EI mass spectra of $Ca(acac)_2$ and $Mg(eeac)_2$ are displayed in Figure 8.3 (a)

and (b), with the respective co-sublimation spectrum displayed in Figure 8.3(c). One can clearly see that novel peaks are present on the co-sublimation spectrum, which is a clear indicator of gas-phase ligand exchange. The spectrum in Figure 8.3(a) is the same baseline spectrum of $Ca(acac)_2$ presented in Figure 8.1 and will not be discussed further. The spectrum presented in Figure 8.3(b) displays the baseline spectrum for $Mg(eeac)_2$, which is also repeated from Figure 3.1 and will not be discussed further.

Figure 8.3(c) displays the co-sublimation spectrum of $Ca(acac)_2$ and $Mg(eeac)_2$ and curiously, only one calcium and three magnesium ligand exchange products were formed. The peak at *m/z* 222 corresponds with the mass of the complete ligand exchange product $[Mg(acac)_2]^+$, while loss of a methyl group to form $[Mg(acac\text{-}CH_3)(acac)]^+$ is present at *m/z* 207. Also present is the magnesium single ligand exchange product $[Mg(acac)]^+$ at *m/z* 123, as well as the only calcium ligand exchange product cluster ion $[Ca_2(acac)]^+$, which is present at *m/z* 180. The respective abundance of each species is presented in Table 8.3. While co-sublimation reactions can verify that ligand exchange does indeed occur, collision-induced reaction with tandem mass spectrometry would provide much more information into the mechanism through which this exchange occurs.

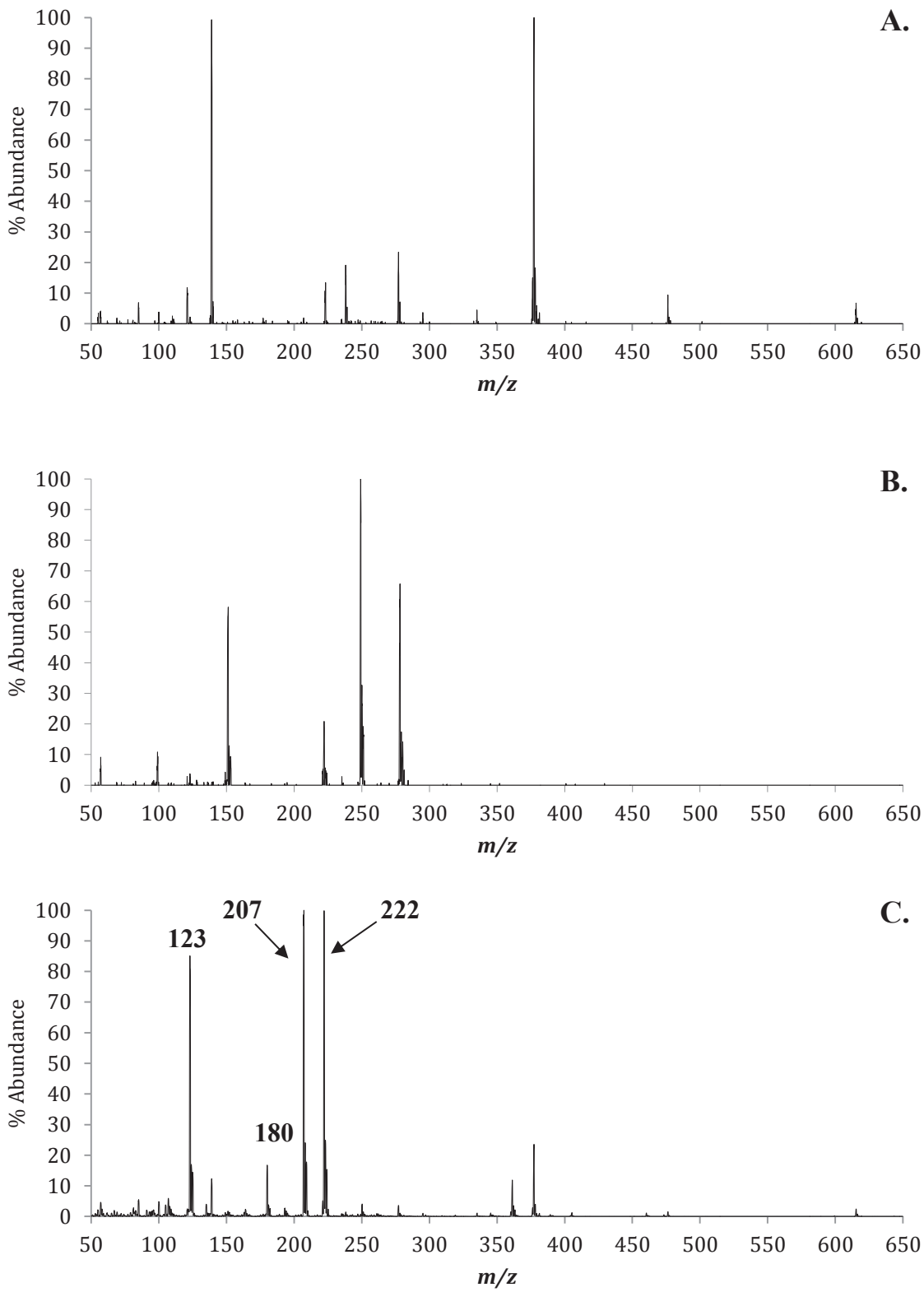

Figure 8.3(a)-(c): The positive EI mass spectra of (a) $Ca(acac)_2$, (b) $Mg(eeac)_2$, and (c) the gas-phase co-sublimation of $Ca(acac)_2$ and $Mg(eeac)_2$. The masses of parent compounds and fragments are labeled in (a) and (b). Masses of ligand exchange products and pertinent fragments and clusters are labeled in (c).

	Mass	Mass	CaL_2	MgL'_2	CaL_2 & MgL'_2	CaL_2 & MgL'_2
Species	**Ca**	**Mg**	**Ca**	**Mg**	**Ca**	**Mg**
$[ML]^+$	139	123	99		1	85
$[ML_2\text{-}CH_3]^+$	223	207	13		24	100
$[ML_2]^+$	238	*222*	*16*		1	*99*
$[M_2L_2]^+$	278	246	23		3	<1
$[M_2L_3]^+$	377	345	100		23	<1
$[M_2L_4]^+$	476	444	9		1	0
$[M_3L_5]^+$	615	583	7		<1	<1
$[ML'_2]^+$	294	278		65	<1	<1
$[ML'_2\text{-}C_2H_5]^+$	265	249		100	<1	<1
$[ML'_2\text{-}2C_2H_5\text{+}2H]^+$	-	*222*		20	-	*99*
$[ML]^+$	167	151		10	<1	1
$[ML'\text{-}C_2H_5]^+$	138	136		<1	<1	1
$[MLL']^+$	266	250			<1	1
$[M_2L]^+$	180	147			16	<1

Table 8.3: The relative mass spectrometric abundances of the $Ca(acac)_2$ and $Mg(eeac)_2$ β-diketonate complexes as well as the co-sublimation experiment, as presented in Figure 8.3(a)-(c). L = (acac); L' = (eeac).

8.5 The Co-Sublimation of $Ca(acac)_2$ and $Cu(eeac)_2$

The next compound selected for co-sublimation with $Ca(acac)_2$ was copper bis-diethylaetylacetonate ($Cu(eeac)_2$). The positive EI mass spectra of $Ca(acac)_2$ and $Cu(eeac)_2$ are presented in Figure 8.4(a) and 8.4(b), with the respective co-sublimation spectrum presented in Figure 8.4(c). The spectra are stacked vertically for ease of clarity and comparison, and the appearance of novel peaks is a clear indicator that gas-phase ligand exchange has indeed occurred. The spectrum in Figure 8.4(a) is the same $Ca(acac)_2$ spectrum presented in Figure 8.1 and will not be discussed further. The

spectrum presented in Figure 8.4(b) is the spectrum for $Cu(eeac)_2$, which is reproduced from Figure 6.1(b) and will also not be discussed further.

The co-sublimation spectrum of $Ca(acac)_2$ and $Cu(eeac)_2$ is displayed in Figure 8.4(c), in which only copper ligand exchange products were generated. The complete ligand exchange product $[Cu(acac)_2]^+$ is displayed at *m/z* 261, with loss of a first methyl group to form $[Cu(acac\text{-}CH_3)(acac)]^+$ at *m/z* 246 and loss of a second methyl group to form $[Cu(acac\text{-}CH_3)(acac\text{-}CH_3)]^+$ at *m/z* 231. The single ligand exchange species $[Cu(acac)]^+$ is also displayed at *m/z* 162, with subsequent loss of a methyl group to form $[Cu(acac\text{-}CH_3)]^+$ depicted at *m/z* 147. Finally, the intact copper mixed ligand exchange species $[Cu(acac)(eeac)]^+$ is present at *m/z* 289. The relative abundance of each of these species is displayed in Table 8.4. While co-sublimation reactions can verify the occurrence of gas-phase ligand exchange, collision-induced reaction analysis with tandem mass spectrometry would provide a far more complete picture of the mechanism by which it proceeds.

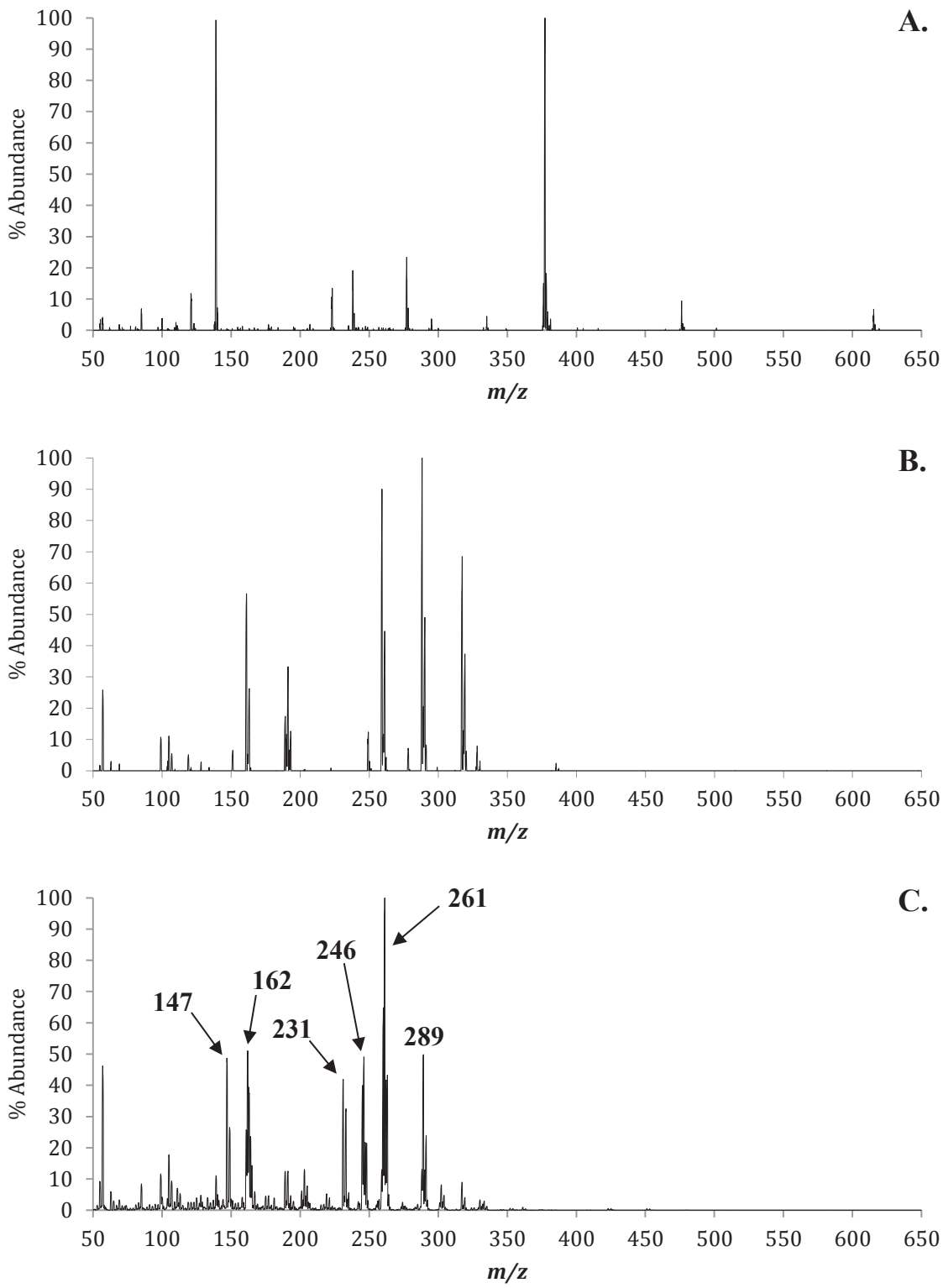

Figure 8.4(a)-(c): The positive EI mass spectra of (a) $Ca(acac)_2$, (b) $Cu(eeac)_2$, and (c) the gas-phase co-sublimation of $Ca(acac)_2$ and $Cu(eeac)_2$. The masses of parent compounds and fragments are labeled in (a) and (b). Masses of ligand exchange products and pertinent fragments and clusters are labeled in (c).

	Mass	Mass	CaL_2	CuL'_2	CaL_2 & CuL'_2	CaL_2 & CuL'_2
Species	**Ca**	**Cu**	**Ca**	**Cu**	**Ca**	**Cu**
$[ML-CH_3]^+$	124	147	<1		<1	48
$[ML]^+$	139	162	99		11	51
$[ML_2]^+$	238	261	16		<1	100
$[ML_2-CH_3]^+$	223	246	13		<1	49
$[ML_2-2CH_3]^+$	208	231	0		<1	40
$[M_2L_2]^+$	278	324	23		<1	<1
$[M_2L_3]^+$	377	423	100		<1	<1
$[M_2L_4]^+$	476	522	9		<1	0
$[M_3L_5]^+$	615	-	7		0	-
$[ML'_2]^+$	294	317		69	<1	9
$[ML'_2-C_2H_5]^+$	265	288		100	1	13
$[ML'_2-2C_2H_5]^+$	236	259		90	<1	13
$[ML]^+$	167	190		11	6	3
$[ML'-C_2H_5]^+$	138	161		57	<1	50
$[MLL']^+$	266	289			<1	49

Table 8.4: The relative mass spectrometric abundances of the $Ca(acac)_2$ and $Cu(eeac)_2$ β-diketonate complexes as well as the co-sublimation experiment, as presented in Figure 8.4(a)-(c). L = (acac); L' = (eeac).

8.6 The Co-Sublimation of $Ca(acac)_2$ and Cobalt Bis-Diethylacetylacetonate ($Co(eeac)_2$)

The next compound selected for co-sublimation with $Ca(acac)_2$ was cobalt bis-diethylacetylacetonate ($Co(eeac)_2$). The positive EI mass spectra of $Ca(acac)_2$ and $Co(eeac)_2$ are presented in Figure 8.5(a) and (b), respectively, and the spectrum depicting their co-sublimation is presented in Figure 8.5(c). The spectra are stacked vertically for purposes of clarity and comparison, and the incidence of new peaks is a clear indicator that gas-phase ligand exchange has indeed occurred. Figure 8.5(a) is the $Ca(acac)_2$

spectrum reproduced from Figure 8.1 and will not be discussed further. The spectrum presented in Figure 8.5(b) is the baseline mass spectrum for $Co(eeac)_2$. Intact $[Co(eeac)_3]^+$ is displayed at *m/z* 440, with loss of one *eeac* ligand to generate $[Co(eeac)_2]^+$ at *m/z* 313. Loss of one ethyl group from $[Co(eeac)_2]^+$ to form $[Co(eeac\text{-}Et)(eeac)]^+$ is present at *m/z* 284, with loss of a second ethyl group to form $[Co(eeac\text{-}Et)(eeac\text{-}Et)]^+$ at *m/z* 256. Finally, the single ligand species $[Co(eeac)]^+$ is displayed at *m/z* 186.

The co-sublimation of $Ca(acac)_2$ and $Co(eeac)_2$ is displayed in Figure 8.5(c), and both calcium and cobalt ligand exchange species are generated. The cobalt complete ligand exchange product $[Co(acac)_2]^+$ is displayed at *m/z* 257, with loss of a methyl group to form $[Co(acac\text{-}CH_3)(acac)]^+$ at *m/z* 242. The single ligand exchange species $[Co(acac)]^+$ is also displayed at *m/z* 158, and the mixed ligand exchange species $[Co(acac)(eeac)]^+$ is present at *m/z* 285. Calcium ligand exchange products were also generated, all of which were in the form of cluster ions. The ligand exchange cluster $[Ca_2(eeac)_2]^+$ is displayed at *m/z* 335, albeit in low abundance while the second cluster ion, $[Ca_2(acac)_2(eeac)]^+$, corresponds to the peak at *m/z* 405. Finally, the peak at *m/z* 644 corresponds to the mass of the cluster ion $[Ca_3(acac)_4(eeac)]^+$. The respective abundances of all species reported herein are presented in Table 8.5. Although co-sublimation is a helpful tool to evaluate the occurrence of ligand exchange, a more complete picture of the mechanism could be provided by collision-induced reaction analysis utilizing the triple quadrupole mass spectrometer with tandem mass spectrometry.

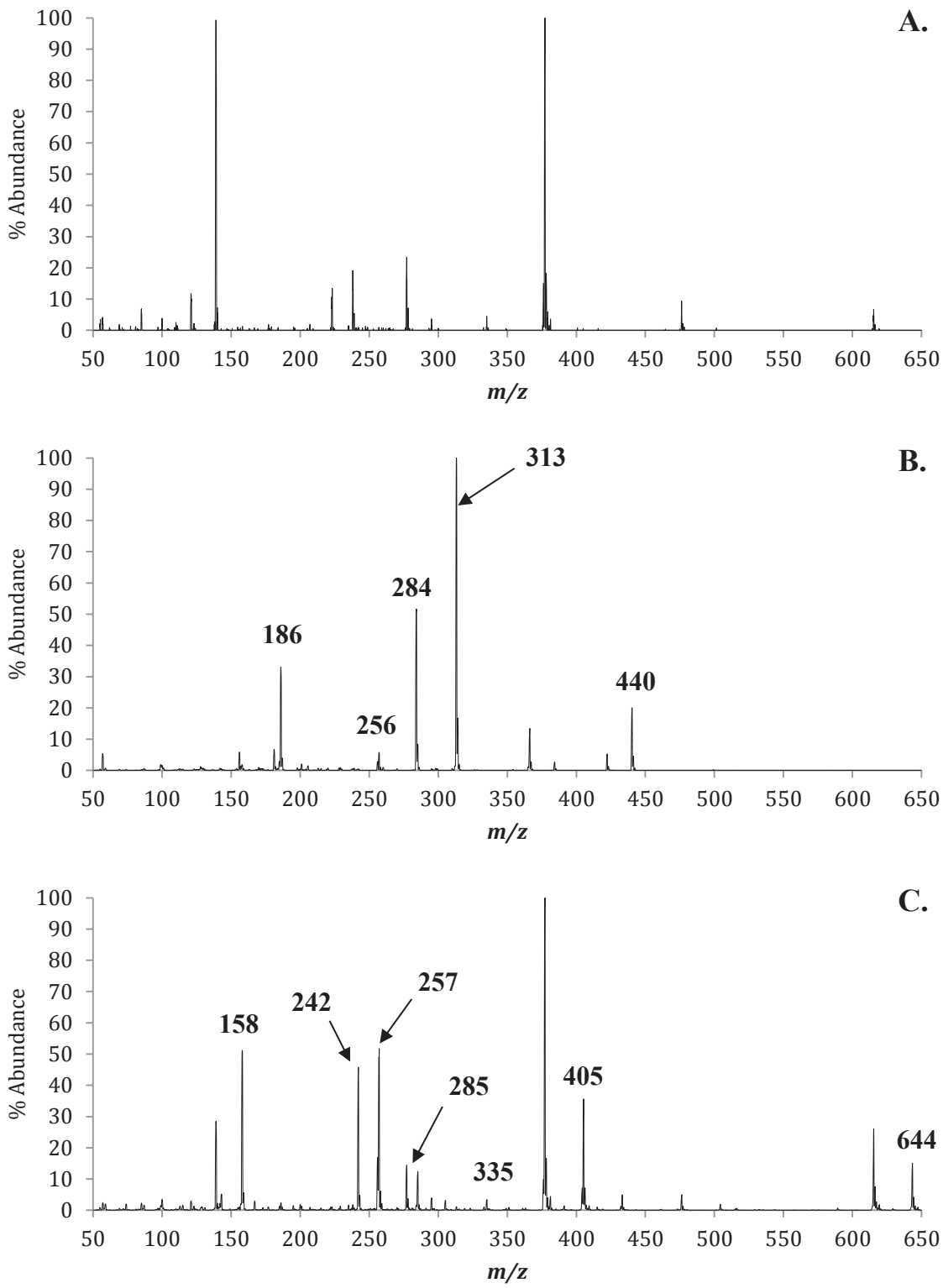

Figure 8.5(a)-(c): The positive EI mass spectra of (a) $Ca(acac)_2$, (b) $Co(eeac)_2$, and (c) the gas-phase co-sublimation of $Ca(acac)_2$ and $Co(eeac)_2$. The masses of parent compounds and fragments are labeled in (a) and (b). Masses of ligand exchange products and pertinent fragments and clusters are labeled in (c).

Species	Mass	Mass	CaL_2	CoL'_2	CaL_2 & CoL'_2	CaL_2& CoL'_2
	Ca	Co	Ca	Co	Ca	Co
$[ML]^+$	139	158	99		28	51
$[ML\text{-}CH_3]^+$	124	143	<1		<1	5
$[ML_2]^+$	238	257	16		2	51
$[ML_2\text{-}CH_3]^+$	223	242	1		<1	45
$[ML_2\text{-}2CH_3]^+$	208	227	0		<1	<1
$[M_2L_2]^+$	278	316	23		3	<1
$[M_2L_3]^+$	377	415	100		100	1
$[M_2L_4]^+$	476	514	9		5	<1
$[M_3L_5]^+$	615	-	7		26	-
$[ML'_3]^+$	421	440		20	<1	<1
$[ML'_2]^+$	294	313		100	<1	1
$[ML'_2\text{-}C_2H_5]^+$	265	284		51	<1	1
$[ML'_2\text{-}2C_2H_5]^+$	236	256		3	<1	16
$[ML']^+$	167	186		33	3	<1
$[ML'\text{-}C_2H_5]^+$	138	157		1	<1	2
$[MLL']^+$	266	285			<1	12
$[M_2L'_2]^+$	335	372			3	<1
$[M_2L_2L']^+$	405	443			35	<1
$[M_2L_3L']^+$	504	542			2	<1
$[M_3L_4L']^+$	644	-			15	-

Table 8.5: The relative mass spectrometric abundances of the $Ca(acac)_2$ and $Co(eeac)_2$ β-diketonate complexes as well as the co-sublimation experiment, as presented in Figure 8.4(a)-(c). L = (acac); L' = (eeac).

8.7 The Co-Sublimation of $Ca(acac)_2$ and Manganese Bis-Dibenzoylmethane ($Mn(dbm)_2$)

The next compound selected for co-sublimation with $Ca(acac)_2$ was manganese bis-dibenzoylmethane, or $Mn(dbm)_2$. The positive EI mass spectra of $Ca(acac)_2$ and $Mn(dbm)_2$ are presented in Figure 8.6(a) and (b), and the resulting co-sublimation mass spectrum is displayed in Figure 8.6(c). The incidence of novel peaks on the co-sublimation spectrum is a strong indicator that ligand exchange has occurred. The spectrum presented in Figure 8.6(a) is reproduced from Figure 8.1 and will not be discussed further. The spectrum presented in Figure 8.6(b) is the baseline mass spectrum for $Mn(dbm)_2$, which reveals two peaks of interest. The peak at *m/z* 501 corresponds to the mass of intact $[Mn(dbm)_2]^+$, and the single ligand species $[Mn(dbm)]^+$ is present at *m/z* 278.

The co-sublimation spectrum for $Ca(acac)_2$ and $Mn(dbm)_2$ displayed in Figure 8.6(c) demonstrates that only manganese ligand exchange products were generated. The peak at *m/z* 253 corresponds to the species $[Mn(acac)_2]^+$, with loss of a methyl group to form $[Mn(acac\text{-}CH_3)(acac)]^+$ at *m/z* 238 and the single ligand species $[Mn(acac)]^+$ displayed at *m/z* 154. The peak at *m/z* 377 is isobaric for the manganese mixed ligand exchange species $[Mn(acac)(dbm)]^+$ and $[Ca_2(acac)_3]^+$, which is the most abundant peak on the $[Ca(acac)_2]^+$ spectrum. The relative abundances of all the species discussed herein are presented in Table 8.6. Collision-induced reactions of the most abundant species in the mass spectra for $Ca(acac)_2$ and $Mn(dbm)_2$ would provide much novel information about the mechanism of ligand exchange between these two β-diketonates.

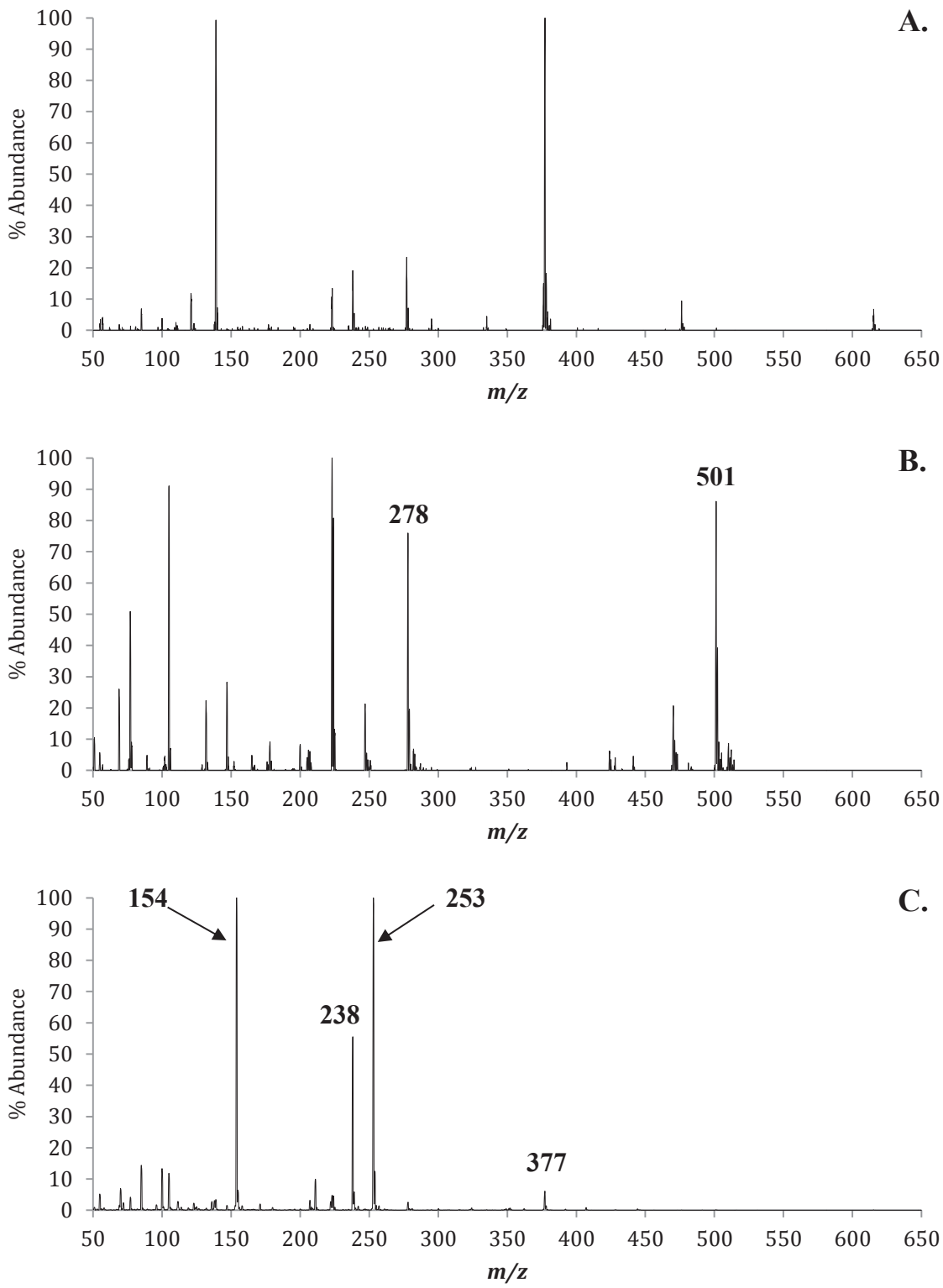

Figure 8.6(a)-(c): The positive EI mass spectra of (a) $Ca(acac)_2$, (b) $Mn(dbm)_2$, and (c) the gas-phase co-sublimation of $Ca(acac)_2$ and $Mn(dbm)_2$. The masses of parent compounds and fragments are labeled in (a) and (b). Masses of ligand exchange products and pertinent fragments and clusters are labeled in (c).

Species	Mass	Mass	CaL_2	MnL''_2	CaL_2& MnL''_2	CaL_2& MnL''_2
	Ca	Mn	Ca	Mn	Ca	Mn
$[ML]^+$	139	154	99		3	100
$[ML\text{-}CH_3]^+$	124	139	<1		<1	3
$[ML_2]^+$	238	253	16		55	99
$[ML_2\text{-}CH_3]^+$	223	238	1		5	55
$[ML_2\text{-}2CH_3]^+$	208	223	0		<1	5
$[M_2L_2]^+$	278	308	23		2	<1
$[M_2L_3]^+$	377	407	100		6	<1
$[M_2L_4]^+$	476	506	9		<1	0
$[M_3L_5]^+$	615	-	7		<1	-
$[ML''_2]^+$	486	501		86	0	<1
$[ML'']^+$	263	278		76	<1	2
$[MLL'']^+$	362	377			<1	6

Table 8.6: The relative mass spectrometric abundances of the $Ca(acac)_2$ and $Mn(dbm)_2$ β-diketonate complexes as well as the co-sublimation experiment, as presented in Figure 8.6(a)-(c). L = (acac); L'' = (dbm).

Chapter 9

Conclusions and Future Work

The work presented in the previous Chapters provides much new insight into the mechanism of ligand exchange between magnesium β-diketonates and nickel and copper β-diketonates. It also provides a more complete picture on the mechanism of ligand exchange between palladium and nickel β-diketonates, as well as new information into co-sublimation reactions involving calcium β-diketonates. However, there is still much work to be done to establish a foundation in the area of gas-phase ligand exchange between metal β-diketonates.

First, the possible combinations of metal β-diketonates cannot be overstated. The periodic table contains 6 alkali metals, 6 alkaline earth metals, 30 transition metals, 7 metalloids, and 7 other metals, all of which could theoretically utilized as chelators to different β-diketonate ligands. Moreover, variations in the functionalities of the β-diketonate ligands themselves generate even more potential combinations. Although the focus of this particular study has been magnesium, nickel, copper, palladium, and calcium β-diketonates, there are endless combinations of metals and ligands that are still available for co-sublimation and CIR analysis.

Second, there is not yet a report in the literature of deuterating a β-diketonate. This would allow certain fragments to be followed throughout a reaction profile and a better mechanism of action be elucidated. This could prove particularly insightful into not only fragmentation patterns but ligand exchange reaction and cluster ion formation as well.

Third, all of the previous work on β-diketonates has centered on cation electron impact mass spectrometry. However, no work has been done with β-diketonates as an anionic species. The setup of the experiments would be virtually the same as those reported herein, but the

instrument would be calibrated to detect negative ionic species instead of those with a positive charge. Modifying the mass spectrometer to detect negative ions could provide brand new insight on the mechanism of action for β-diketonates in the gas phase.

Finally, the EI mass spectra reported herein were obtained under an inert atmosphere, as are all examinations of β-diketonates in the literature. Never before has a group obtained spectra wherein β-diketonates exchange their ligands in the presence of a reactive gas, such as oxygen or ammonia. The gas would either be injected in the first quadrupole at the ionization source or evaporated in the second quadrupole. Regardless of how it is injected, mass-to-charge scanning and tandem mass spectrometry would be utilized to better understand how these compounds interact with each other and exchange their ligands in a reactive atmosphere.

Ultimately, this examination of the gas-phase ligand exchange of metal β-diketonate complexes is in its infancy stages. No previous work has been done to gas-phase ligand exchange, and there are many variables that must be studied to establish this foundation. Much of the future work on this project is conducted with the intent of building a foundation of knowledge for future groups to expand on, and hopefully the research reported herein has aided in this endeavor.

References

1. Lerach, J. O. Investigations into the Gas-Phase Rearrangements of Some Transition Metal β-Diketonate Complexes. (Youngstown State University, 2008).
2. Binnemans, K. Rare-Earth Beta-Diketonates, Vol. 35. *Handb. Phys. Chem. Rare Earths* **35,** 107–272 (2005).
3. Wilson, J. J. & Lippard, S. J. In Vitro Anticancer Activity of cis-Diammineplatinum(II) Complexes with beta-Diketonate Leaving Group Ligands. *J. Med. Chem.* **55,** 5326–5336 (2012).
4. Sun, J., Song, B., Ye, Z. & Yuan, J. Mitochondria Targetable Time-Gated Luminescence Probe for Singlet Oxygen Based on a β-Diketonate–Europium Complex. *Inorg. Chem.* **54,** 11660–11668 (2015).
5. Reyes, R., Cremona, M., Teotonio, E. E. S., Brito, H. F. & Malta, O. L. Molecular electrophosphorescence in (Sm, Gd)-β-diketonate complex blend for OLED applications. *J. Lumin.* **134,** 369–373 (2013).
6. Archives of Materials Science and Engineering. Available at: http://www.archivesmse.org/. (Accessed: 3rd March 2016)
7. Hänninen, P. & Härmä, H. *Lanthanide Luminescence: Photophysical, Analytical and Biological Aspects*. (Springer Science & Business Media, 2011).
8. Adachi, C., Baldo, M. A., Thompson, M. E. & Forrest, S. R. Nearly 100% internal phosphorescence efficiency in an organic light-emitting device. *J. Appl. Phys.* **90,** 5048–5051 (2001).
9. New photo-stable lanthanide complexes for OLED display and lighting applications. *Isis Innovation* Available at: http://isis-innovation.com/licence-details/new-photo-

stable-lanthanide-complexes-oled-display-lighting-applications/. (Accessed: 3rd March 2016)

10. PLOS ONE: Faster Synthesis of Beta-Diketonate Ternary Europium Complexes: Elapsed Times & Reaction Yields. Available at: http://journals.plos.org/plosone/article?id=10.1371/journal.pone.0143998. (Accessed: 3rd March 2016)
11. Zhu, X. L., Sun, J. X., Yu, X. M., Wong, M. & Kwok, H. S. 29.3: Very Bright and Efficient Top-Emitting OLED with Ultra-Thin Yb as Effective Electron Injector. *SID Symp. Dig. Tech. Pap.* **37,** 1292–1295 (2006).
12. Küster, T. *et al.* A New Promising Application for Highly Cytotoxic Metal Compounds: η6-Areneruthenium(II) Phosphite Complexes for the Treatment of Alveolar Echinococcosis. *J. Med. Chem.* **55,** 4178–4188 (2012).
13. Bischoff, H., Berger, M. R., Keppler, B. K. & Schmähl, D. Efficacy of β-diketonato complexes of titanium, zirconium, and hafnium against chemically induced autochthonous colonic tumors in rats. *J. Cancer Res. Clin. Oncol.* **113,** 446–450 (1987).
14. Vock, C. A., Renfrew, A. K., Scopelliti, R., Juillerat-Jeanneret, L. & Dyson, P. J. Influence of the Diketonato Ligand on the Cytotoxicities of [Ru(η6-p-cymene)(R2acac)(PTA)]+ Complexes (PTA = 1,3,5-triaza-7-phosphaadamantane). *Eur. J. Inorg. Chem.* **2008,** 1661–1671 (2008).
15. Kostova, I. Ruthenium complexes as anticancer agents. *Curr. Med. Chem.* **13,** 1085–1107 (2006).

16. Wu, A., Kennedy, D. C., Patrick, B. O. & James, B. R. Ruthenium(II) acetylacetonato–sulfoxide complexes. *Inorg. Chem. Commun.* **6,** 996–1000 (2003).
17. Lord, R. M. *et al.* Mechanistic and Cytotoxicity Studies of Group IV beta-Diketonate Complexes. *Chemmedchem* **9,** 1136–1139 (2014).
18. Pasko, S., Hubert-Pfalzgraf, L. G., Abrutis, A. & Vaissermann, J. Synthesis and molecular structures of cobalt(II) beta-diketonate complexes as new MOCVD precursors for cobalt oxide films. *Polyhedron* **23,** 735–741 (2004).
19. Tiitta, M. & Niinistou, L. Volatile Metal β-Diketonates: ALE and CVD precursors for electroluminescent device thin films. *Chem. Vap. Depos.* **3,** 167–182 (1997).
20. Chen, I.-S. *et al.* Metalorganic Chemical Vapor Deposition of Thin Film ZrO2 and Pb(Zr,Ti)O3: Precursor Chemistry and Process Characteristics. *Jpn. J. Appl. Phys.* **41,** 6695 (2002).
21. Song, H. Z., Wang, H. B., Zhang, J., Peng, D. K. & Meng, G. Y. Properties characterization of Ce(DPM)4 served as precursor for MOCVD. *Mater. Res. Bull.* **37,** 1487–1497 (2002).
22. Yamane, H. *et al.* Y-Ba-Cu-O superconducting films prepared on SrTiO3 substrates by chemical vapor deposition. *Appl. Phys. Lett.* **53,** 1548–1550 (1988).
23. Dickinson, P. H. *et al.* Chemical vapor deposition of YBa2Cu3O7−x superconducting films. *J. Appl. Phys.* **66,** 444–447 (1989).
24. Langlet, M. & Shannon, R. D. Nd2O3 thin films deposited by a new chemical vapour deposition technique. *Thin Solid Films* **186,** L1–L5 (1990).
25. Thin film growth of gadolinia by metal-organic chemical vapour deposition (MOCVD). Available at:

http://www.sciencedirect.com/science/article/pii/S0040609095085130. (Accessed: 17th March 2016)

26. Sloop, J. C. *et al.* Keto–enol and enol–enol tautomerism in trifluoromethyl-β-diketones. *J. Fluor. Chem.* **127,** 780–786 (2006).
27. Macdonald, C. & Shannon, J. Mass spectrometry and structures of metal acetylacetonate vapours. *Aust. J. Chem.* **19,** 1545–1566 (1966).
28. Dean, L. K. L., DiDonato, G. C., Wood, T. D. & Busch, K. L. Cluster ions in the electron and chemical ionization mass spectra of transition-metal acetylacetonates. *Inorg. Chem.* **27,** 4622–4627 (1988).
29. Wyatt, M. F., Havard, S., Stein, B. K. & Brenton, A. G. Analysis of transition-metal acetylacetonate complexes by matrix-assisted laser desorption/ionization time-of-flight mass spectrometry. *Rapid Commun. Mass Spectrom.* **22,** 11–18 (2008).
30. Saraswathi, M. & Miller, J. Fast-Atom-Bombardment Mass-Spectrometry of 2,4-Diketonate Complexes of Transition-Metals [v(iii), Cr(iii), Mn(iii), Fe(iii), Co(iii) Ru(iii) and Os(iii)]. *Rapid Commun. Mass Spectrom.* **9,** 1101–1105 (1995).
31. Hunter, G. O. & Leskiw, B. D. The gas-phase ligand exchange reactions of cobalt and zinc acetylacetonate, hexafluoroacetylacetonate, and trifluorotrimethylacetylacetonate complexes. *Rapid Commun. Mass Spectrom.* **26,** 369–376 (2012).
32. Hunter, G. O., Lerach, J. O., Lockso, T. R. & Leskiw, B. D. The gas-phase ligand exchange of copper and nickel acetylacetonate, hexafluoroacetylacetonate and trifluorotrimethylacetylacetonate complexes. *Rapid Commun. Mass Spectrom.* **24,** 129–137 (2010).

33. Gross, J. H. *Mass Spectrometry*. (Springer Berlin Heidelberg, 2011).

34. Schildcrout, S. High-Pressure Mass-Spectra and Gaseous Ion Chemistry of Metal Acetylacetonates. *J. Phys. Chem.* **80,** 2834–2838 (1976).

35. Macha, S. F., McCarley, T. D. & Limbach, P. A. Influence of ionization energy on charge-transfer ionization in matrix-assisted laser desorption/ionization mass spectrometry. *Anal. Chim. Acta* **397,** 235–245 (1999).

36. Watson, W. & Lin, C. Crystal Structure of Trisilver Dinitrate Tris(acetylacetonato)nickelate(2) Monohydrate. *Inorg. Chem.* **5,** 1074- (1966).

37. Hunter, G. O., Lerach, J. O., Lockso, T. R. & Leskiw, B. D. The gas-phase ligand exchange of copper and nickel acetylacetonate, hexafluoroacetylacetonate and trifluorotrimethylacetylacetonate complexes. *Rapid Commun. Mass Spectrom.* **24,** 129–137 (2010).

38. Lerach, J. O. & Leskiw, B. D. Gas-phase ligand exchange of select transition-metal acetylacetonate and hexafluoroacetylacetonate complexes. *Rapid Commun. Mass Spectrom.* **22,** 4139–4146 (2008).

Sources for Figures:

Figure 2.1: http://www.newworldencyclopedia.org/entry/File:Ms_block_schematic.gif

Figure 2.2: http://www.noble.org/plantbio/sumner/ionization-technique/

Figure 2.3: http://www.sigmaaldrich.com/technical-documents/articles/biology/custom-dna-oligos-qc-analysis-by-mass-spectrometry.html

Figure 2.4: http://www.analyticalspectroscopy.net/ap8-7.htm

Figure 2.5: http://www.bbioo.com/experiment/14-1273-7.html

Figure 2.6:

http://en.wikipedia.org/wiki/Electron_ionization#mediaviewer/File:Electron_Ionization.svg